2016

Modeling Embankment Breach Due To Overtopping

Ali Asghari Tabrizi
University of South Carolina

MODELING EMBANKMENT BREACH DUE TO OVERTOPPING

by

Ali Asghari Tabrizi

Bachelor of Science
Isfahan University of Technology, 2006

Master of Science
Shiraz University, 2009

Master of Science
University of California Los Angeles, 2011

Submitted in Partial Fulfillment of the Requirements

For the Degree of Doctor of Philosophy in

Civil Engineering

College of Engineering and Computing

University of South Carolina

2016

Accepted by:

M. Hanif Chaudhry, Major Professor

Jasim Imran, Committee Member

Shamia Hoque, Committee Member

Jamil Khan, Committee Member

Cheryl L. Addy, Vice Provost and Dean of the Graduate School

DEDICATION

I wish to express my gratitude to my mom Shahin, my dad Akbar, my wife Sara, my sister Negin, and my brother Nima for their continuous love and support. I would like to dedicate this dissertation to Iman Valizadeh and Jasmin Somborn.

ACKNOWLEDGEMENTS

The author would like to thank the National Science Foundation (NSF) and the SPARC Graduate Fellowship sponsored by the Office of the Vice President for Research University of South Carolina for the financial support to this study. Special thanks are extended to the Civil Engineering Research Institute for Cold Region, Hokkaido, Japan for providing their technical reports and other materials. The student Scholarship awarded by the United States Society on Dams (USSD) is greatly acknowledged. The author's great appreciation to Dr. M. Hanif Chaudhry, major professor of this research, for his invaluable support and guidance and to the distinguished members of the research committee: Drs. Jasim Imran, Enrica Viparelli, Jamil Khan, and Shamia Hoque for their input.

ABSTRACT

Despite numerous embankment failures around the world, in-depth assessments as well as reliable, comprehensive sets of data of such failures are limited. Detailed understanding of the earthen embankment failure process and the dominant parameters affecting the failure are needed to predict and model the breach process precisely. Therefore, a series of laboratory experiments on embankment (i.e., dam and levee) overtopping as well as erodibility measurements using the Submerged Jet test are conducted. Also, to study the influence of different model parameters (e.g., turbulence model, bedload formula), one of the dam embankment experiments is simulated. The main goal of this research is to quantitatively determine the failure process of earthen embankments due to overtopping and to investigate the effects of compaction and cohesion. Results of the current research are as follow: 1) For the non-cohesive dam breach tests with different levels of compaction, two dimensionless equations are developed to predict the variation of crest height and embankment bottom length with time as a function of dry density of the embankment material. A simple model assuming a triangular shaped embankment is proposed to predict the development of breach with time for different compaction levels of the embankment. Except during the initial stage of the failure, the match between the proposed model and the observed data is satisfactory. The proposed model for the crest height is also validated against a laboratory test reported in the literature and three dam failures in South Carolina during October 2015. 2) For the numerical simulation of the non-cohesive, non-compacted dam breach test, the

bedload transport formula is the main component. A comparison between the simulated and observed breach outflow hydrograph shows that the simulations and observations are in better agreement by using the Meyer-Peter and Muller (M.P.M.) formula than the Ashida and Michiue (A.M.) formula. However, the A.M. formula predicts better the bed and water surface profiles after the initial failure stage. 3) For the Jet tests of cohesive samples with different levels of compaction, erodibility varies over a wide range and the effects of compaction energy and water content on the erodibility coefficients are investigated. 4) For the non- cohesive, non-compacted levee breach tests, breach shape with time is measured using a sliding rod technique developed by the author, and water surface velocity distribution is recorded using particle image velocimetry. Breach outflow is also estimated by using a calibrated sharp-crested weir. Erodibility coefficients in both vertical and horizontal directions are determined from the experimental results and corresponding bed-load transport formulas are proposed. 5) For the laboratory investigation of the effects of hydraulic loads on the failure of non-cohesive, non-compacted levees, non-dimensional relations are proposed for the breach top width and depth. Moreover, a trapezoidal shape model is presented to predict the breach evolution. 6) The effects of compaction and cohesion on the failure of an overtopped levee are studied. From the results of the experiments, three non-dimensional relationships are developed which express the breach widening rate, breach deepening rate, and breach eroded-load as a function of the excess Shields number and compaction energy for non-cohesive levees. The proposed models of breach morphology compare satisfactorily with the results of the current laboratory tests. Furthermore, the levee material cohesion and specifically the clay content is found to be the dominant parameter controlling the failure

process. Based on the experimental observations, envelope curves are presented to express the effects of compaction and cohesion on the breach characteristics (i.e., breach depth, breach top width, breach eroded volume, breach total area, and breach submerged area).

TABLE OF CONTENTS

DEDICATION iii

ACKNOWLEDGEMENTS iv

ABSTRACT v

LIST OF TABLES xi

LIST OF FIGURES xii

CHAPTER 1 INTRODUCTION 1

1.1 EARTHEN EMBANKMENT 1

1.2 MOTIVATION AND OBJECTIVES 2

1.3 ORGANIZATION OF THE DISSERTATION 4

CHAPTER 2 LITERATURE REVIEW 5

2.1 EARTHEN DAM FAILURE 5

2.2 SOIL ERODIBILITY MEASUREMENTS USING THE SUBMERGED JET TEST 8

2.3 EARTHEN LEVEE FAILURE 10

CHAPTER 3 EXPERIMENTAL STUDY ON EMBANKMENT BREACH DUE TO OVERTOPPING: EFFECTS OF COMPACTION 11

3.1 EXPERIMENTAL SETUP 11

3.2 TEST PROCEDURE 12

3.3 RESULTS 14

CHAPTER 4 NUMERICAL MODELING OF EARTHEN DAM BREACH DUE TO OVERTOPPING: INFLUENCE OF DIFFERENT MODEL PARAMETERS 40

4.1 Experimental Setup 40

4.2 Test Procedure 41

4.3 Model Description 42

4.4 Results 47

Chapter 5 Investigating the Effect of Compaction Characteristics on the Erodibility of a Cohesive Soil Using the Jet Method 71

5.1 Test Procedure 71

5.2 Results 72

Chapter 6 Experimental Modeling of Levee Failure Process due to Overtopping 78

6.1 Experimental Setup 78

6.2 Measurement Methods 79

6.3 Results 81

Chapter 7 Experimental Modeling of Earthen Levee Failure by Overtopping: Effects of Hydraulic Loads 92

7.1 Experimental Setup 92

7.2 Test Procedure 93

7.3 Measurement Methods 94

7.4 Results 94

7.5 Analysis of Breach Characteristics 98

Chapter 8 Experimental Modeling of Earthen Levee Failure by Overtopping: Effects of Compaction and Cohesion 119

8.1 Experimental Description 119

8.2 Results for Compaction Effects 121

8.3 Results for Cohesion Effects 128

8.4 Comparing Compaction with Cohesion Effects 129

Chapter 9 Summary and Conclusions 159

9.1 Experimental Study on Embankment Breach due to Overtopping: Effects of Compaction 159

9.2 Numerical Modeling of Earthen Dam Breach due to Overtopping: Influence of Different Model Parameters 160

9.3 Investigating the Effect of Compaction Characteristics on the Erodibility of a Cohesive Soil Using the Jet Method 161

9.4 Experimental Modeling of Levee Failure Process due to Overtopping 161

9.5 Experimental Modeling of Earthen Levee Failure by Overtopping: Effects of Hydraulic Loads 162

9.6 Experimental Modeling of Earthen Levee Failure by Overtopping: Effects of Compaction and Cohesion 163

9.7 Recommendations 165

References 167

Appendix A: Permission to Reprint 173

LIST OF TABLES

Table 3.1 Numerical cases by various modeling parameters.....26

Table 3.2 Numerical cases by various modeling parameters.....26

Table 4.1 Numerical cases by various modeling parameters.....52

Table 4.2 Averaged root mean square error for numerical cases with A.M. formula and M.P.M. formula.....52

Table 5.1 Soil sample properties used in Submerged Jet tests 74

Table 7.1 Test data.....103

Table 7.2 RMSE of the breach shape predictions at different times 103

Table 8.1 Test characteristics.....130

LIST OF FIGURES

Figure 3.1 Schematic diagram of the experimental tests (a) side view, (b) plan view 27

Figure 3.2 Repeatability of the progressive failure process for N_b = 10 blows/layer at: (a) t = 5 s; (b) 10 s; (c) 15 s; (d) 25 s; (e) 40 s; and (f) 60 s 28

Figure 3.3 Breach evolution for different compaction efforts: N_b = 0 (a); N_b = 10 (b); N_b = 20 (c); and N_b = 30 (d) 29

Figure 3.4 Degradation rate of the embankment crest for different compaction levels 30

Figure 3.5 Downstream hydrograph for different compaction efforts.....30

Figure 3.6 Correlation of normalized peak breach discharge and normalized dry density of the embankment.....31

Figure 3.7 Correlation of normalized time to peak discharge and normalized dry density of the embankment.....31

Figure 3.8 Comparison between experimental and empirical results of the breach outflow hydrograph for: (a) N_b = 0; (b) N_b = 10; (c) N_b = 20; and (d) N_b = 30 32

Figure 3.8 (continued) Comparison between experimental and empirical results of the breach outflow hydrograph for: (a) N_b = 0; (b) N_b = 10; (c) N_b = 20; and (d) N_b = 30 33

Figure 3.9 Time variation of dimensionless embankment crest height for different compaction levels using Eq. (3.3).....34

Figure 3.10 Comparison between experimental and empirical results of temporal changes of normalized crest height for: (a) N_b = 0; and (b) N_b = 20 34

Figure 3.11 Time variation of dimensionless embankment length for different compaction levels using Eq. (3.4).....35

Figure 3.12 Comparison between experimental and empirical results of temporal changes of normalized embankment bottom length for: (a) N_b = 10; and (b) N_b = 30.....36

Figure 3.13 Schematic diagram of proposed triangular model to predict the progressive breach shape (image by author).....36

Figure 3.14 Measured and predicted bed surface profiles using the triangular model for N_b = 20 at: (a) t = 10 s; (b) t = 25 s; (c) t = 40 s; and (d) t = 60 s.....37

Figure 3.15 Observed and predicted normalized crest height variation with time 38

Figure 3.16 Outflow Characteristics vs. eroded volume.....38

Figure 3.17 Breach development time vs. eroded volume.....39

Figure 3.18 Time variation of dam crest level using the experimental data of no-compaction and the results of the mathematical model with different values of α_2 39

Figure 4.1 Breach outflow hydrograph according to experimental tests 53

Figure 4.2 Embankment surface profile z (x) and water surface profiles h(x) at various times t for three experimental tests 54

Figure 4.3 Averaged outflow hydrograph of the three tests 56

Figure 4.4 Averaged embankment surface profiles z(x) of three tests at various times t ..56

Figure 4.5 Turbulent model effect: simulated bed and water surface profiles at various times for Case 15 with constant eddy viscosity model and Case 16 with zero equation model.....57

Figure 4.6 Finite difference approximations of advection terms effect: simulated bed and water surface profiles at various times for Case 1 with upwind scheme method and Case 9 with CIP method.....59

Figure 4.7 Suspended load effect: simulated bed and water surface profiles at various times for Case 1 with bedload and suspended load and Case 5 with bedload only 61

Figure 4.8 Outflow hydrographs for Case 1 with bedload and suspended load and Case 5 with bedload only.....63

Figure 4.9 Suspended load effect for d = 0.125 mm: simulated bed and water surface profiles at various times for Case 1 with bedload and suspended load and Case 5 with bedload only.....64

Figure 4.10 Bedload transport formula effect: simulated bed and water surface profiles at various times for Case 1 with A.M. formula and Case 3 with M.P.M.

formula 66

Figure 4.11 Bed and water surface profiles at various times t according to averaged experimental tests and numerical simulations for Case 10 (A.M.) and 12 (M.P.M) 68

Figure 4.12 Outflow hydrographs according to the averaged experimental tests and simulations for Case 4 (M.P.M.) with Case 1 (A.M.) 70

Figure 5.1 Submerged Jet test apparatus and the standard proctor compaction mold and rammer 74

Figure 5.2 Standard proctor compaction test curve 75

Figure 5.3 Relationship of k_d and τ_c from the Submerged Jet test results for three levels of compaction and water content 75

Figure 5.4 k_d vs. water content for 25 B/L, 15 B/L, and 10 B/L compaction effort 76

Figure 5.5 Averaged k_d vs. water content for 25 B/L, 15 B/L, and 10 B/L compaction effort.....76

Figure 5.6 Averaged τ_c vs. water content for 25 B/L, 15 B/L, and 10 B/L compaction effort.....77

Figure 6.1 Plan view of experimental setup (dimensions are in meter).....85

Figure 6.2 Front view of the proposed method for measuring the breach shape with time 85

Figure 6.3 Spatial variation of water surface velocity at different times.....86

Figure 6.4 Time series of breach width for the left and right bank of the breach (flow direction in the channel is from left to right) 86

Figure 6.5 Hydrographs of inflow to the flume, outflow from the downstream weir, and outflow from the breach.....87

Figure 6.6 Time series of breach evolution (flow direction in the channel is from right to left) 87

Figure 6.7 Time series of water depth at breach location (flow direction in the channel is from right to left) 88

Figure 6.8 Time variation of average breach width and depth 89

Figure 6.9 Non-dimensional deepening and widening rate with time 90

Figure 6.10 Correlation of deepening and widening rate with excess shear stress.....91

Figure 7.1 Time history of: (a) maximum breach depth; (b) top width of the breach; (c) breach area along the centerline of the crest; and (d) total breach volume....104

Figure 7.2 Breach evolution along the center of the levee crest.....105

Figure 7.3 Breach evolution for Test A3 (flow direction in the main channel is from right to left).....107

Figure 7.4 Longitudinal profiles along the centerline of the pilot channel at different times for Test A3 108

Figure 7.5 Breach top width for the downstream and upstream breach walls at different times for Test A3 (centerline of the pilot channel is shown as dash line) 109

Figure 7.6 Water surface velocity distribution for Test A3 at different times.....110

Figure 7.7 Weir flow and breach overflow hydrographs for all tests 111

Figure 7.8 Comparison of experimental and empirical normalized breach top width with time for: (a) Test A2; and (b) Test B3.....112

Figure 7.9 Empirical results of normalized breach top width with time for all tests.....113

Figure 7.10 Comparison of experimental and empirical normalized maximum breach depth with time for: (a) Test A3; and (b) Test B2.....114

Figure 7.11 Empirical results of normalized maximum breach depth with time for all tests.....115

Figure 7.12 Comparison of experimental and empirical normalized breach volume with time for: (a) Test A2; and (b) for Test B1 116

Figure 7.13 Empirical results of normalized breach volume with time for all tests.....117

Figure 7.14 Comparison of the experimental and the predicted breach shape at different times using the trapezoidal model for Test A3.....118

Figure 8.1 Experimental setup in: (a) schematic view; and (b) plan view. Location of the Baumer ultrasonic devices are indicated by stars (dimensions are in meter) 131

Figure 8.2 Time history of the breach top width along the centerline of the levee crest for four levels of compaction.....132

Figure 8.3 Time history of the maximum breach depth along the centerline of the levee crest for four levels of compaction 132

Figure 8.4 Breach profiles along the crest centerline at various times for: (a) N_b = 0; (b) N_b = 2; (c) N_b = 4; and (d) N_b = 10.....133

Figure 8.5 Breach evolution for test with N_B = 0 at t = 10, 20, 25, 30, 35, and 40 s 135

Figure 8.6 Breach evolution for test with N_B = 2 at t = 10, 25, 35, 45, 50, and 60 s 136

Figure 8.7 Breach evolution for test with N_B = 4 at t = 10, 25, 35, 45, 55, and 60 s 137

Figure 8.8 Breach evolution for test with N_B = 10 at t = 10, 25, 35, 45, 55, and 70 s 138

Figure 8.9 Time series of longitudinal bed profiles along the centerline of the pilot channel for: (a) N_b = 0; (b) N_b = 2; (c) N_b = 4; and (d) N_b = 10 139

Figure 8.10 Cumulative breach eroded volume with time for four levels of compaction.....141

Figure 8.11 Time series of the submerged area along the centerline of the levee crest for four levels of compaction.....141

Figure 8.12 Weir flow and breach overflow for four levels of compaction: (a) N_b = 0; (b) N_b = 2; (c) N_b = 4; and (d) N_b = 10 142

Figure 8.13 Correlation of the breach deepening rate along the crest centerline and the excess shear stress on the bed.....144

Figure 8.14 Correlation of the breach widening rate along the crest centerline and the excess shear stress on the sidewalls 144

Figure 8.15 Comparisons of observed and predicted normalized deepening rate 145

Figure 8.16 Comparisons of observed and predicted normalized widening rate.....145

Figure 8.17 Normalized eroded load versus the excess Shields number for different tests.....146

Figure 8.18 Comparisons of observed and predicted normalized eroded volume.....146

Figure 8.19 Breach evolution for Test 5 at t = 5, 20, 40, 60, 80, and 110s 147

Figure 8.20 Breach evolution for Test 6 at t = 10, 40, 80, 120, 150, and 170s 148

Figure 8.21 Breach evolution for Test 7 at t = 10, 40, 80, 120, 150, and 170s 149

Figure 8.22 Breach evolution for Test 8 at t = 1, 5, 10, 15, 19, and 21 min 150

Figure 8.23 Time changes of breach top width for levees with different cohesion 151

Figure 8.24 Time changes of breach depth for levees with different cohesion 151

Figure 8.25 Breach profiles at different times for: (a) Test 5; (b) Test 6; (c) Test 7; and and (d) Test 8 152

Figure 8.26 Weir flow and breach overflow for four levels of cohesion: (a) Test 5; (b) Test 6; (c) Test 7; and (d) Test 8 154

Figure 8.27 Envelope curves of breach top width for different levels of compaction and cohesion 156

Figure 8.28 Envelope curves of breach depth for different levels of compaction and cohesion 156

Figure 8.29 Envelope curves of breach eroded volume for different levels of compaction and cohesion 157

Figure 8.30 Envelope curves of breach submerged area for different levels of compaction and cohesion 157

Figure 8.31 Envelope curves of breach total area for different levels of compaction and cohesion 158

CHAPTER 1

INTRODUCTION

1.1 Earthen Embankment

Embankment structures are volume of erodible (earthen) and/or non-erodible (concrete) material built by humans or formed naturally. These are used for flood protection and water storage for drinking and irrigation, energy production, and recreation purposes. The number of extreme hydrological events, e.g. hurricanes, rainstorms, and typhoons, has increased in recent years due to climate change (Kakinuma and Shimizu, 2014), thereby increasing the risk of embankment failure and flooding. Earthen embankments are emplaced to control water flow and provide protection from flood. They may be classified based on their orientation with respect to the flow direction, namely, 1) built along a river to prevent overflow, called a levee or dike, and 2) built perpendicular to the general flow direction, called a dam.

Flood disasters are common worldwide, due to levee breach and occasionally dam failure resulting in fatalities and considerable economic losses. Failure of earthen embankments may be due to various reasons, such as overtopping, seepage, internal erosion and piping, and slope instability. However, overtopping is the most common cause of the embankment failure (ASCE/EWRI Task Committee on Dam/Levee Breaching, 2011). Moreover, the embankment breach by overtopping may be classified as plane or spatial (Schmocker and Hager, 2009). The spatial mechanism includes both vertical and lateral erosion, while the plane mechanism involves only vertical erosion.

An accurate prediction of the embankment failure by overtopping (i.e., breach shape, breach outflow and flow field) is necessary for emergency planning, proper risk assessment and management, and protection measures. Estimating the soil erodibility by flowing water is an essential step in studying, modeling, and predicting earthen embankment failures. An embankment breach is influenced by both hydraulic load and geotechnical properties of the embankment material (Schmocker and Hager, 2012). The most important geotechnical parameters affecting the embankment erodibility are: grain size distribution which implies cohesion and plasticity, compaction energy, and water content.

1.2 Motivation and Objectives

Despite numerous examples of embankment breaching around the world (e.g., the Elbe flood disaster in 2002 and 2013, the New Orleans flood in 2005, and most recently the October 2015 flood in the Midlands area of South Carolina), in-depth assessments as well as useful data of such failures are limited due to a variety of reasons, including the lack of proper documentation and organization in data collection. Furthermore, detailed understanding of the embankment failure process and the dominant parameters affecting the failure is a crucial step in predicting and modeling the breach process for risk assessment and preparing emergency plans and hazard maps.

The objectives of the present study are:

1) To conduct a series of laboratory experiments on dam breach due to overtopping, considering different levels of compaction energy for the embankments consisting of uniform homogenous sand and investigate the effects of the soil compaction energy on the breach process. Of particular interest is the time evolution of the

breach, downstream outflow hydrograph, and rate of erosion of the embankment crest for different compactions. The main goal is to develop non-dimensional relationships for the crest height and embankment bottom length as a function of time and compaction energy based on the measured data and to develop a simple relationship which enables the prediction of the progressive breach shape.

2) To model the overtopping failure of the homogenous, non-compacted, non-cohesive embankment dam case, applying the iRIC-Nays2D software developed by Foundation of Hokkaido River Disaster Prevention Research Center to study the influence of different model parameters, i.e. turbulence model, finite-difference approximation of the advection term, sediment transport type, and bedload formula, on model prediction.
3) To measure the erodibility of the cohesive (sandy loam) soil samples for three levels of compaction and water content (i.e., low, medium, and high) assuming erosion detachment model using the Submerged Jet method.
4) To conduct a series of levee embankment overtopping experiments in which the levee is aligned parallel to the dominant flow direction, similar to field conditions and quantitatively determine the effects of hydraulics loads, compaction level, and cohesion on the failure process of overtopped homogenous levees (i.e., breach evolution using a sliding-rod technique, measurement of breach outflow, and water surface velocity distributions using a particle-image velocimetry method). Erodibility coefficients in both vertical and horizontal directions are estimated from the experimental results to assess the compaction effects and the corresponding non-dimensional breach geometry relations and bed-load transport

formulas are proposed. Envelope curves of breach characteristics (e.g., breach top width and breach depth with time) are also developed from experimental results for a range of compaction and cohesion.

1.3 Organization of the Dissertation

This dissertation has nine chapters. Characteristics and importance of the embankment structures and their failure modes are presented in this chapter. The motivation and objectives of the study are identified. The background and the literatures relevant to the current study are reviewed in Chapter 2. The experimental setup, procedure, and results of the overtopping dam breach tests to investigate the effects of compaction are presented in Chapter 3. In Chapter 4, the iRIC-Nays2D modeling of the overtopping failure of the homogenous, non-compacted, non-cohesive embankment dam case is presented and the effects of different model parameters on the failure prediction are introduced. The Submerged Jet method procedure and erodibility measurements of the cohesive (sandy loam) soil samples with three levels of compaction and water content are reported in Chapter 5. In Chapter 6, the experimental setup and the methodology of the overtopping levee breach experiments are described and the results of the erodibility measurements in both vertical and horizontal directions are presented for a non-cohesive non-compacted levee embankment. In Chapter 7, the laboratory test results are presented for the investigation of the effects of hydraulic loads on the failure of a non-cohesive, non-compacted levee. The effects of compaction energy and cohesion on the failure of an overtopped non-cohesive levee are investigated in Chapter 8. Summary and conclusions are presented and the recommendations for the future work are outlined in Chapter 9.

CHAPTER 2

LITERATURE REVIEW

Literature on earthen dam failure (experimental and numerical investigations), soil erodibility measurements using the Submerged Jet test, and earthen levee failure are reviewed in this chapter.

2.1 Earthen Dam Failure

Morris (2009) and a forum paper by the ASCE/EWRI Task Committee on Dam/Levee Breaching (2011) summarized the state of the knowledge on earthen embankment breaching. Wahl (2007) reviewed the laboratory investigations on embankment breach process conducted over the past decades. Furthermore, Schmocker and Hager (2009) and Schmocker (2011) have summarized the past hydraulic modeling of embankment breach due to overtopping.

Experimental Investigations

Several investigators studied experimentally the embankment failure due to overtopping, ranging from small scale to field scale, to gain an in-depth understanding of the failure process. Simmler and Sametz (1982) investigated the erosion process of an overtopped embankment dam. They found that the erosion process is affected by the dam material, dam geometry, reservoir volume, and the location of impervious element. A relationship for the breach flow as a function of the breach volume was presented. Powledge et al. (1989) discussed the key parameters that affect the erosion process and also discussed erosion protection systems. They recognized three hydraulic and erosion zones for flow

over an embankment: 1) subcritical flow from the reservoir to the upstream portion of the embankment crest; 2) supercritical flow on the remainder of the crest; and 3) rapidly accelerating turbulent supercritical flow on the downstream slope of the embankment.

Coleman et al. (2002) investigated the overtopping failure of non-cohesive homogeneous embankments subject to a constant-head reservoir. The evolution of breach was discussed and non-dimensional relationships for the breach cross-section width and breach discharge were presented. Hanson et al (2003) defined four stages for the erosion process based on the observations on large-scale overtopping failure experiments on cohesive embankment. Chinnarasri et al. (2003) analyzed the results from nine experimental runs of overtopping failure of non-cohesive embankments with variations of the downstream slope of the dike. They classified the progressive failure of the embankment into four stages, namely: 1) small erosion on the embankment crest; 2) slope sliding failure; 3) wavelike-shape embankment profile; and 4) large wedge of eroded embankment with a small bed slope along the flume. The degradation rate of the dike crest was found to be dependent on and directly correlated to the downstream slope. Dupont et al. (2007) performed an experimental study of the progressive breaching of an overtopped dam. Just before the actual overtopping, they observed sliding at the lower portion of the downstream slope because of water seepage. Then, the erosion advances from the downstream face to the upstream face of the embankment by rotation of the downstream face around a pivot point. Antidunes are then formed on the downstream face and the embankment profile stabilizes.

Chinnarasri et al. (2004) investigated the breach evolution of nine overtopped embankments under the condition of falling head reservoir. It was observed that the

breach section develops vertically at the beginning and enlarges further laterally. They presented non-dimensional relations for the peak outflow through the breached embankment and breach deformation time from their measured data and a number of historical dataset. Schmocker and Hager (2009) conducted a series of laboratory tests on non-cohesive plane dike breach to examine model limitations regarding the test repeatability, side wall effects, and scale effects. More recently, Schmocker and Hager (2012) performed several hydraulic model tests to investigate the effects of dike dimension, sediment diameter, and inflow discharge on the failure of the overtopped embankments. They presented non-dimensional relations for the maximum dike height, dike volume, and maximum breach discharge.

Numerical Investigations

According to the forum paper by the ASCE/EWRI Task Committee on Dam/Levee Breaching (2011), embankment breach models are classified as parametric, simplified physically-based, or detailed physically based. Parametric models use regression equations that are developed based on the data from historic dam failures (Kirkpatrick 1977; Hagen 1982; Von Thun and Gillette 1990; Xu and Zhang 2009; Pierce et al. 2010).

Simplified physically based approaches typically involve the estimation of the flow rate through a specified breach cross section with triangular, rectangular, or trapezoidal cross section. Both analytical and numerical models are used to solve the simplified governing equations obtained through assumptions and simplifications (Singh and Scarlatos 1988; Franca and Almeida 2004; DAMBRK (Fread 1984; similar one used by HEC-RAS); NWS BREACH (Fread 1988); HR BREACH (Mohamed et al. 2002; Morris et al. 2009)).

Detailed physically-based models of breaching process are relatively recent and include one-dimensional, depth-averaged two-dimensional and three-dimensional hydrodynamic models and various sediment transport models (Tingsanchali and Chinnarasri 2001; Wang and Bowles 2006; Wang et al. 2008; Cao et al. 2011). There is considerable amount of diversity in these models in terms of solution methods, numerical accuracy, sediment entrainment and transport modeling. The depth-averaged 1D and 2D models are computationally efficient and preferable over 3D models due to the requirement of considerable amount of computational resources and run time for the application of the latter. For both 2D and 3D Reynolds-averaged models, local equilibrium in turbulence and sediment transport are assumed. These assumptions may lead to inaccurate results due to rapid changes in bed level and high sediment concentration during breach evolution. Systematic sensitivity studies of numerical models are necessary to study the effect of turbulence models, choice of numerical scheme, sediment transport formula, and mode of sediment transport on model predictions.

2.2 Soil Erodibility Measurements Using the Submerged Jet Test

Estimating the soil erodibility by flowing water is an essential step in studying, modeling, and predicting embankment failures which can be widely used in emergency action plans and risk assessments. Furthermore, estimating erodibility of cohesive soil is more complex because of the large number of parameters controlling the erosion behavior and the difficulty of estimating these parameters.

Hanson and Cook (2004) assumed a sediment detachment process for the erosion rates of cohesive soils rather than the sediment transport processes and defined erodibility by two parameters in a widely accepted detachment model: the erodibility coefficient and

the critical shear stress. The detachment model is a fundamental and widely accepted equation used in characterizing erodibility for embankment overtopping (Temple et al., 2005) and has been used by several investigators (Hutchinson, 1972; Foster et al., 1977; Dillaha and Beasley. 1983; Temple, 1985; Hanson, 1989; Stein and Nett, 1997; Wan and Fell, 2004).

$$\varepsilon = k_d(\tau_e - \tau_c) \tag{2.1}$$

where ε is the erosion rate (m/s), k_d is the erodibility or detachment coefficient (m^3/N-s), τ_e is the hydraulically applied shear stress (Pa), and τ_c is the critical shear stress (Pa).

Historically, many investigators tried to develop simple relationships between these parameters and soil properties (Smerdon and Beasley, 1959; Kamphius and Hall, 1983; Briaud et al., 2001). However, no widely accepted and reliable relation was obtained due to the complexity of soil properties. This complexity becomes even more significant for aged soils (Gheibi 2016). These investigations show that the best approach to determine these parameters is to measure them by using both field and laboratory methods developed for assessing earthen material erodibility, including large and small flumes, submerged jet test, hole erosion test, flume with lifting mechanism test, slot test. Clark and Wynn (2007) compared different methods for determining k_d and τ_c and field validation of these methods over a wide range of soil types was recommended. Hanson and Hunt (2007) conducted a submerged jet test to investigate the effects of compaction on erodibility. They also conducted three large-scale, outdoor-laboratory breach widening tests with the flow direction perpendicular to the embankment and compared the k_d values from these experiments (calculated in the horizontal direction) to those from the jet test.

2.3 Earthen Levee Failure

An accurate prediction of the levee failure process by overtopping (i.e., breach shape, breach outflow, and flow field) is necessary for emergency planning, risk assessment and management, and protection measures. Estimating the soil erodibility by flowing water is an essential step in studying, modeling, and predicting earthen embankment failures. Characterizing erodibility of levees becomes even more complicated considering downward and lateral directions of erosion. Majority of the levee breach experiments have been conducted in flumes with the flow direction perpendicular to the embankment (Wahl 2007).

The failure process of embankment (i.e., riverine levee and/or dam) has been categorized into stages by several investigators (e.g., Hanson et al. 2003, Kakinuma and Shimizu 2014). The very initial stages of levee failure include vertical erosion which is similar to dam failure. In later stages, horizontal advancement of levee breach starts increasing after the deepening process reaches a certain state. Kakinuma and Shimizu (2014) conducted several large-scale levee breach experiments with variations of inflow rate, levee shape, and levee material, and proposed a bed load transport formula by analyzing the breach lateral widening process. They applied the proposed bedload equation into a new numerical model to clarify the mechanism of levee breach with a focus on widening process. Most of the embankment breach experiments (e.g., Chinnarasri et al. 2003; Schmocker and Hager 2009; Coleman et al. 2002; Hunt et al. 2005) addressed the dam breach scenario which has different characteristics than levee breach.

CHAPTER 3

EXPERIMENTAL STUDY ON EMBANKMENT BREACH DUE TO OVERTOPPING: EFFECTS OF COMPACTION*

The effects of the soil compaction energy on the plane embankment breach process due to overtopping are investigated in this chapter. Experiments were conducted in the Hydraulics Laboratory, University of South Carolina, considering four levels of compaction energy and a simple trapezoidal shape for embankments consisting of uniform sand. Of particular interest was time evolution of the breach, downstream outflow hydrograph, and degradation rate of the embankment crest for different compactions. The main goal was to develop non-dimensional relationships for the crest height and embankment bottom length as a function of time and compaction energy based on the measured data and ultimately to introduce a simple relationship which enables the prediction of the progressive breach shape.

3.1 Experimental Setup

The experiments were carried out in a 6.1 m long, 0.25 m deep, and 0.2 m wide horizontal rectangular flume. Figure 3.1 shows the schematic diagram of the plan and side view of the setup. One sidewall of the flume is made of Plexiglas to enable video recording of the longitudinal breach evolution process, i.e., changes of sediment surface profiles with time. Recording was done using a high-definition (HD) video camera, at a

* Asghari Tabrizi, A., Elalfy, E., Elkholy, M., Chaudhry, M.H., Imran, J. 2016. "Effects of compaction on embankment breach due to overtopping." Published online by *Journal of Hydraulic Research*. Reprinted here with permission of publisher.

resolution of 1280 x 720 pixels, facing the cross profile of the embankment. To visually differentiate the bed and water surfaces, dye was injected into water close to the upstream face of the embankment during the breach evolution. The intake length was 0.5 m and a flow straightener honeycomb was used to reduce the inflow turbulence. A basin was located at the downstream end of the flume to collect the water discharging from the breached embankment. The inflow discharge was kept constant at 0.0005 m^3/s.

3.2 Test Procedure

Prior to the embankment overtopping tests, Standard Proctor Compaction tests (ASTM D698) were carried out to determine the optimum water content of the homogenous, non-cohesive soil (i.e., sand only) used in the experiments. The optimum water content was found to be 5.2% and the corresponding maximum dry unit weight, $\gamma_{d,max}$, is 15.44 kN/m^3. The trapezoidal earthen embankments of uniform sand with the mean diameter of 0.55 mm were placed 3.1 m downstream from the intake in the streamwise direction. The upstream toe of the embankment was considered to be the origin of the coordinate system. The dimensions of the embankment for all the tests were: embankment height = 0.15 m, embankment width = 0.2 m, embankment crest length = 0.1 m, upstream and downstream embankment slopes, s (V: H) = 1:2. Four different cases were considered by applying different levels of compaction to build the embankments using a 4.54 kg rammer (impact surface of 10 cm by 10 cm) to manually compact the material. For each experiment, the soil was uniformly mixed with water to attain the optimum water content. The soil was then placed into three loose layers (5 cm for the no compaction case and 10 cm for the compacted cases) and each layer was compacted by the rammer with the release height of 10 cm with different number of blows per layer, N_b, for each case: 0 (no

compaction), 10, 20, and 30. For each layer, the soil surface was trimmed and levelled to 5 cm precisely after the compaction. After placing and compacting the third layer, the upstream and downstream faces of the embankment were trimmed carefully to reach the final trapezoidal shape. The seepage through the embankment was controlled and reduced by a thin clay layer with low permeability placed on the upstream face of the embankment. The parameters for the test cases are presented in Table 3.1. The compaction energy is denoted by C_e.

To reduce the contact time between water and the upstream embankment face prior to overtopping and in turn to reduce the seepage through the embankment, the reservoir was filled at a relatively fast rate using two additional hoses along with the pump inflow. As the water surface reached about 5 cm below the embankment crest, the extra supply of water was cut off (i.e., the inflow was provided by the pump only). Small initial waves generated due to the rapid filling of the reservoir dissipated after a few seconds and the water surface was almost horizontal when the overtopping started. The valve for the dye container was opened slightly to add color to the water (the inflow from the color container was negligible). The starting time of the failure process was considered to be the time when the water surface reached the upstream edge of the embankment crest. Furthermore, sand-cone tests were conducted to determine the dry unit weight of the embankment material for each compaction level. The dry unit weights, γ_d, were found to be 13.35, 14.75, 15.46, and 15.47 kN/m^3 for N_b = 0, 10, 20, and 30, respectively.

Because of the limited width (i.e., 0.2 m), all of the embankments were overtopped by the flow over the entire width resulting in a plane breach process (Pontillo

et al. 2010, Schmocker and Hager 2009). So, the longitudinal embankment profile observed through the Plexiglas side of the flume represents the entire embankment. As observed by Schmocker and Hager (2009), the sidewall effect was negligible. During the breach evolution, the bed surface profiles were recorded by an HD camera. The videos were first converted into frames for one-second time intervals and then the longitudinal bed surface profiles were obtained by digitizing the frames with an expected error of ± 1 mm. The breach outflow was measured at the downstream end of the flume using the volumetric technique. Each test was repeated at least three times to confirm the repeatability of the tests. With the repeatability confirmed, the measured temporal changes of longitudinal embankment bed profile were averaged and analyzed.

3.3 Results

Repeatability

To ensure the reliability of the measurements, the repeatability of the tests was checked by considering both the embankment bed evolution and also the breach outflow hydrograph for all four cases of compaction prior to analyzing the results. Each case was repeated at least three times using identical conditions to reduce uncertainty of the measured data. Figure 3.2 shows the development of the breach with time for three different runs for the case with N_b = 10 blows/layer. Bed surface profiles of different runs generally overlap at all time steps. Small differences are seen between t = 25 s to t = 40 s and they mainly occur close to the embankment crest area and toe of the downstream face, and with time, these deviations decrease and the three bed profiles converge to a single embankment profile. The repeatability was confirmed for all the compaction rates. From the visual observations and quantitative analysis, the case with no compaction was

found to have better repeatability as compared to the cases with compaction. The averaged RMSE, over the time and over the repetitions, was calculated for all the test cases, and was about 0.005 m for all of the test cases for the bed evolution. A better repeatability was also observed for the breach hydrograph for the case with no compaction (RMSE = 0.001 $m^3s^{-1}m^{-1}$ for no-compaction case and RMSE = 0.002 $m^3s^{-1}m^{-1}$ for the compacted cases). The better repeatability for the case with no-compaction may be due to the fact that surface erosion was the only mechanism that governed the failure process, while for the cases with compaction both head cut erosion (i.e., irregular detachment of soil chunks) and surface erosion controlled the failure process.

Breach Shape Evolution

Figure 3.3 shows the progressive failure of the embankment for different levels of compaction, N_b = 0, 10, 20, and 30. A relatively similar erosion process was observed for the overtopped embankments with different compaction efforts, but the failure process was faster in the case of non-compacted embankment. The starting time of the overtopping process, i.e. t = 0 s, is the time when the water surface at the reservoir reached the upstream edge of the crest. The upstream and downstream faces of the embankment remained relatively intact until about t = 5 s and 15 s for N_b = 0 and N_b = 10, 20, 30, respectively while the embankment crest height decreased with rounded-shape edges. Then, with increased flow velocity on the downstream face of the embankment, erosion started and the eroded material was deposited directly beyond the original location of the downstream toe. This resulted in a wedge-shaped embankment profile, with the downstream slope rotating around a pivot point, roughly located at x = 0.64 m and on the original embankment downstream slope and the crest point moving downward

on the fixed upstream slope. At around t = 60±5 s (as the time step of image processing was 5 s), the erosion process reached an equilibrium condition (i.e., when the bed and water surface profiles remained almost unchanged) and the stable embankment surface profiles were formed with a relatively small downstream slope. The observations of the temporal advance of embankment erosion in the current study are consistent with the erosion processes described by Dupont et al. (2007) and Schmocker and Hager (2009).

Some irregular bed surface profiles from t = 25 to 40 s were observed on the downstream face of the compacted embankments as compared to the non-compacted one. This may be due to the effects of combined head cut and surface erosion processes for the compacted embankments, while the surface erosion is the only mechanism during the failure of the non-compacted embankment. The equilibrium embankment crest height (i.e., the height of the crest at the end of the failure process when the bed and water surface profiles remained almost unchanged) increased with compaction effort, with no major differences between N_b = 20 and N_b = 30 since the soil dry unit weight reached its maximum value (based on the standard proctor compaction test) for N_b = 20.

Figure 3.4 shows the variation of the crest degradation rate with time for various levels of compaction. The crest degradation plots of compacted embankments are generally similar. For the non-compacted embankment, the degradation rate of the crest increased rapidly and reached its maximum value ($D_{rate,max}$ = 0.0035 m/s) during the early stage of the failure (t = 15 s) and then decreased with almost the same slope of the rising limb, while for the compacted embankments, the peak degradation rate was reached at later stages of failure (t = 25 s) with a lower peak ($D_{rate,max} \approx$ 0.0027 m/s) and then decreased

with a milder slope such that the final degradation rates were higher as compared to the non-compacted embankment.

Downstream Hydrograph

The discharge from the breached embankment constructed with different compaction levels was measured at the downstream end of the flume (Figure 3.5). The starting time of the hydrographs is the time when the water reached the end of the flume. The breach discharge increased at a fast rate during initial stages of failure until it reached its peak. Then, it decreased with a smaller rate until it was constant and equal to the inflow discharge. A minor rise was observed on the falling limb of the hydrographs at around t = 15 s. This minor increase may be due to the release of water stored behind the embankment when the headcut erosion reached the upstream edge of the crest. The amplitude of the second rise increased with the compaction level. This was consistent with the experimental observation that the dominance of the headcut erosion mechanism increased with the compaction level compared to the surface erosion mechanism and resulted in more abrupt water release. It was found that the peak discharge decreased while the time to peak increased with the compaction level. As mentioned previously, the embankment overtopping tests were run for different number of blows per layer, N_b. To have a more general variable representing compaction, normalized dry density, $\alpha = \gamma_d/\gamma_{d,max}$, is used in this study, corresponding to each N_b where γ_d is the dry unit weight of the embankment material obtained from sand-cone test and $\gamma_{d,max}$ is the maximum dry unit weight from the standard proctor compaction test. The relationship between these two variables is $\alpha = 0.045{N_b}^{0.37} + 0.86$ with R^2 = 0.95. The fitted non-dimensional relations for the peak discharge and for the time to peak as functions of the

normalized dry density are derived as $q_{peak}/q_{base} = -12.80\alpha + 17.42$ (R^2 of 0.93) and $t_{peak}/t_0 = 16.62\alpha - 10.74$ (R^2 of 0.64), respectively (Figure 3.6 and Figure 3.7), where q_{peak} is peak discharge per unit width, q_{base} is constant inflow discharge to the flume per unit width, t_{peak} is time to peak, and t_0 is the travel time of a wave in the upstream reservoir defined as $t_0 = L_o/\sqrt{gh_o}$, where L_o is the length of the upstream reservoir and h_o is the initial height of water in the upstream reservoir. Although there are only limited data points in these figures, a clear trend can be observed. The last two data points in these figures have almost the same α value since the optimum compaction level was reached with N_b = 20 and further compaction did not change the value of α significantly.

Using the experimental results of the breach outflow and regression analysis, two non-dimensional fitted equations are developed that express the rising limb and the falling limb of the breach outflow hydrograph separately for different levels of compaction and they are presented as

$$q_{rising}/q_{base} = (-6.4\alpha + 7.1)(t/t_0) \quad \text{for } t \le t_{peak} \tag{3.1}$$

$$q_{falling}/q_{base} = (35.1\alpha - 11.5)(t/t_0)^{-0.8} \quad \text{for } t > t_{peak} \tag{3.2}$$

where q_{rising} is the unit discharge on the rising limb of the hydrograph and $q_{falling}$ is the unit discharge on the falling limb of the hydrograph. The fitted equation of the rising limb of the breach hydrograph (Eq. 3.1) is chosen as a linear equation because of the rapid changes of the outflow hydrograph during this stage, while the falling limb equation is chosen as a power equation since the temporal change of the hydrograph is more gradual with a slower rate at this stage. To confirm the validity of the proposed equations, the predicted hydrographs by using Eqs. 3.1 and 3.2 are compared with the experimental

results for different levels of compaction as shown in Figure 3.8. The predicted and the experimental results correlate well for all the compaction levels with the average RMSE of 0.31, except some minor differences for the case with N_b = 20.

Crest Height

The temporal changes of the maximum embankment height were measured for different normalized dry densities. Using regression analysis, the best fit curve for these changes is obtained as

$$Z_{crest}/Z_{initial} = \left[6.34 \times 10^{-5}(t/t_0)^3 - 0.0014(t/t_0)^2 - 0.024(t/t_0) + \frac{1}{\alpha^{-2.502}}\right](\alpha)^{-2.502} \quad (3.3)$$

where Z_{crest} = crest height at each time step, $Z_{initial}$ = initial height of the crest before overtopping, and t = time from starting of overtopping. The fitted equation (Eq. 3.3) was chosen as a 3rd order polynomial equation since it satisfactorily describes the physical phenomenon which includes acceleration and deceleration of the crest height changes. Figure 3.9 shows the variation of the normalized crest height, $Z_{crest}/Z_{initial}$, with normalized time, t/t_0, for different compaction levels using Eq. 3.3. For a given normalized time, differences between the normalized crest height decreased with the compaction effort such that increasing the compaction beyond N_b = 20 (which corresponds to the maximum dry unit weight from the standard proctor compaction test) had insignificant effect on the crest height. The equilibrium crest height was between 0.3 and 0.4 of the initial crest height for different compaction levels, which agree with the experimental measurements. To determine the validity of the proposed equation (Eq. 3.3), empirical and experimental results of temporal changes of the crest height are

compared for different levels of compaction. Except for some small deviations, the measured data from laboratory experiments and the estimated ones from Eq. 3.3 are in satisfactory agreement with R^2 values greater than 0.94 for all the cases. Figures 3.10(a and b) show the comparison between the empirical and experimental results for N_b = 0 (R^2 of0.94) and 20 (R^2 of 0.99), respectively.

Embankment Length

The development of the embankment bottom length (i.e., distance from the upstream toe to the downstream toe of the embankment at each time step), L_{base}, was measured during the failure process of the overtopped embankments. The empirical relation of the normalized embankment length as a function of time and dry unit weight is obtained by regression analysis as

$$L_{base}/L_{initial} = [-4.95 \times 10^{-4}(t/t_0)^3 + 1.56 \times 10^{-2}(t/t_0)^2 - 5.99 \times 10^{-2}(t/t_0) + 1.01](\alpha)^{-0.5} \quad (3.4)$$

where $L_{initial}$ = initial length of the embankment before overtopping. Similar to the crest height regression analysis, a 3rd order equation better explains the actual changes of the embankment bottom length. Figure 3.11 shows the time variation of the normalized embankment length, $L_{base}/L_{initial}$, for different compaction levels by applying Eq. 3.4. The deviation between the curves at a given time step decreases with increasing the compaction and the compaction effect becomes insignificant beyond N_b = 20. Figures 3.12(a and b) show the comparison between the empirical (Eq. 3.4) and experimental results for N_b = 10 (R^2 of 0.94) and 30 (R^2 of 0.97), respectively. The empirical and the experimental measurements are in satisfactory agreement for all cases with R^2 higher than 0.81.

Modeling Evolution of the Breach

As mentioned previously, when the water overtopped the embankment, first, the crest eroded from the downstream to the upstream edge. With time, a wedge-shaped embankment formed with the downstream face rotating around a pivot point which resulted in an advance of the downstream toe of the embankment and degradation of the crest point along the fixed upstream slope. Therefore, by applying the empirical equations for the crest height and the bottom length (Eqs. 3.3 and 3.4, respectively), a triangular embankment model is proposed to predict the progressive failure of embankments with different dry unit weights. Figure 3.13 shows the schematic diagram of the proposed triangular model with Cartesian coordinates of the three edges: 1) upstream toe which is a fixed point with $x = 0$ and $z = 0$; 2) crest point with $z = Z_{crest}$ from Eq. 3.3 and $x = (1/\mathrm{s})Z_{crest}$ since the crest point is located on the fixed upstream slope of the embankment, s (V:H), with s =1/2 in this study; 3) downstream toe with $x = L_{base}$ from Eq. 3.4 and $z = 0$.

The temporal changes of longitudinal embankment bed surface profiles from experimental tests are compared with those from the proposed model for different compaction levels. Some deviations are observed during the initial stages of the breach development, i.e. $t < 10$ s, with smaller deviations for the compacted embankments, while at the later stage, the measured and the predicted results agree well for all compaction levels. Except the very initial stages of the failure of the non-compacted case, the triangular model satisfactorily predicted the location and the height of the crest point for all of the test cases during the failure process. This is the key advantage of the model since the maximum crest height is controlling the breach outflow. Figure 3.14 shows the

comparison between the experimental and modeled bed surface profiles at different times for N_b = 20. At early stages of the failure, the compacted cases were predicted relatively better than the case with no compaction. The time-averaged RMSE was calculated for the test cases and it was almost the same (0.009 m) for all of the tests.

Comparison with Laboratory and Real-life cases

The proposed model of the breach crest height is compared against data from the work of Coleman et al. (2002) to test the model against similar cases. The experiments presented by Coleman et al. (2002) were originally conducted by Jack (1996) and Andrews (1998). This study is selected for the following reasons: 1) the availability of the input parameters required for the proposed model; 2) similarity of the grain sizes; and 3) use of non-cohesive soil.

Using Eq. 3.3, variation of the maximum breach crest height with time was predicted for the case with medium sand (0.5 mm). The following parameters are used in the model: upstream reservoir length L_o = 11.16 m; initial water height in the upstream reservoir h_o = 0.3 m; initial height of the crest $Z_{initial}$ = 0.3 m; and non-dimensional dry unit weight α = 1 assuming that the embankment was compacted to the maximum compaction level. Although the erosion process in the experiment of Coleman et al. (2002) was spatial (i.e., included both vertical and lateral erosion) unlike the erosion process in the present study, the proposed model can reasonably predict the time variation of the embankment crest height (Figure 3.15). As indicated by Coleman et al. (1997), the breach crest is the dominant factor controlling the breach discharge. Moreover, the present results of the longitudinal breach profiles and breach crest degradation with time were consistent with those from Coleman et al. (2002) (Figure 6 therein) as the breach

crest degraded mostly on a fixed upstream slope while the breach invert rotated around a pivot point. However, the pivot point in their study was along the base of the embankment which prevented the embankment bottom length to advance farther downstream. In the present study, the pivot point was located above the base and on the original downstream slope of the embankment, thereby allowing the advancement of the embankment bottom length with time. The proposed model (Eq. 3.3) is also used to estimate the final crest height for three small dam failures, i.e. Spring Lake Dam, Lower Rocky Ford Dam, and Upper Rocky Ford Dam, during the October 2015 flood in the Midlands area of South Carolina. The failure times for the above three cases are estimated by using USBR (1988) or Froehlich (1995). The comparison between the predicted and observed crest heights is in satisfactory agreement, as shown in Table 3.2 with RMSE equals to 0.28 m.

Moreover, the applicability of two selected models available in the literature, i.e. MacDonald and Monopolis (1984) and Singh and Scarlatos (1988), to predict the experimental data presented in this study is examined. MacDonald and Monopolis (1984) studied 42 reported dam failure cases and developed two graphical relationships. The first one is relating the breach formation factor (BFF) which is the product of the outflow volume of water and the difference in elevation of the peak reservoir water surface and breach base plotted against the volume of the breach material removed, as shown in Figure 3.16 for earthen dams. The dashed line in the figure is the extension of their relationships since all their data were for field-scale dams. From the figure, it is seen that there is a small deviation between the experimental results and the fitted line. The relationship proposed by MacDonald and Monopolis (1984) for BFF versus volume of

eroded material matches the recent cases of three small dam failures in South Carolina. The second relationship is relating the breach development time versus the volume of material removed during breaching. The relation for breach development time versus volume of eroded material proposed by MacDonald and Monopolis (1984) underpredicts breach time for both the experiments and the aforementioned field cases (Figure 3.17). Singh and Scarlatos (1988) developed analytical models for the analysis of non-compacted gradual earth-dam failure. They used mass balance equation of reservoir, broad crested weir equation with the assumption of critical flow condition over the dam crest, and a breach-erosion equation. They applied the model to three breach shapes: rectangular, triangular, and trapezoidal. The comparison with the present work is only based on the rectangular breach shape to render the assumption of plane embankment erosion valid. The breach width is assumed to be equal to the entire width of the dam and the dam crest erodes vertically downward. According to the experimental data for the case with no-compaction, the relation between crest level (Z_{crest}) and time is non-linear as shown in Figure 3.18. Therefore, non-linear erosion model of Singh and Scarlatos (1988) is applied. The input data for their model are as follows: H_o = 0.155 m, Z_o = 0.15 m, α_1 = 1.5, A_s = 0.72 m^2, b = 0.2 m. Singh and Scarlatos (1988) suggested a range of α_2 = 0.00015 to 0.0021 based on the comparison with historical data. When these values are tested with the present experimental data no agreement is found. Thus, four other different values of α_2 = 0.15, 0.2, 0.25, 0.3 are tested. Based on the comparison in Figure 3.18, the model dose not adequately capture the observed crest evolution with any of these values. The predicted crest elevation decreases rapidly during the first 15 s and then become constant, while the changes of the crest elevation in the experimental data were

more gradual. As stated by Singh and Scarlatos (1988) the main drawback of their model is the value of α_2 which is taken arbitrary and does not reflect any of the soil characteristics.

Table 3.1 Test case characteristics

Test case	N_b (B/L)	γ_d (kNm^{-3})	C_e* ($kgcm^{-2}$)
1	0	13.35	0.00
2	10	14.75	0.91
3	20	15.46	1.82
4	30	15.47	2.72

* The compaction energy, C_e, is defined as $C_e = \frac{(N_b \times Number\ of\ layers \times Rammer\ weight \times Release\ height)}{Soil\ volume\ under\ rammer}$

Table 3.2 Comparison between the predicted and observed crest heights for the SC floods

	Lake area (m^2)	Breach width (m)	Breach depth (m)	Observed Z_{crest} (m)	Predicted Z_{crest} (m)
Spring Lake	192311	21.4	3.16	1.11	0.67
Lower Rocky Ford	102856	18	4.6	1.47	1.56
Upper Rocky Ford	132954	22.2	5.3	1.70	1.87

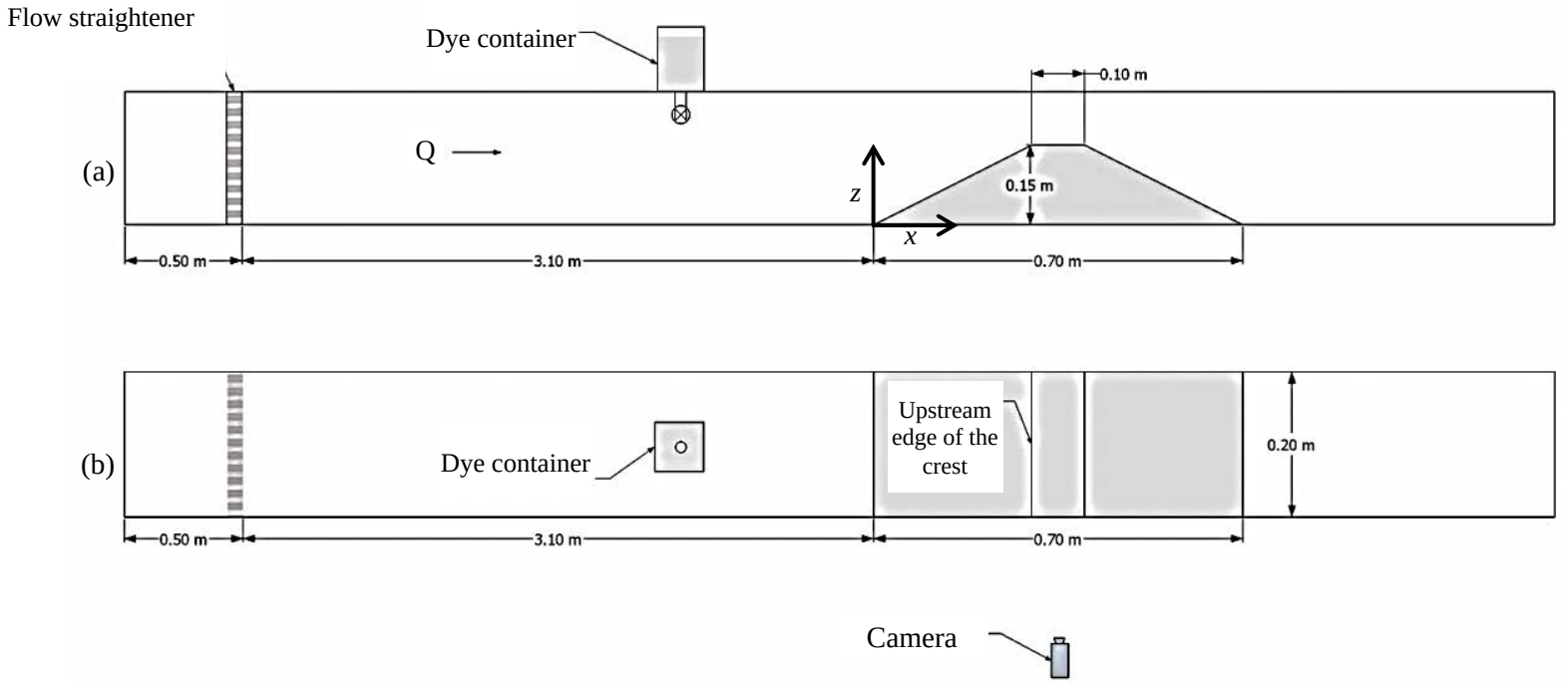

Figure 3.1 Schematic diagram of the experimental tests: (a) side view; (b) plan view

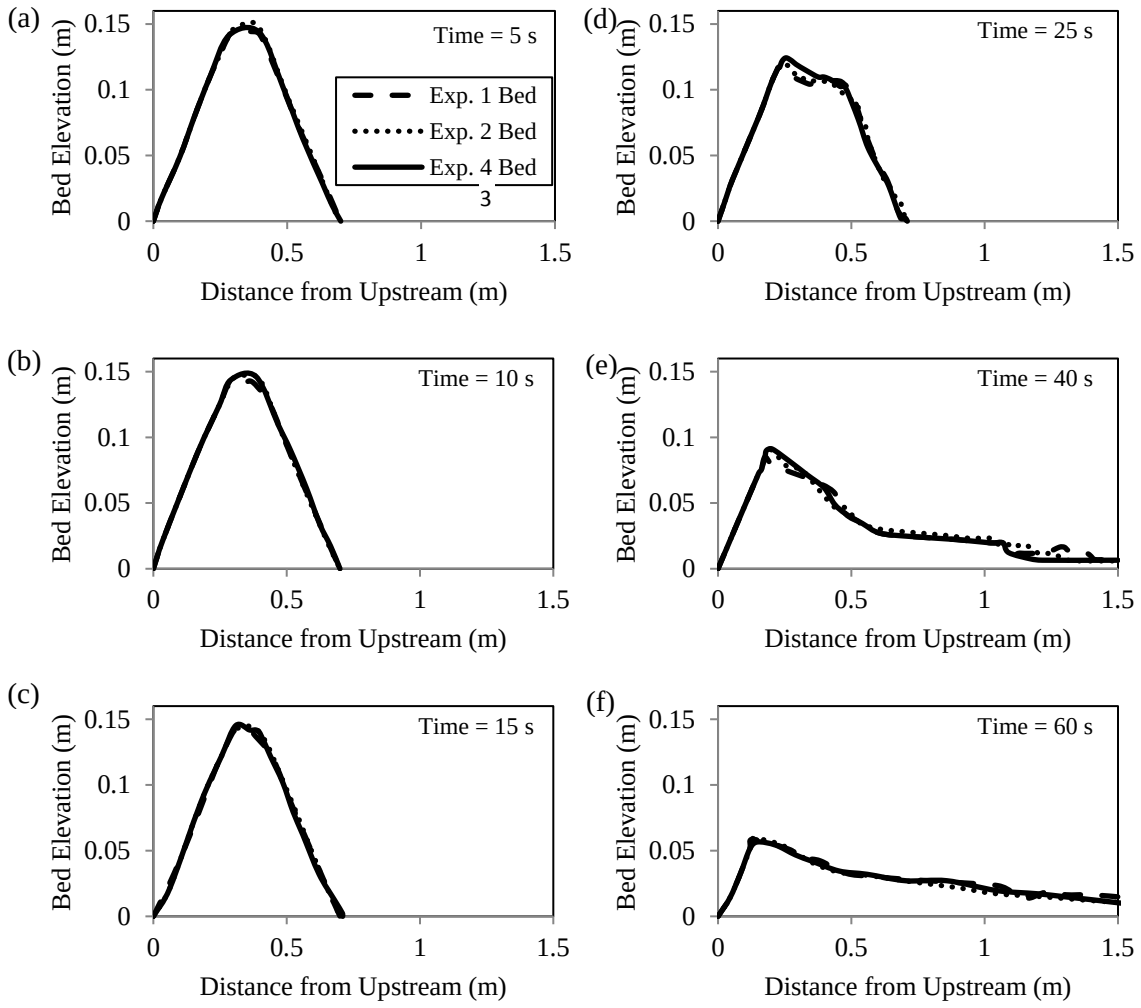

Figure 3.2 Repeatability of the progressive failure process for N_b = 10 blows/layer at: (a) t = 5 s; (b) 10 s; (c) 15 s; (d) 25 s; (e) 40 s; and (f) 60 s

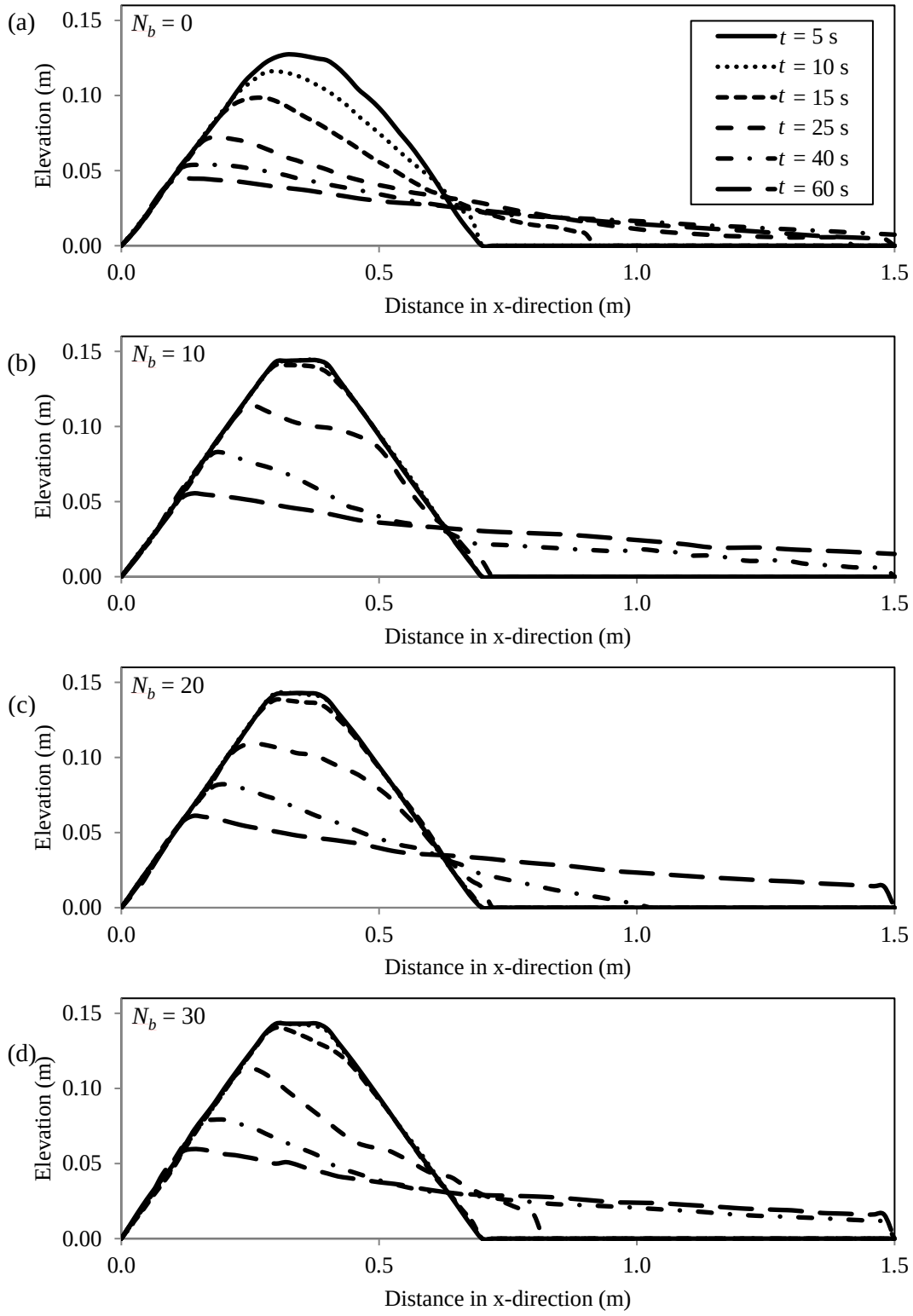

Figure 3.3 Breach evolution for different compaction efforts: N_b = 0 (a); N_b = 10 (b); N_b = 20 (c); and N_b = 30 (d)

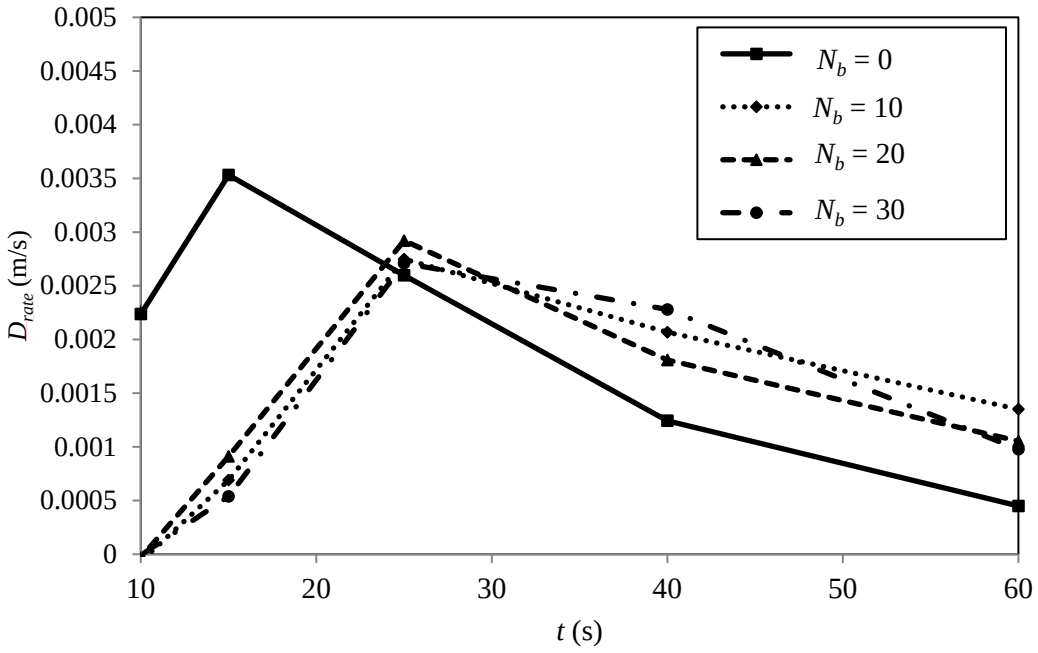

Figure 3.4 Degradation rate of the embankment crest for different compaction levels

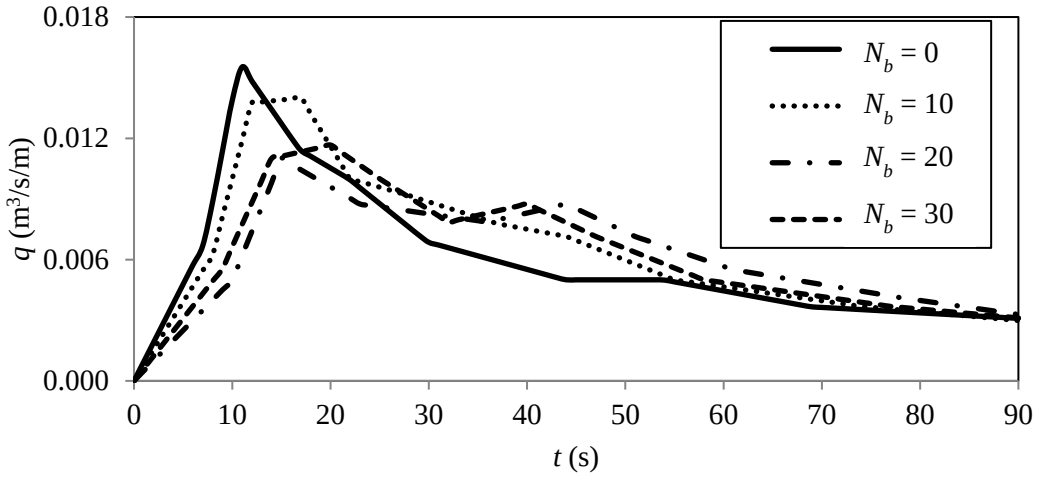

Figure 3.5 Downstream hydrograph for different compaction efforts

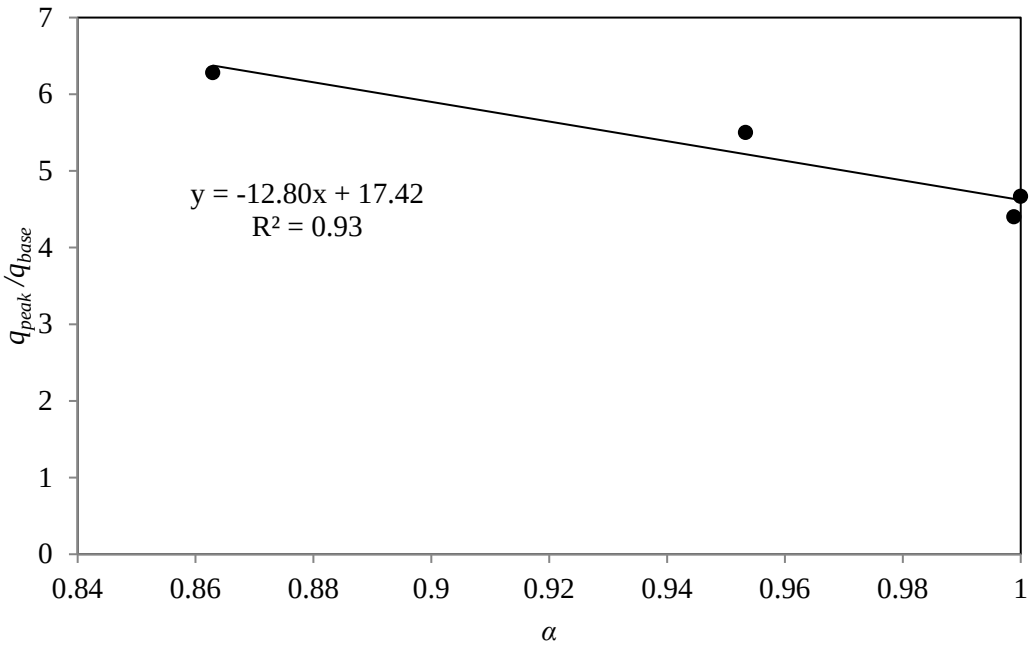

Figure 3.6 Correlation of normalized peak breach discharge and normalized dry density of the embankment

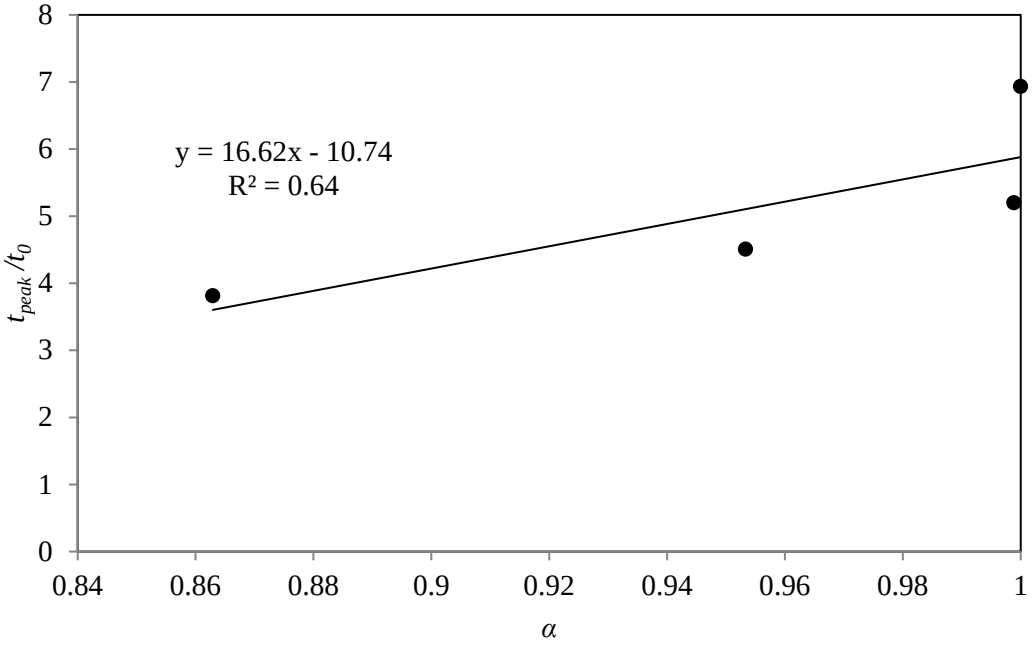

Figure 3.7 Correlation of normalized time to peak discharge and normalized dry density of the embankment

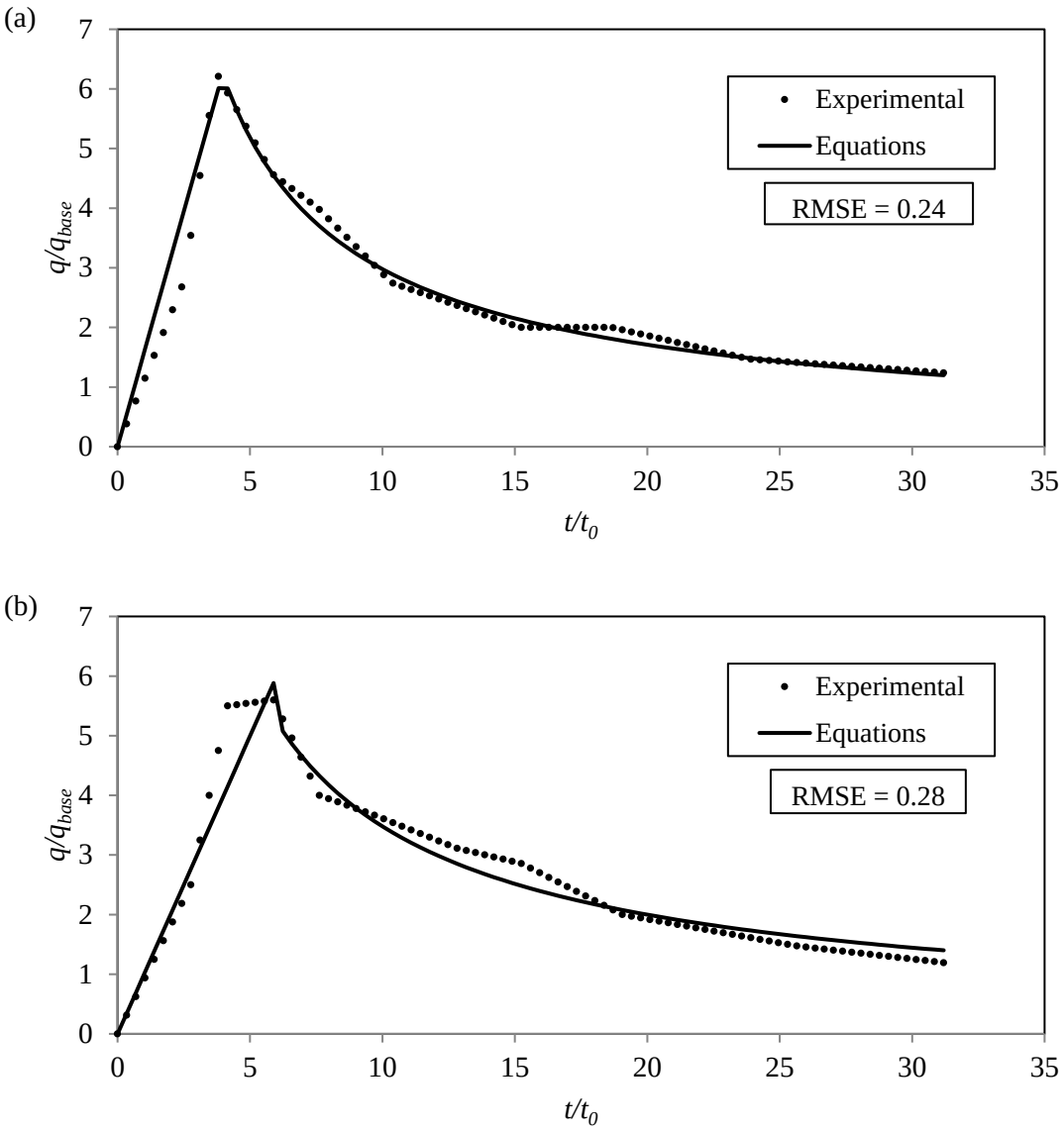

Figure 3.8 Comparison between experimental and empirical results of the breach outflow hydrograph for: (a) N_b = 0; (b) N_b = 10; (c) N_b = 20; and (d) N_b = 30

(c)

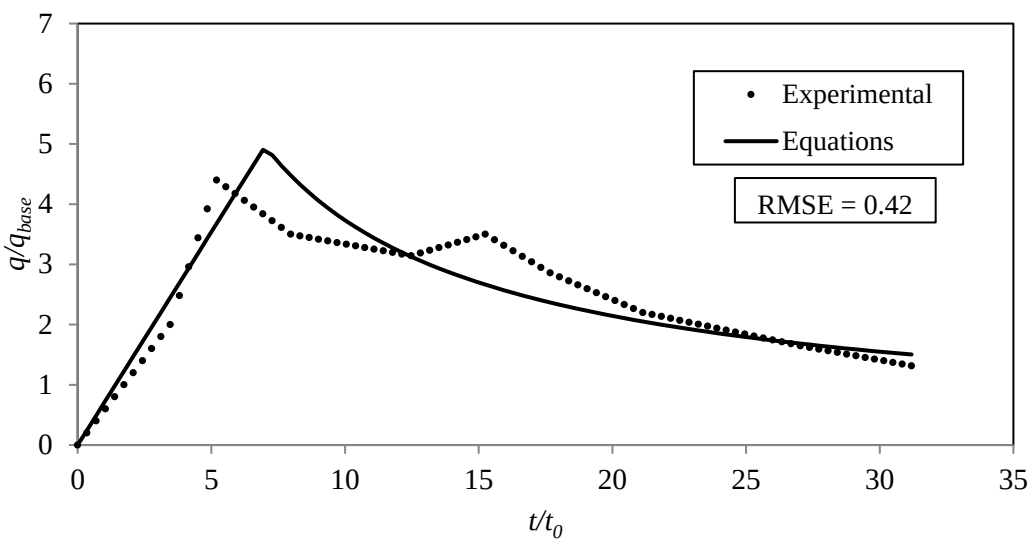

(d)

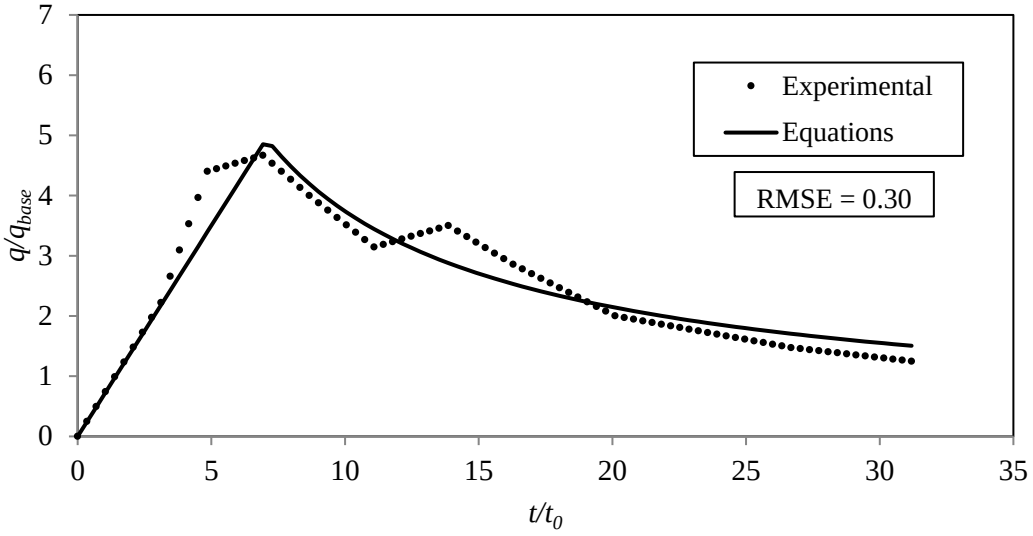

Figure 3.8 (continued) Comparison between experimental and empirical results of the breach outflow hydrograph for: (a) N_b = 0; (b) N_b = 10; (c) N_b = 20; and (d) N_b = 30

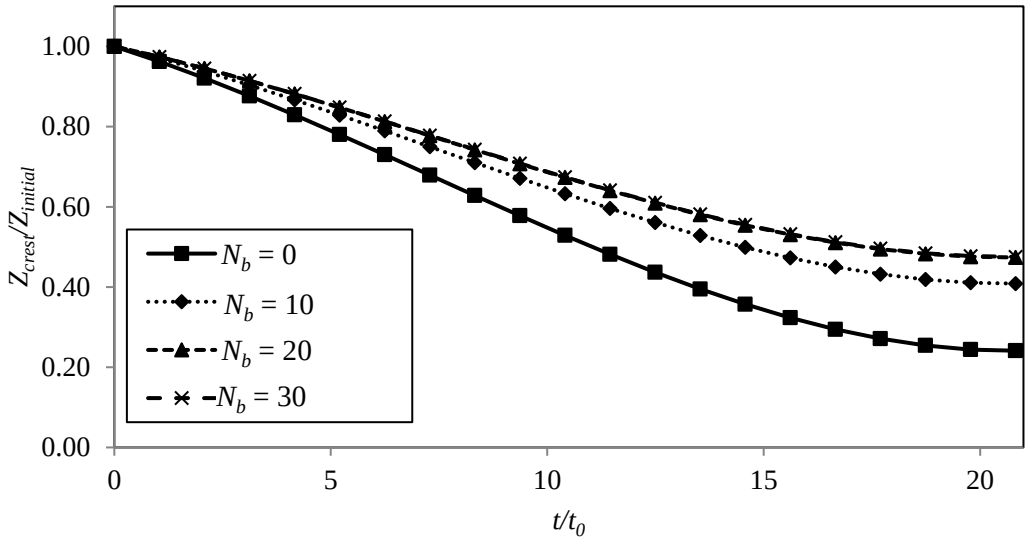

Figure 3.9 Time variation of dimensionless embankment crest height for different compaction levels using Eq. 3.3

(a)

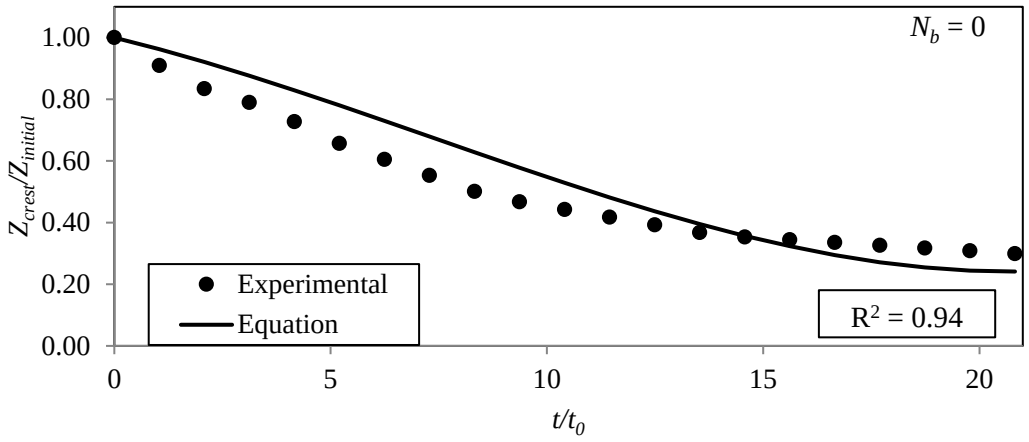

(b)

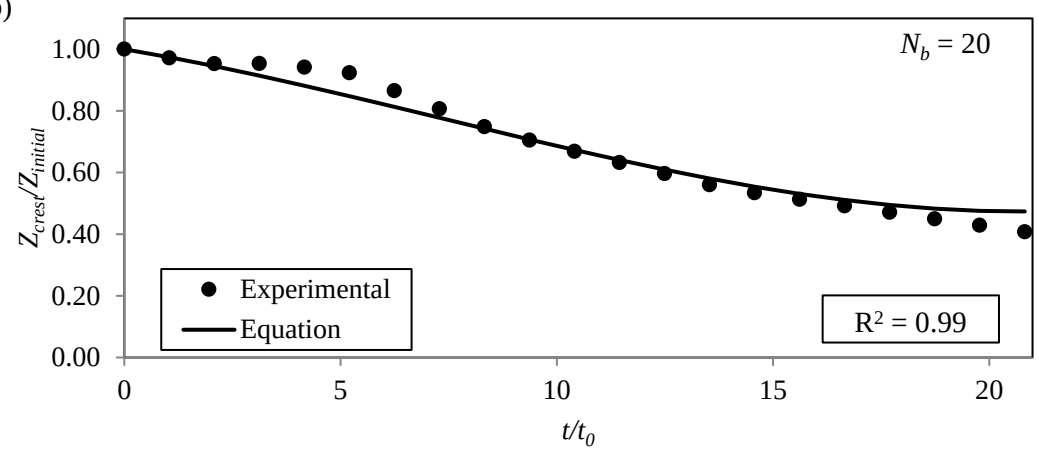

Figure 3.10 Comparison between experimental and empirical results of temporal changes of normalized crest height for: (a) N_b = 0; and (b) N_b = 20

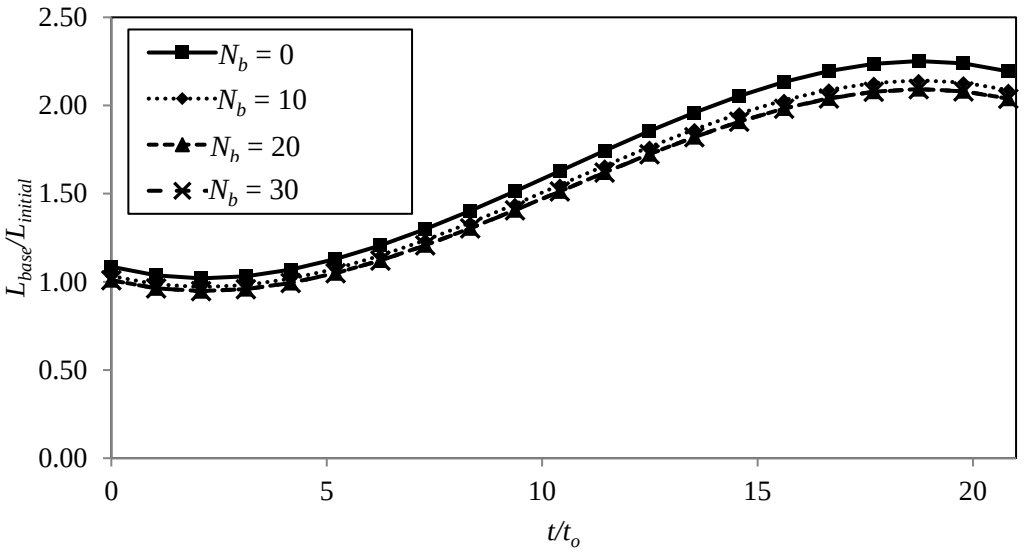

Figure 3.11 Time variation of dimensionless embankment length for different compaction levels using Eq. 3.4

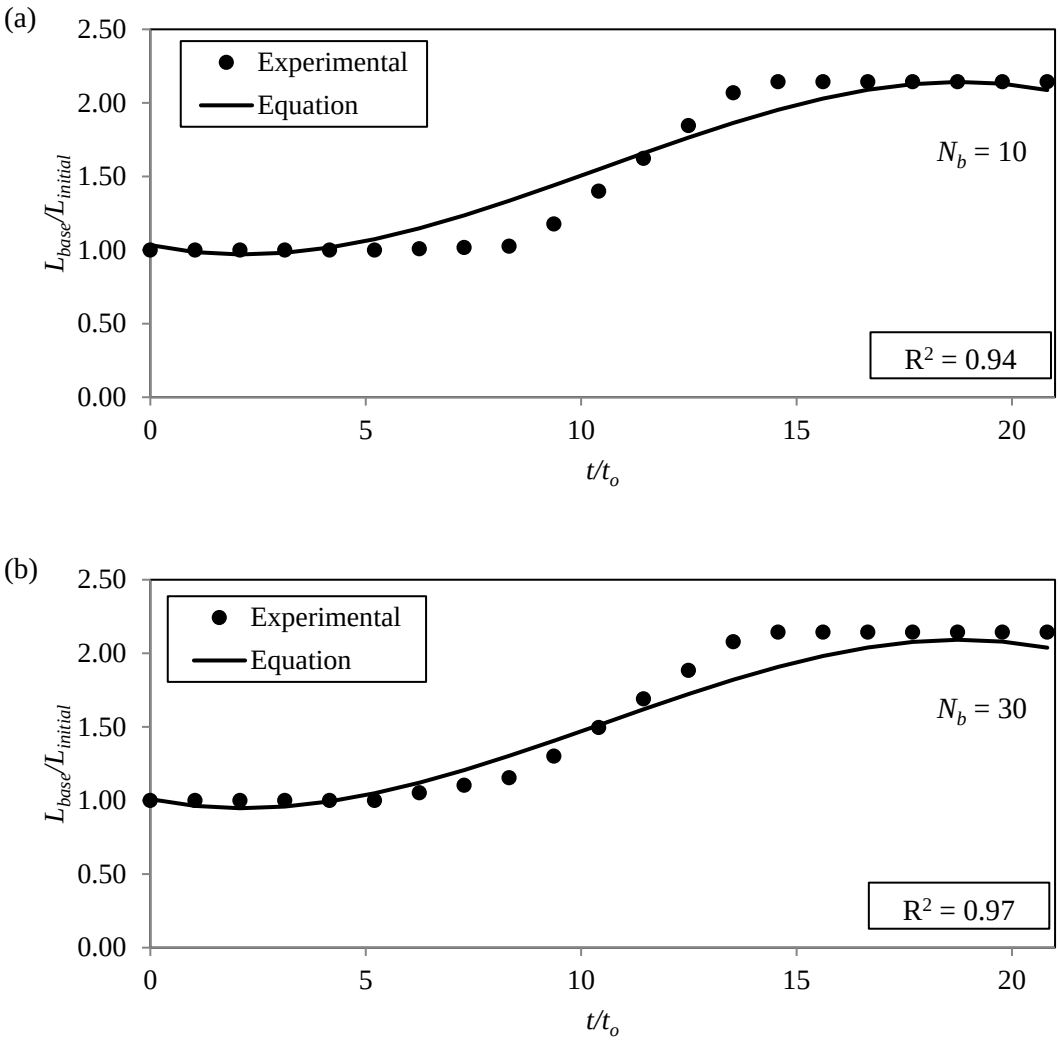

Figure 3.12 Comparison between experimental and empirical results of temporal changes of normalized embankment bottom length for: (a) N_b = 10; and (b) N_b = 30

Figure 3.13 Schematic diagram of proposed triangular model to predict the progressive breach shape (image by author)

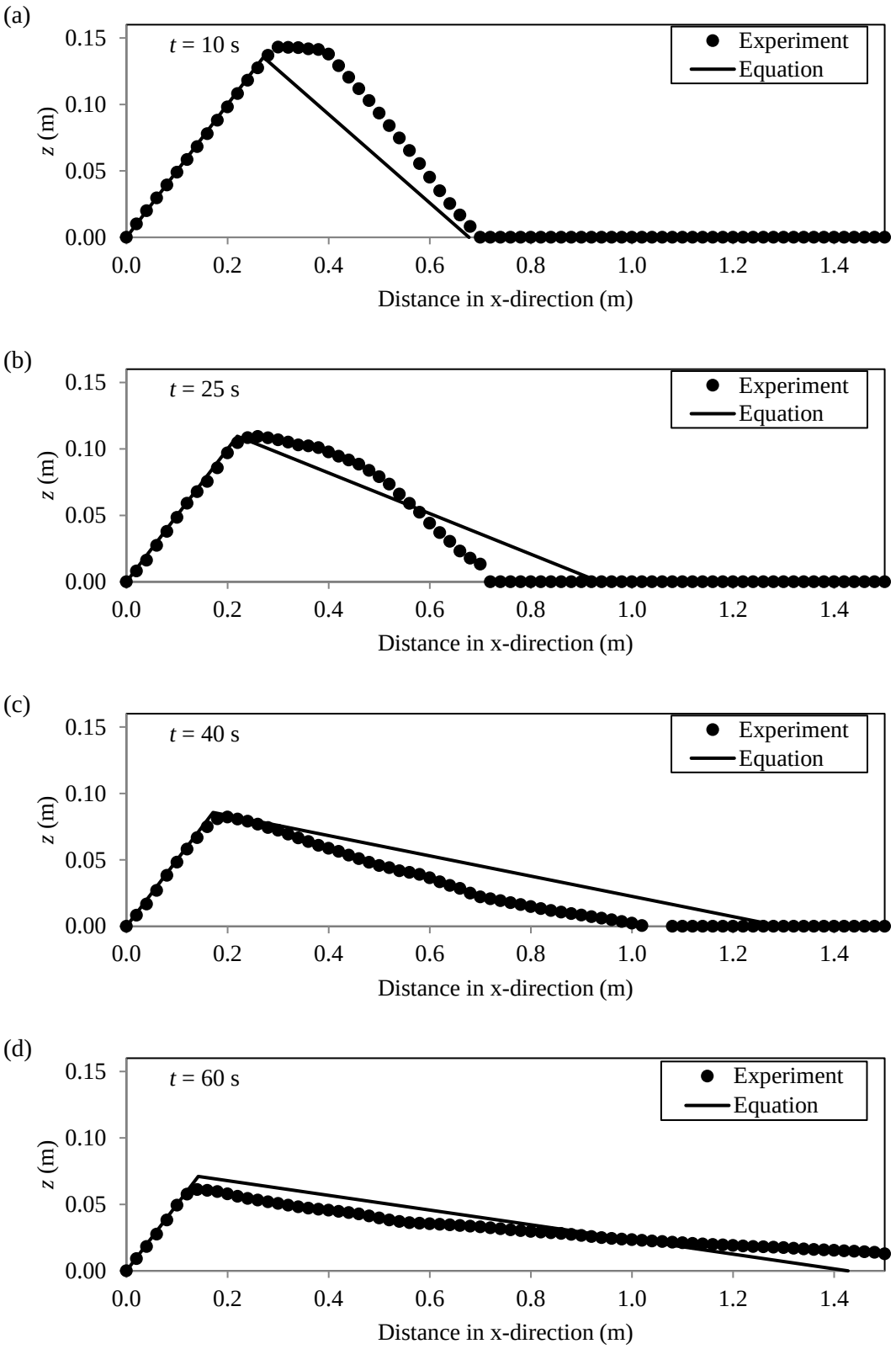

Figure 3.14 Measured and predicted bed surface profiles using the triangular model for N_b = 20 at: (a) t = 10 s; (b) t = 25 s; (c) t = 40 s; and (d) t = 60 s

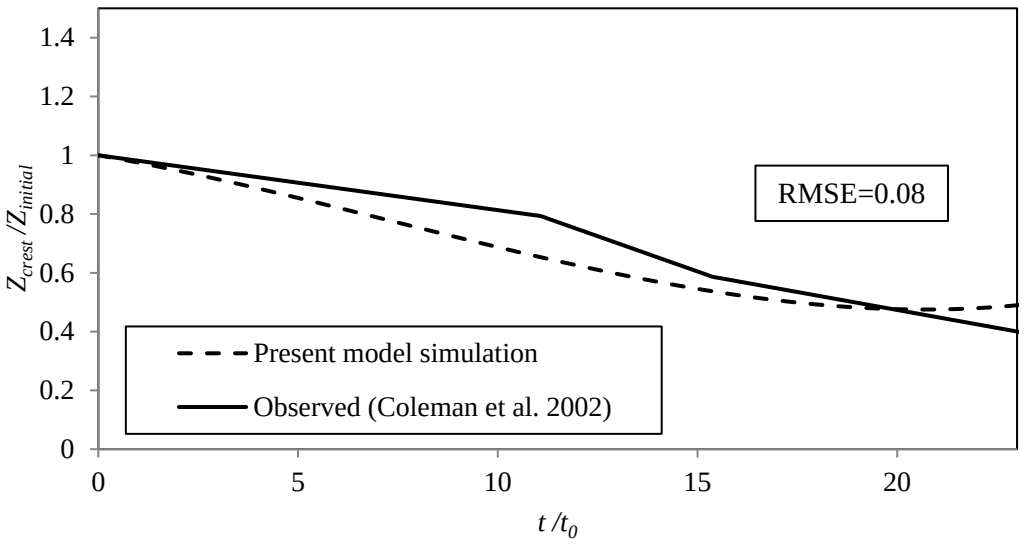

Figure 3.15 Observed and predicted normalized crest height variation with time

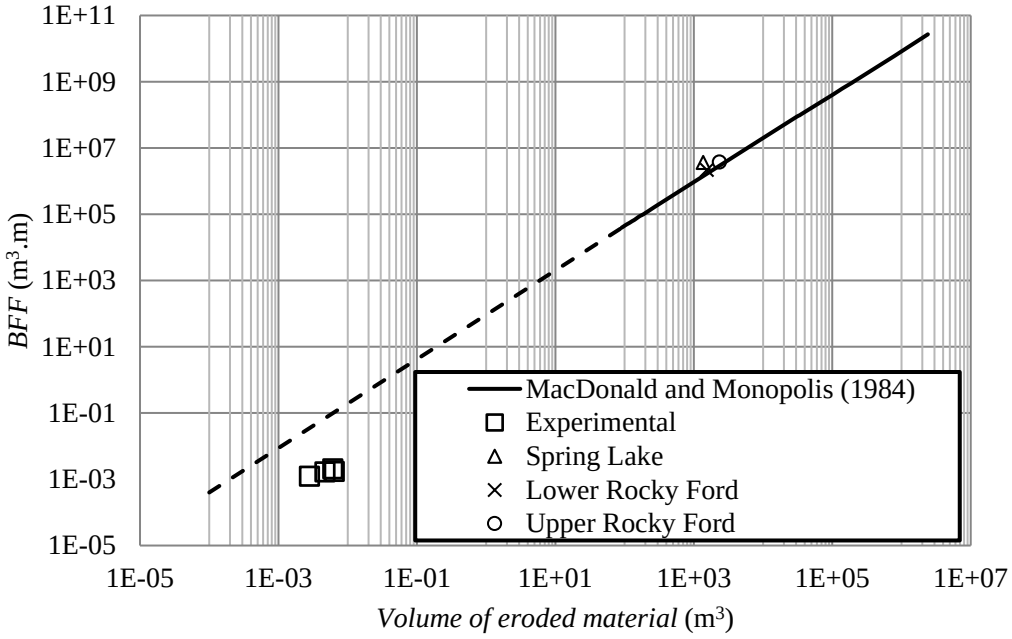

Figure 3.16 Outflow Characteristics vs. eroded volume

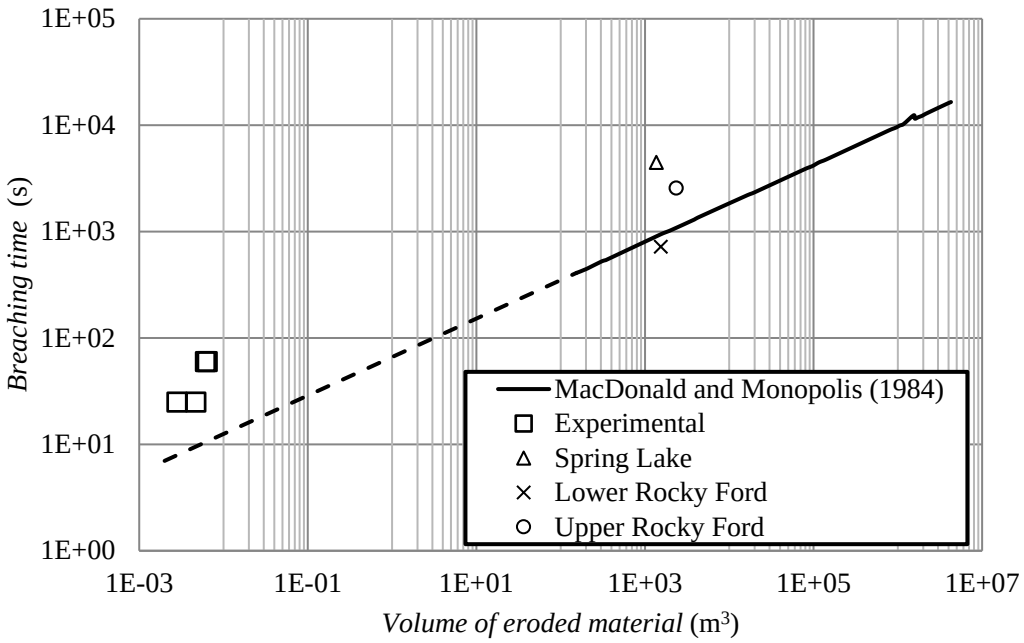

Figure 3.17 Breach development time vs. eroded volume

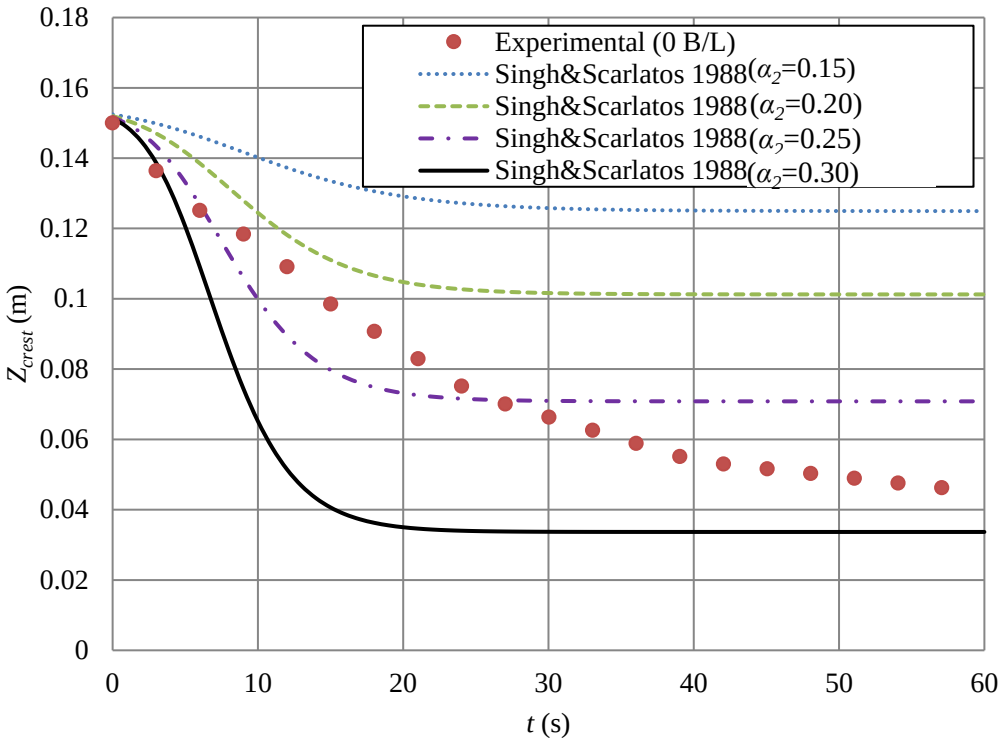

Figure 3.18 Time variation of dam crest level using the experimental data of no-compaction and the results of the mathematical model with different values of α_2

CHAPTER 4

NUMERICAL MODELING OF EARTHEN DAM BREACH DUE TO OVERTOPPING: INFLUENCE OF DIFFERENT MODEL PARAMETERS

In this chapter, the iRIC-Nays2D software, developed by Foundation of Hokkaido River Disaster Prevention Research Center for the calculation of unsteady 2D plane flow based on depth-averaged shallow water equations and morphology, is applied to a homogenous dam failure to study the influence of the different model parameters on dam failure prediction. Experiments on embankment failure by overtopping were conducted in a flume at the Hydraulics Laboratory, University of South Carolina. The model was run using different solution schemes, turbulence models, bedload formulas, and sediment transport mode (bed load only or bed load and suspended load). The Manning roughness coefficient and void ratio are selected by conducting a number of preliminary model runs.

4.1 Experimental Setup

The experimental setup is the same as the setup explained in chapter 3 (Figure 3.1). Three identical experiments were done to study the failure process of a non-cohesive, non-compacted embankment dam and the measured temporal changes of longitudinal embankment bed profile as well as water surface profile were averaged. Further, the breach outflow was measured at the downstream end of the flume using the volumetric technique. The trapezoidal earthen embankments of uniform sand with the mean diameter of 0.55 mm were placed 3.1 m downstream from the intake in the streamwise direction.

The upstream toe of the embankment was considered to be the origin of the coordinate system. The embankment dimensions for all three tests were: embankment height = 0.15 m, embankment width = 0.2 m, embankment crest length = 0.1 m, upstream and downstream embankment slopes (V: H) = 1:2.

4.2 Test Procedure

Prior to the embankment overtopping tests, Standard Proctor Compaction tests (ASTM D698) were carried out to determine the optimum water content of the homogenous, non-cohesive soil (i.e., sand only) used in the experiments. The optimum water content was found to be 5.2%. For each overtopping experiment, the soil was uniformly mixed with water to attain the optimum water content. To avoid compression, the soil was placed into three, 5 cm loose layers and no compaction was applied. For each layer, the soil surface was levelled precisely. After placing the third layer, the upstream and downstream faces of the embankment were trimmed carefully to reach the final trapezoidal shape. The seepage through the embankment was controlled and reduced by a thin clay layer with low permeability placed on the upstream face of the embankment.

To reduce the contact time between water and the upstream embankment face prior to overtopping and in turn seepage, the reservoir was filled at a relatively fast rate using two additional hoses along with the pump inflow. After the water surface reached a level about 5 cm below the embankment crest, the extra supply of water was cut off (i.e., the inflow was provided by the pump only). Small initial waves generated due to the rapid filling of the reservoir dissipated after a few seconds and the water surface was almost horizontal when the overtopping started. The valve for the dye container was opened slightly to add color to the water (the inflow from the color container was

negligible). The starting time of the failure process was considered to be the time when the water surface reached the front edge of the embankment crest.

Because of the limited width (i.e., 0.2 m), all three embankments were overtopped by the flow over the entire width resulting in a plane breach process (Pontillo et al. 2010, Schmocker and Hager 2009). So, the longitudinal embankment profile observed through the Plexiglas side of the flume represents the entire embankment. As indicated by Schmocker and Hager (2009), the sidewall effect was negligible. During the breach evolution, the water surface and bed surface profiles were recorded by an HD camera. By an image processing MATLAB code, the videos were converted into frames for one-second time intervals and then the longitudinal water and bed surface profiles were obtained by digitizing the frames.

4.3 Model Description

Numerical simulations were carried out using the iRIC software-Nays2D solver developed by the Foundation of Hokkaido River Disasters Prevention Center, Japan. This is a physically-based numerical solver for the calculation of 2D unsteady flow and bed deformation using boundary-fitted coordinates in a general curvilinear coordinate system. One of the three turbulence closure models can be selected: constant eddy viscosity, zero-equation, and k-ε. The total bed shear stress is evaluated from the Manning's equation. To calculate the bed deformation, two types of sediment transport models may be used: 'bed load only' and 'bed load and suspended load'. The total bed load transport rate in the depth-averaged, velocity direction may be estimated by using two different formulas: Ashida and Michiue, A.M., formula (1972) and Meyer-Peter and Muller, M.P.M, formula (1948).

In the following paragraphs, the basic flow and sediment transport equations in orthogonal coordinate system (*x*,*y*) are presented. To conserve space, the transformed forms of these equations into general coordinate system are not discussed here. The equations in general coordinate system are solved using the finite-difference method on the boundary-fitted structured grids. In addition, the software has a slope collapse model. If the angle of the bed exceeds a specified critical angle, the bed elevation is modified to satisfy the critical angle. The slope collapse model was not used in this investigation.

Following is the sequence of computations in the model: First, the 2D depth-averaged flow filed is calculated on the boundary-fitted structured grid using the finite-difference method based on the initial and boundary conditions Second, sediment transport rate equations (i.e., bedload and suspended load) are calculated; finally, the bed deformation is determined using the 2D sediment continuity equation and bed elevation for all nodes is updated. An iterative process is applied to solve the equations for the unknown nodal values and these steps are repeated for a given time duration.

Flow Equations

The depth-averaged continuity equation for two-dimensional unsteady flow is:

$$\frac{\partial h}{\partial t} + \frac{\partial (uh)}{\partial x} + \frac{\partial (vh)}{\partial y} = 0 \qquad (4.1)$$

in which t = time, h = water depth, x = streamwise coordinate, y = transverse coordinate, u = velocity in the x direction, and v = velocity in the y direction.

The depth-averaged momentum equations in the *x*- and *y*- direction are

$$\frac{\partial (uh)}{\partial t} + \frac{\partial (hu^2)}{\partial x} + \frac{\partial (huv)}{\partial y} = -hg\frac{\partial h}{\partial x} - \frac{\tau_x}{\rho} + D^x \qquad (4.2)$$

$$\frac{\partial(vh)}{\partial t}+\frac{\partial(huv)}{\partial x}+\frac{\partial(hv^2)}{\partial y}=-hg\frac{\partial h}{\partial y}-\frac{\tau_y}{\rho}+D^y \tag{4.3}$$

where

$$\frac{\tau_x}{\rho}=C_f u\sqrt{u^2+v^2} \tag{4.4}$$

$$\frac{\tau_y}{\rho}=C_f v\sqrt{u^2+v^2} \tag{4.5}$$

$$D^x=\frac{\partial}{\partial x}\left[V_t\frac{\partial(uh)}{\partial x}\right]+\frac{\partial}{\partial y}\left[V_t\frac{\partial(uh)}{\partial y}\right] \tag{4.6}$$

$$D^y=\frac{\partial}{\partial x}\left[V_t\frac{\partial(vh)}{\partial x}\right]+\frac{\partial}{\partial y}\left[V_t\frac{\partial(vh)}{\partial y}\right] \tag{4.7}$$

where g = gravitational acceleration, τ_x = bed shear stress in the *x* direction, τ_y = bed shear stress in the *y* direction, C_f = bed shear coefficient, and V_t = eddy viscosity coefficient. The D^x and D^y in the momentum equations are known as diffusion terms. Two available finite-difference methods in the model can be applied to the advection terms in the momentum equations: 'the upwind difference method' and the 'CIP method'. The bed friction coefficient, C_f, is estimated using Manning constant, n_m, as follows

$$C_f=\frac{\mathrm{g}{n_m}^2}{h^{1/3}} \tag{4.8}$$

Sediment Transport and Bed Deformation Equations

In order to calculate the bedload transport rate by using either the A.M. formula or the M.P.M formula, the value of the dimensionless bed shear stress, τ_*, should be known. By applying Manning equation, τ_* can be expressed as follows

$$\tau_*=\frac{hI_e}{s_g d}=\frac{C_f V^2}{s_g g d}=\frac{{n_m}^2V^2}{s_g g h^{1/3}} \tag{4.9}$$

where I_e = the energy or friction slope, s_g = submerged specific gravity, *d* = grain size of

bed material, and *V* is the composite velocity defined by the following equation

$$V = \sqrt{u^2 + v^2} \tag{4.10}$$

A.M. formula for bedload transport rate, (1972)

The total bedload transport rate in the depth-averaged velocity direction (in the *V* direction), q_b, is given by

$$q_b = 17{\tau_*}^{3/2}\left(1 - \frac{\tau_{*c}}{\tau_*}\right)\left(1 - \sqrt{\frac{\tau_{*c}}{\tau_*}}\right)\sqrt{s_g g d^3} \tag{4.11}$$

The dimensionless critical shear stress,τ_{*c}, is obtained from the Iwagaki's equation (Iwagaki 1956).

M.P.M formula for bedload transport rate, (1948)

$$q_b = 8(\tau_* - \tau_{*c})^{1.5}\sqrt{s_g g d^3} \tag{4.12}$$

Two-dimensional continuity equation of sediment transport, Exner equation

$$\frac{\partial z}{\partial t} + \frac{1}{1-\lambda}\left[\frac{\partial q_b^x}{\partial x} + \frac{\partial q_b^y}{\partial y} + q_{su} - w_f c_b\right] = 0 \tag{4.13}$$

in which *z* = bed elevation, q_b^x and q_b^y = bed load transport rate per unit width in the *x* and *y* directions, respectively, q_{su} = suspended load supplied per unit area of bed and is calculated based on the equation proposed by Itakura and Kishi (1980), w_f = settling velocity of suspended sediment which is obtained with Rubey's equation (Rubey 1933), c_b = concentration at the control point (i.e., near the bottom), and λ = void ratio of bed material.

Modeling Procedure

Using cross-sectional data of the experimental setup (i.e., flume with trapezoidal embankment), a grid shape is created containing 150 and 6 cells (1057 nodes) in the longitudinal and transvers directions, respectively. To confirm the grid size independence, the number of cells was increased to 300 and 12 in the longitudinal and transvers directions, respectively and no major changes were observed in the simulation results. The flume, flow, and embankment parameters are selected in conformity with those of the experimental tests. For the boundary condition, the upstream discharge is specified as $Q = 0.0005\ m^3s^{-1}$ and the downstream water surface elevation is specified as a time series equal to those from the experimental test. The values of various parameters for all simulations are: density of water = 1000 kgm^{-3}, reduced specific gravity of embankment material = 1.65, void ratio of embankment material = 0.4, Manning roughness coefficient for the wooden sections of the flume = 0.012, Manning roughness coefficient for the embankment material = 0.017, computational time step = 0.005 s, and the grain size of bed material = 0.55 mm.

The numerical simulations are designed to assess the effect of turbulence model, finite-difference approximation of the advection terms, sediment transport type, and bedload transport formula to predict the breach process of a homogenous, non-cohesive embankment due to overtopping. Furthermore, to gain a better insight of the failure process and other parameters affecting the breach process, simulations are carried out with different bed material grain size and downstream slope of the embankment.

In this study, two turbulence models (i.e., ‘constant eddy viscosity model’ and ‘zero-equation model’), two finite-difference approximation of the advection terms (i.e.,

the ‘upwind difference method’ and the ‘CIP method’), two sediment transport type (i.e., ‘bedload and suspended load, and ‘bedload only), and two bedload transport formulas (i.e., A.M. and M.P.M.) were investigated. Thus, a total of 16 simulation cases were carried out (Table 4.1) and the results of the temporal longitudinal breach profiles as well as the breach discharge hydrograph are compared with the measured results.

4.4 Results

Experimental Observations

The embankment overtopping test is repeated three times with the same embankment dimensions and flow parameters. Figure 4.1 shows the breach hydrographs for these three tests. The peak breach outflow, Q_{peak}, and time to peak, t_{peak}, are about 0.014 $m^3s^{-1}m^{-1}$ and 12 s, respectively for all the three tests. Further, Figure 4.2 shows the embankment surface *z* and the water surface *h* profiles at various times for the three tests. Both the embankment and the water surface profiles at different times are generally similar, except minor deviations during the first 15 seconds of the tests. Most likely, these minor deviations are due to difference in the start time of overtopping for each experiment and/or different speeds of overtopping water front on the crest in the tests.

With the repeatability of the tests confirmed, the averaged values of the three tests for the breach discharge, embankment surface profile, and water surface profile at various times are considered acceptable for general embankment overtopping failure and thus may be used to compare with the numerical results. Figures 4.3 and 4.4 show the averaged breach discharge per unit width, *q (t)*, and the averaged embankment surface profiles, *z(x)*, at various times, *t*, respectively. Covering the embankment upstream slope with a thin layer of clay along with the rapid filling of the reservoir is adequate to control

the seepage as overtopping started before the seepage line reached the downstream slope. The observations of the temporal advance of embankment erosion in the current study are in conformity with the erosion processes described by other investigators (e.g., Chinnarasri et al. 2003, Schmocker and Hager 2009). The starting time of the overtopping process, i.e. t = 0 s, is the time when the water surface at the reservoir reaches the upstream edge of the crest. Until about t = 5 s, the embankment remains relatively intact. At t = 10 s, the downstream edge of the crest as well as the upper section of the downstream embankment face are eroded. After t = 10 s, the downstream face of the embankment starts to rotate around a pivot point roughly located at x = 0.64 m and z = 0.025 m. At t = 15 s, a round shaped crest forms with almost one-fourth drop in the height and a wavy deposition pattern is observed beyond the original toe of the embankment. At t = 25 s, the embankment height drops to almost half. At t = 60 s, the erosion process reaches an equilibrium condition and stable embankment surface is formed with a relatively small downstream slope.

Numerical Simulations

Similar to the experimental embankment breach, the simulated streamwise embankment and water surface profiles are identical over the entire embankment width at each time step. Therefore, one of the streamwise profiles is considered to represent the entire cross section. Several preliminary simulations are carried out prior to the original simulations to determine the best fitted embankment Manning roughness coefficient, and the void ratio. By comparing the computed bed and water surface profiles at t = 5, 10, 15, 25, 40, and 60 s and also the breach hydrograph with those from the averaged experimental results, the selected parameters for the Manning roughness coefficient and the void ratio

are 0.017 and 0.4, respectively. These fitted parameters are used to model the 16 cases.

No significant difference is observed in the simulated results (i.e., Case 1 vs. 2, 3 vs. 4, 5 vs. 6, 7 vs. 8, 9 vs. 10, 11 vs. 12, 13 vs. 14, and 15 vs. 16) when using the constant eddy viscosity and zero equation models, by keeping all the other parameters the same. Figures 4.5 and 4.6 show the results of using two different turbulent models and two different finite-difference approximation of the advection terms on the calculated bed and water surface profiles at various times for Case 15 versus 16 and Case 1 versus 9, respectively. No significant deviation is seen in the simulated bed and water surface profiles for the two different finite-difference approximations of the advection terms. Only less wavy shape is observed in both bed and water surface profiles after t = 15 s at the upstream section of the embankment when the CIP method is used. To determine the effect of the suspended load on the simulation, the simulated bed and water surface profiles as well as the breach hydrograph from the cases with bedload only are compared with those of bedload and suspended load while keeping all other simulation conditions constant. As an example, Figure 4.7 shows the simulated bed and water surface profiles at various times by using bedload only and bedload and suspended load for the Cases 1 and 5, respectively. Also in Figure 4.8 the breach discharge hydrographs are compared for those two cases and it shows no significant effect of considering the suspended load on the simulated results. The deviations in both the profiles and the hydrographs are very small and this is expected since the bed material grain size of 0.55 mm would make the suspended load contribution negligible compared to the bedload. To magnify the effect of the suspended load, similar simulations were carried out using grain sizes of d = 0.2 mm and 0.125 mm. For d = 0.2 mm the deviations were slightly more compared to the

simulations for d = 0.55 mm, while for d = 0.125 mm (Figure 4.9) the deviations were considerable and the run considering the suspended load alone is more erosional and the final height of the embankment is less than 0.04 m. The small deviations in Figures 4.6 and 4.7 are only observed for the first 15 s of the simulation runs after which almost no deviation is seen between the two cases.

To assess the effect of bedload transport formulas, A.M. and M.P.M., on the simulation results, the bed and water surface profiles are compared in Figure 4.10 for the Cases 1 and 3. Erosion rate is faster when A.M. formula is used and large deviations are observed between the two cases especially at the upstream section where the original embankment was placed. Further, the deviations decrease with time.

To determine the simulation that reproduces better the embankment and water surface profiles with time and also the breach discharge hydrograph, the experimental results are compared with the computed results for all the cases. To compare the results for the M.P.M and the A.M. formulas, Figure 4.11 shows the embankment and water level profiles for Cases 12 (M.P.M) and 10 (A.M.). The bed and water surface profiles are overestimated at all the times by the M.P.M. formula, especially at the upstream part of the toe of the embankment, i.e., x = 0 to 0.7 m, while the erosion process is represented qualitatively better after x = 0.7 m. Table 4.2 shows the averaged root mean square errors of all the numerical cases with A.M. and M.P.M. formulas for the bed and water surface profiles at various times. According to the errors, during the initial failure stage, t = 0 s to 15 s, the M.P.M. formula predicts better the bed and water surface profiles, while after t = 15 s the A.M. formula reproduces the failure process better. For both A.M. and M.P.M. cases, a sudden drop is seen around the original location of the downstream toe of the

embankment, i.e., x = 0.7 m in the simulated bed and water surface profiles which was not observed in the experimental results. The simulations were carried out with a milder embankment downstream slope ($V:H$ = 4:1) and again, the discontinuity was seen in both bed and water surface profiles around the downstream toe of the embankment.

The computed outflow hydrographs are compared with the observed hydrograph from the experiments. The A.M. formula overestimates Q_{peak}, but t_{peak} is estimated relatively well. However, the simulations with the M.P.M. formula resulted in a reasonable prediction of the outflow hydrograph as shown in Figure 4.12 which compares the simulated hydrographs for Case 4 (M.P.M.) with Case 1 (A.M.).

Table 4.1 Numerical cases by various modeling parameters

Cases	Turbulent model	Finite difference approximation of advection terms	Sediment transport type	Bedload transport formula
1	Constant eddy viscosity	upwind scheme	bedload and suspended load	A.M.
2	Zero equation	upwind scheme	bedload and suspended load	A.M.
3	Constant eddy viscosity	upwind scheme	bedload and suspended load	M.P.M.
4	Zero equation	upwind scheme	bedload and suspended load	M.P.M.
5	Constant eddy viscosity	upwind scheme	bedload	A.M.
6	Zero equation	upwind scheme	bedload	A.M.
7	Constant eddy viscosity	upwind scheme	bedload	M.P.M.
8	Zero equation	upwind scheme	bedload	M.P.M.
9	Constant eddy viscosity	CIP	bedload and suspended load	A.M.
10	Zero equation	CIP	bedload and suspended load	A.M.
11	Constant eddy viscosity	CIP	bedload and suspended load	M.P.M.
12	Zero equation	CIP	bedload and suspended load	M.P.M.
13	Constant eddy viscosity	CIP	bedload	A.M.
14	Zero equation	CIP	bedload	A.M.
15	Constant eddy viscosity	CIP	bedload	M.P.M.
16	Zero equation	CIP	bedload	M.P.M.

Table 4.2 Averaged root mean square error for numerical cases with A.M. formula and M.P.M. formula

Bedload formula	t = 5 s		t = 10 s		t = 15 s		t = 25 s		t = 40 s		t = 60 s	
	z	h	z	h	z	h	z	h	z	h	z	h
A.M.	0.009	0.017	0.016	0.017	0.015	0.018	0.010	0.011	0.009	0.008	0.009	0.007
M.P.M.	0.009	0.017	0.012	0.013	0.012	0.013	0.016	0.018	0.015	0.016	0.014	0.014

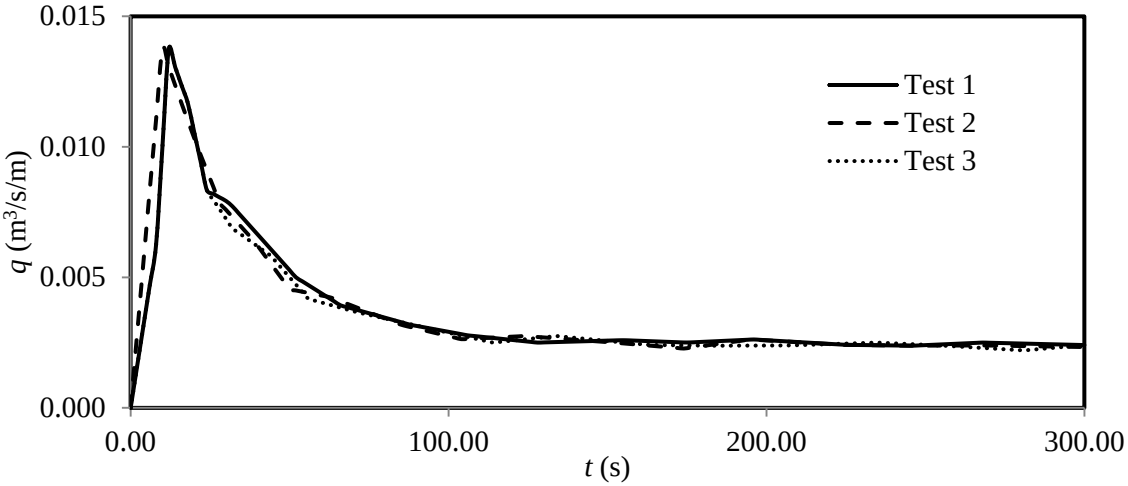

Figure 4.1 Breach outflow hydrograph according to experimental tests

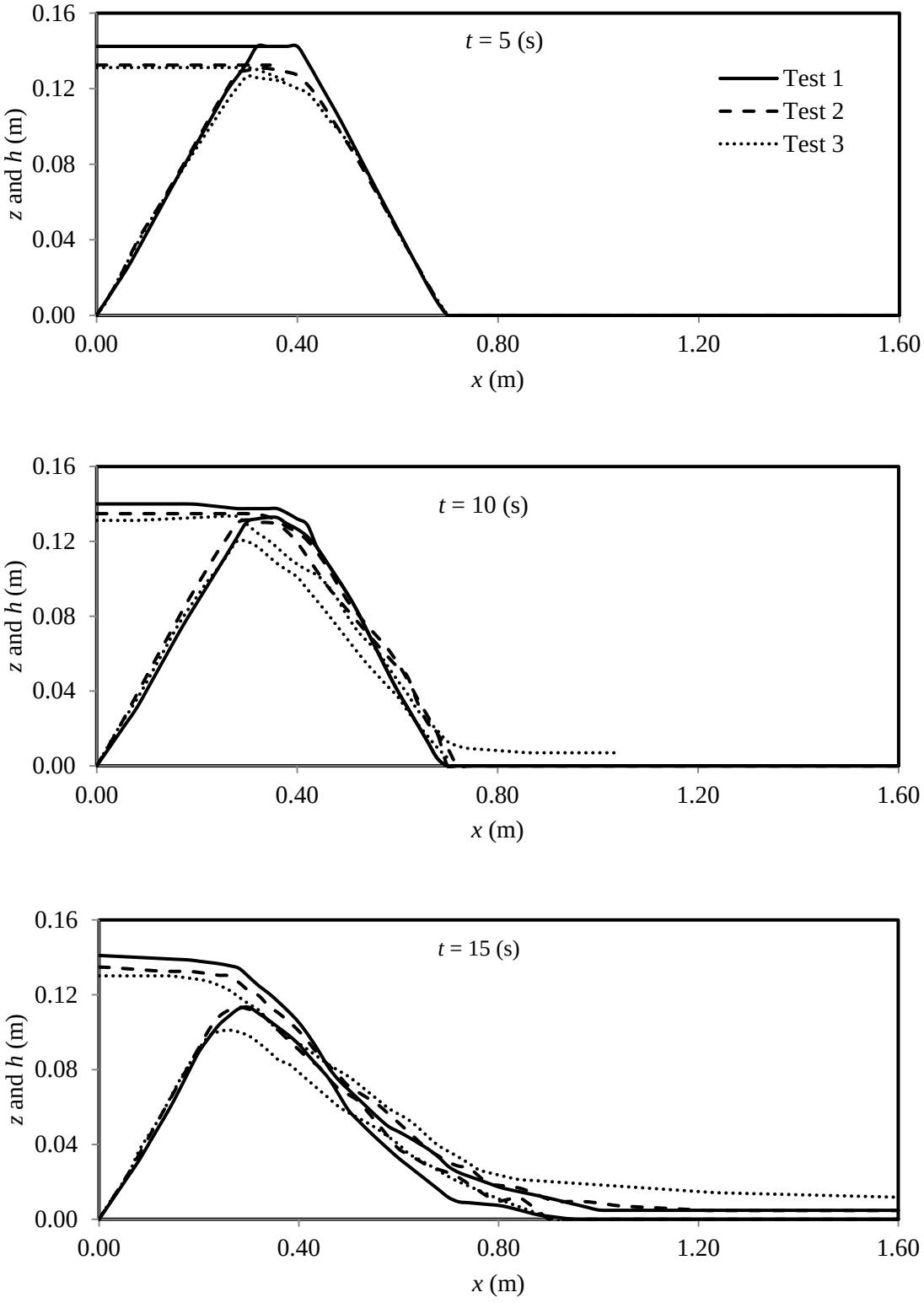

Figure 4.2 Embankment surface profile z (x) and water surface profiles h(x) at various times t for three experimental tests

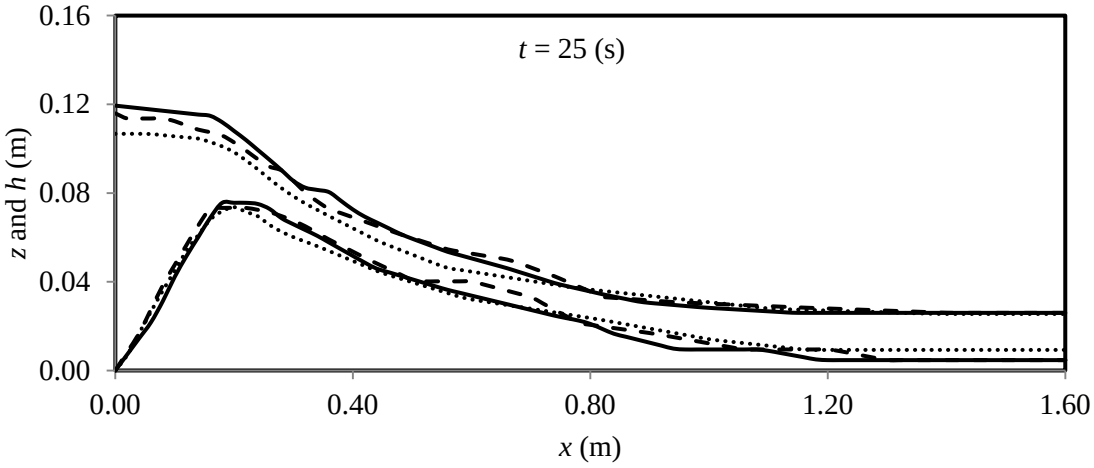

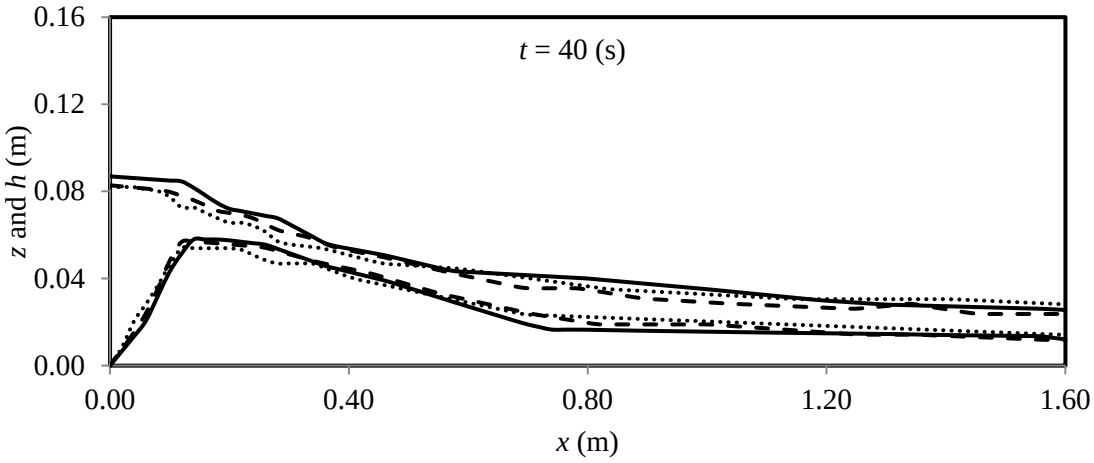

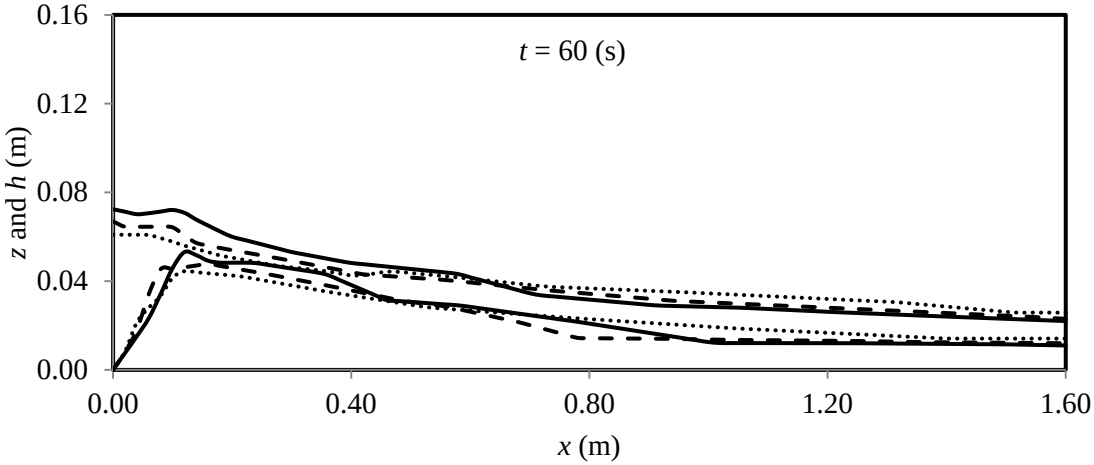

Figure 4.2 (continued) Embankment surface profile z (x) and water surface profiles h(x) at various times t for three experimental tests

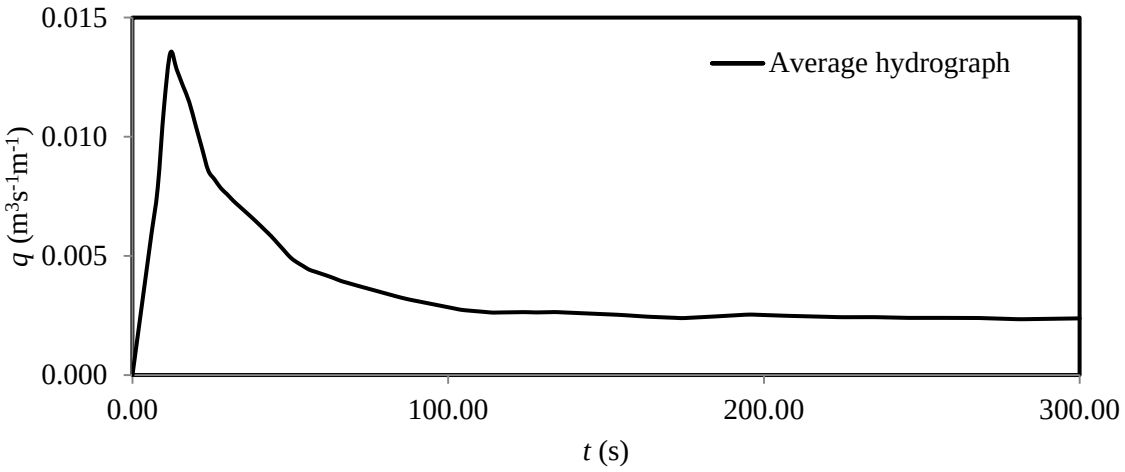

Figure 4.3 Averaged outflow hydrograph of the three tests

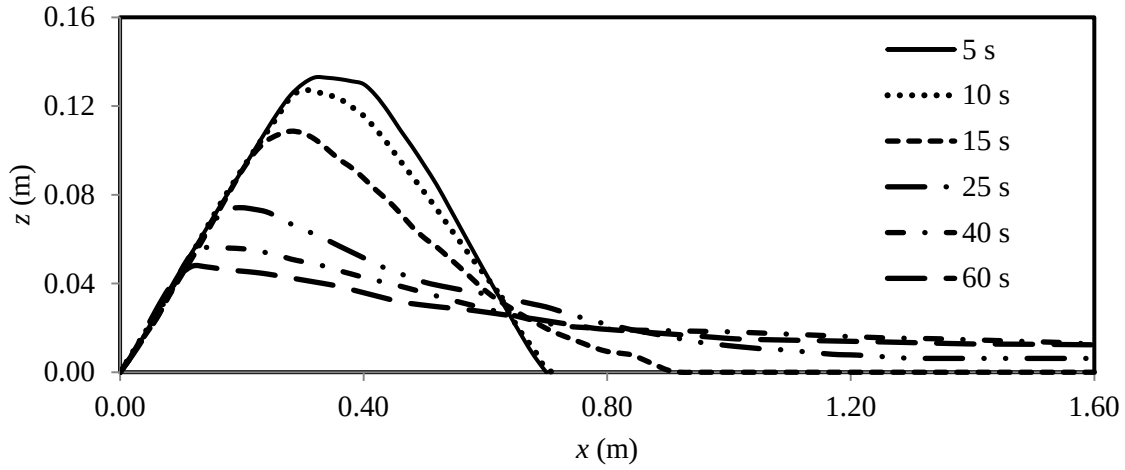

Figure 4.4 Averaged embankment surface profiles $z(x)$ of three tests at various times t

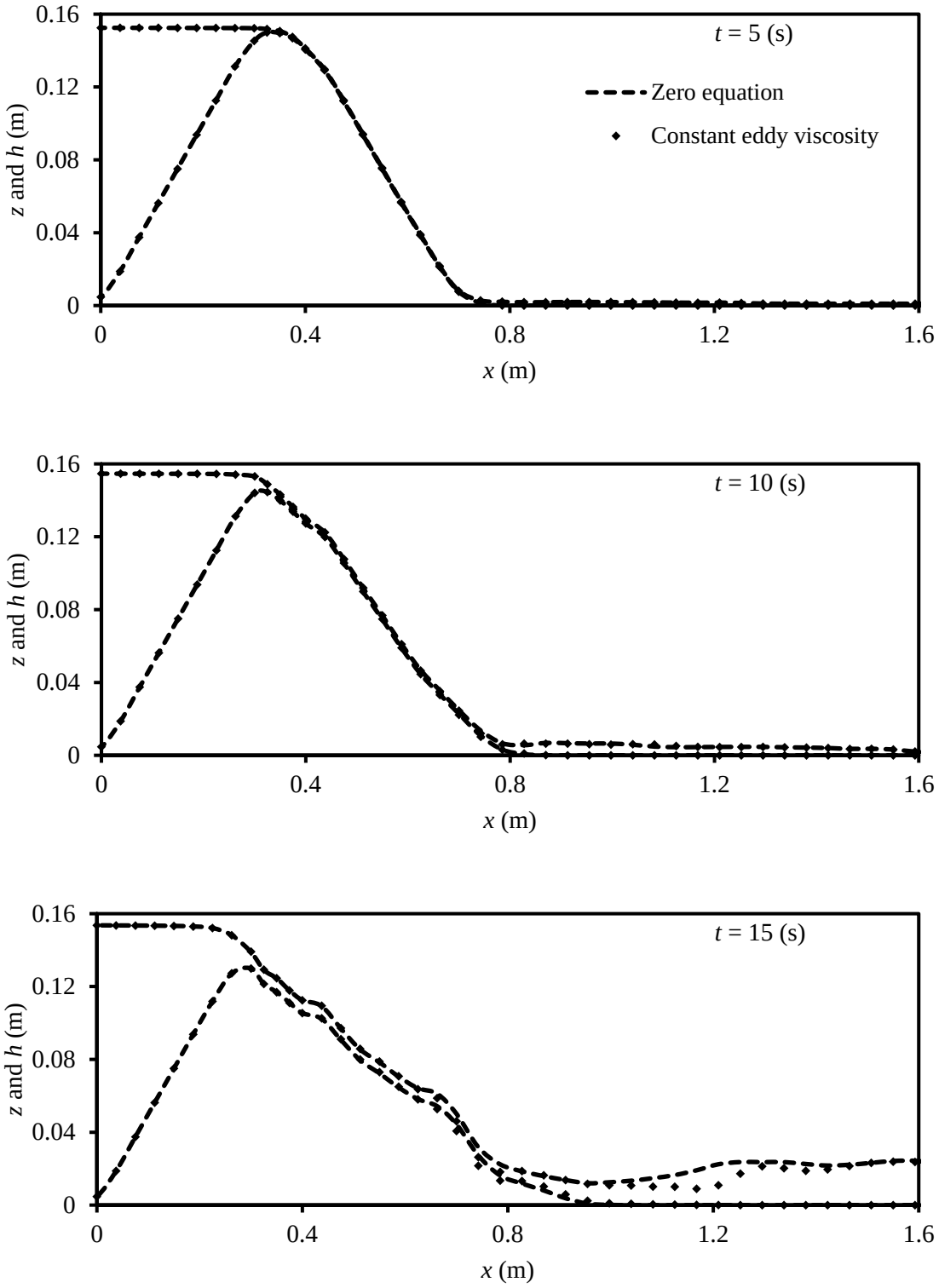

Figure 4.5 Turbulent model effect: simulated bed and water surface profiles at various times for Case 15 with constant eddy viscosity model and Case 16 with zero equation model

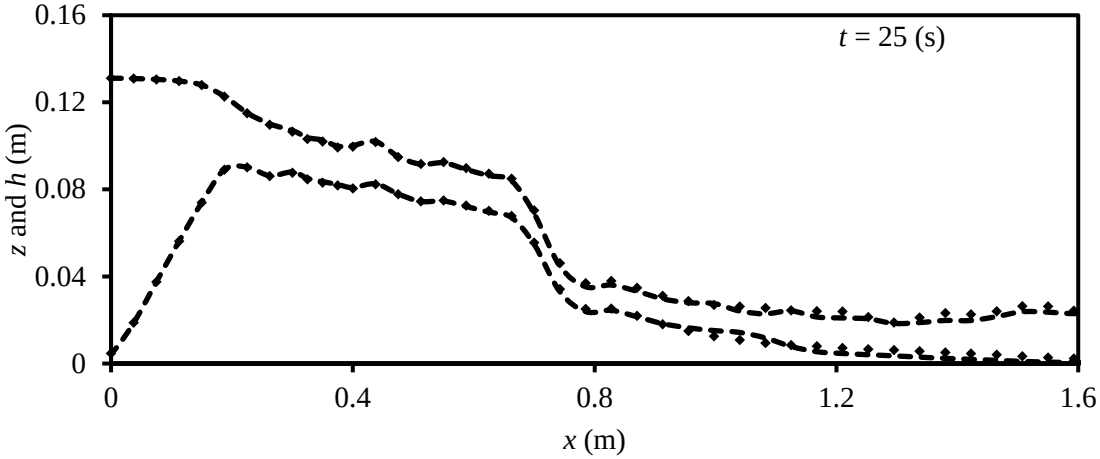

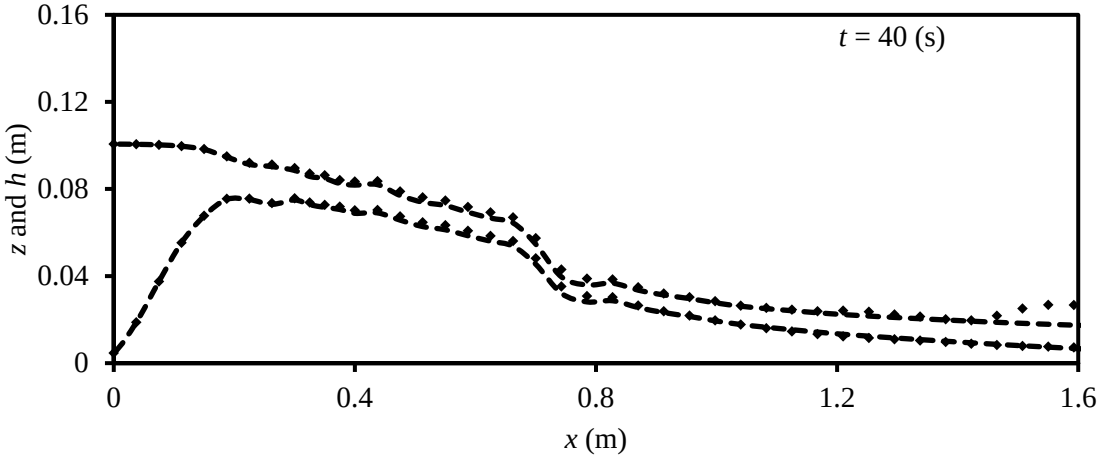

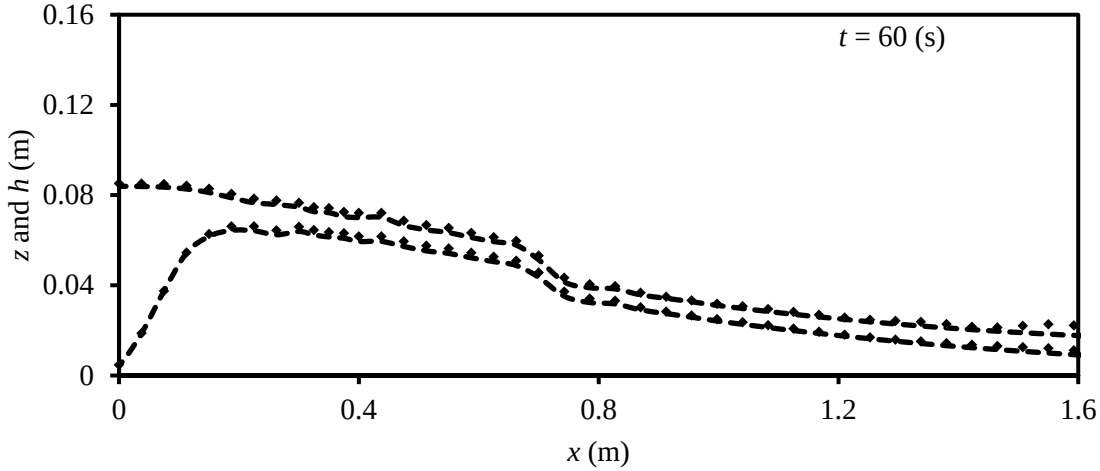

Figure 4.5 (continued) Turbulent model effect: simulated bed and water surface profiles at various times for Case 15 with constant eddy viscosity and Case 16 with zero equation model

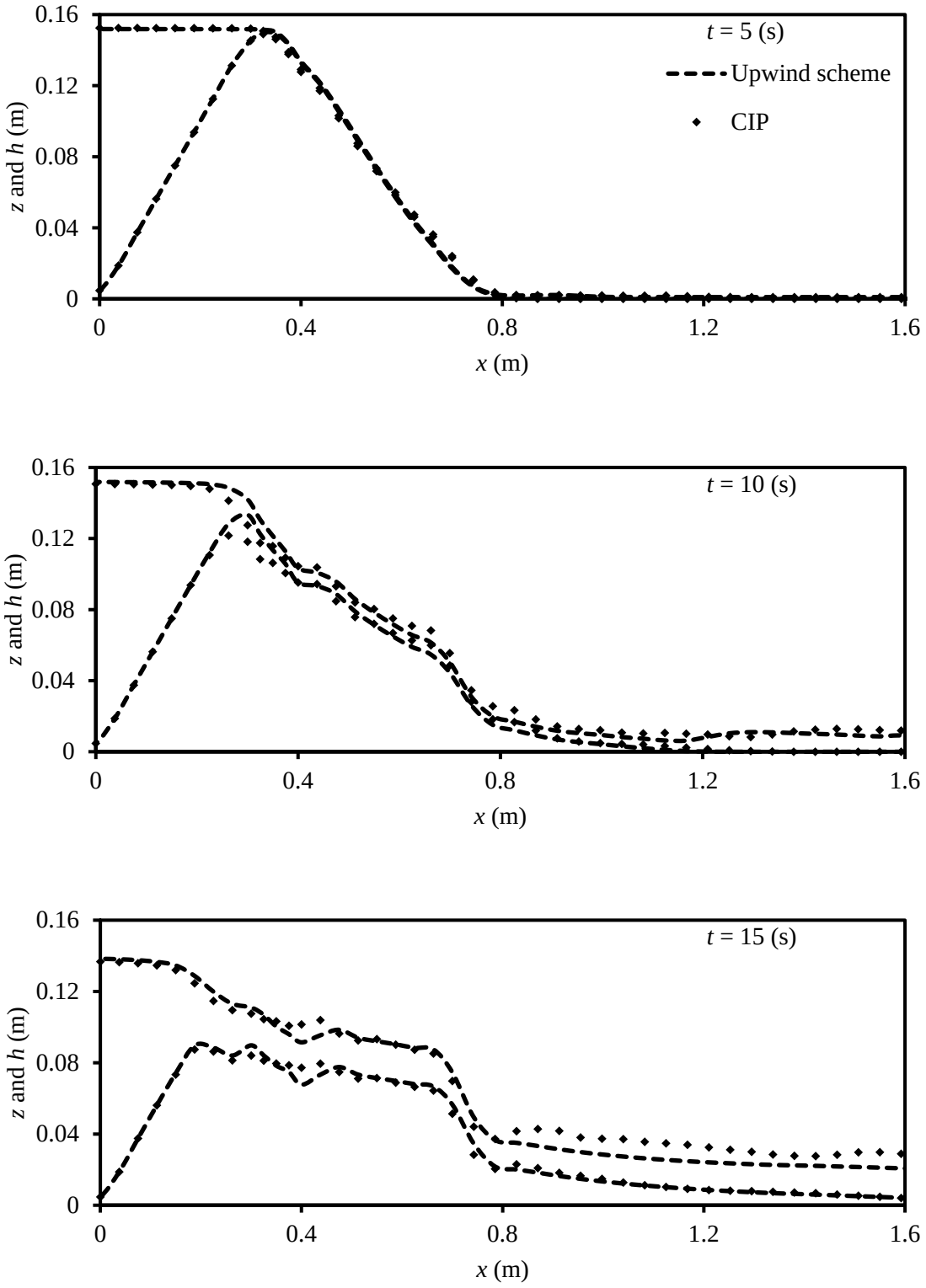

Figure 4.6 Finite difference approximations of advection terms effect: simulated bed and water surface profiles at various times for Case 1 with upwind scheme method and Case 9 with CIP method

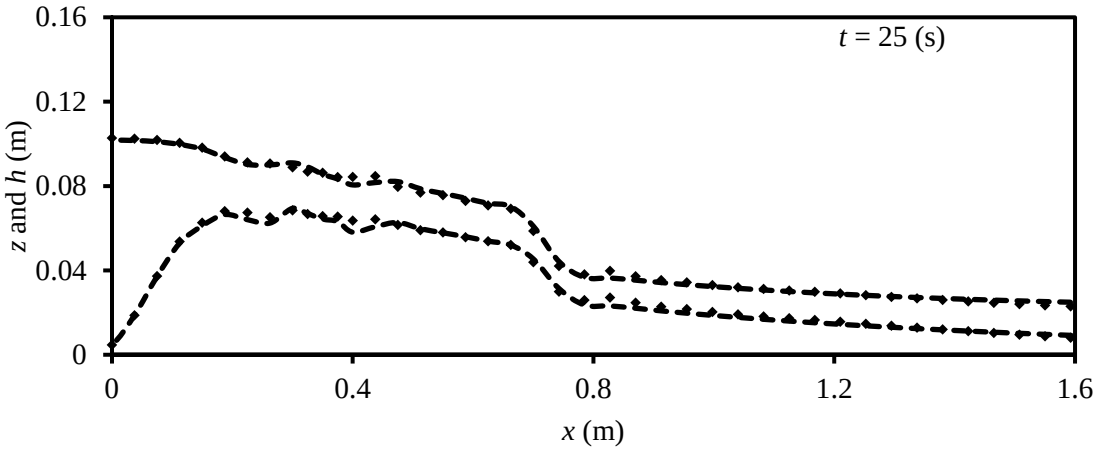

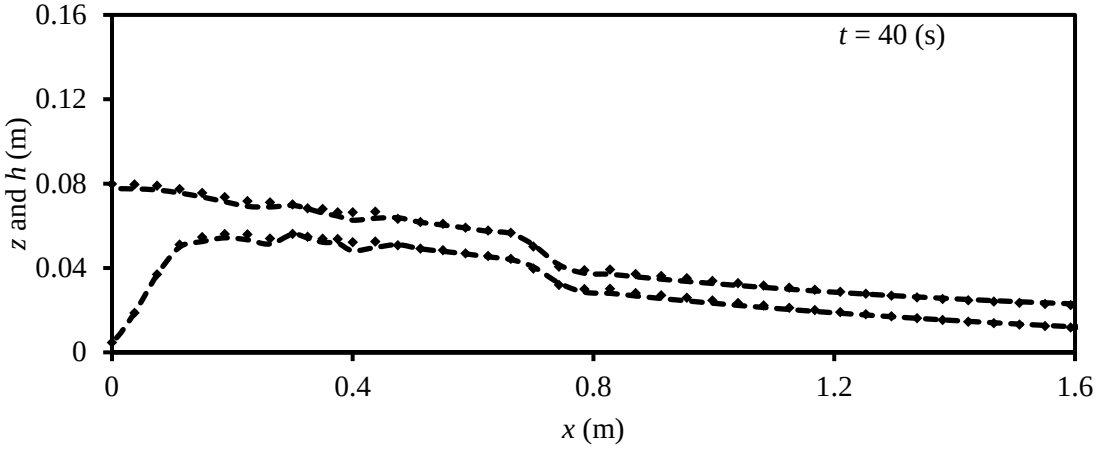

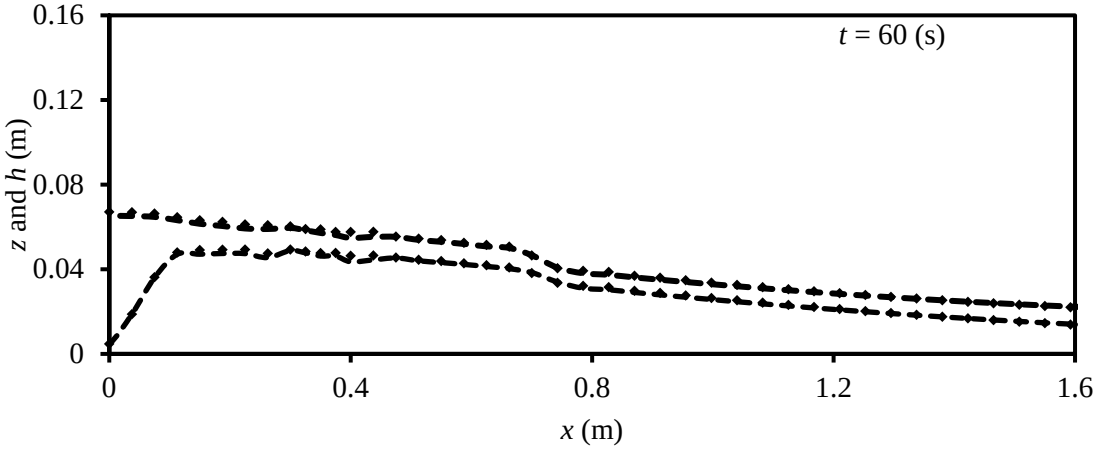

Figure 4.6 (Continued) Finite difference approximations of advection terms effect: simulated bed and water surface profiles at various times for Case 1 with upwind scheme method and Case 9 with CIP method

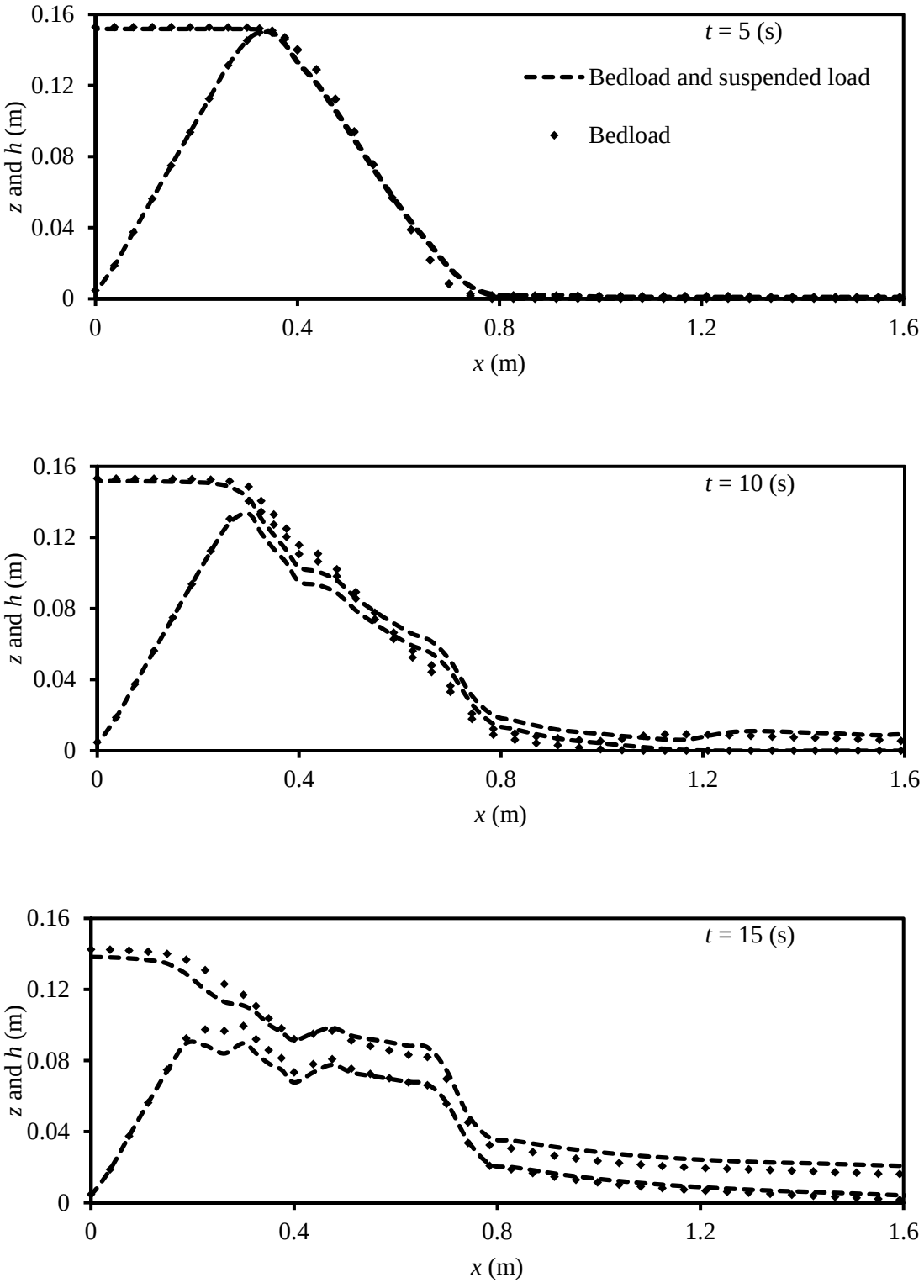

Figure 4.7 Suspended load effect: simulated bed and water surface profiles at various times for Case 1 with bedload and suspended load and Case 5 with bedload only

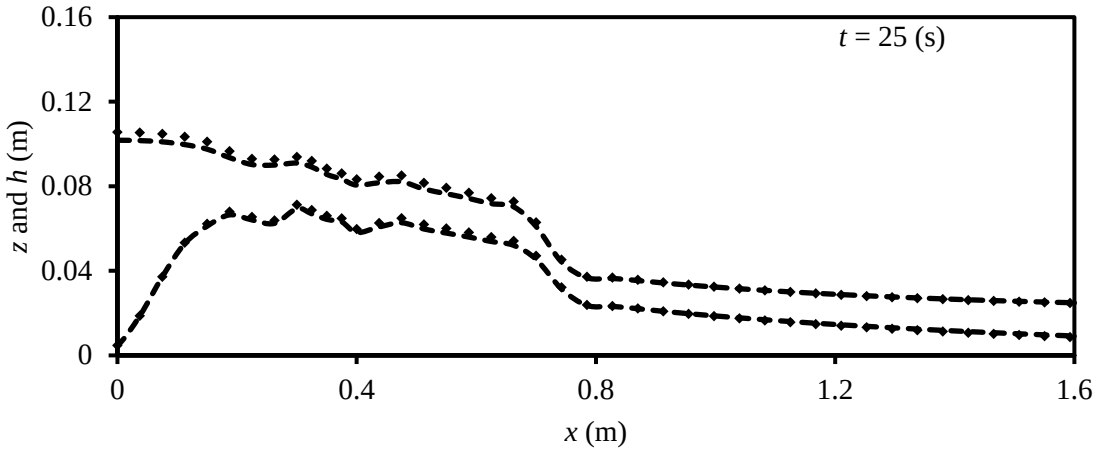

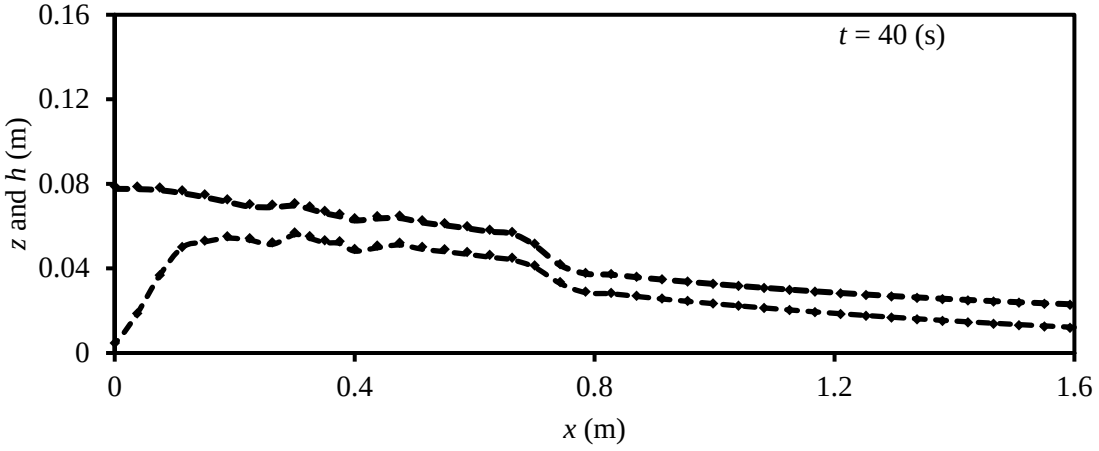

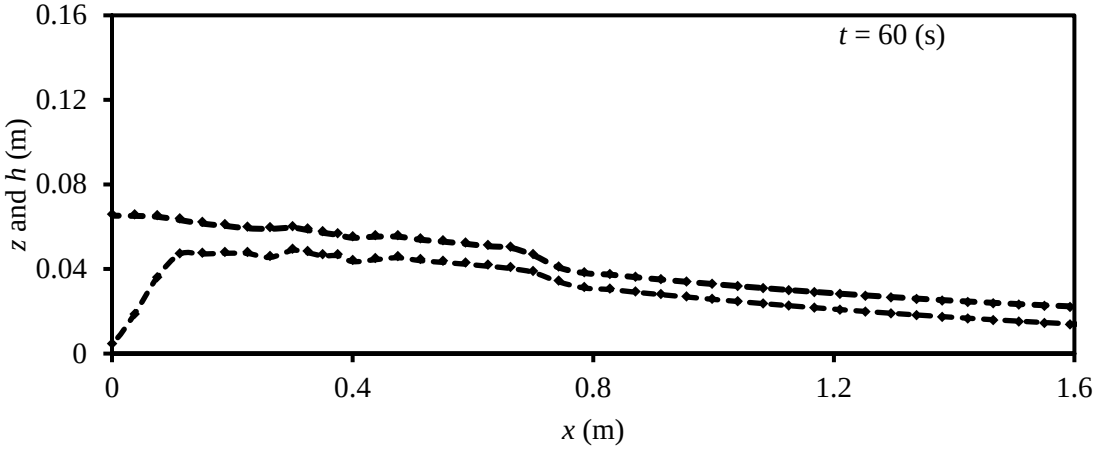

Figure 4.7 (continued) Suspended load effect: simulated bed and water surface profiles at various times for Case 1 with bedload and suspended load and Case 5 with bedload only

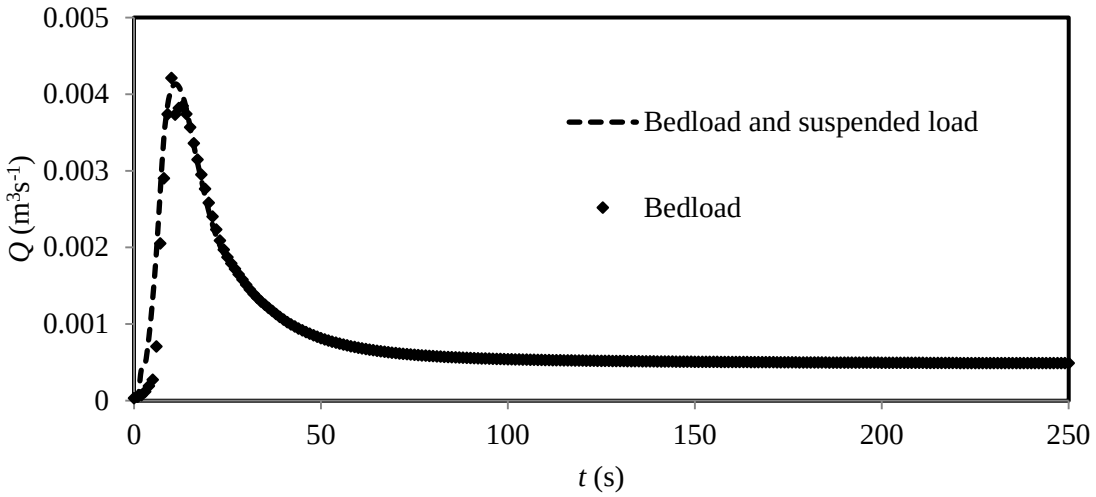

Figure 4.8 Outflow hydrographs for Case 1 with bedload and suspended load and Case 5 with bedload only

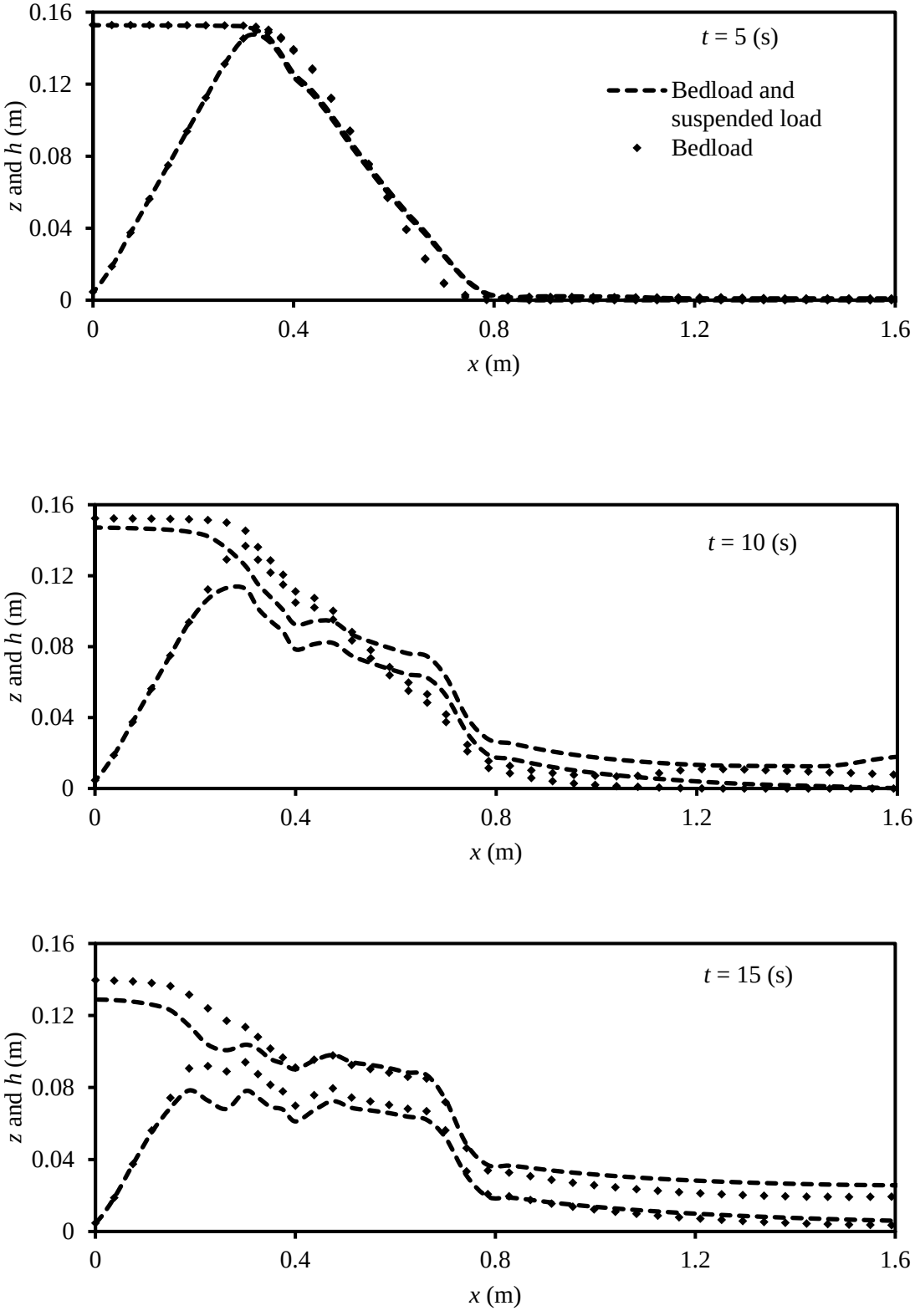

Figure 4.9 Suspended load effect for $d = 0.125$ mm: simulated bed and water surface profiles at various times for Case 1 with bedload and suspended load and Case 5 with bedload only

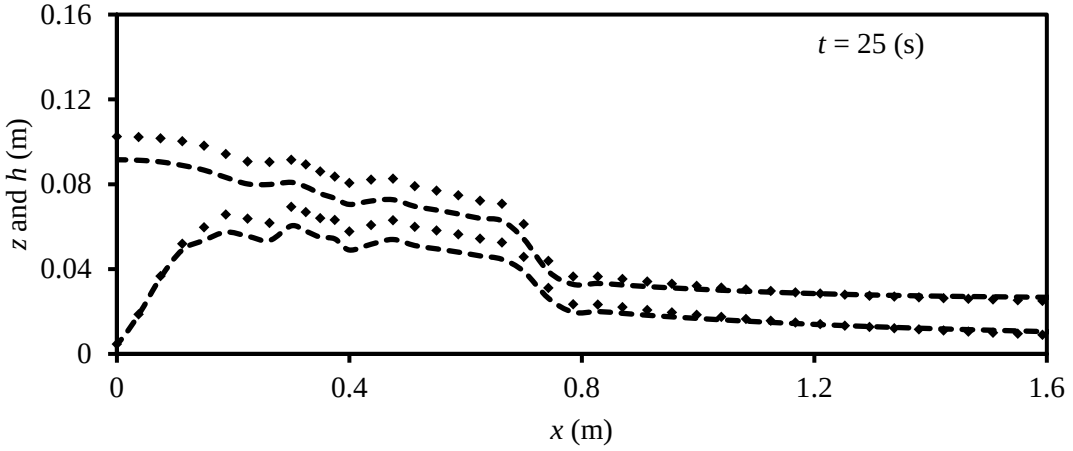

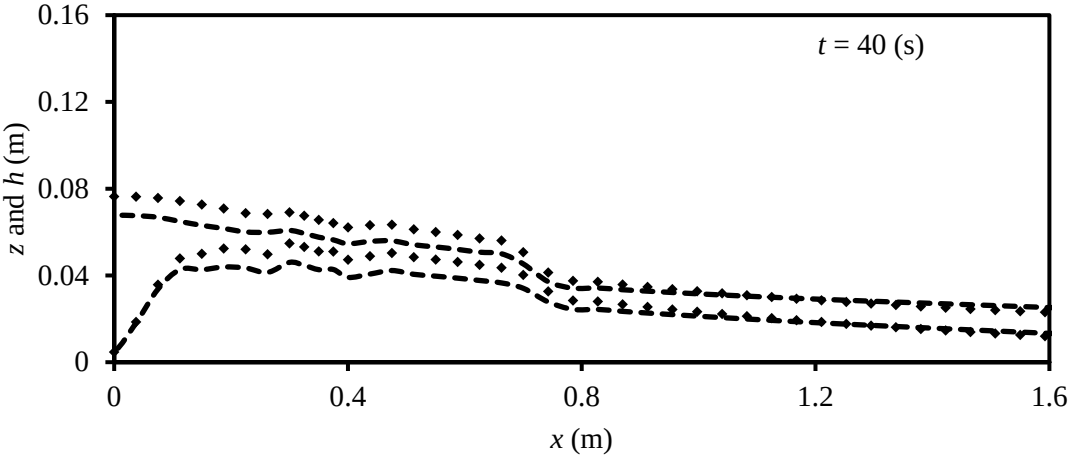

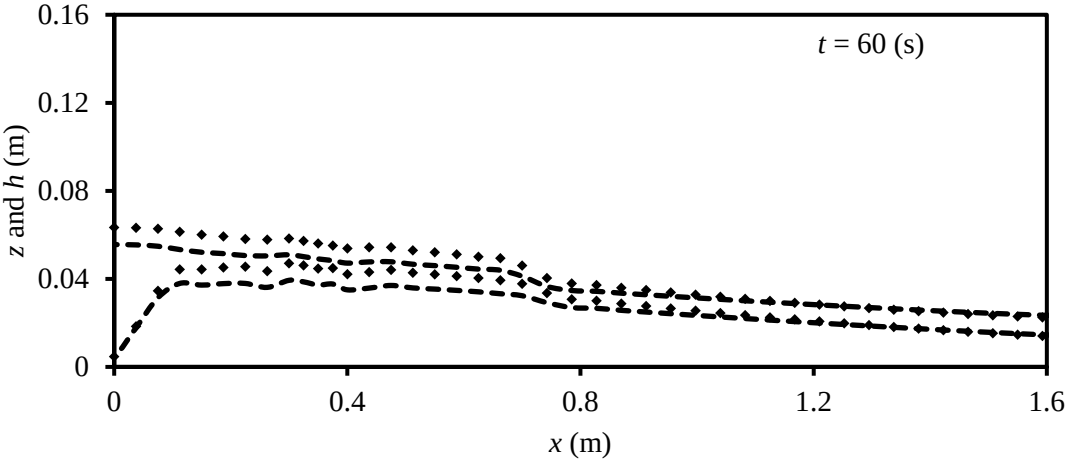

Figure 4.9 (continued) Suspended load effect for $d = 0.125$ mm: simulated bed and water surface profiles at various times for Case 1 with bedload and suspended load and Case 5 with bedload only

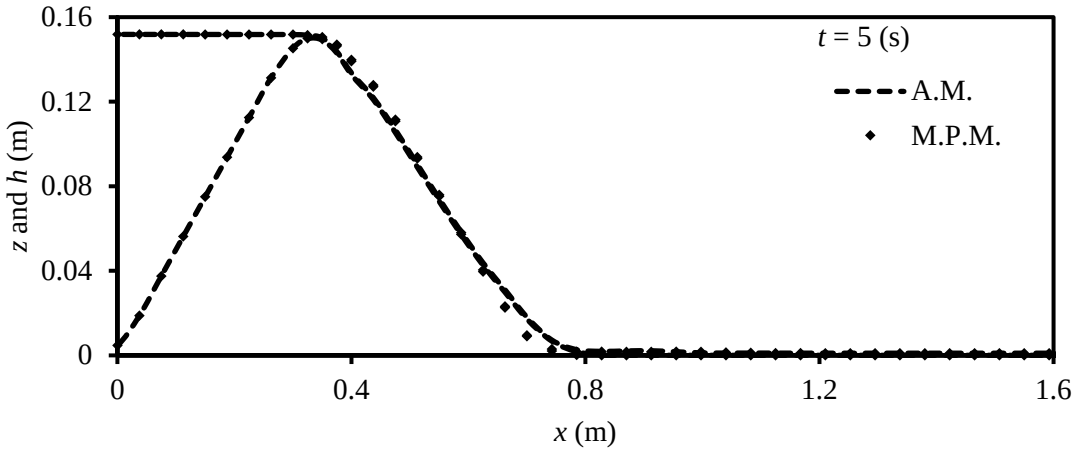

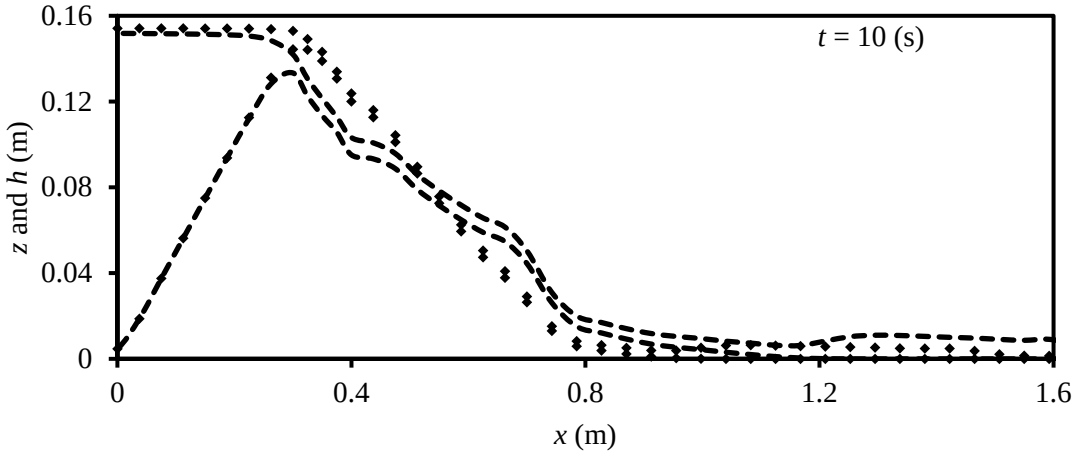

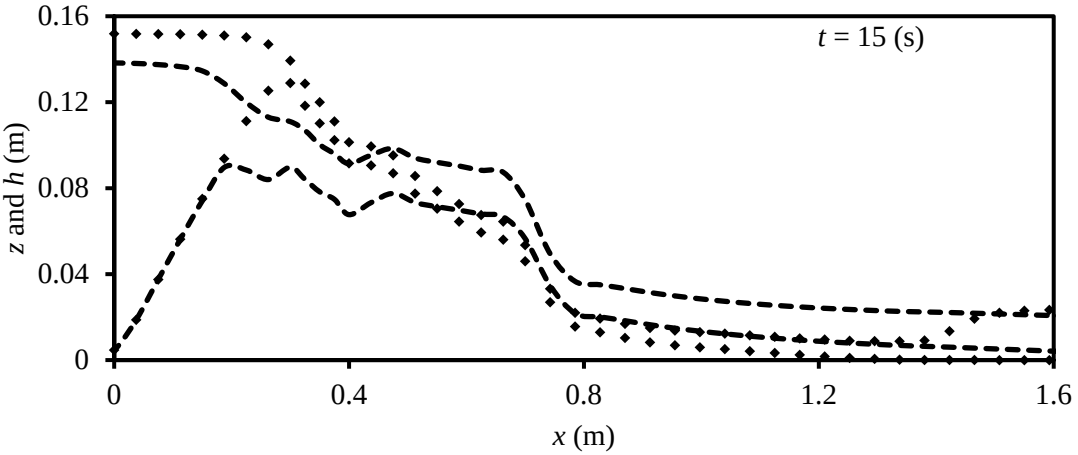

Figure 4.10 Bedload transport formula effect: simulated bed and water surface profiles at various times for Case 1 with A.M. formula and Case 3 with M.P.M. formula

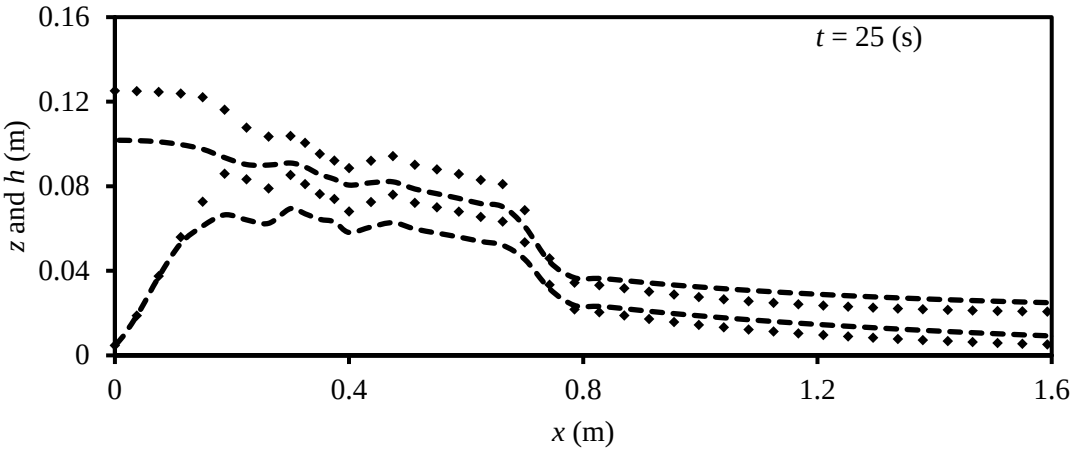

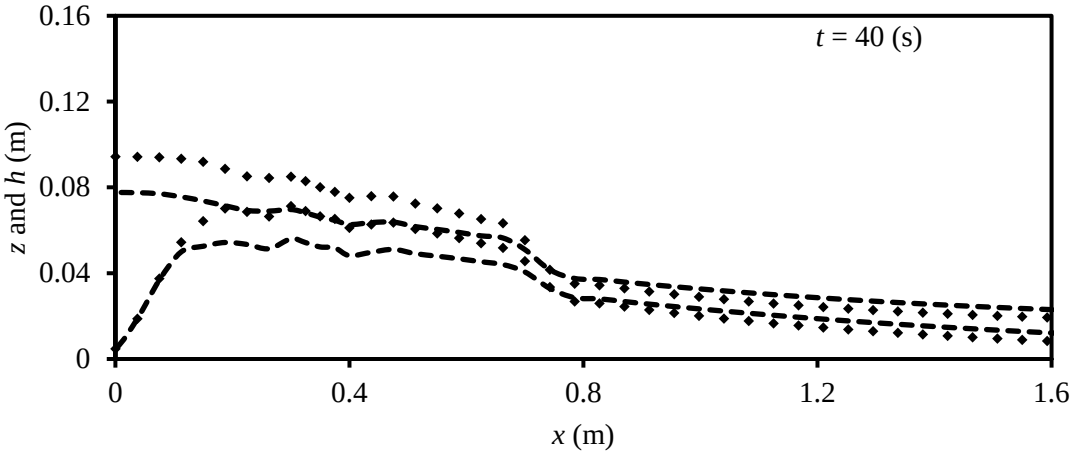

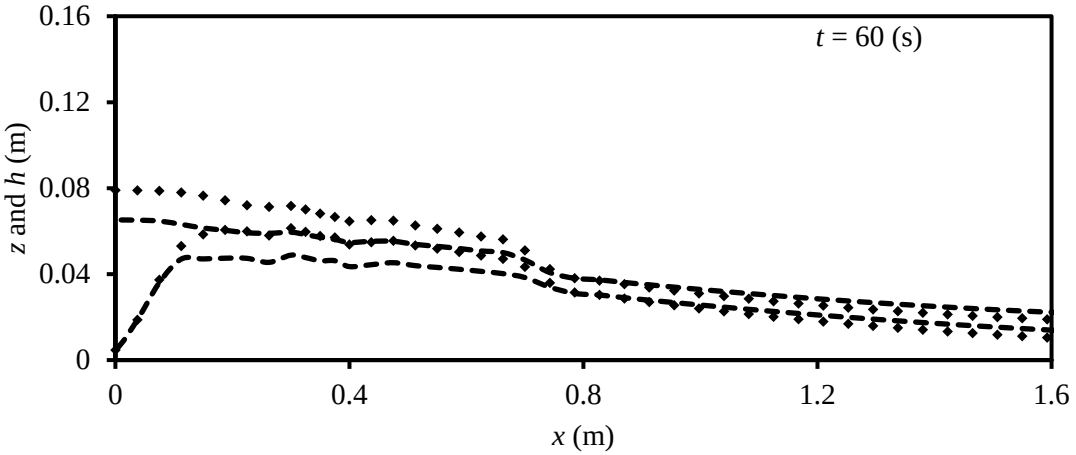

Figure 4.10 (continued) Bedload transport formula effect: simulated bed and water surface profiles at various times for Case 1 with A.M. formula and Case 3 with M.P.M. formula

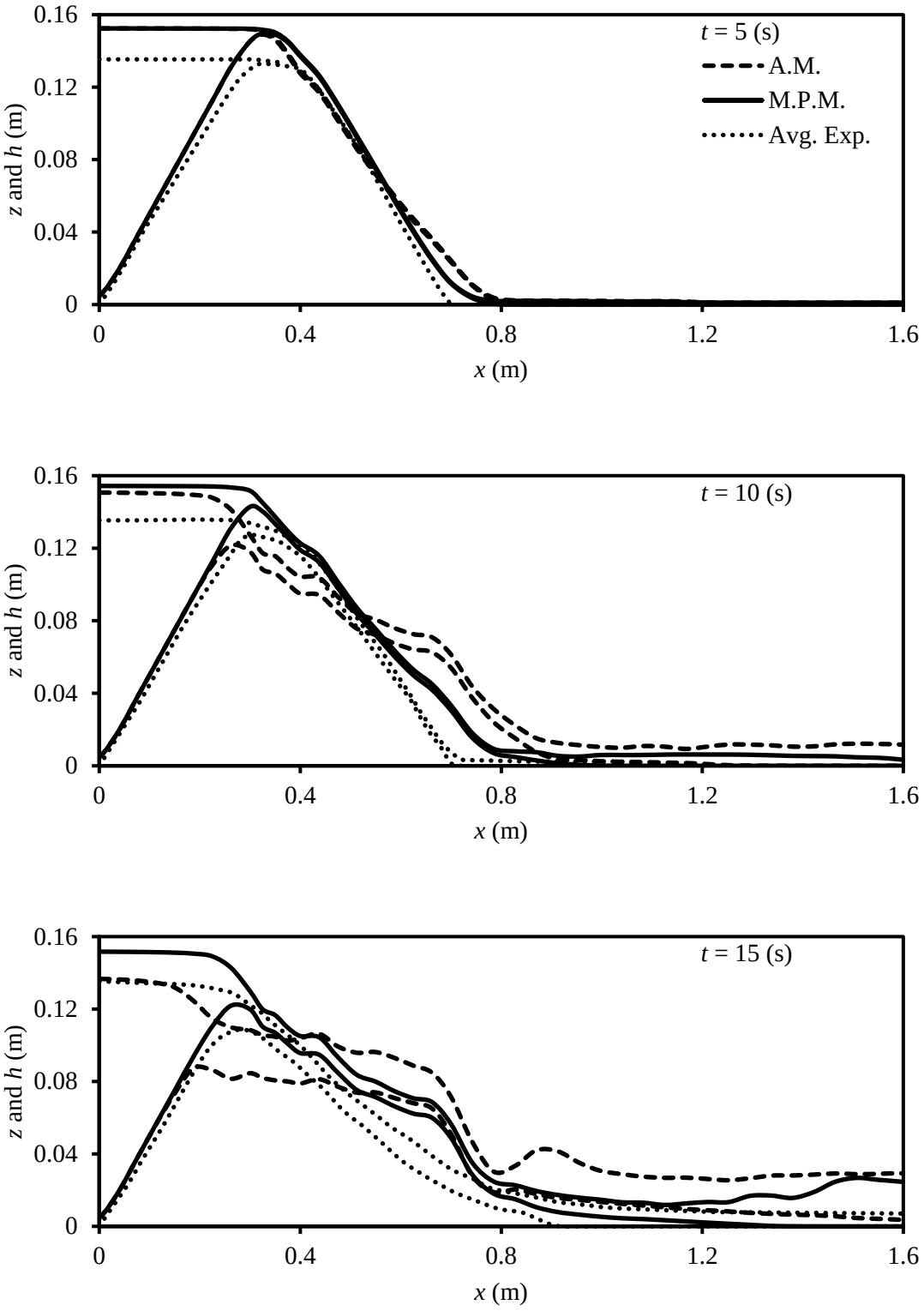

Figure 4.11 Bed and water surface profiles at various times *t* according to averaged experimental tests and numerical simulations for Case 10 (A.M.) and 12 (M.P.M)

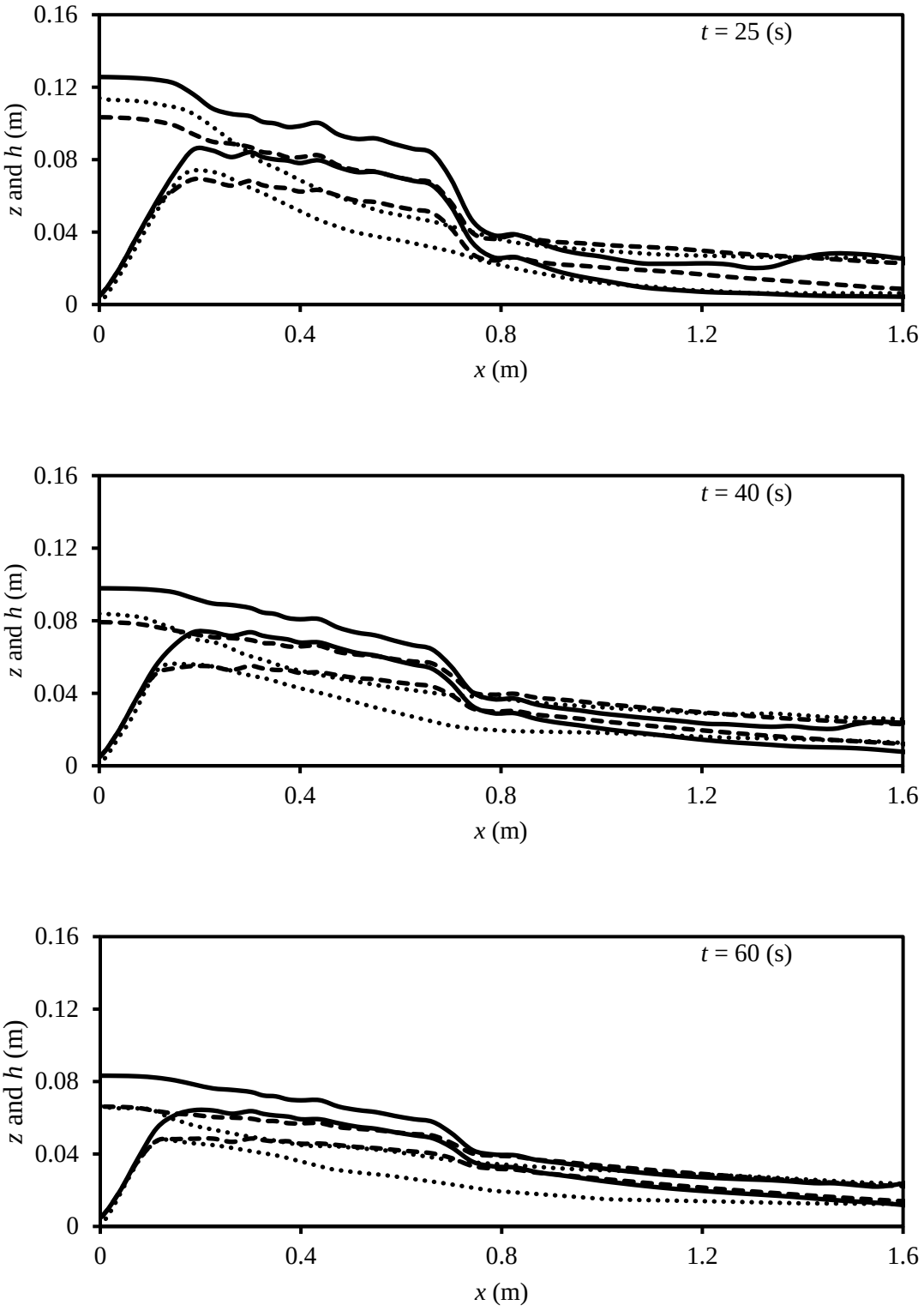

Figure 4.11 (continued) Bed and water surface profiles at various times *t* according to averaged experimental tests and numerical simulations for Case 10 (A.M.) and 12 (M.P.M)

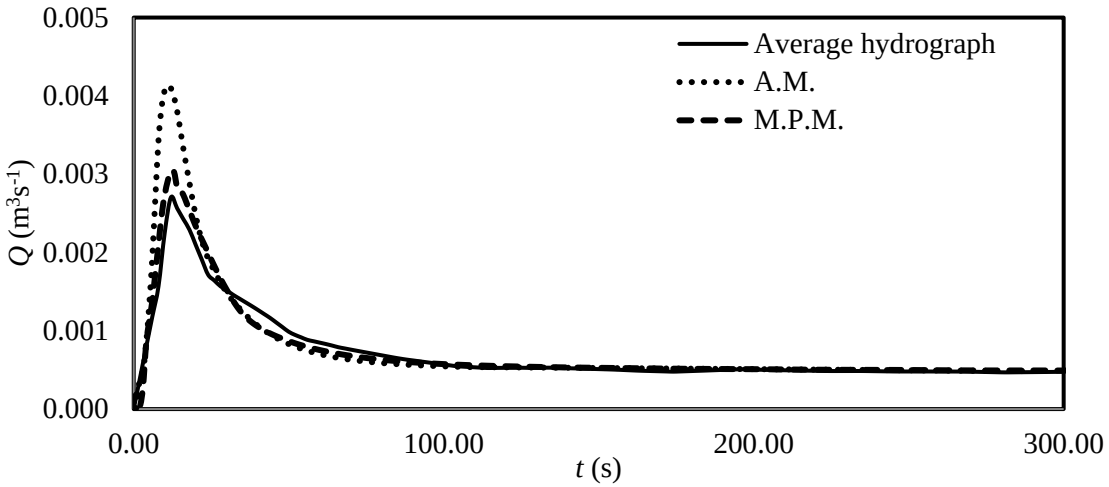

Figure 4.12 Outflow hydrographs according to the averaged experimental tests and simulations for Case 4 (M.P.M.) with Case 1 (A.M.)

CHAPTER 5

INVESTIGATING THE EFFECT OF COMPACTION CHARACTERISTICS ON THE ERODIBILITY OF A COHESIVE SOIL USING THE JET METHOD*

5.1 Test Procedure

To measure the cohesive soil erodibility based on the detachment model (k_d and τ_c in Eq. 2.1) a Submerged Jet apparatus, made by the author, is used (Figure 5.1). The test is simple, quick, and relatively inexpensive to perform and it can be used for laboratory and in-situ measurements of soil erodibility. The Jet apparatus, procedures, and analyses are similar to the device described by Hanson and Cook (2004). However, in order to have better accuracy, some modifications in the scour depth measurement system of the apparatus are made. The depth of scour is monitored with time during the test.

The cohesive samples of a sandy loam soil are prepared and compacted in a standard compaction mold, diameter of 101.6 mm, described in ASTM D698 and are examined for erodibility measurements for three levels of compaction energy and water content. The soil characteristics are presented in Table 5.1. The soil samples where compacted in three layers using the standard rammer with 10, 15, and 25 number of blows per layer (B/L). Two repetitions are required for each case (18 tests total). The goal is to produce a wide range of erodibility, from very resistant to very erodible, for a sandy loam soil by changing the water content and compaction effort of laboratory compacted

* Presented at the American Geophysical Union Fall Meeting 2013, San Francisco, CA

samples and to assess the effect of the water content and compaction effort on the erodibility of soil samples.

5.2 Results

Prior to the Submerged Jet tests, Standard Proctor Compaction tests (ASTM D698) were carried out to determine the optimum water content of the sandy loam soil used in the experiments. The optimum water content was found to be 7.98% and the corresponding maximum dry unit weight is 126.47 lb/ft^3 (Figure 5.2). To produce three levels of water content, the soil samples were prepared with the amount of water content less than the optimum water content (Low WC), close to the optimum water content (Medium WC), and higher than the optimum water content (High WC). Figure 5.3 shows Jet test results of the measured values of k_d and τ_c for three levels of compaction and water content. A wide range of erodibility was produced by changes in the compaction characteristics. Except the case with 15 B/L and Medium WC, the tests were repeatable. With the repeatability of the tests confirmed, the averaged values of the two repetitions may be used for further analyses of each case.

Figure 5.4 shows the relationship of k_d and water content for three levels of compaction and Figure 5.5 shows the same plot for the averaged values. For a given compaction energy, the erosion resistance based on the detachment rate coefficient k_d tends to become maximum near the optimum compaction water content. On the dry side of optimum compaction water content, k_d decreases with steep gradients by increasing the water content, while it increases with a flatter gradient on the wet side. For a given water content, the erosion resistance increases with the compaction energy. Compaction water content influences soil erodibility more than compaction energy, especially on the dry

side of the optimum compaction water content. Figure 5.6 shows the relationship of τ_c and water content for the averaged values. For a given compaction effort, the critical shear stress increases with water content up to an optimum water content and then it decreases which is in consistent with the k_d trends.

Table 5.1 Soil sample properties used in Submerged Jet tests

Grain size			Soil Classification	Standard compaction	
%Sand	%Silt	%Clay		γ_{dmax} (lb/ft^3)	WC_{opt} (%)
75	15	10	Sandy Loam	126.47	7.98

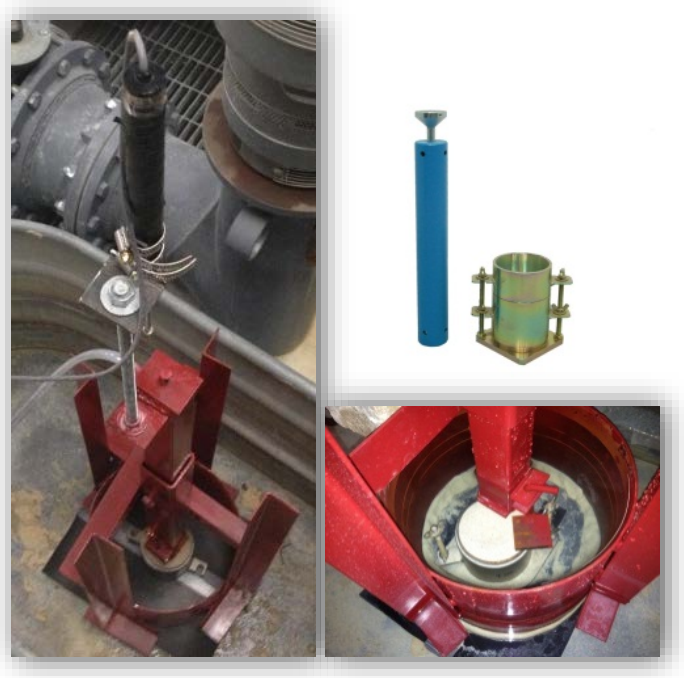

Figure 5.1 Submerged Jet test apparatus and the standard proctor compaction mold and rammer

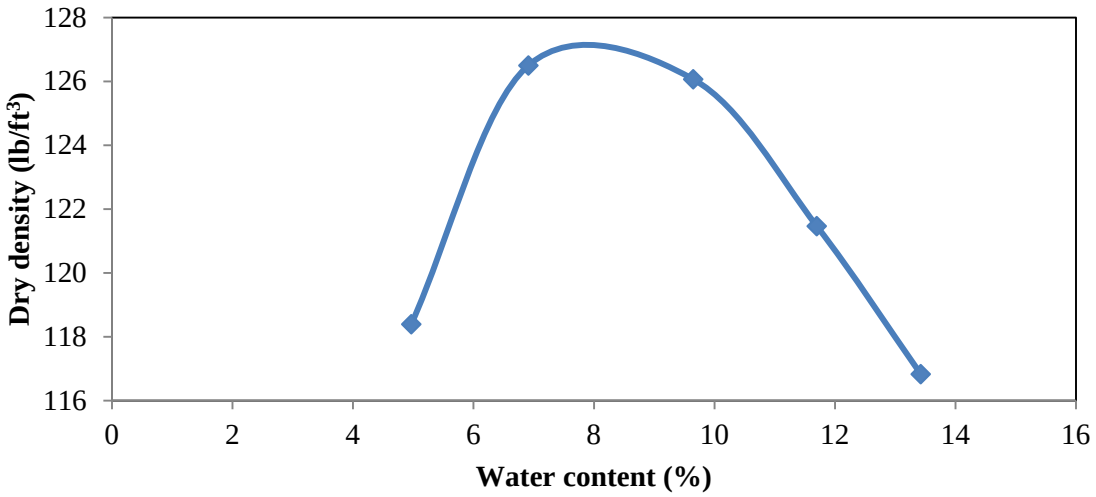

Figure 5.2 Standard proctor compaction test curve

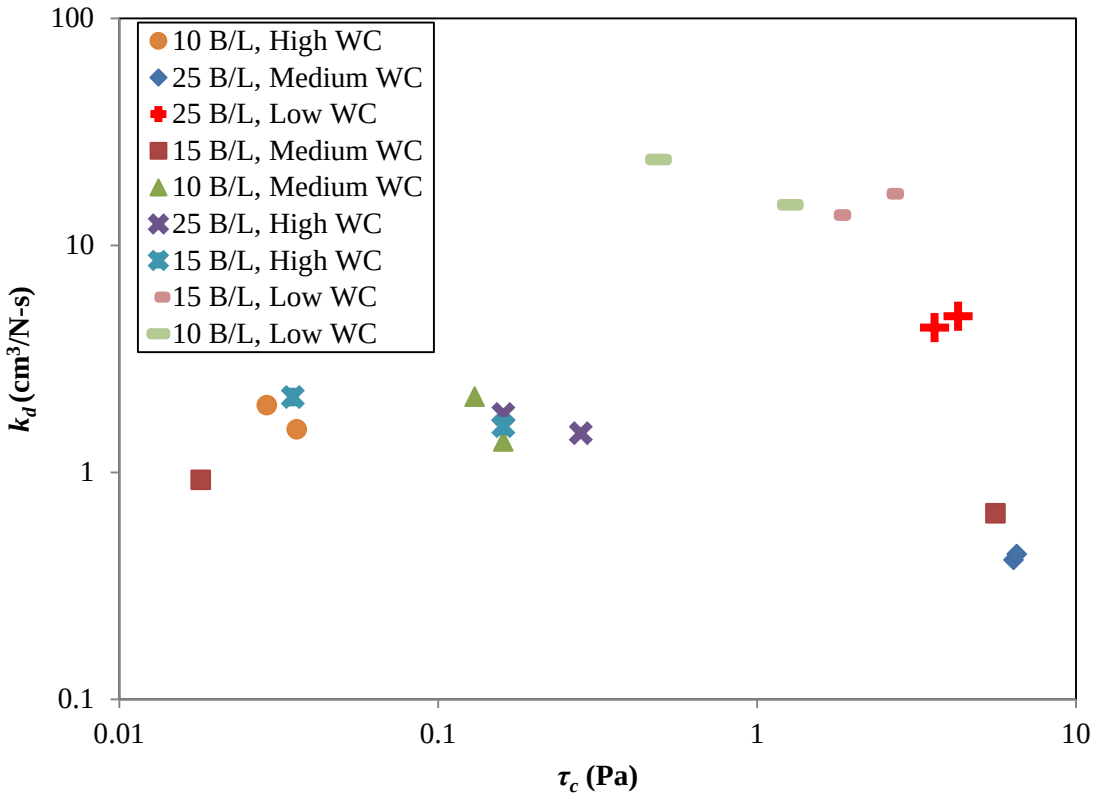

Figure 5.3 Relationship of k_d and τ_c from the Submerged Jet test results for three levels of compaction and water content

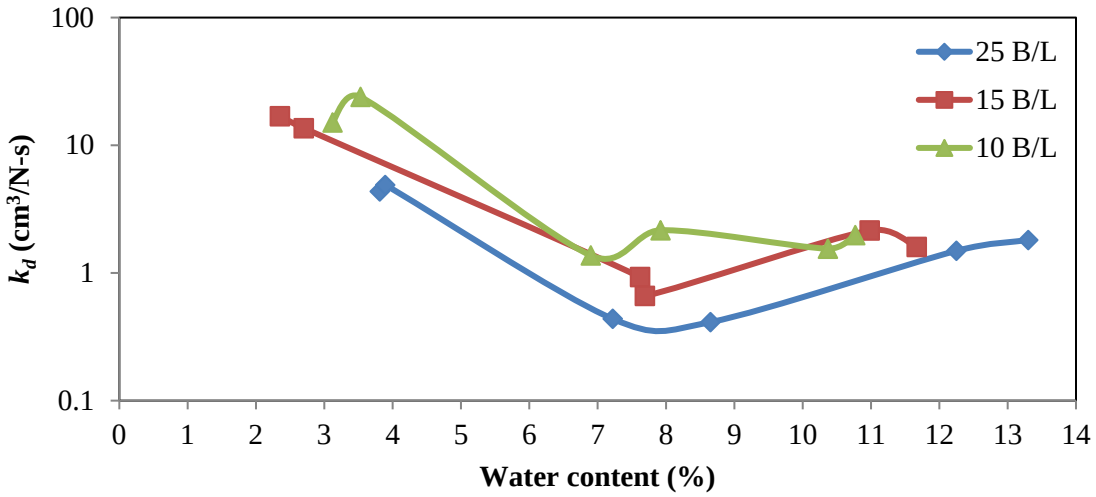

Figure 5.4 k_d vs. water content for 25 B/L, 15 B/L, and 10 B/L compaction effort

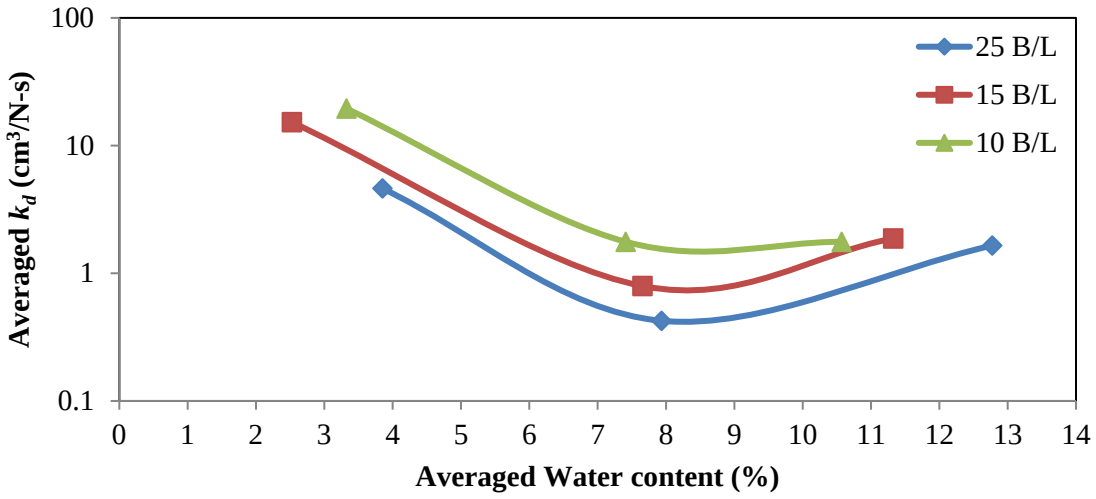

Figure 5.5 Averaged k_d vs. water content for 25 B/L, 15 B/L, and 10 B/L compaction effort

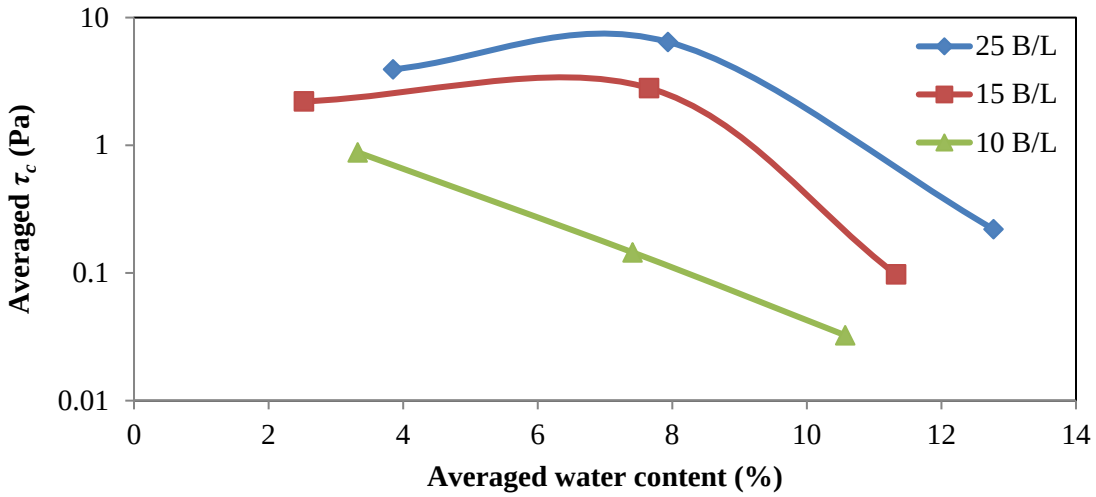

Figure 5.6 Averaged τ_c vs. water content for 25 B/L, 15 B/L, and 10 B/L compaction effort

CHAPTER 6

EXPERIMENTAL MODELING OF LEVEE FAILURE PROCESS DUE TO OVERTOPPING*

This study aims to gain an in-depth understanding of the levee breach process by conducting a series of experiments in which the levee is aligned parallel to the dominant flow direction, similar to field conditions. Experiments were performed at the Hydraulics Laboratory, University of South Carolina to quantitatively determine the failure process of an overtopped homogenous, non-cohesive, and non-compacted levee (i.e., breach evolution using a sliding rod technique, measurement of breach outflow, and water surface velocity distributions using a particle image velocimetry method). Erodibility coefficients in both vertical and horizontal directions are estimated from the experimental results and the corresponding bed-load transport formulas are proposed.

6.1 Experimental Setup

Figure 6.1 shows the schematic diagram of the plan view of the physical model test facility which consists of a flume, a floodplain adjacent to one side of the flume, and a calibrated sharp-crested weir (height = 0.05 m) with a Baumer ultrasonic probe for recording water surface elevation at the downstream side of the flume. The flume is constructed with vertical plywood walls on one side and levee-shaped wall on the other side, except for a 0.70 m long centrally located section where the earthen embankment

* Published in the Proceedings Dam Safety 2015 Conference, New Orleans, LA (Student Paper Competition Award)

test section is emplaced. The earthen levee cross section has a trapezoidal shape with 0.2m height, 1:2 (v:h) side slopes, and 0.10 m crest width. A flow straightener honeycomb and a wave suppressor were used at the intake section of the flume to reduce the inflow turbulence. The inflow discharge was kept constant at 0.06 m^3s^{-1} and a continuous downstream flow measurement (Q_{out}) was made to calculate the breach outflow rate.

The trapezoidal earthen embankments of non-compacted uniform sand with a mean diameter of 0.55 mm were placed and trimmed to the final shape. The pilot channel was made at one third of the length from the upstream beginning of the earthen levee section with 0.05 m depth and 0.10 m width to initiate the overtopping.

6.2 Measurement Methods

Three sets of experimental measurements were done in this study: 1) Estimating the flow field and water surface velocity distribution using Particle Image Velocimetry: a continuous HD-quality video recording is performed from the top and a large number of small floating particles were added to the upstream section of the flume. The PIVLab software (Thielicke and Stamhuis 2014a,b; Thielicke, 2014) were used for post-test analysis. The downstream water head over the sharp crested weir was monitored continuously and used to measure the breach outflow. To confirm repeatability, three identical experiments were carried out; 2) Measuring breach evolution using rods technique: the author uniquely developed this method. This technique consists of four rows of thin rods with 0.10 m distance passing vertically through two horizontal parallel Plexiglas sheets with a few centimeter distance in-between to insure that the rods are dropping vertically and each row has seven rods (Figure 6.2). Each rod is of a specific

color representing a specific location along the levee. The rods are placed on the downstream face of the levee, with the first row of the rods along the centerline of the levee crest. The bottom of the rods rest on the soil and drops when the soil is eroded. To make sure that the rods do not float in water, small weights are attached to the top of the rods. The top of the rods are tracked by a Sony HDR-XR160 high definition video camera with 60 frames/s for recording. The video is then split into single frames, each is then digitized and the top of the rods is tracked by applying simple threshold technique to the image. Thus, the breach shape with time is determined using these measurements. The widening of the breach is monitored using an overhead video camera to delineate the boundary between the water and the soil mixture. Moreover, the water surface velocity distribution is measured with time using the particle image velocimetry technique. A continuous video recording is done looking from the top and a large number of small black objects are added to the most upstream section of the flume to cover the water surface and have a better visualization. The video is then converted to still frames and the PIVLab software is used for the post processing of the images. To exclude the effects of the fixed side walls in the analyses, only the measurements from the starting time of overtopping until the time when one of the breach banks reaches the fixed side wall are used.; 3) Measuring water surface elevations at the breach location using three Baumer probes: in order to estimate the water surface elevation, the probes were placed along the centerline of the pilot channel; one close to the upstream toe, one on the crest, and one close to the downstream toe.

6.3 Results

Water Surface Velocity Distributions

Figure 6.3 shows the time series of water surface velocity distributions in the flume and the floodplain. Time starts when the water reaches the upstream toe of the pilot channel. During initial stages of the breach development (i.e., first 30 sec), the velocity distribution on the floodplain appears to be relatively symmetric. However, after the breach is fully developed, higher velocities tend to spread towards the downstream direction on the floodplain, while the areas on both sides of this high-velocity band have negligible velocity with minor circulations. Figure 6.4 shows time variation of the breach width for left and right bank of the breach. The breach wall on the downstream side is struck by higher velocities which results in faster breach development towards the downstream direction. Comparing the results of the three runs confirms the repeatability of the experiments. The measured breach outflow hydrograph is shown in Figure 6.5.

Breach Evolution

Figure 6.6 shows the time series of the breach evolution. The failure process starts with deepening along the pilot channel, while the width of the opening remains relatively small. After this stage, the widening starts to accelerate and then decelerate. By subtracting the bed elevations from the water surface elevation measurements at each time step, water depth is estimated at each location along the breach for every time step (Figure 6.7). Figure 6.8 shows the time series of the average breach width and average breach depth. The dimensionless forms of the deepening and widening rate can be calculated as

$$\epsilon_d^* = (\frac{\Delta D}{\Delta t})^* = \frac{\Delta D}{\Delta t} \times \frac{1}{\sqrt{RgD_g}} \quad (6.14)$$

$$\epsilon_w^* = (\frac{\Delta W}{\Delta t})^* = \frac{\Delta W}{\Delta t} \times \frac{1}{\sqrt{RgD_g}} \quad (6.2)$$

where $\epsilon_d^* = (\frac{\Delta D}{\Delta t})^*$ and $\epsilon_w^* = (\frac{\Delta W}{\Delta t})^*$ are dimensionless deepening and widening rate, respectively; $\frac{\Delta D}{\Delta t}$ and $\frac{\Delta W}{\Delta t}$ are deepening and widening rates, respectively; R is sediment submerged specific gravity; g is gravitational acceleration; and D_g is mean diameter of the soil. The non-dimensional deepening and widening rates were estimated every 5 sec, as shown in Figure 6.9. For measuring the deepening rate, only a small section of the levee along the pilot channel is used to separate the effects from the widening process.

Levee Erodibility Coefficients in Vertical and Horizontal Directions

Similar to the proposed bedload formula of Kakinuma and Shimizu (2014), an erosion model is proposed in this study which enables the estimation of erosion in vertical and lateral directions:

$$\epsilon_d^* = \alpha_d(\tau_{ed}^* - \tau_c^*)^{\beta_d} \quad (6.3)$$

$$\epsilon_w^* = \alpha_w(\tau_{ew}^* - \tau_c^*)^{\beta_w} \quad (6.4)$$

where ϵ_d^* and ϵ_w^* are the erosion rates for deepening and widening stages of the failure, respectively; α_d, β_d and α_w, β_w are the correspondent erodibility coefficients; τ_{ed}^* and τ_{ew}^* are the non-dimensional applied shear stresses on bed and side walls of the breach opening, respectively; and τ_c^* is the non-dimensional critical shear stress and can be calculated as (Parker et al., 2003)

$$\tau_c^* = 0.5\left[0.22R_{ep}^{-0.6} + 0.06 \times 10^{(-7.7R_{ep}^{-0.6})}\right] \quad (6.5)$$

$$R_{ep} = \frac{\sqrt{RgD_g}D_g}{\vartheta} \quad (6.6)$$

where R_{ep} is particle Reynolds number; and ϑ is kinematic viscosity of water.

Applied shear stress on the bed for deepening $\tau_{ed}^*$is calculated as follow by using Manning's equation

$$\tau_{ed}^* = \frac{N_m^2 V^2}{RD_g h^{\frac{1}{3}}} \quad (6.7)$$

where N_m is Manning's roughness coefficient; V water surface velocity measured by PIV at each location; and h is water depth at each location. The applied shear stress on sidewalls of the breach τ_{ew}^* can be estimated as (Chow, 1959)

$$\tau_{ew}^* = 0.7\tau_{ed}^* \quad (6.8)$$

By measuring ϵ_d^*, ϵ_w^*, τ_{ed}^* and τ_{ew}^* from the experimental results, erodibility coefficients in vertical and lateral directions can be estimated and the resulting erosion models may be used as input for estimating the levee breach process in numerical models. The test results of the breach widening and deepening rate versus the excess shear stress are plotted in Figure 6.10. The correlation equations of the plotted results for the deepening and widening rates are as

$$\epsilon_d^* = 58.19(\tau_{ed}^* - \tau_c^*)^{2.47} \quad (6.9)$$

$$\epsilon_w^* = 2 \times 0.16(\tau_{ew}^* - \tau_c^*)^{0.11} \quad (6.10)$$

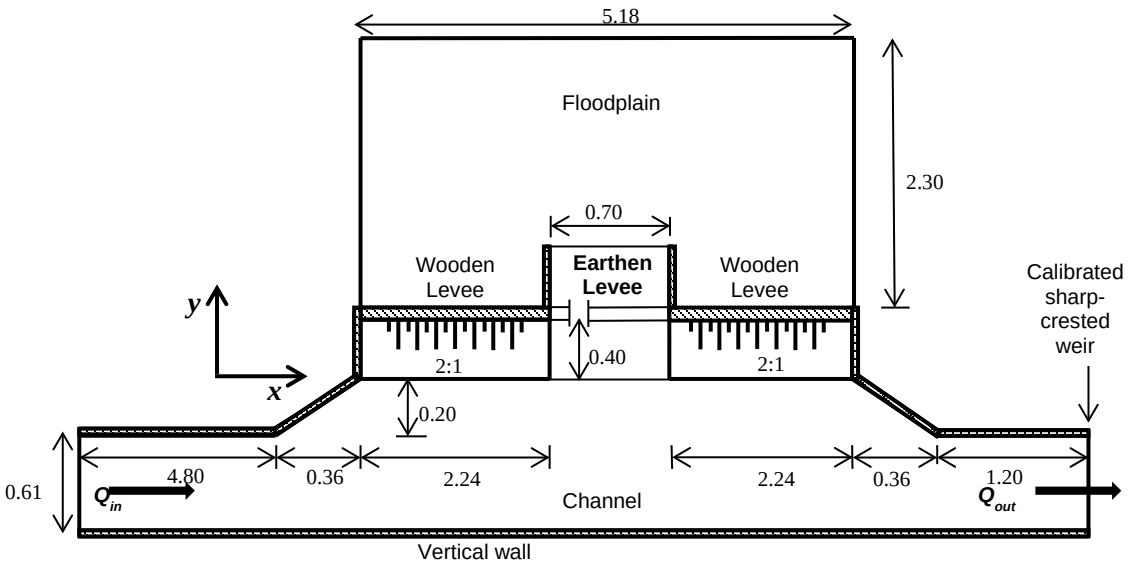

Figure 6.1 Plan view of experimental setup (dimensions are in meter)

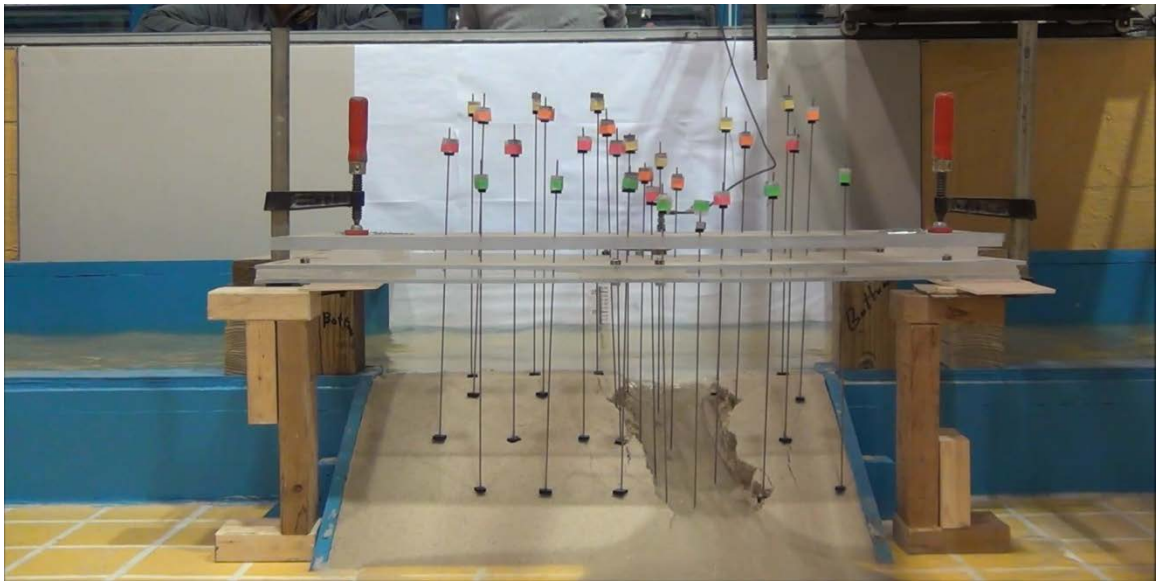

Figure 6.2 Front view of the proposed method for measuring the breach shape with time.

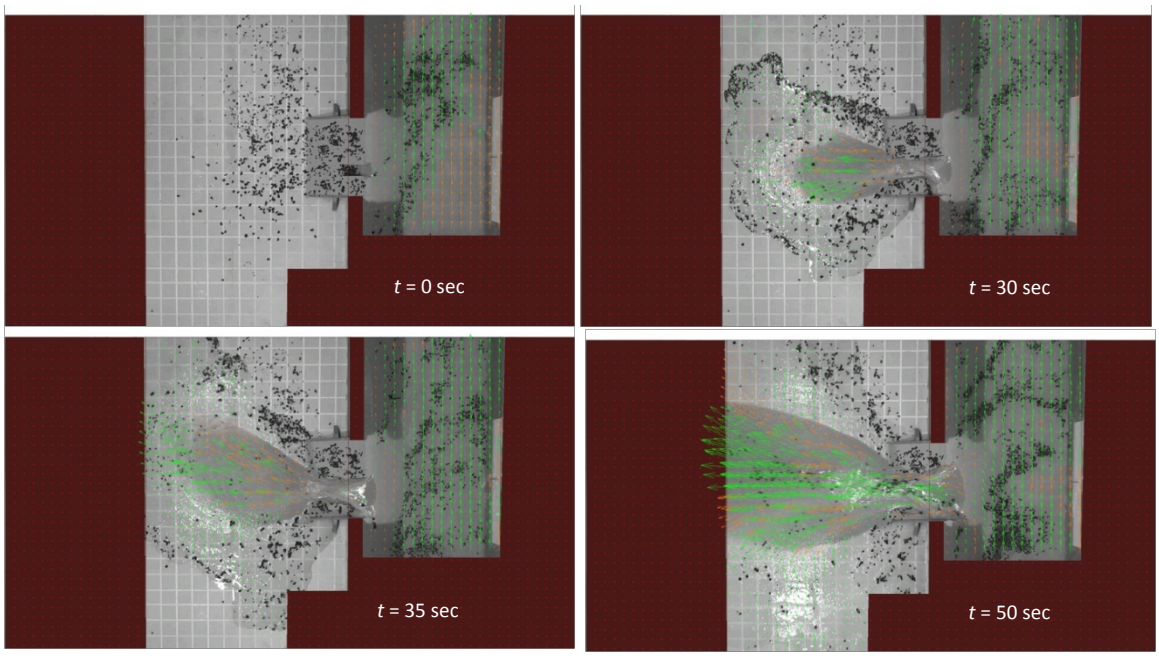

Figure 6.3 Spatial variation of water surface velocity at different times

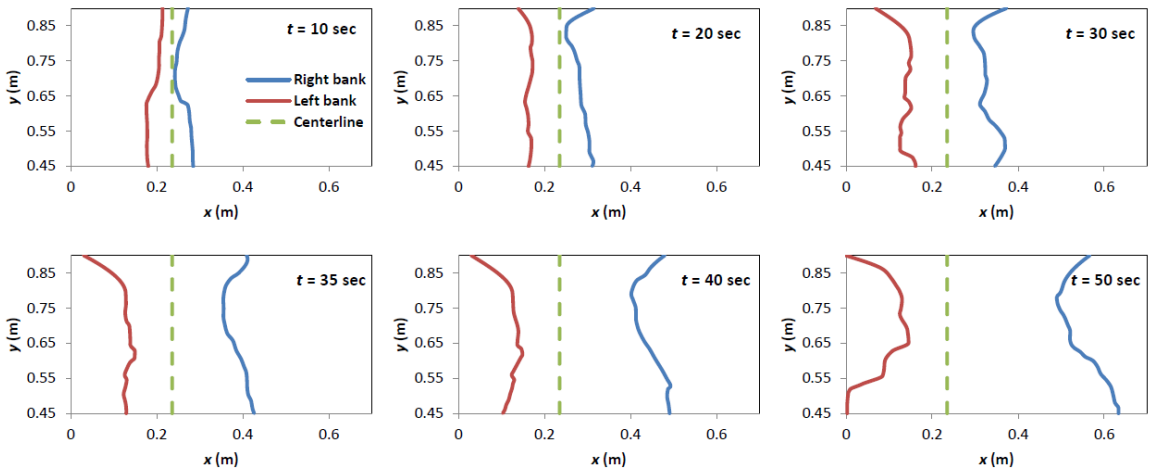

Figure 6.4 Time series of breach width for the left and right bank of the breach (flow direction in the channel is from left to right)

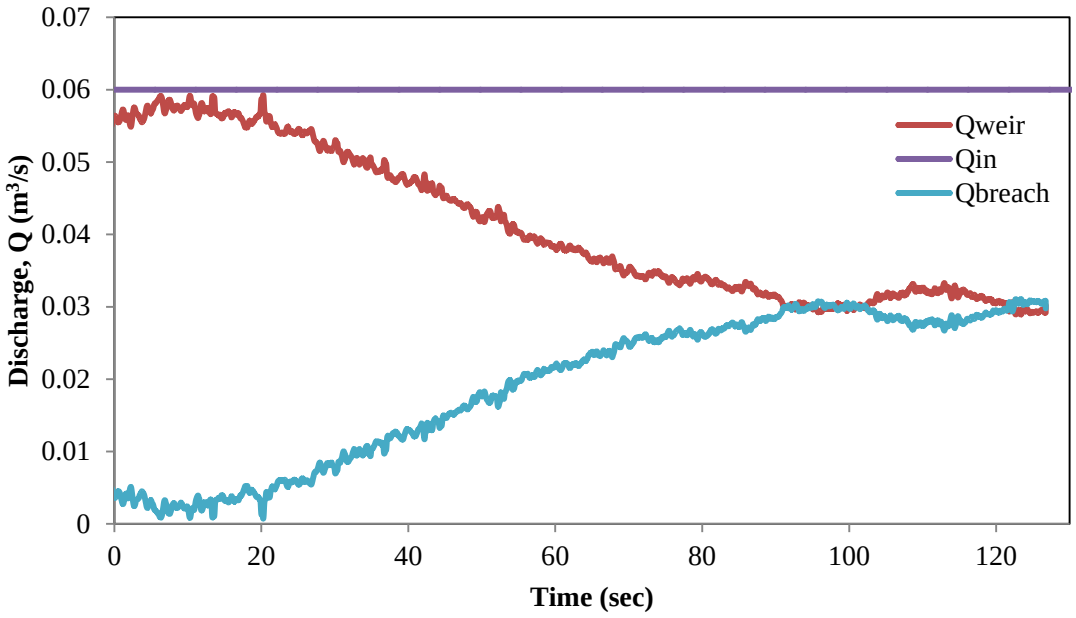

Figure 6.5 Hydrographs of inflow to the flume, outflow from the downstream weir, and outflow from the breach

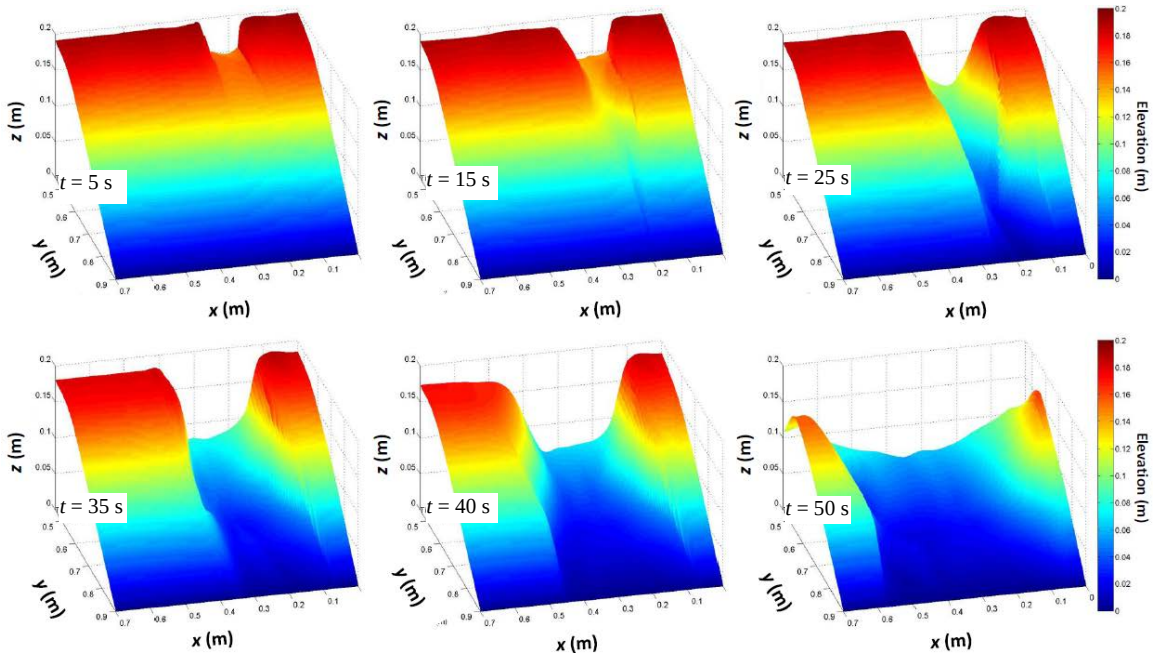

Figure 6.6 Time series of breach evolution (flow direction in the channel is from right to left)

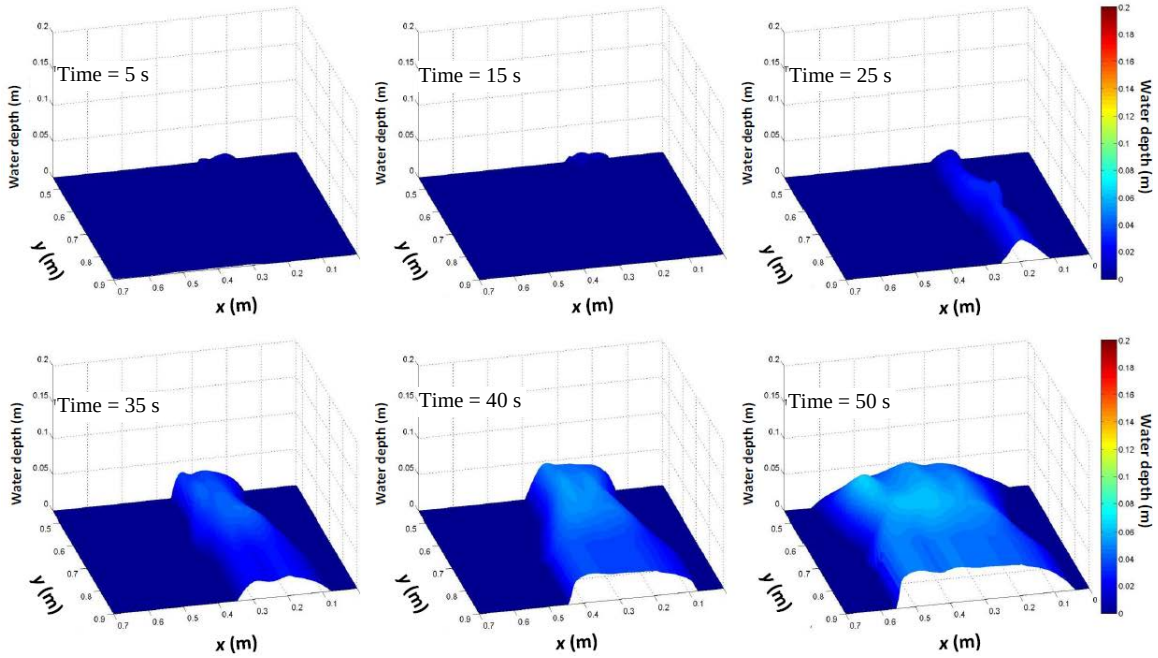

Figure 6.7 Time series of water depth at breach location (flow direction in the channel is from right to left)

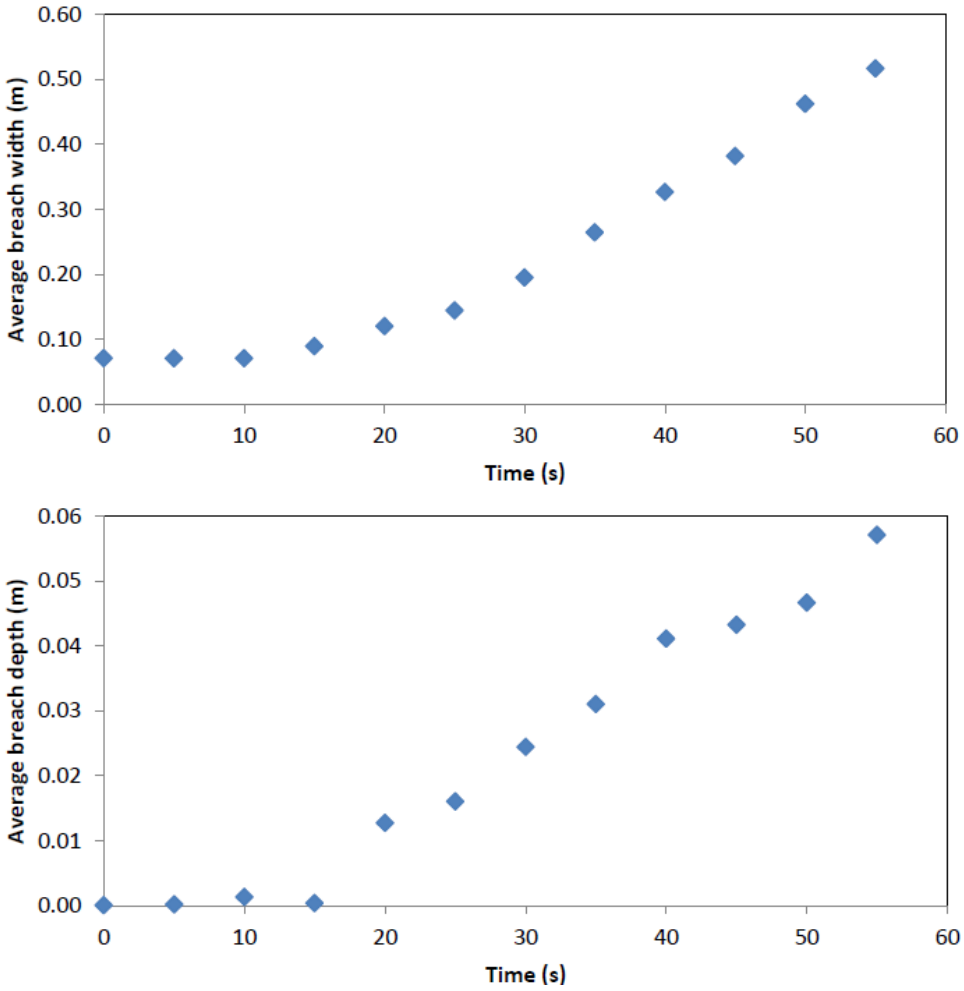

Figure 6.8 Time variation of average breach width and depth

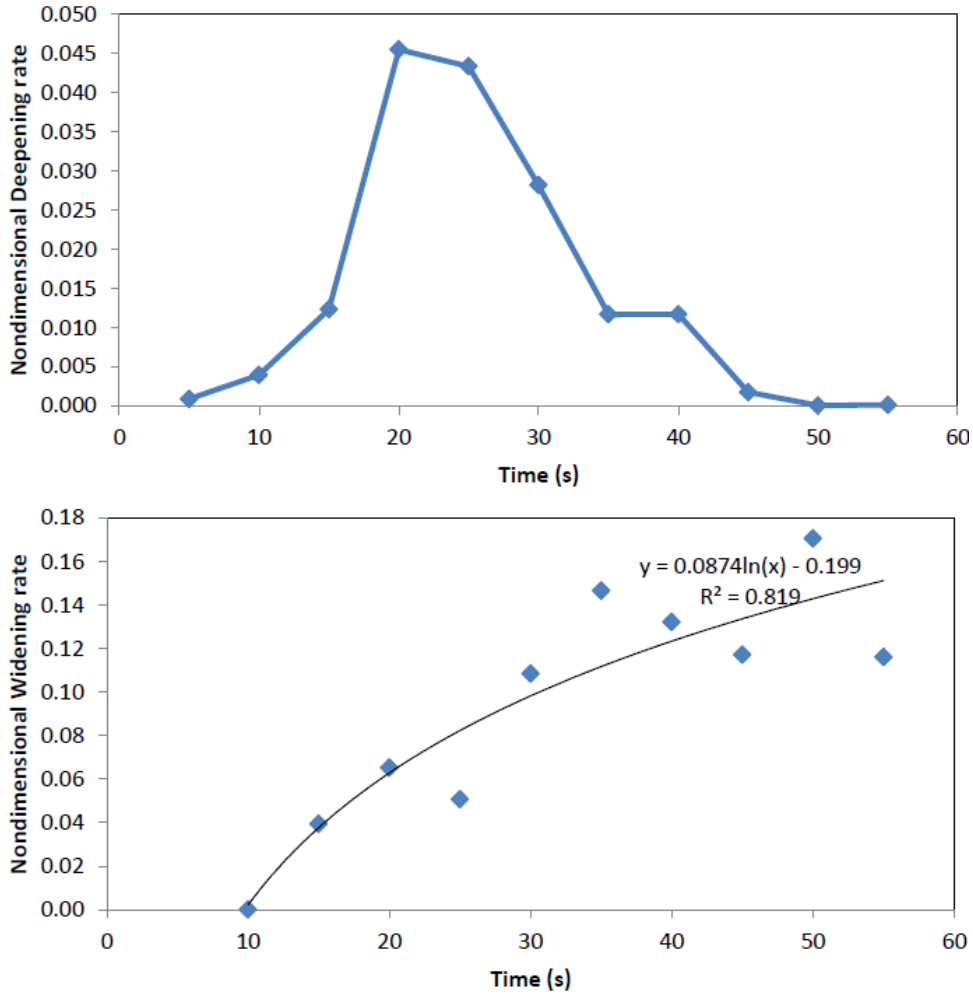

Figure 6.9 Non-dimensional deepening and widening rate with time

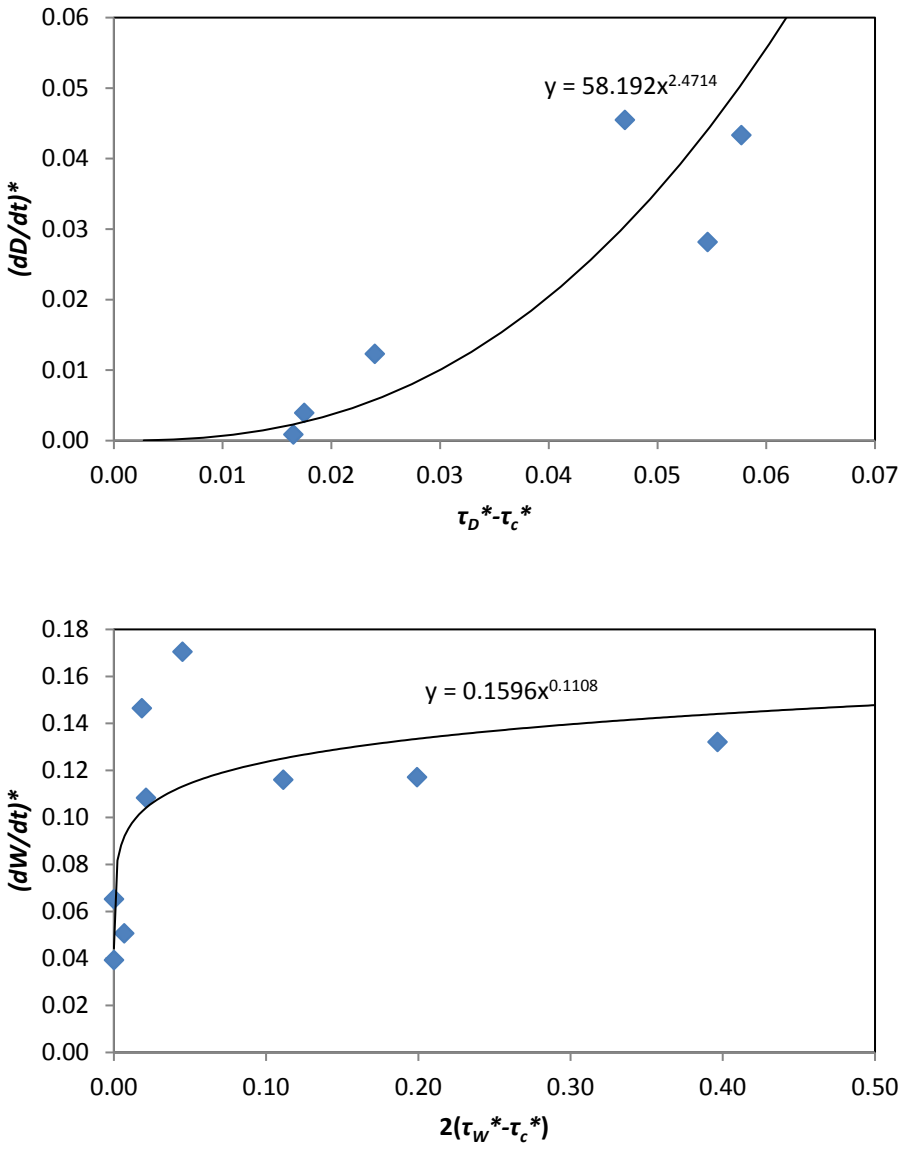

Figure 6.10 Correlation of deepening and widening rate with excess shear stress

CHAPTER 7

EXPERIMENTAL MODELING OF EARTHEN LEVEE FAILURE BY OVERTOPPING: EFFECTS OF HYDRAULIC LOADS*

The objective of this study is to gain an in-depth understanding of the levee breach process and to investigate the effects of various hydraulic parameters on the failure process by conducting a series of experiments in which the levee is aligned parallel to the dominant flow direction, similar to field conditions. Six tests are performed at the Hydraulics Laboratory, University of South Carolina, with variations of inflow discharge and initial downstream water depth in the flume to quantitatively determine the failure process of an overtopped homogenous, non-cohesive, and non-compacted levee (i.e., breach evolution, measurement of breach outflow, and flow field measurements). Of particular interest is the development of non-dimensional relationships for breach top width and breach depth at levee crest, and for the breach volume as a function of time, inflow discharge, and initial downstream water depth and to propose a simple trapezoidal model to predict the evolution of the breach.

7.1 Experimental Setup

The experimental setup is the same as the setup explained in Chapter 6.

* Submitted to the Journal of Hydraulic Engineering

7.2 Test Procedure

Prior to the embankment overtopping tests, Standard Proctor Compaction tests (ASTM D698) are carried out to determine the optimum water content of the homogenous, non-cohesive soil (i.e., sand only) used in the experiments. Non-compacted sand is used as embankment material to allow for the surface erosion to be the only mechanism for the erosion process. The optimum water content is 5.2% and the corresponding maximum dry unit weight, $\gamma_{d,max}$, is 15.44 kN/m^3. For each overtopping experiment, the soil is uniformly mixed with water to attain the optimum water content. The trapezoidal earthen embankments of non-compacted uniform sand with a mean diameter of 0.55 mm are placed and trimmed to the final shape. A 0.05 m deep and 0.10 m wide pilot channel is made at one third of the crest length from the upstream edge of the earthen levee section to initiate overtopping. The seepage through the embankment is controlled and reduced by a thin clay layer with low permeability, placed on the upstream face of the embankment. The pump is started to fill the channel and the starting time of the failure process is considered to be the time when the water surface reaches the upstream edge of the pilot channel.

Six tests are conducted with different inflow rates and downstream weir heights to produce a range of hydraulic conditions, i.e. Froude number at downstream end of the flume before overtopping starts, as shown in Table 7.1. The inflow discharge is kept constant at specified values during each experiment and downstream flow is measured (Q_{out}) continuously to calculate the rate of breach outflow. Tests A2 and A3 are repeated three times to confirm the repeatability of the experiment.

7.3 Measurement Methods

A Baumer ultrasonic water level sensor, having an accuracy of ± 0.3 mm, is used at the downstream end of the flume to continuously measure the flow discharge out of the flume, Q_{out} (using a calibrated sharp-crested weir). The breach outflow is calculated from the balance of the inflow discharge and the measured outflow discharge. The breach evolution is measured using a sliding rods technique. This technique is explained in section 6.2.

7.4 Results

Breach Geometry and Surface Velocity Observations

Figures 7.1(a and b) show the time history of the maximum breach depth and the breach top width along the centerline of the levee crest, respectively as measured by the rods technique for all the tests (only the first row measurements located along the crest of the embankment are used). The breach deepening and widening at the crest do not proceed until about $t = 10$ s, and then they start to increase first with a mild slope and then accelerate with a sharper slope. At the final stages of the failure, breach widening and deepening start to decelerate and reach a constant value, except the widening of tests A3 and B3 since the inflow discharge is so high that it maintains the widening acceleration while the erodible levee section length is limited by the fixed side walls. Therefore the widening deceleration stage could not be captured in these two tests. These observations are consistent with those of Kakinuma and Shimizu (2014) experiments. The change of the breach area along the centerline of the crest with time is shown in Figure 7.1(c). Again, acceleration and then deceleration phases are observed for the breach area

changes for all tests. The breach area increases with the inflow discharge for a given time and a given downstream weir height.

Figure 7.1(d) shows the time history of the total breach volume for all the tests for the downstream half of the levee as measured by the sliding rods technique (measurements from all four rows of rods are used). The erosion volume is negligible until about $t = 15$ s and then the rate of eroded volume starts to accelerate. The rate of eroded volume is increasing with the inflow discharge for a given downstream weir height. Similar to the breach geometry observations, the volume of eroded material increases with the inflow discharge for a given time and a given downstream condition as the higher inflow rate result in higher shear stress.

The breach evolution along the centerline of the crest is shown in Figure 7.2 for all the six tests. The flow direction in the main channel is from left to right in these figures. The breach wall on the downstream side is impacted by higher velocities as compared to the upstream side which result in a faster breach development in the downstream direction. This is different from the dam-break case, where the breach is almost symmetrical on the two sides. From the figures, although the initial shape of the breach cross-sectional area has a rectangular shape, the breach cross section assumes a trapezoidal shape later on with an almost a triangular shape during the early stages. This may be due to the fact that as the breach widens, the side wall collapses, resulting in a wider top width and a narrower bottom width. Besides, the breach channel side wall is resting on a steep angle at the beginning and the angle becomes milder close to the angle of repose afterwards. Also, it can be noticed from the figure that the angle of the breach side slope on the downstream side is steeper than that on the upstream side most of the

times. This is due to the unsymmetrical flow distribution along the breach crest as mentioned earlier, having more breach outflow on the downstream side than on the upstream side. All the tests have similar breach shape along the crest centerline except for Test A1 in which the breach shape is mostly triangular.

Figure 7.3 shows the time history of the total breach evolution for the Test A3. This is estimated using all four rows of rods along with interpolation and extrapolation techniques. Furthermore, the time variation of the longitudinal bed surface profiles along the pilot channel centerline is presented in Figure 7.4 for the same test. At the beginning of overtopping, a small amount of overflow through the pilot channel erodes a very shallow and narrow stream through the downstream face of the levee (roughly along the centerline of the pilot channel) from the crest to the downstream toe of the embankment. During this stage, the upright side walls of the pilot channel collapse due to the partial submergence and slope instability, thereby leading to an increase in the top width. Then, the flow through the pilot channel increases which results in the degradation of the crest. The failure process continues with deepening along the pilot channel from the downstream toe of the levee towards the levee crest, while changes in the opening width remain relatively small. After this stage, the widening starts to accelerate (while the changes of the breach depth decelerate), with a faster advancement of the downstream breach wall as it is impacted by higher velocities compared to the upstream bank, and then it decelerates. From the overhead camera, the time variation of the breach top width for the downstream and upstream banks is monitored and is shown in Figure 7.5 for Test A3 along with the centerline of the pilot channel. As seen in the figure, the downstream bank is eroding faster than the upstream bank. Figure 7.6 shows the particle image

velocimetry measurements of the surface velocity distribution at different times for Test A3. During initial stages of the breach development, the velocity distribution on the floodplain is relatively symmetric. However, after the breach is fully developed, higher velocities tend to spread towards the downstream direction on the floodplain, while the areas on both sides of this high velocity band have negligible velocity with minor circulations. As mentioned earlier, the breach wall on the downstream side is impacted by higher velocities resulting in faster breach development towards the downstream direction. The change in the flow intensity from low at the upstream end to high at the downstream end of the breach is reported by Hager (1987) for his experiments on lateral outflow over side weirs. On the upstream end, the curvature of the streamlines is small and it increases moving downstream and becomes almost perpendicular to the channel axis as far as at the downstream end. This in turn leads to more erosion on the downstream side. It is observed in the current experiments that the widening of the crest at the upstream side is due to surface erosion only while at the downstream side it is due to both surface erosion (which is higher because of the higher flow intensity and results in steeper slope) and slope instability.

Breach Outflow Hydrograph Observations

Figure 7.7 shows the hydrographs of the weir flow as well as the breach outflow which is estimated from the constant inflow and the weir flow at downstream end of the flume. The breach overflow remains relatively small in each test at the initial stage of the failure and then starts to accelerate and increase with almost a constant rate and reaches its maximum value, then it decelerates and reaches roughly a constant value until the end of

the failure process. These changes correspond to the widening and deepening phases of the failure.

Although the inflow discharge is smaller for the tests with a 0.075 m downstream weir height (i.e., Tests B1, B2, and B3), the breach overflow is larger for a given time and the time rate of the breach overflow changes is higher, as compared to the tests with the 0.05 m weir height. This also results in the breach overflow to exceed the weir flow at a certain point in Tests B1, B2, and B3, while in Tests A1, A2, and A3 less water passes through the breach and more passes over the downstream weir throughout the failure process. This is due to the fact that using higher downstream weir crest elevation (Test B's) backs up the water resulting in higher depths on the levee embankment and leading to more erosion than when using a lower crest elevation. But this effect may diminish if the downstream weir is placed far from the levee embankment. The peak breach overflow is 0.027, 0.019, 0.024, 0.034, 0.032 and 0.031 m^3/s for Tests A1, A2, A3, B1, B2 and B3, respectively. The relative breach overflow, $Q_r = Q_{breach,max}/Q_{in}$ where $Q_{breach,max}$ is the maximum breach overflow at the final stage of the failure and Q_{in} is the constant inflow discharge, is 0.46, 0.31, 0.32, 0.94, 0.67, and 0.61 for Tests A1, A2, A3, B1, B2, and B3, respectively.

7.5 Analysis of Breach Characteristics

Breach Top Width

The temporal changes of the breach top width at the centerline of the levee crest are measured for different inflow discharges and downstream conditions. Using the normalized values and regression analysis, the following equation is fitted to predict the

breach top width as a function of time, inflow discharge, and initial downstream water depth with R^2=0.96 for all the tests:

$$W^* = W^*_{initial} + (0.056t^{*3} - 0.184t^{*2} + 1.015t^*)H^{*12.3}Q^{*0.4} \qquad (7.1)$$

where $W^* = W/h$, is the normalized top width of the breach; h is the initial height of the levee; $W^*_{initial}$ is the normalized initial top width of the breach (initial width of the pilot channel = 0.10 m); $t^* = t/t_0$, is the normalized time where t_0 is the travel time of a wave in the upstream reservoir area defined as $t_0 = L_0/\sqrt{gh_o}$, where L_o is the length of the upstream reservoir area (i.e., from the beginning of the main channel to the centerline of the pilot channel, 7.63 m) and h_o is the initial height of water in the upstream reservoir to initiate overtopping (i.e., 0.15 m); $H^* = H/h$, is the normalized initial downstream water height, $Q^* = Q_{in}/\sqrt{g \times h^5}$, is the normalized inflow discharge, and g is the gravitational acceleration.

To determine the validity of the proposed equation (Eq. (7.1)), empirical and experimental results of temporal changes of the breach top width are compared for different tests. Except for some deviations in Test A1, the measured data from laboratory experiments and the estimated ones from Eq. (7.1) are in satisfactory agreement for all the tests. Figures 7.8(a and b) show the comparison of the empirical and experimental results along with their R^2 values for tests A2 and B3, respectively. Figure 7.9 shows the time history of normalized breach width for all test tests using Eq. (7.1). For a given normalized time, differences between the normalized top width increases with the inflow discharge for the tests with 0.05 m downstream weir height (A1, A2, A3), while it decreases for the tests with 0.075 m weir height(B1, B2, B3).

Maximum Breach Depth

Temporal changes in the maximum breach depth along the centerline of the levee crest are measured during the levee failure process for all the tests using the sliding rods technique. The empirical relationship for the normalized breach depth as a function of the normalized time, inflow discharge, and initial downstream water depth is obtained by regression analysis as follow with R^2=0.97 for all the tests:

$$D^* = D^*_{initial} + (-6.66e^{-3}t^{*3} + 0.098t^{*2} - 0.167t^*)H^{*7.5}Q^{*0.27} \qquad (2)$$

where D^* is the normalized maximum breach depth expressed as $D^* = D/h$, and $D^*_{initial}$ is the normalized initial breach depth (i.e., initial depth of the pilot channel = 0.05 m).

Figures 7.10(a and b) show the comparison of the empirical equation (Eq. (7.2)) and experimental results along with their R^2 values for Tests A3 and B2, respectively. The empirical and the experimental measurements are in satisfactory agreement for all of the tests. Figure 7.11 shows time history of normalized breach depth for all the tests using Eq. (7.2). Similar to the top width changes, differences between the normalized breach depth increases with the inflow discharge at a given time for the tests with 0.05 m downstream weir height (A1, A2, A3), while it decreases for the tests with 0.075 m weir height(B1, B2, B3). A third-order polynomial fit is used herein to better represent the actual physical deepening process of the breach, i.e. Eq. (7.2), and capture the acceleration and deceleration stages.

Breach Volume

As mentioned earlier, the variation of levee shape with time is measured using the rods mechanism. The erosion volume is then calculated between two consecutive time steps applying the trapezoidal integration over the grid points of elevation. From the measured cumulative breach volume of the downstream half of the levee for different normalized inflow discharges and initial downstream water depth, the best fit curve is obtained as follow for all the tests (R^2=0.97):

$$V^* = 0.06{t^*}^{1.77}{H^*}^{10.2}{Q^*}^{0.44} \quad (7.3)$$

where V^* is the normalized cumulative breach volume obtained as $V^* = V/V_{initial}$, and $V_{initial}$ is the initial volume of downstream half of the levee. A comparison of the results from the measurements and values obtained from Eq. (7.3) are shown in Figures 7.12(a and b) along with their R^2 values for Tests A2 and B1, respectively. The results demonstrate that the proposed empirical equation may be used satisfactorily to predict the eroded volume of the levee material. A family of curves of normalized breach volume for different inflow discharge and initial downstream water depth is plotted in Figure 7.13 as calculated by using Eq. (7.3). Similar to the trends observed in Figure 7.9 and Figure 7.11, the curves start to deviate after about t^*= 2 from starting time of the overtopping.

Modeling Breach Evolution

Using the aforementioned empirical equations for the breach top width and the breach depth, a trapezoidal model with a fixed bottom width is proposed to predict the temporal changes in the breach shape along the centerline of the levee crest as a function of inflow discharge and initial downstream water depth. The bottom width is assumed to be equal

to the initial width of the pilot channel and the centerline of the trapezoidal model is assumed to overlie on the centerline of the pilot channel. The top width and the height of the trapezoid may be calculated using Eqs. (7.1) and (7.2), respectively.

The experimental results of temporal changes of the breach shape profile along the centerline of the crest are compared with those from the proposed model for different tests. Except some deviations of the top width for Test A1 in which the breach shape evolves mostly in a triangular shape, the measured and the predicted results agree well for all other tests. The Root Mean Square Error (RMSE) of the predictions is calculated for all the tests at different time steps, as shown in Table 7.2. The time-averaged Root Mean Square Error (RMSE) of all of the tests is 0.01 m. Figure 7.14 shows the comparison of the experimental and modeled breach shapes at different times for Test A3. Due to the non-symmetric evolution of the levee breach in the experiments (i.e., faster breach widening towards the downstream direction), the proposed model dose not capture the exact location of the breach especially at the final stage of the failure. However, the proposed model is simple and may be used satisfactorily to estimate the total area of the breach cross section and hence the breach shape at different times.

Table 7.1 Test data

Test	Downstream weir height (m)	Inflow discharge Q_{in} (m^3/s)	Initial water depth at downstream end of the flume, H (m)	Froude number at downstream end before overtopping
A1	0.050	0.059	0.163	0.466
A2	0.050	0.063	0.164	0.490
A3	0.050	0.073	0.169	0.552
B1	0.075	0.036	0.168	0.273
B2	0.075	0.048	0.171	0.356
B3	0.075	0.051	0.172	0.373

Table 7.2 RMSE of the breach shape predictions at different times

Test	t=5 s	t=10 s	t=15 s	t=20 s	t=25 s	t=30 s	t=35 s	t=40 s	$RMSE_{avg}$
A1	0.001	0.001	0.003	0.003	0.014	0.021	0.023	0.029	0.012
A2	0.001	0.003	0.014	0.009	0.011	0.013	0.006	0.019	0.009
A3	0.002	0.004	0.011	0.005	0.004	0.017	0.017	0.024	0.010
B1	0.001	0.003	0.008	0.010	0.013	0.010	0.009	0.019	0.009
B2	0.002	0.004	0.006	0.011	0.017	0.009	0.016	0.012	0.010
B3	0.003	0.006	0.002	0.006	0.008	0.019	0.024	0.016	0.011

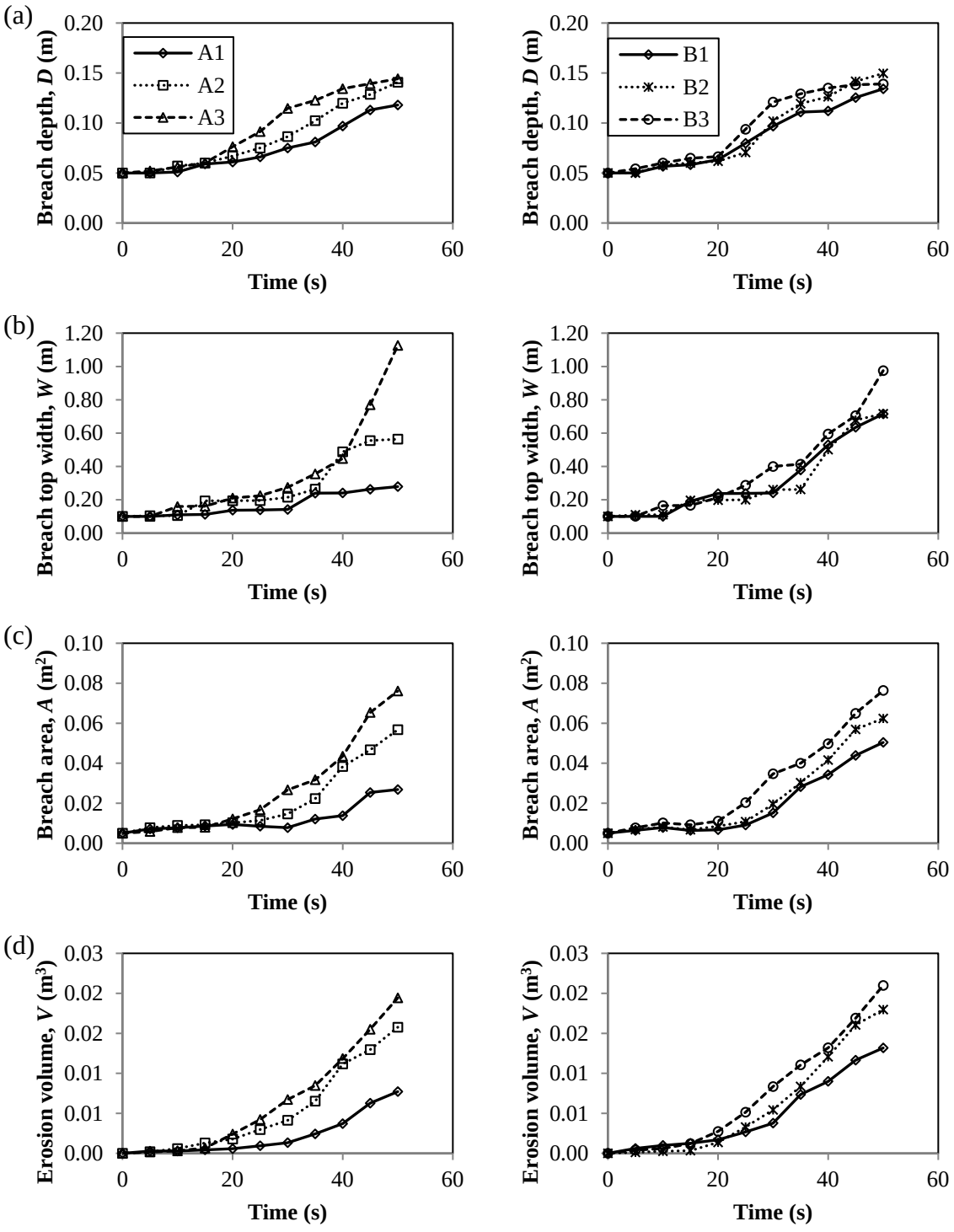

Figure 7.1 Time history of: (a) maximum breach depth; (b) top width of the breach; (c) breach area along the centerline of the crest; and (d) total breach volume

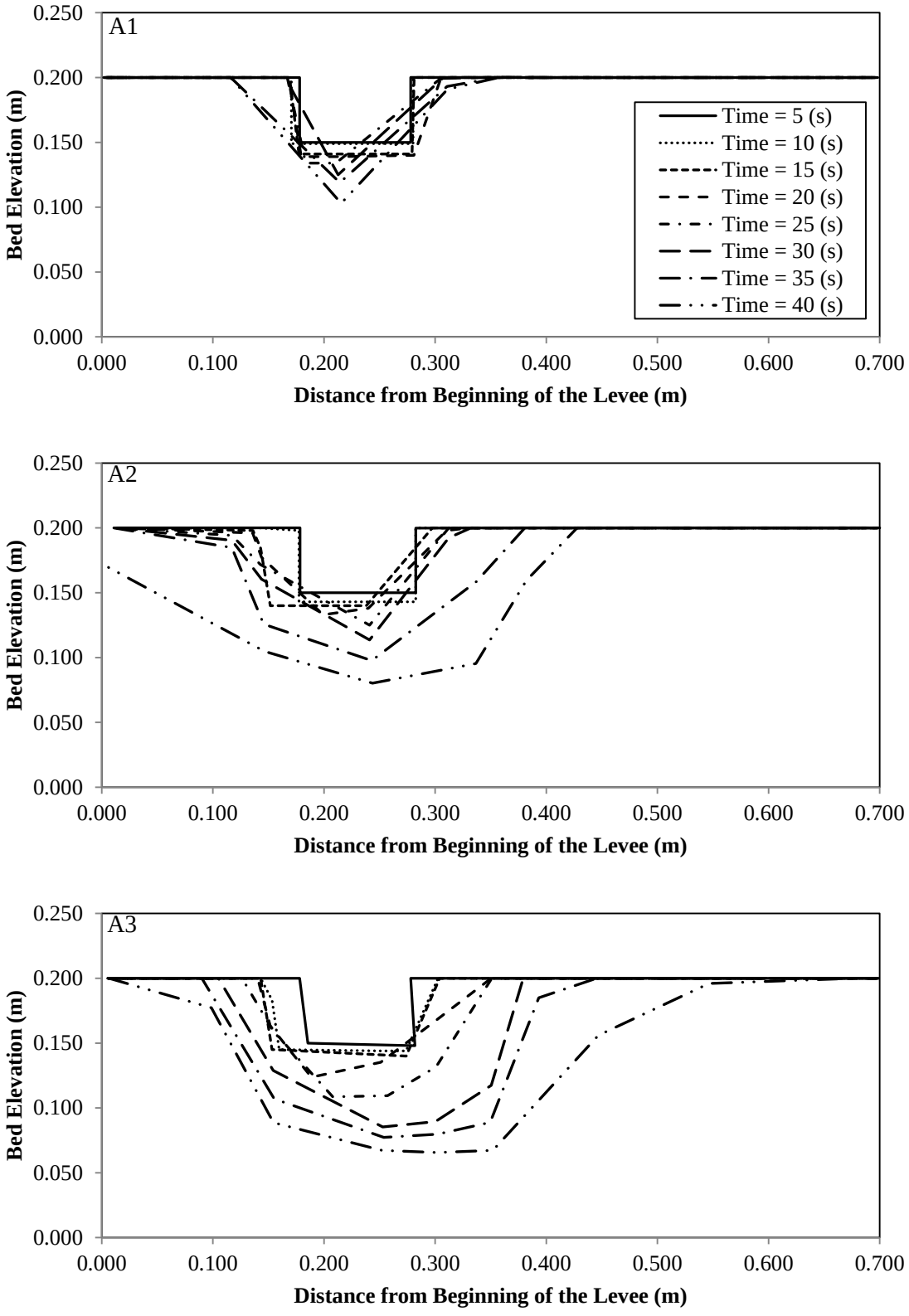

Figure 7.2 Breach evolution along the center of the levee crest

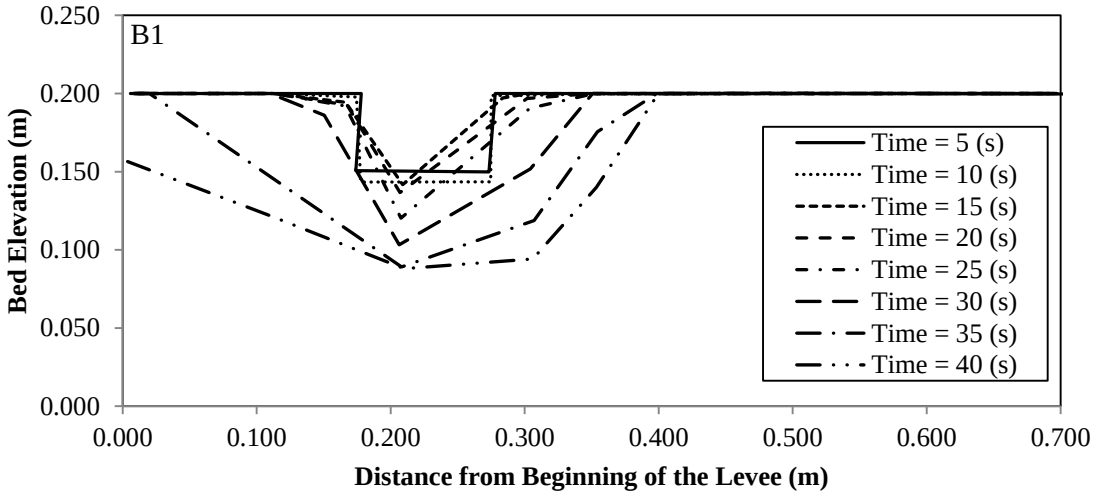

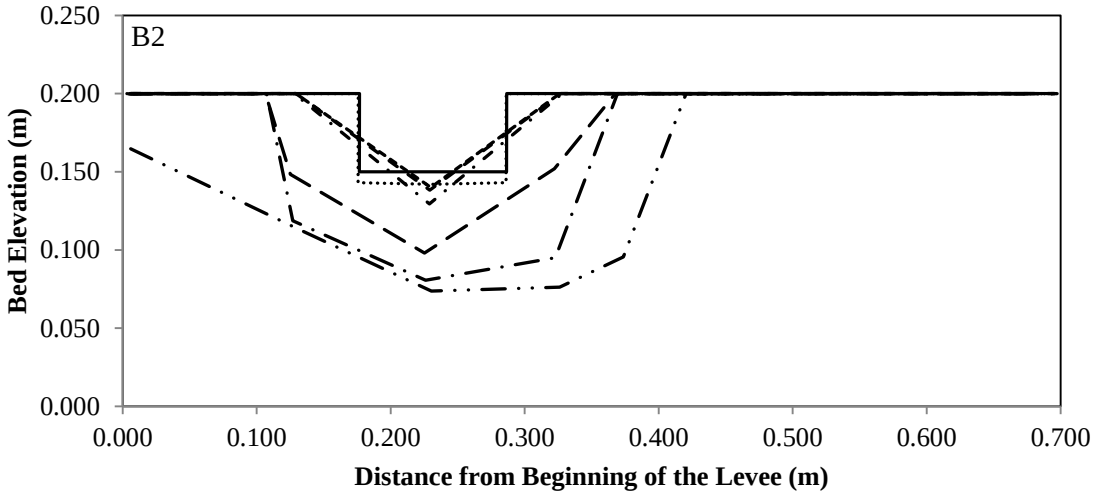

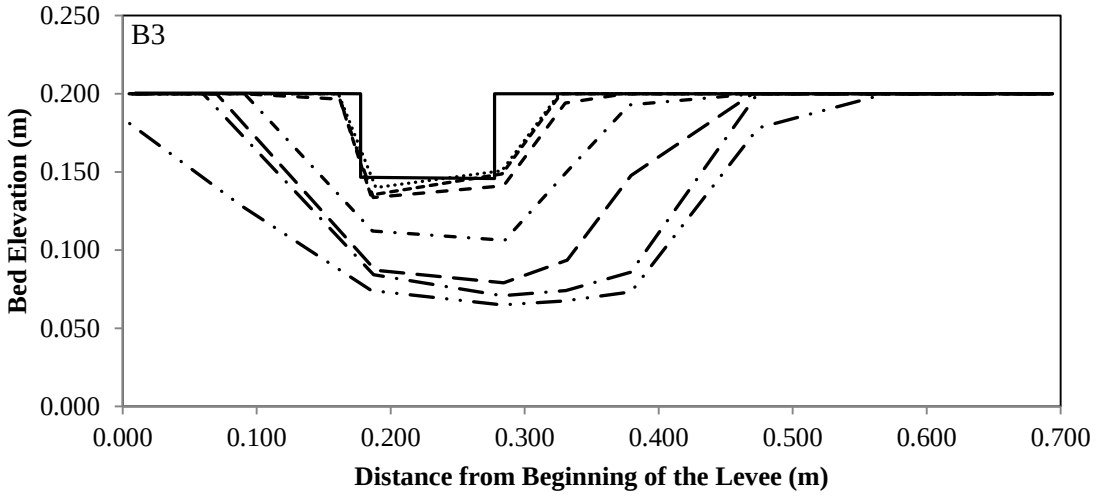

Figure 7.2 (Continued) Breach evolution along the center of the levee crest

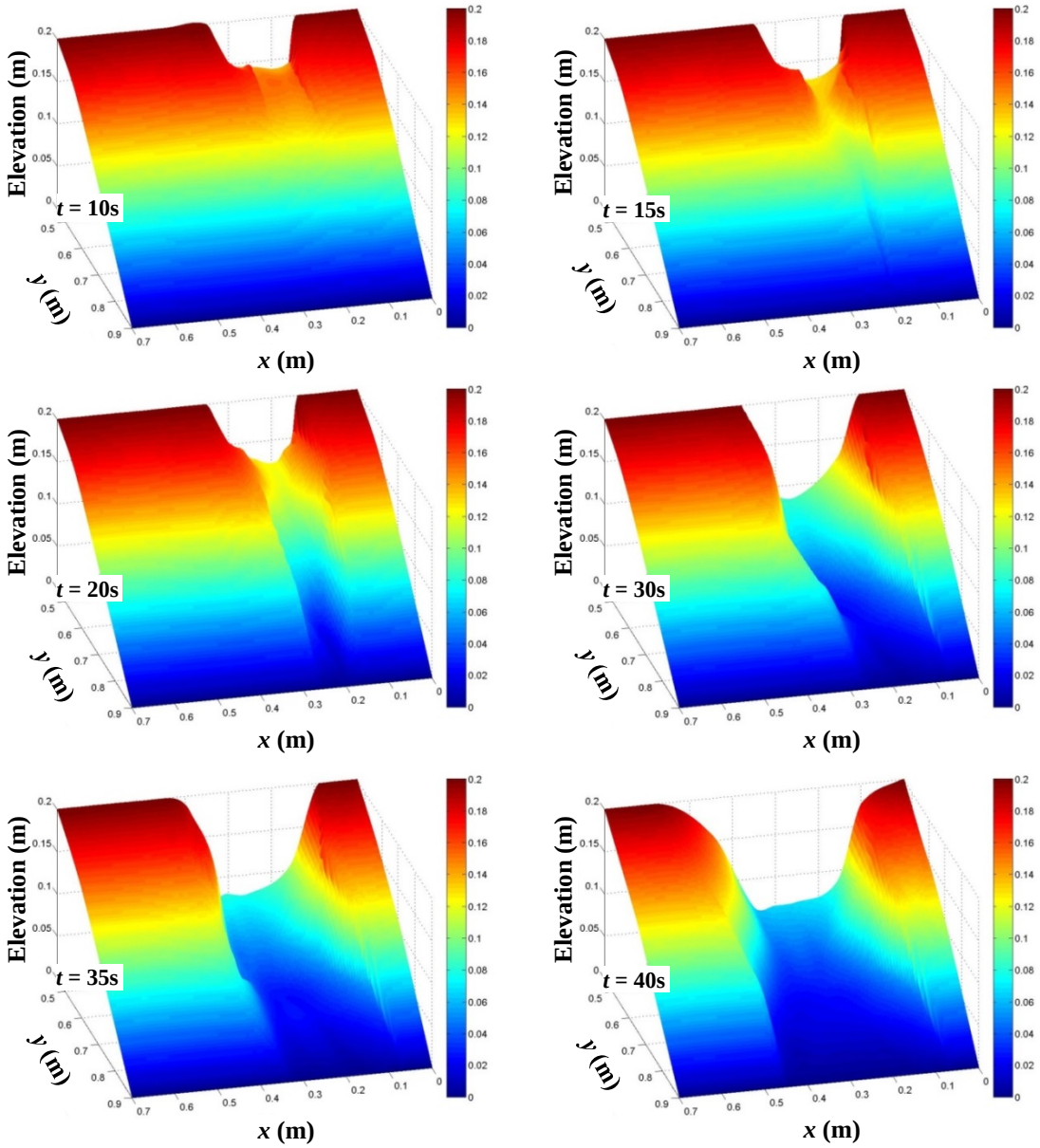

Figure 7.3 Breach evolution for Test A3 (flow direction in the main channel is from right to left)

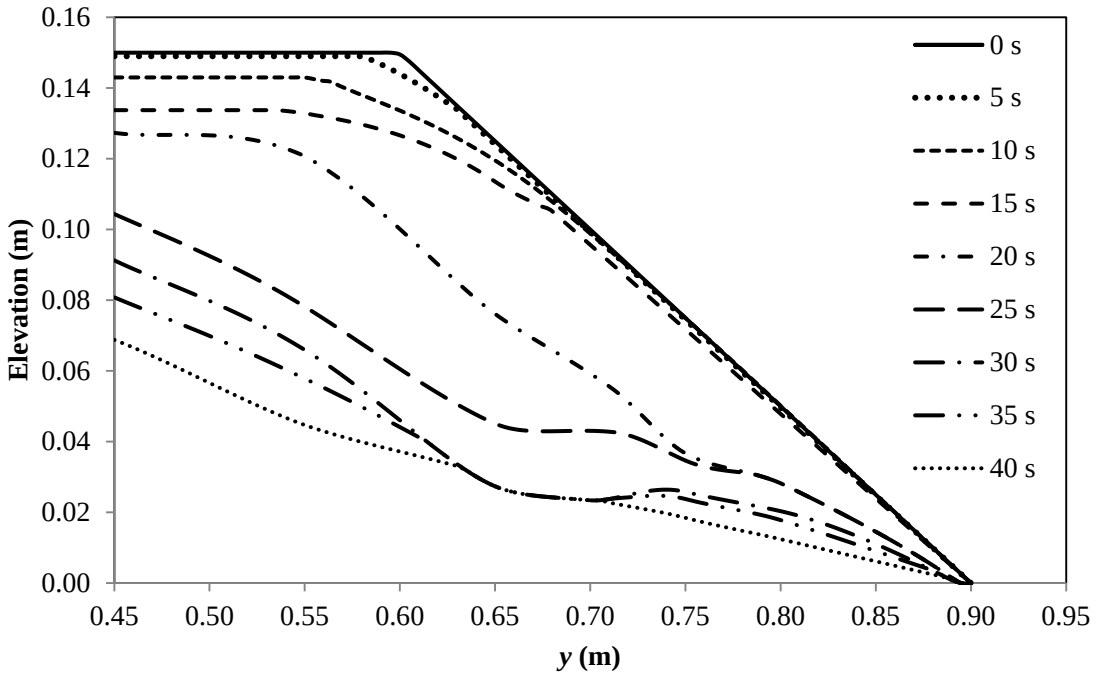

Figure 7.4 Longitudinal profiles along the centerline of the pilot channel at different times for Test A3

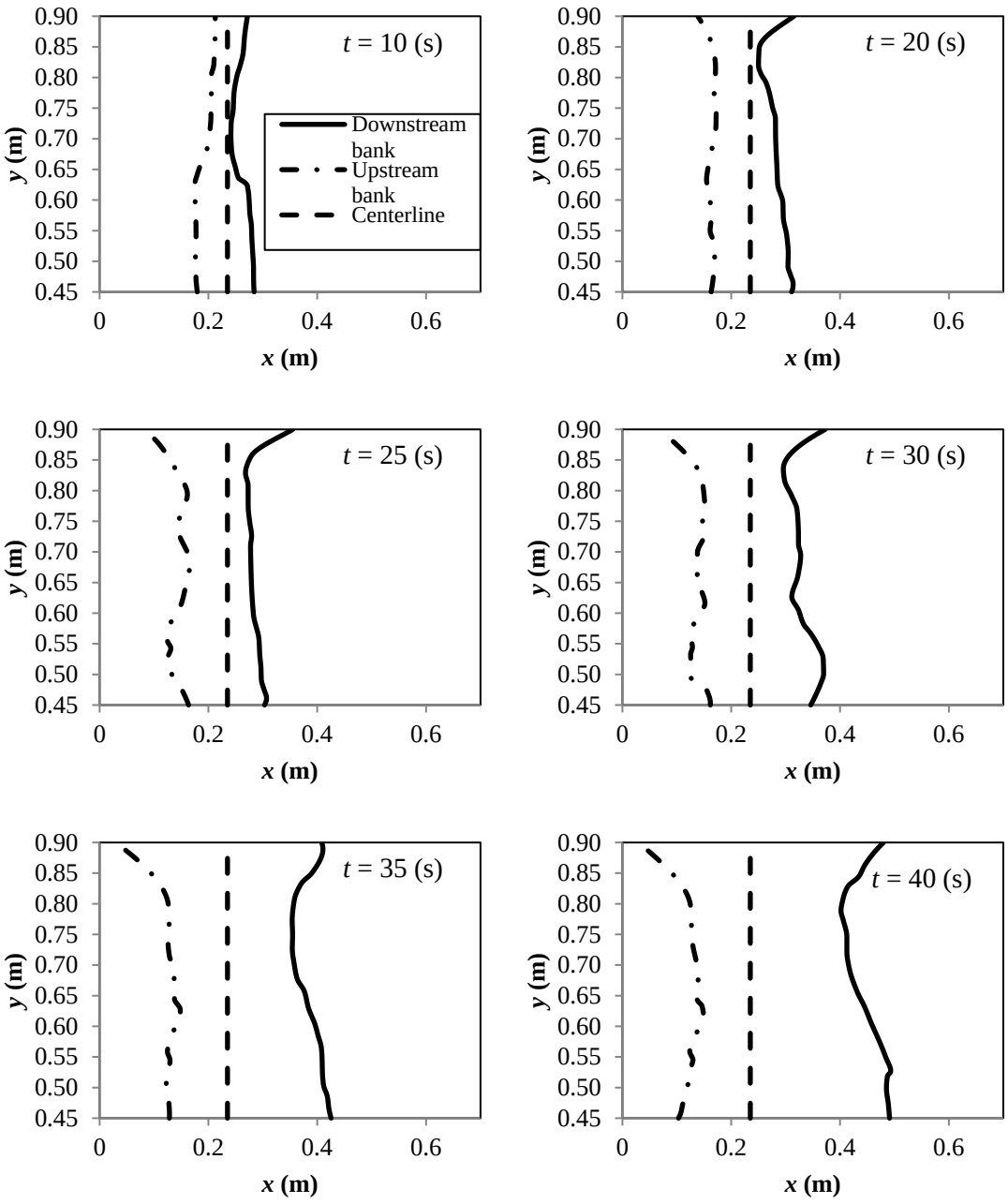

Figure 7.5 Breach top width for the downstream and upstream breach walls at different times for Test A3 (centerline of the pilot channel is shown as dash line)

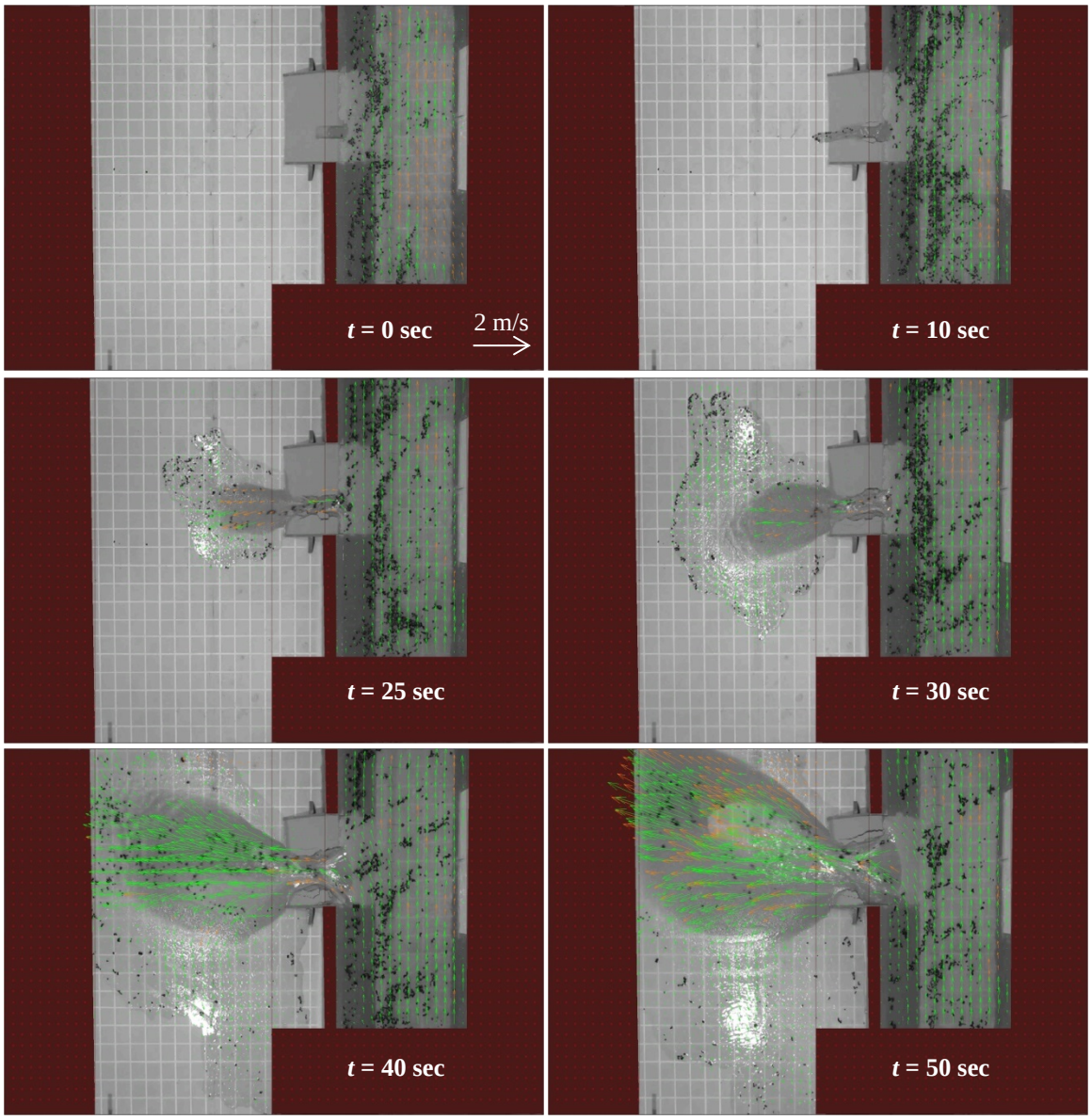

Figure 7.6 Water surface velocity distribution for Test A3 at different times

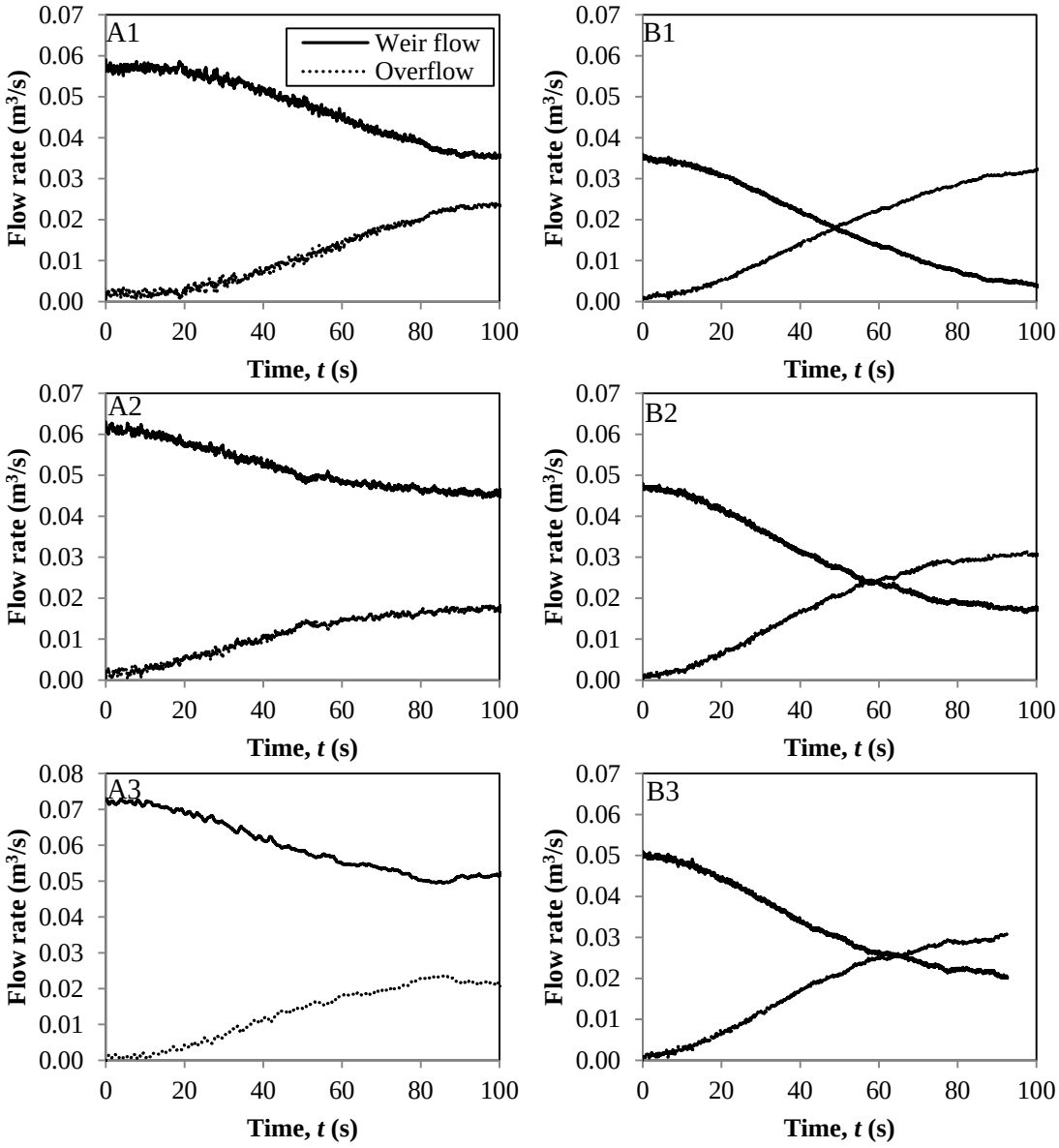

Figure 7.7 Weir flow and breach overflow hydrographs for all tests

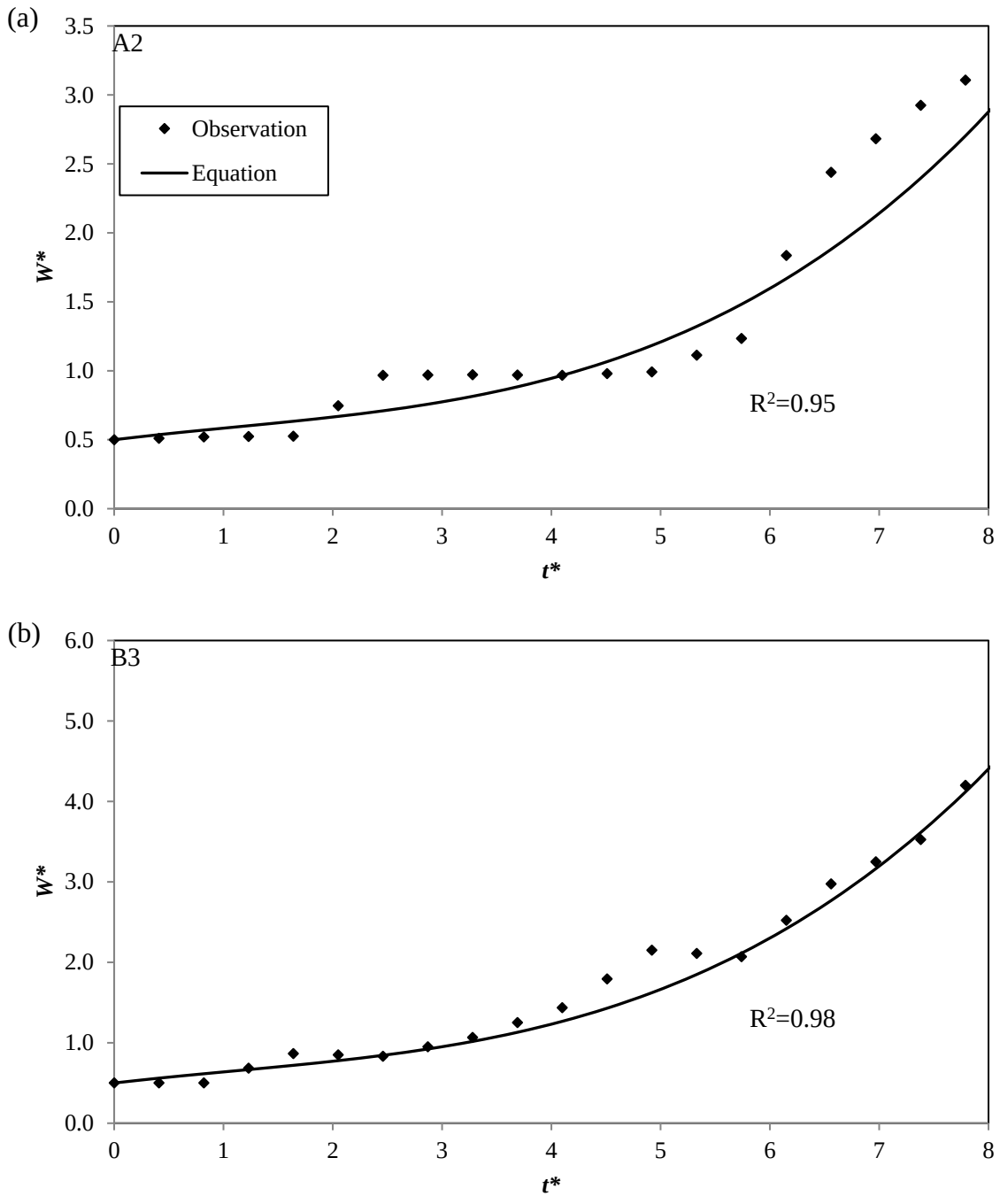

Figure 7.8 Comparison of experimental and empirical normalized breach top width with time for: (a) Test A2; and (b) Test B3

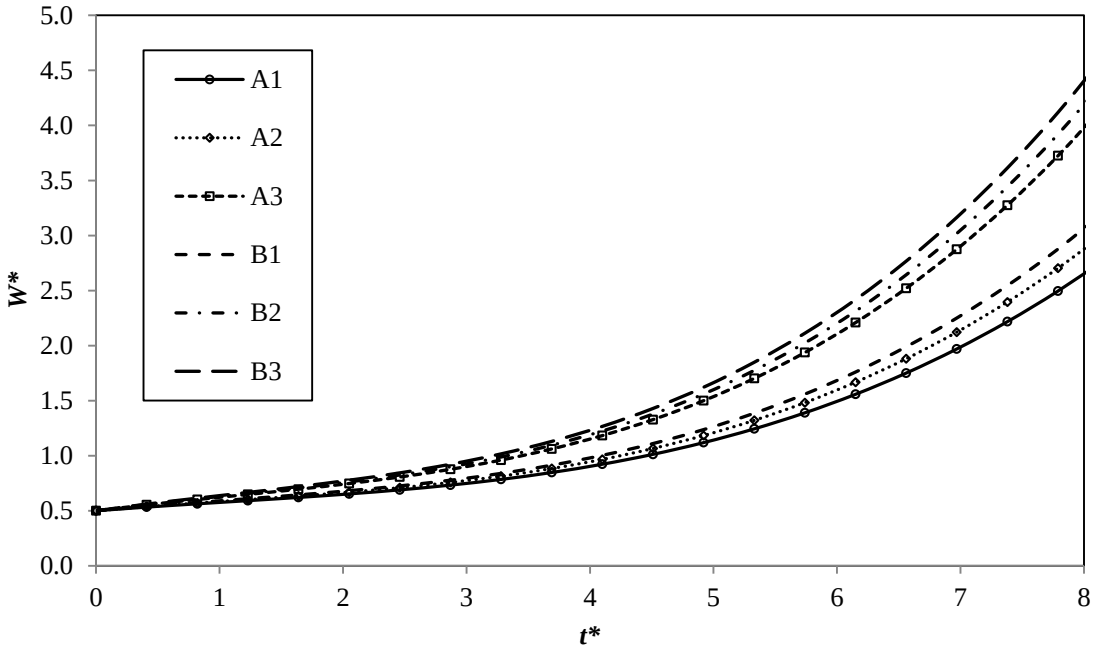

Figure 7.9 Empirical results of normalized breach top width with time for all tests

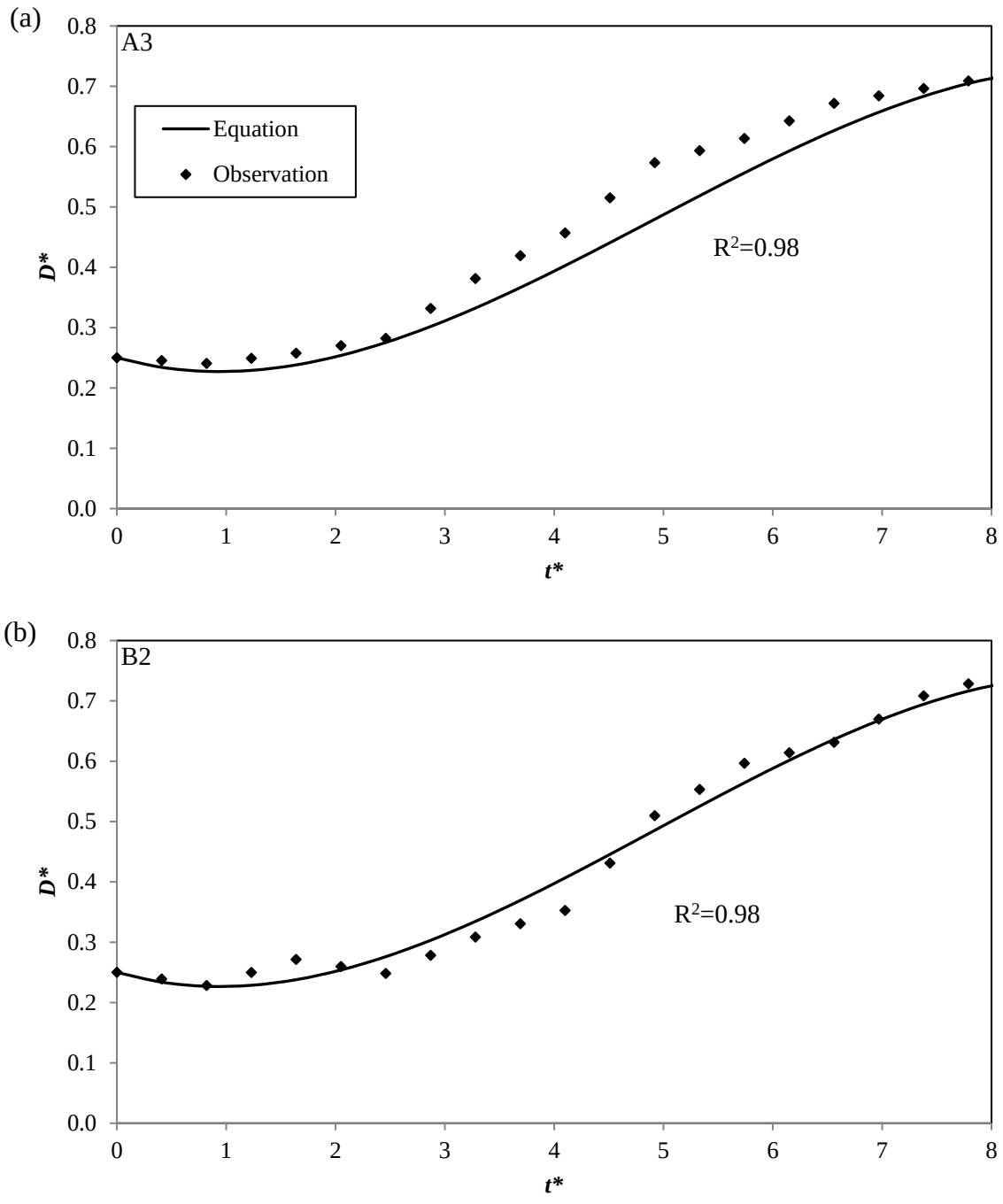

Figure 7.10 Comparison of experimental and empirical normalized maximum breach depth with time for: (a) Test A3; and (b) Test B2

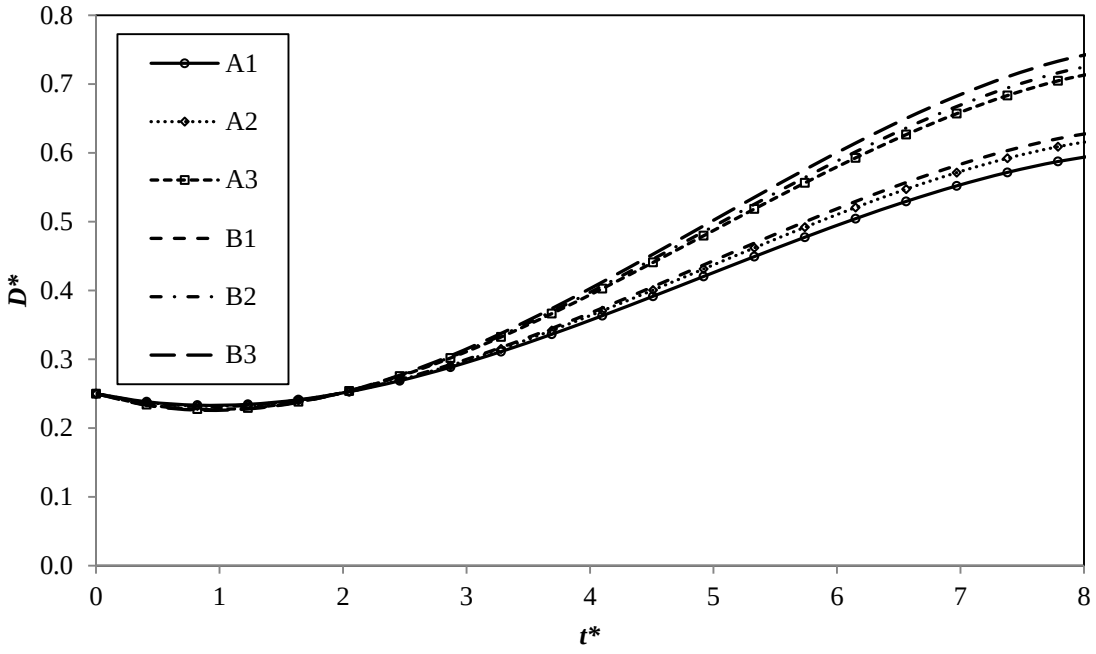

Figure 7.11 Empirical results of normalized maximum breach depth with time for all tests

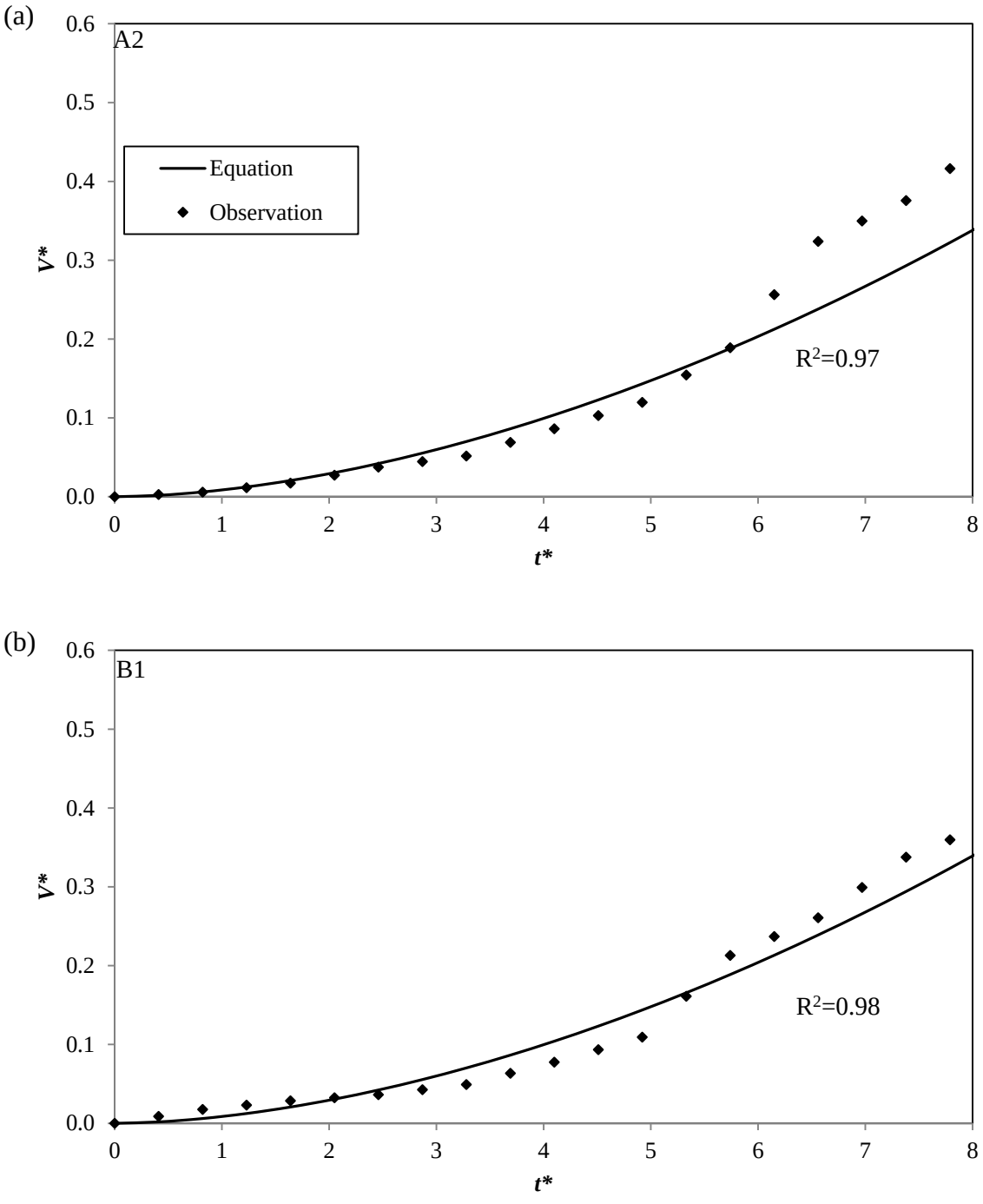

Figure 7.12 Comparison of experimental and empirical normalized breach volume with time for: (a) Test A2; and (b) for Test B1

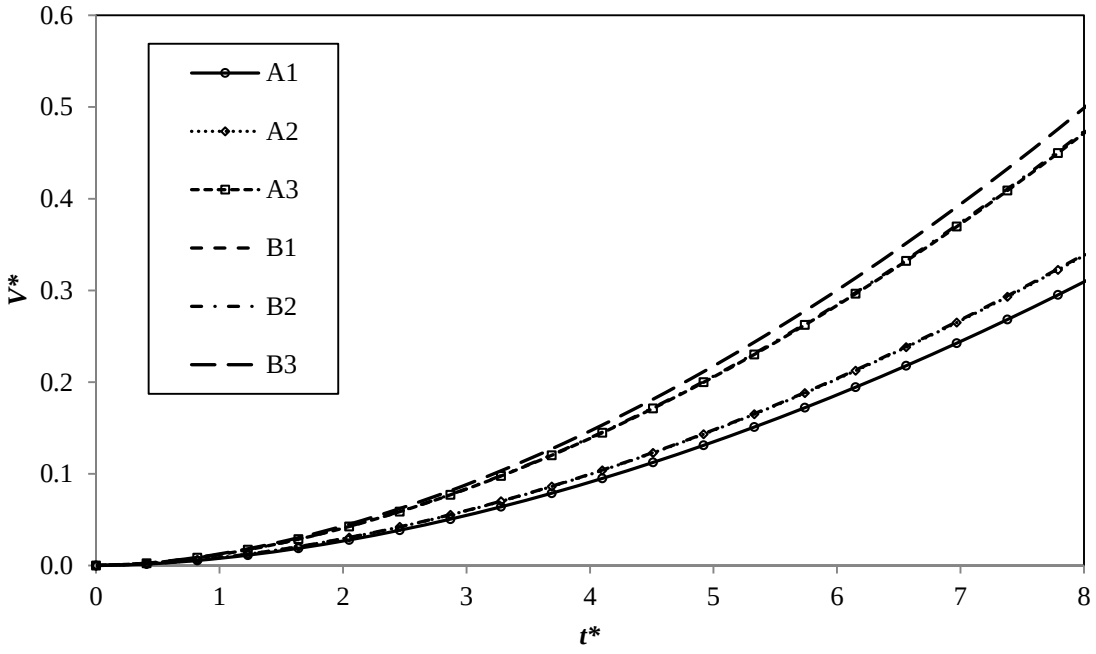

Figure 7.13 Empirical results of normalized breach volume with time for all tests

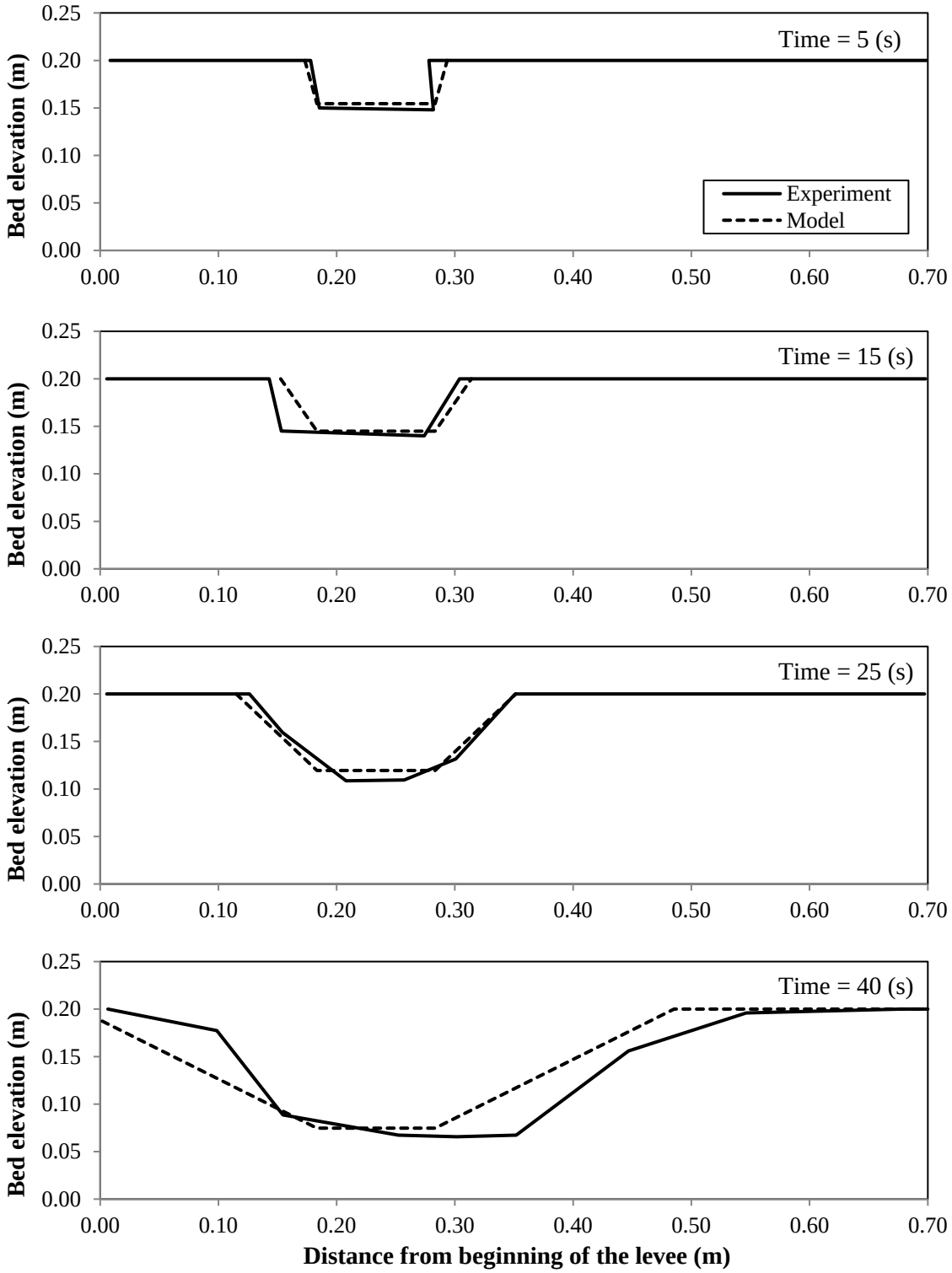

Figure 7.14 Comparison of the experimental and the predicted breach shape at different times using the trapezoidal model for Test A3

CHAPTER 8

EXPERIMENTAL MODELING OF EARTHEN LEVEE FAILURE BY OVERTOPPING: EFFECTS OF COMPACTION AND COHESION

The aim of this research is to investigate the effects of the compaction level and cohesion on the erodibility and failure process of a levee due to overtopping. This study fills the gap in the existing literature by analyzing the deepening and the widening stages separately with considering the compaction and cohesion effects. Eight experiments of levee breach failure are conducted in the Hydraulics Laboratory, University of South Carolina, by varying the compaction level and cohesion of embankment material to determine the breach characteristics (e.g., breach shape and dimensions evolution, breach eroded volume, and breach outflow); four of those tests are on sand-only levees with different levels of compaction and four other tests are on cohesive levees with different percentages of silt and clay while the compaction level is kept constant. Of particular interest is to use the experimental observations to develop non-dimensional relations for breach widening and deepening as a function of embankment-compaction characteristics.

8.1 Experiment description

The schematic and plan view of the experimental setup are shown in Figure 8.1 which is the same setup explained in detail in Chapter 6. Four Baumer ultrasonic probes, having an accuracy of ± 0.3 mm, are used in this experiment to precisely monitor the water surface elevation at different locations, one on top of the crest, one in the main channel

upstream of the levee, one in the main channel downstream of the levee, and one in the main channel at downstream end.

Table 8.1 shows the characteristics of the laboratory tests. Prior to the embankment overtopping tests of compaction effect, Standard Proctor Compaction tests (ASTM D698) are carried out to determine the optimum water content and maximum dry unit weight of the homogenous, non-cohesive soil used in four of the experiments. The optimum water content is 5.2% and the corresponding maximum dry unit weight, $\gamma_{d,max}$, is 15.44 kN/m^3.The trapezoidal earthen embankments of uniform sand with mean diameter of 0.55 mm and water content of 5.2% are placed in four loose layers. Each layer is compacted by a 4.54 kg rammer with the release height of 5 cm with different number of blows per layer, N_b, for each test: 0 (no compaction), 2, 4, and 10. After compaction, the levee is trimmed to the final shape. Similarly, for the tests with effects of cohesion, all four soil mixtures are mixed with 10% water and each layer is compacted with 5 blows per layer. To initiate overtopping, a pilot channel, 0.05 m deep and 0.10 m wide, is carved at one third of the length from the upstream edge of the earthen levee. The upstream face of the embankment is covered with a thin layer of clay to control the seepage through the embankment. Furthermore, after building the embankment, the leftover weight of the soil mixture used to build the levee is measured to determine the dry unit weight of each embankment (Table 8.1). The test with N_b = 10 B/L and all the tests with cohesive material almost reach the maximum compaction from the Proctor Compaction test.

The inflow discharge is kept constant at 0.05 (m^3/s) for all the tests. The pump is started to fill the main channel and the starting time of the breach process is considered to

be the time when the water surface reaches the upstream front of the pilot channel. The flow through the breach is calculated from the balance of constant inflow and the measured outflow discharge from the channel. The breach shape is monitored using a front camera and a sliding rods technique developed by the author (section 6.2) along with image processing.

8.2 Results for compaction effects

Breach shape evolution

Time history of the breach top width, *W*, and the maximum breach depth, *D*, along the centerline of the levee crest are presented in Figures 8.2 and 8.3 for all the tests (Tests 1 to 4), respectively. The breach top width remains relatively constant at the initial stage of the failure process and then starts to accelerate, while the changes in maximum breach depth include acceleration and deceleration phases. The breach width, maximum breach depth, widening rate, and deepening rate decrease with the compaction level for a given time step. Breach profiles along the centerline of the levee crest at different times are presented in Figure 8.4 for all the tests. The flow direction in the flume is from left to right in these figures. Until about $t = 35$ s the breach profile evolves only in vertical direction for the compacted embankments and after that the widening becomes dominant, while for the non-compacted test the breach starts to widen short after the onset of overtopping (i.e., after $t = 5$ s). For all the tests, the downstream side-wall of the breach is struck by higher velocities as compared to the upstream side which results in a faster erosion in the downstream direction. This is different from the dam breach scenario where the breach develops with the same rate in both sides. From the figures, as the

breach starts to widen, the breach cross-section assumes an almost trapezoidal shape with a wider top width and narrower bottom width. For most of the times, the breach side-walls are resting on steeper slope for the compacted tests comparing to the non-compacted test.

The three-dimensional breach shape is estimated from the sliding rods technique and is compared for all the four tests (Figures 8.5 to 8.8). Moreover, the time series of the longitudinal bed surface profiles along the centerline of the pilot channel is presented in Figure 8.9 for all the experiments. The erosion starts on the downstream face of the levee and it retrograded from the downstream edge to the upstream edge of the levee crest and it continues with the degradation of the crest. Then the breach starts to widen and shortly the widening accelerates. The observed failure stages (i.e., levee breach initiation, onset of widening, and widening acceleration) are consistent with those from Kakinuma and Shimizu (2014) large-scale experiments. However, the last stage of widening deceleration is not observed in the current study due to the limited length of the earthen section. Duration of the failure increases with compaction as expected. Besides, it is observed from the figures that as the compaction increases, the irregularity of the breach shape increases. This can be due to the fact that as the compaction increases, the head-cut erosion dominants as compared to the surface erosion which is mostly the controlling erosion mechanism in the test with no-compaction.

The time history of the accumulated breach eroded volume for downstream half of the breach is shown in Figure 8.10 for all the tests as measured by the sliding rods technique. The time rate of change of the breached volume is almost the same for the compacted tests, while it is higher for the non-compacted embankment. The changes of

the submerged area along the centerline of the levee crest versus time are calculated using the recorded water surface elevations on top of the pilot channel and are presented in Figure 8.11 for all the tests. A similar trend is observed for the compacted and non-compacted tests; the submerged area is negligible until about $t = 20$ s and then it starts to accelerate with almost a constant slop. However, the slope is relatively higher for the non-compacted test.

Breach outflow discharge

The flow discharge over the sharp-crested calibrated weir at the downstream end of the flume is monitored, and the breach outflow hydrograph is computed by balancing the weir overflow and the constant inflow discharge for all the tests (Figure 8.12). The breach outflow includes acceleration and deceleration phases. It remains relatively small in each test at the initial stage of the failure and then starts to accelerate and increase with almost a constant rate, then it decelerates and reaches roughly a constant value until the end of the failure process (0.035 m^3/s for all the tests). However, the time rate of breach over flow changes is higher for the non-compacted test as compared to the compacted tests. These changes correspond to the deepening phase of the failure as well. Besides, at a certain point (i.e., at about $t = 50$ s in the non-compacted test and at about $t = 70$ s in the compacted tests) the breach outflow exceeds the weir flow in all the tests.

Formula for breach morphology as widening and deepening rates

The non-dimensional relationship between the deepening rate and widening rate of the breach cross-section, along the crest centerline, with the excess shear stress can be expressed in a form similar to the Meyer-Peter and Muller bedload formula as:

$$\epsilon_d^* = \alpha_d(\tau_{ed}^* - \tau_c^*)^{\beta_d} \tag{8.1}$$

$$\epsilon_w^* = 2\alpha_w(\tau_{ew}^* - \tau_c^*)^{\beta_w} \tag{8.2}$$

where ϵ_d^* and ϵ_w^* are the non-dimensional erosion rates for deepening and widening stages of the failure, respectively (* denotes the normalized form, and *d* and *w* denote deepening and widening, respectively); α_d, β_d and α_w, β_w are the correspondent erodibility coefficients; τ_{ed}^* and τ_{ew}^* are the non-dimensional applied shear stresses on bed and side walls of the breach opening, respectively; and τ_c^* is the non-dimensional critical shear stress. The normalized erosion rates, ϵ_d^* and ϵ_w^*, are calculated as

$$\epsilon_d^* = (\frac{\Delta D}{\Delta t})^* = \frac{\Delta D}{\Delta t} \times \frac{1}{\sqrt{RgD_g}} \tag{8.3}$$

$$\epsilon_w^* = (\frac{\Delta W}{\Delta t})^* = \frac{\Delta W}{\Delta t} \times \frac{1}{\sqrt{RgD_g}} \tag{8.4}$$

where $\Delta D/\Delta t$ and $\Delta W/\Delta t$ are deepening and widening rates, respectively; t is time; R is sediment submerged specific gravity; g is gravitational acceleration; and D_g is the mean diameter of the soil. The non-dimensional deepening and widening rates are calculated every 5 s from the experimental observations for each test.

The non-dimensional critical shear-stress is calculated using the relation proposed by Parker et al. (2003) as follow

$$\tau_c^* = 0.5\left[0.22R_{ep}^{-0.6} + 0.06 \times 10^{(-7.7R_{ep}^{-0.6})}\right] \tag{8.5}$$

$$R_{ep} = \frac{\sqrt{RgD_g}D_g}{\vartheta} \tag{8.6}$$

where R_{ep} is particle Reynolds number; and ϑ is kinematic viscosity of water. Moreover, the applied shear stress on the bed and side-wall of the breach, τ_{ed} and τ_{ew}, are being normalized using the following relations

$$\tau_{ed}{}^{*} = \frac{\tau_{ed}}{\rho RgD_g} \tag{8.7}$$

$$\tau_{ew}{}^{*} = \frac{\tau_{ew}}{\rho RgD_g} \tag{8.8}$$

where ρ is the density of water.

Similar to the procedure expressed by Hunt et al. (2005), a rectangular cross-section and a critical flow depth are assumed along the centerline of the levee crest. These assumptions are used to estimate the applied shear stress on the bed, τ_{ed}, and on the side walls of the breach, τ_{ew}, as

$$\tau_{ed} = \gamma_w d S_f \tag{8.9}$$

$$S_f = \frac{gn^2}{d_c{}^{\frac{1}{3}}} \tag{8.10}$$

$$\tau_{ew} = 0.7\tau_{ed} \tag{8.11}$$

where γ_w is the specific weight of water; d is the average water depth across the breach cross section which is assumed to be the critical depth, d_c; S_f is the energy slope which is calculated from the Manning equation; and n is the Manning coefficient. Eq. (8.11)

Incorporating the observed data of the observations of the breach widening and deepening processes into the aforementioned relations, the erodibility relations can be obtained in vertical and horizontal direction for each compacted embankment test. Figures 8.13 and 8.14 show the test results of the correlation between the deepening and widening rate with the excess shear stress, respectively for four levels of compaction. The correlations are expressed by their corresponding fitted equations in the plots for different compaction levels. These results of the coefficients of these equations are summarized in Table 8.1.

To have a more general variable representing compaction, normalized compaction energy, $C_e^* = C_e/(\rho_{dry,max} \times h)$, is used herein, corresponding to each N_b, where $\rho_{dry,max}$ is the maximum dry density from the proctor compaction test; h is the height of the levee; and C_e is compaction energy which is calculated as

$$C_e = \frac{N_b \times Number\ of\ layers \times Hammer\ weight \times Release\ height}{Soil\ volume\ under\ hammer} \quad (8.12)$$

Using regression analysis, the non-dimensional relationships of the breach deepening and widening rate as a function of the compaction energy were obtained as:

$$\epsilon_d^* = 0.068e^{-0.158C_e^*}(\tau_{ed}^* - \tau_c^*)^{0.462} \quad (8.13)$$

$$\epsilon_w^* = 0.544e^{-0.043C_e^*}(\tau_{ew}^* - \tau_c^*)^{2.67} \quad (8.14)$$

To verify the validity of the proposed relations, i.e. Eqs. (8.13) and (8.14), predicted and observed results of the breach deepening and widening rates are compared

for different tests in Figures 8.15 and 8.16, respectively. A relatively better prediction is observed for the breach widening rate as compared to the deepening rate.

Formula for breach morphology as breached-load transport

The normalized total volume of eroded levee material transported per unit time per unit width, $q_b{}^*$, can be expressed in a general form with reference to the Meyer-Peter and Muller bedload formula (Kakinuma and Shimizu, 2014)

$$q_b{}^* = \alpha(\tau_{ed}^* - \tau_c^*)^\beta \tag{8.15}$$

where $q_b{}^* = q_b / \sqrt{RgD_g{}^3}$; and α and β are coefficients. The eroded load can be calculated from the experimental measurements between two consecutive time steps as

$$q_b = (1-\lambda)\frac{\Delta V}{\Delta t}\frac{1}{L} \tag{8.16}$$

where λ is the embankment porosity calculated as $\lambda = 1 - \gamma_{dry}/(s \times \gamma_w)$; s is the specific gravity of soil particles; $\Delta V/\Delta t$ is the change of total eroded volume during time Δt; and L is the characteristic length, selected as the length of the earthen section herein. The calculated breached loads are plotted against the excess Shields number in Figure 8.17 for each compaction level. The corresponding fitted equations to these observations are also shown on the plot. As shown in Table 8.1, the coefficient α in Eq. (8.15) has the values of 21.40, 10.78, 9.46, and 8.85 for the tests of N_b = 0, 2, 4, and 10, respectively. Coefficient β is also found to have the values of 2.23, 1.63, 1.91, and 1.69 for the tests of N_b = 0, 2, 4, and 10, respectively. The coefficients α and β have the values of 8 and 1.5 in

Meyer-Peter and Muller equation, and values of 18 and 1.5 in the proposed equation by Kakinuma and Shimizu (2014), respectively.

From the measured cumulative eroded volume of the downstream half of the levee for different normalized compaction levels and excess shear stresses, the best fit curve is obtained as follow for all of the tests (R^2=0.84):

$$q_b^* = 16.8e^{-0.022C_e^*}(\tau_{ed}^* - \tau_c^*)^{1.898} \quad (8.17)$$

A comparison of the results from the observations and values predicted from Eq. (8.17) is shown in Figure 8.18 for all tests. The comparison demonstrates that the proposed equation may be used satisfactorily to approximate the eroded volume of the levee material with an averaged RMSE of 1.73 for all the tests.

8.3 Results for cohesion effects

Breach evolution and breach overflow

Three-dimensional breach evolutions are shown in Figures 8.19 to 8.22 for Tests 5 to 8, respectively. The erosion process starts on the downstream face with head-cuts progression from the downstream toe of the levee towards the crest, while the breach width remains constant during this stage. After the head-cut reaches the crest, the breach along the centerline of the crest first starts to deepen until it almost reaches the bottom and then the widening stage starts. Comparing to non-cohesive levees, the transition from the breach deepening to breach widening is more distinct in the tests with cohesive material. The time changes of the breach width and breach depth along the crest centerline are shown in Figures 8.23 and 8.24 for all the cohesive tests, respectively.

Furthermore, the breach profiles along the crest centerline are shown in Figure 8.25 at different time steps for all four cohesive tests. It is found that increasing the silt content increases the erosion resistant of the embankment. However, the clay content is found to be more dominant than the silt content in controlling the erosion. Herein, by only changing the clay content from 6% to 12% the levee becomes remarkably resistant towards erosion so that it takes about 22 minutes to fail, while the failure time for the test with 40% silt content is only about 3 minutes.

Figure 8.26 shows the weir flow and breach overflow for the tests with cohesion. For Tests 5, 6, and 7, the breach discharge remains almost negligible in the first 60 s (t^* = 10) and then it increases with a sharp gradient until it reaches an almost constant value. While, for Test 8, the breach overflow remains almost negligible until about 1200 s (t^* = 200) and then it increases. The same trend is observed for the weir flow for all the four tests.

8.4 Comparing compaction with cohesion effects

To compare the compaction effects to cohesion effects on the erosion process of the overtopped levees, the envelope curves are developed and presented herein for the breach characteristics by combining the results from all 8 tests. The envelope curves of breach top width, breach depth, breach eroded volume, breach submerged area, and breach total area along the crest centerline are shown in Figures 8.27 to 8.31, respectively. It is found that the cohesion effect by changing the clay content is the most dominant parameter affecting the erosion process as compared with the compaction.

Table 8.1 Test characteristics

Test	Tests with effect of compaction								
	N_b (B/L)	γ_{dry} (kN/m^3)	C_e^*	α_d	β_d	α_w	β_w	α	β
1	0	12.01	0.00	0.10	0.87	0.53	2.67	21.40	2.23
2	2	14.29	2.88	0.07	0.75	0.17	2.77	10.78	1.63
3	4	15.29	5.77	0.06	0.71	0.28	4.06	9.46	1.91
4	10	15.49	14.42	0.02	1.10	0.12	5.87	8.85	1.69
	Tests with effect of cohesion								
	N_b (B/L)	**Sand (%)**	**Silt (%)**	**Clay (%)**					
5	5	74	20	6					
6	5	64	30	6					
7	5	54	40	6					
8	5	68	20	12					

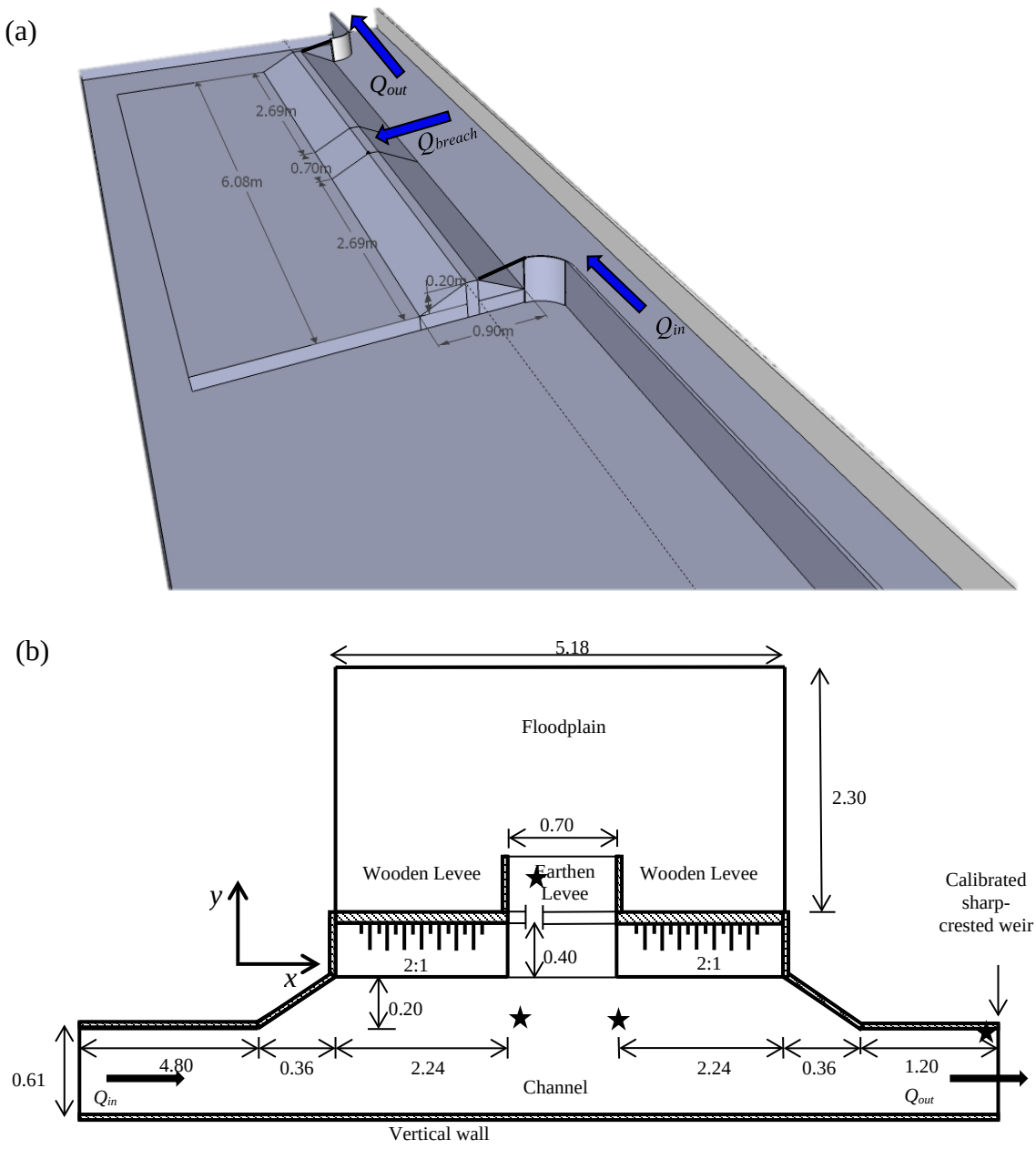

Figure 8.1 Experimental setup in: (a) schematic view; and (b) plan view. Location of the Baumer ultrasonic devices are indicated by stars (dimensions are in meter)

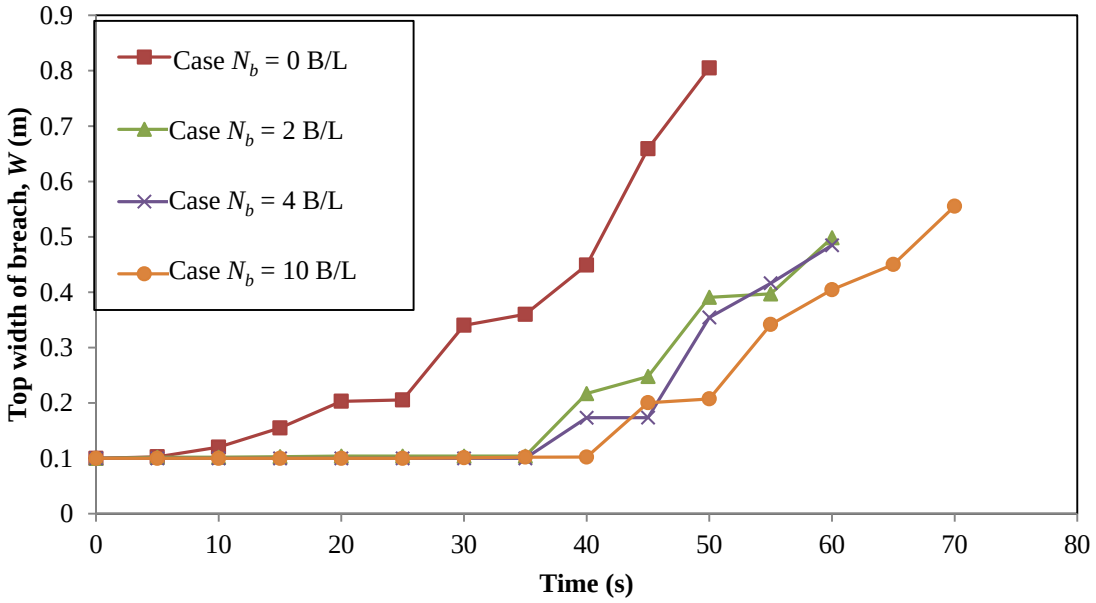

Figure 8.2 Time history of the breach top width along the centerline of the levee crest for four levels of compaction

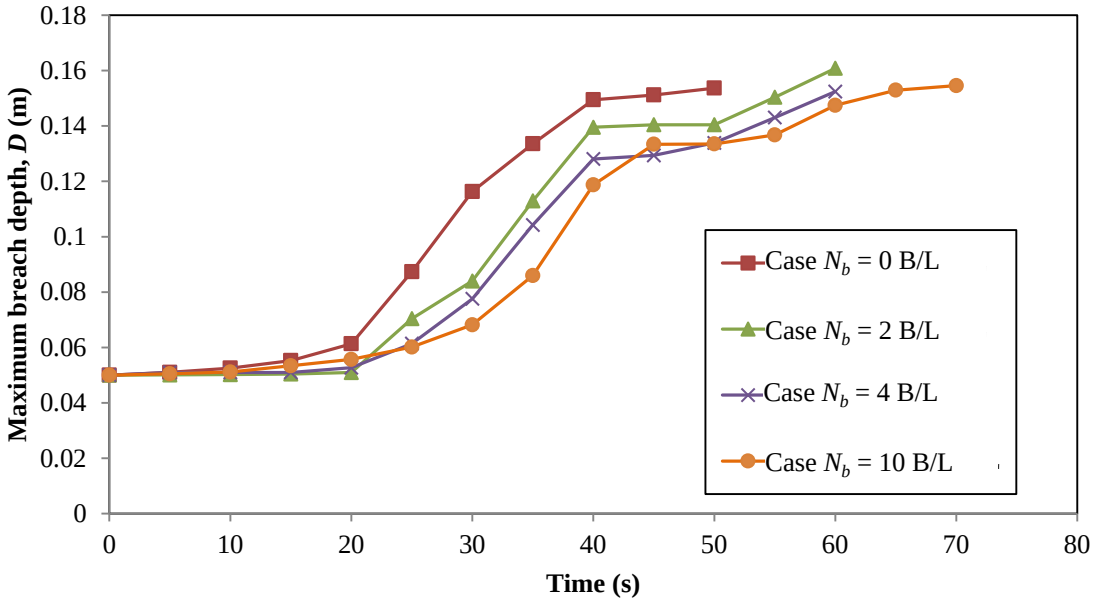

Figure 8.3 Time history of the maximum breach depth along the centerline of the levee crest for four levels of compaction

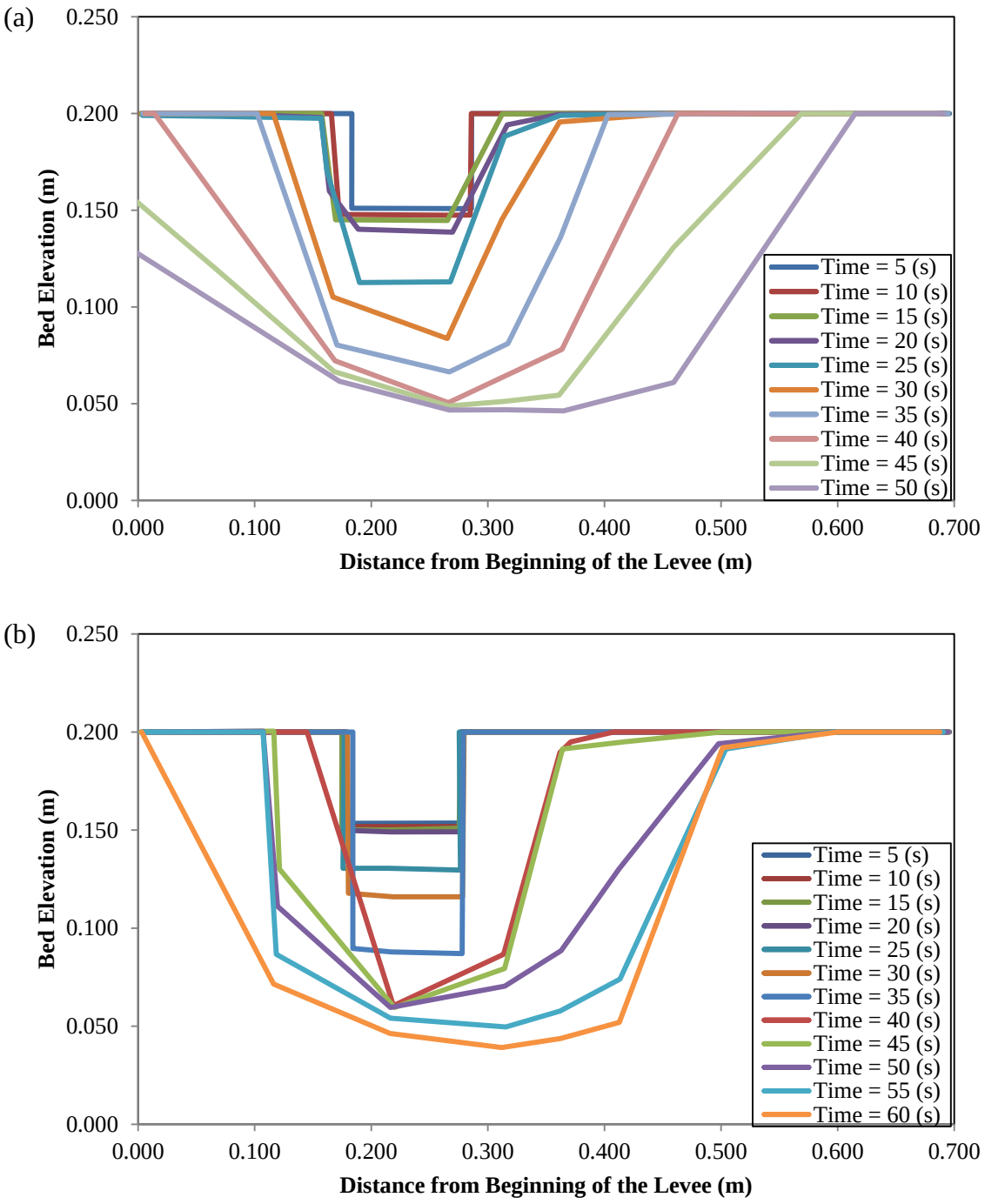

Figure 8.4 Breach profiles along the crest centerline at various times for: (a) $N_b = 0$; (b) $N_b = 2$; (c) $N_b = 4$; and (d) $N_b = 10$

(c)

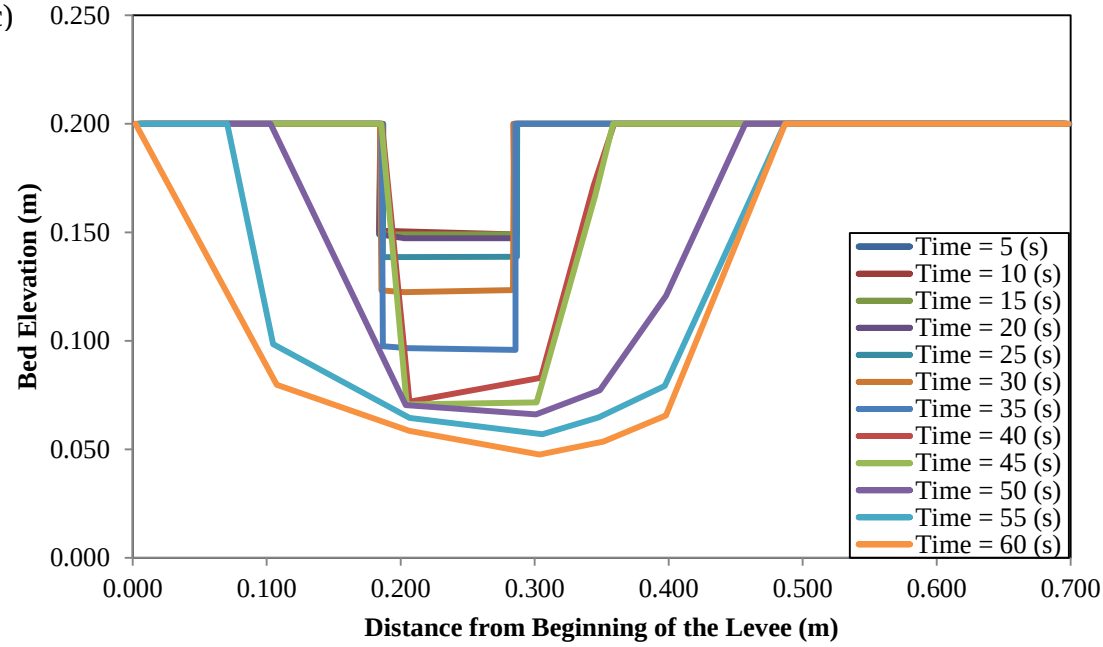

(d

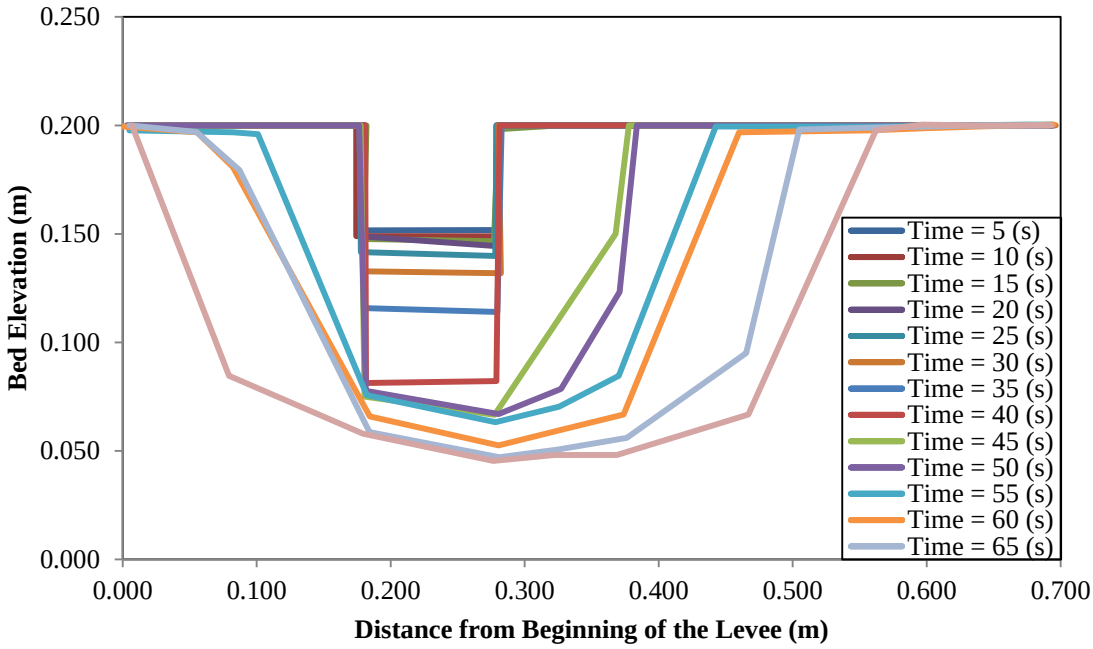

Figure 8.4 (Continued) Breach profiles along the crest centerline at various times for: (a) $N_b = 0$; (b) $N_b = 2$; (c) $N_b = 4$; and (d) $N_b = 10$

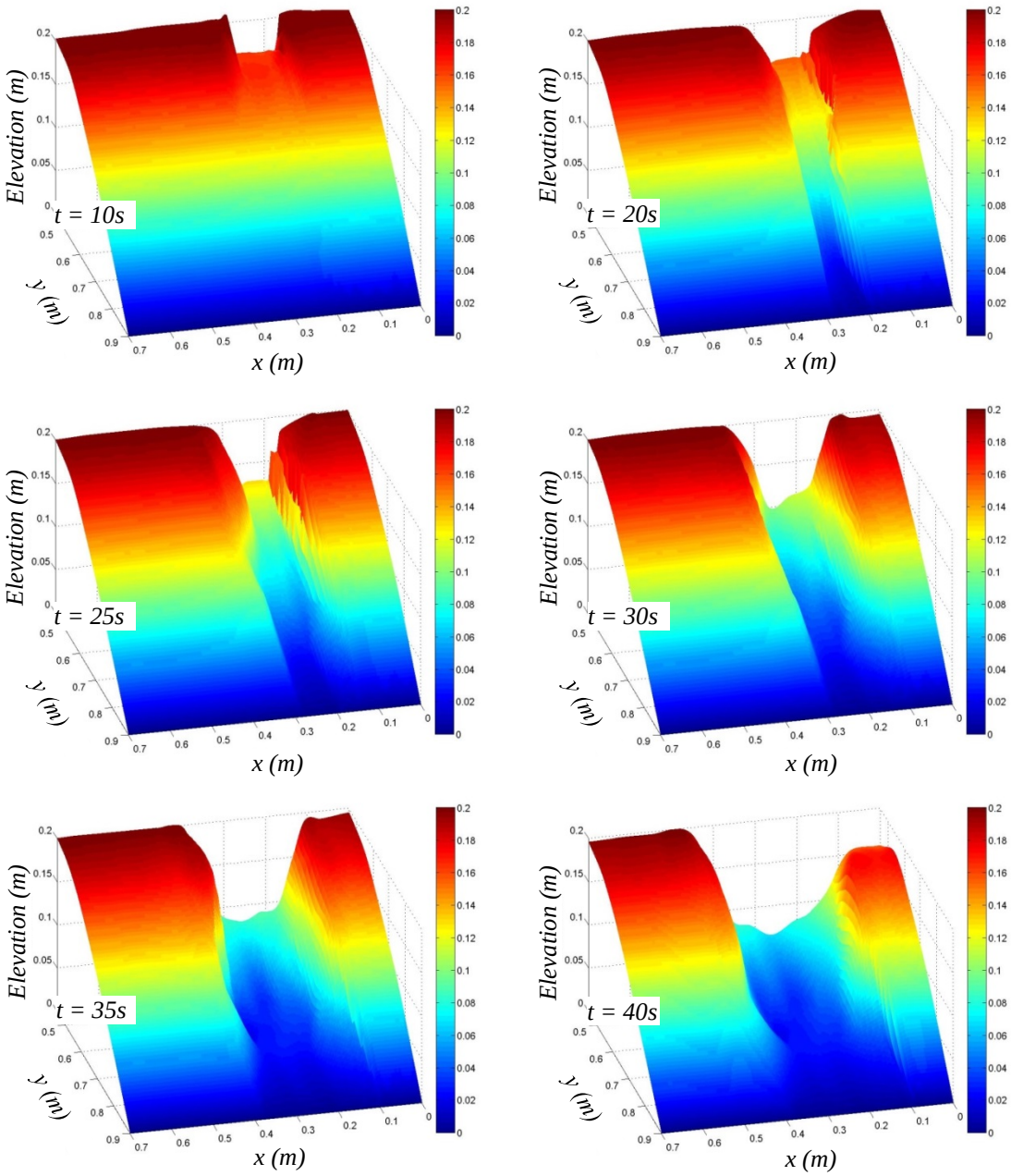

Figure 8.5 Breach evolution for test with N_B = 0 at t = 10, 20, 25, 30, 35, and 40 s

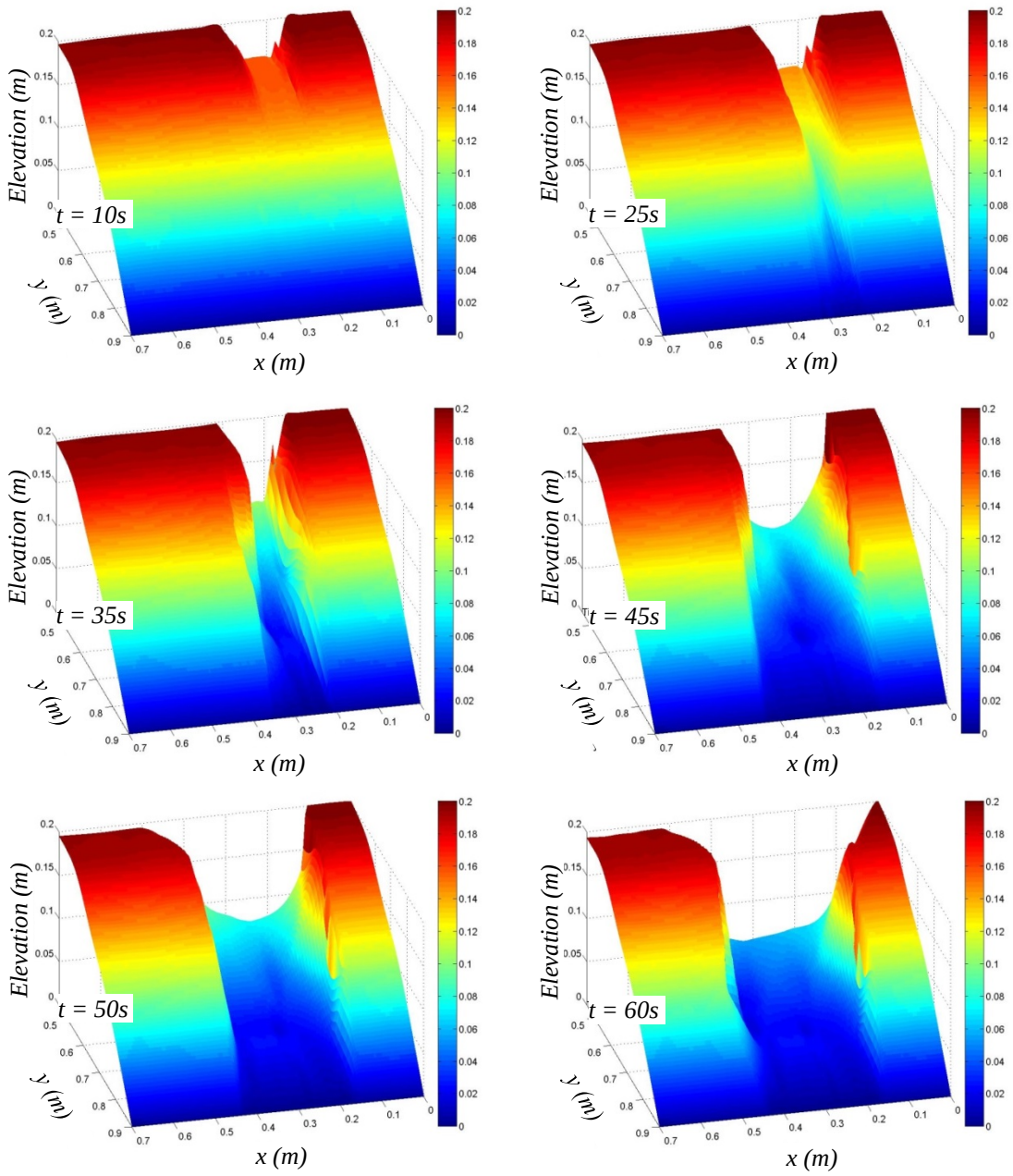

Figure 8.6 Breach evolution for test with N_B = 2 at t = 10, 25, 35, 45, 50, and 60 s

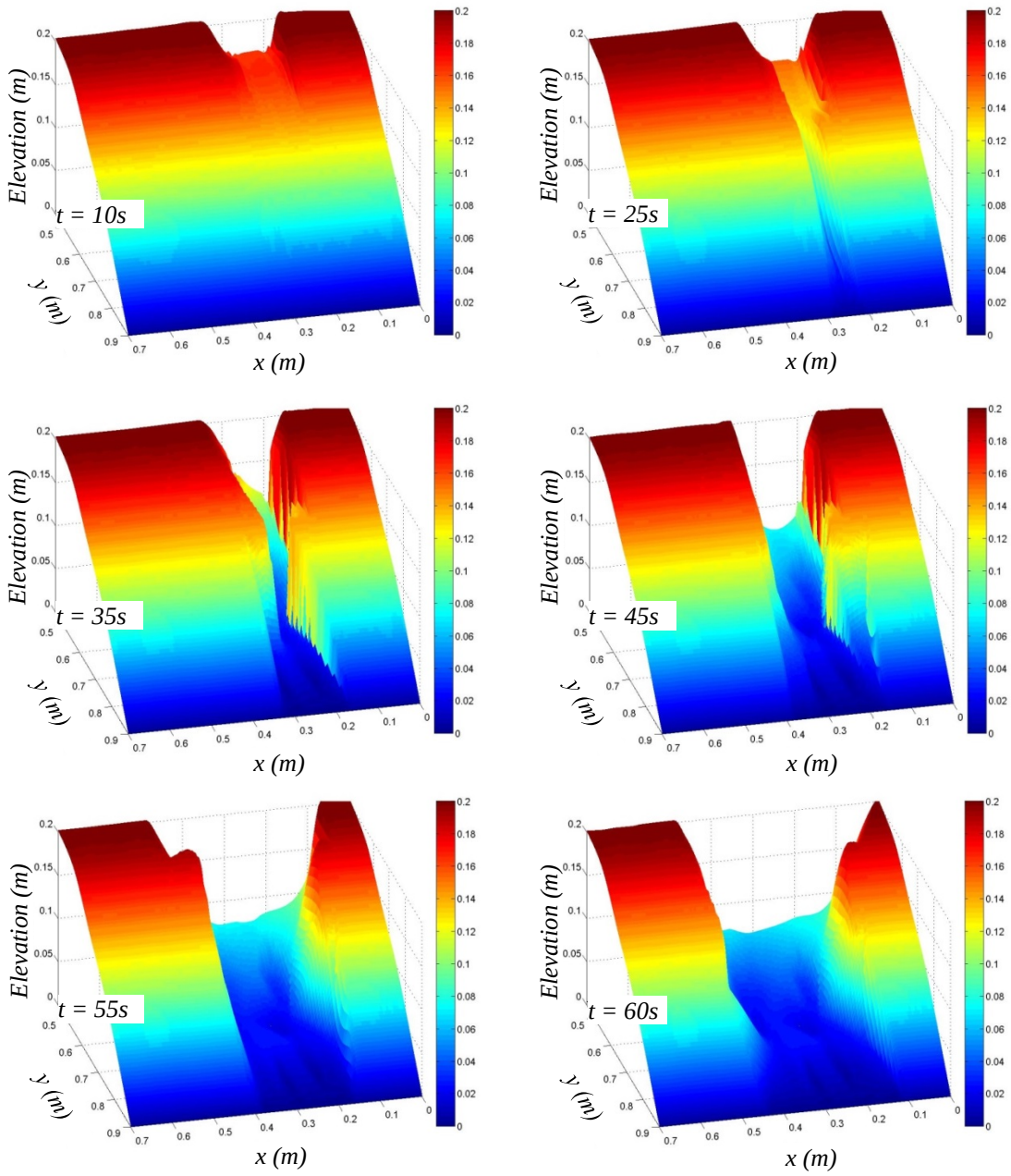

Figure 8.7 Breach evolution for test with N_B = 4 at t = 10, 25, 35, 45, 55, and 60 s

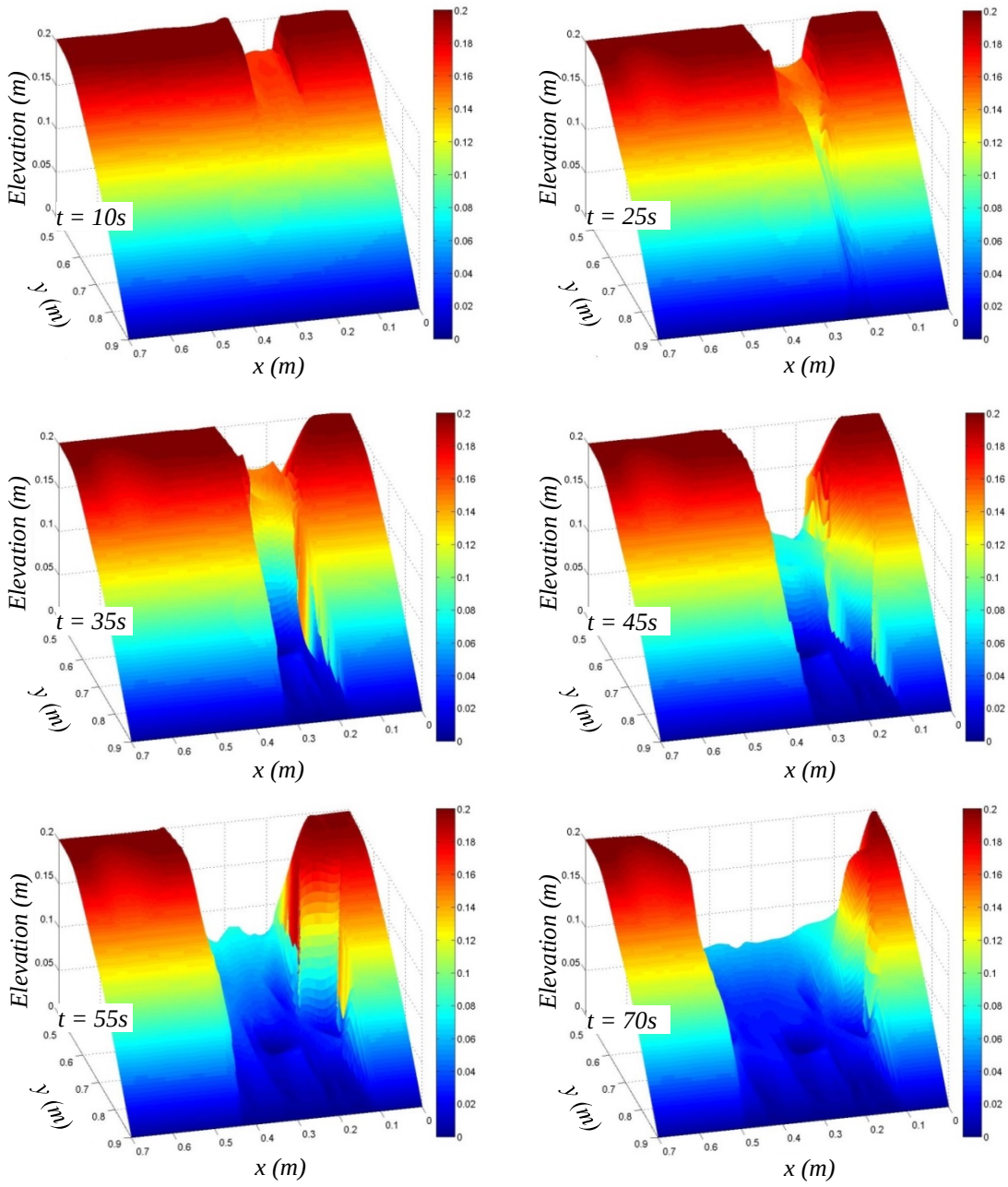

Figure 8.8 Breach evolution for test with N_B = 10 at t = 10, 25, 35, 45, 55, and 70 s

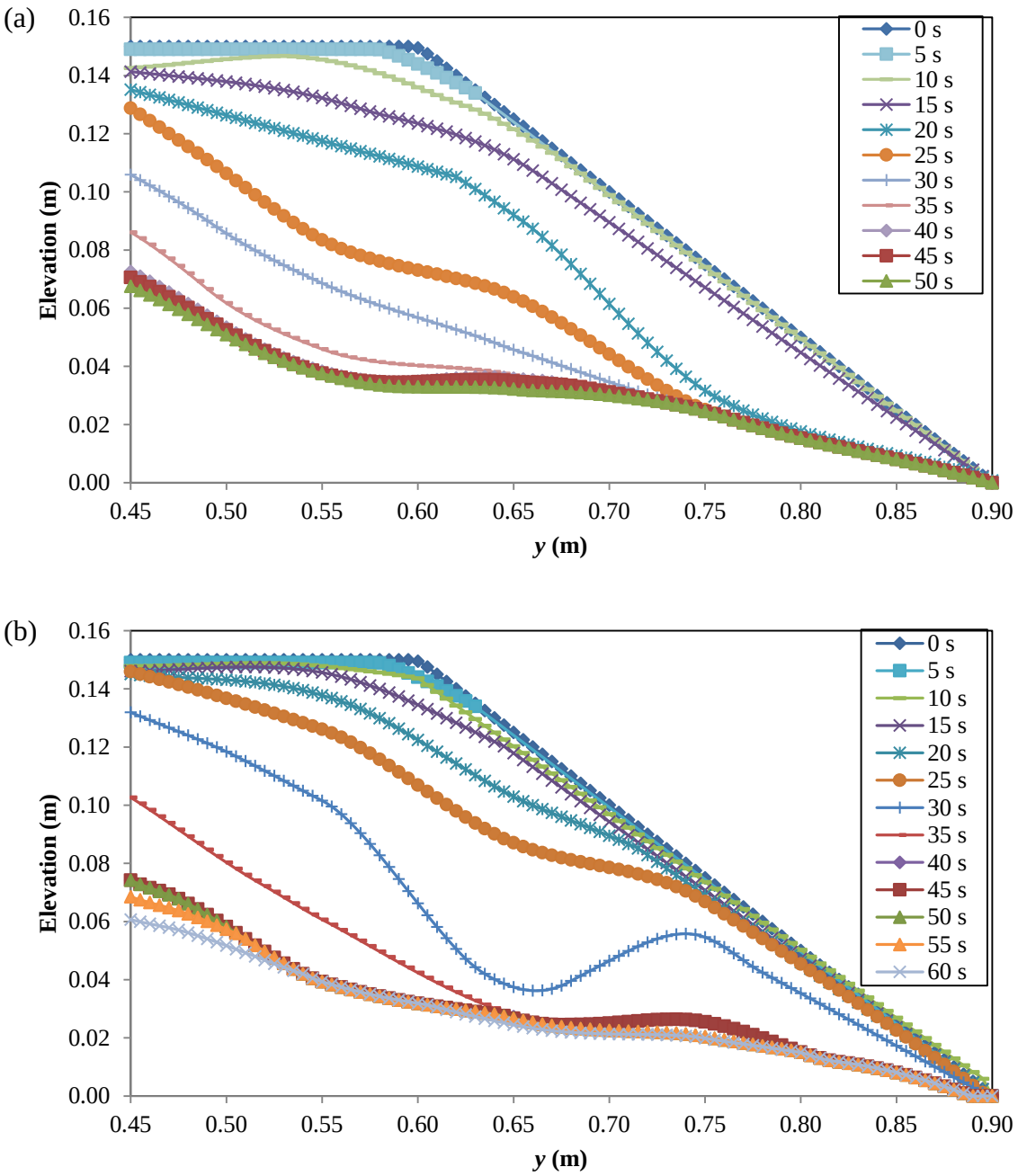

Figure 8.9 Time series of longitudinal bed profiles along the centerline of the pilot channel for: (a) $N_b = 0$; (b) $N_b = 2$; (c) $N_b = 4$; and (d) $N_b = 10$

(c)

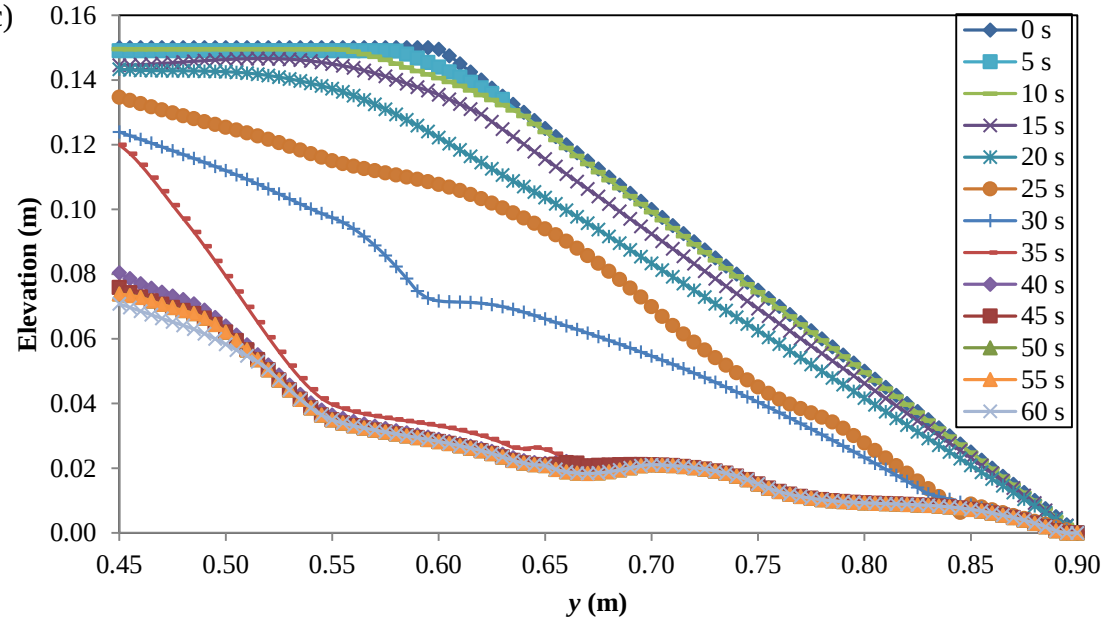

(d)

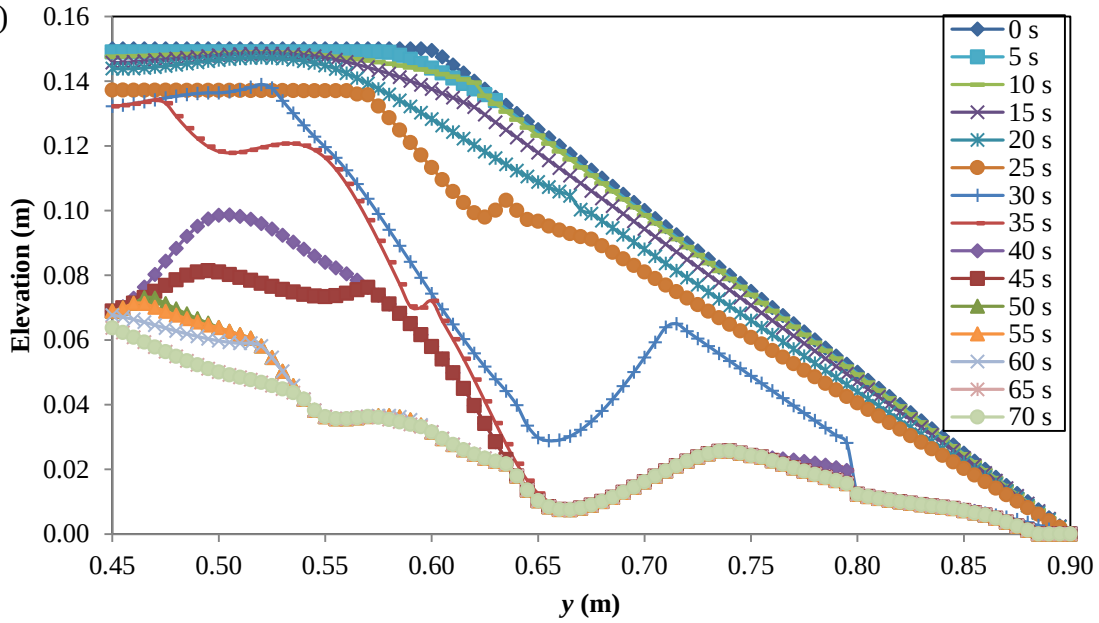

Figure 8.9 (Continued) Time series of longitudinal bed profiles along the centerline of the pilot channel for: (a) $N_b = 0$; (b) $N_b = 2$; (c) $N_b = 4$; and (d) $N_b = 10$

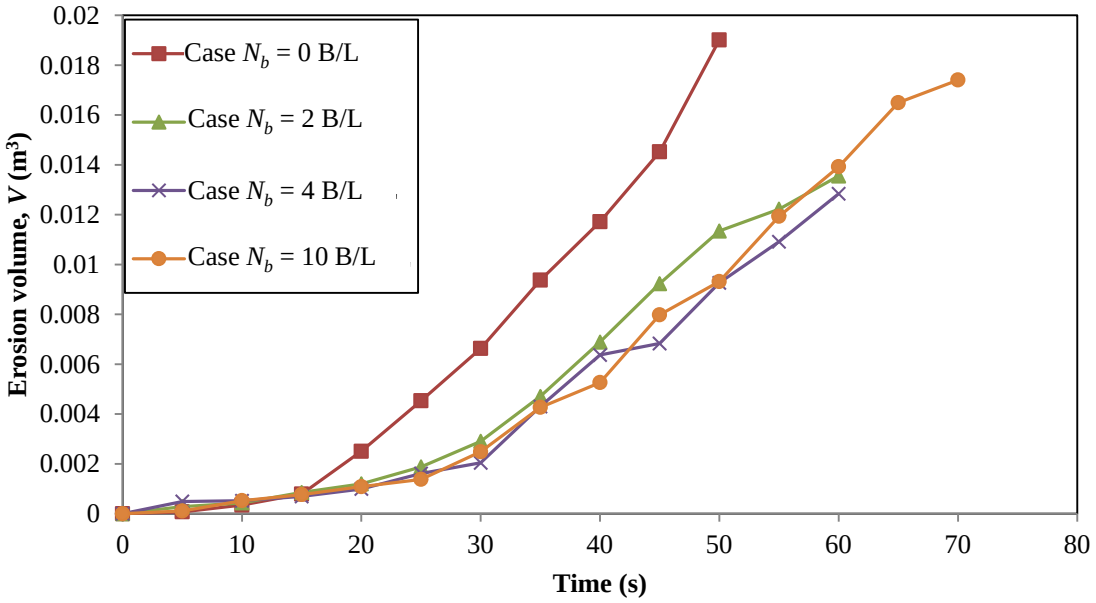

Figure 8.10 Cumulative breach eroded volume with time for four levels of compaction

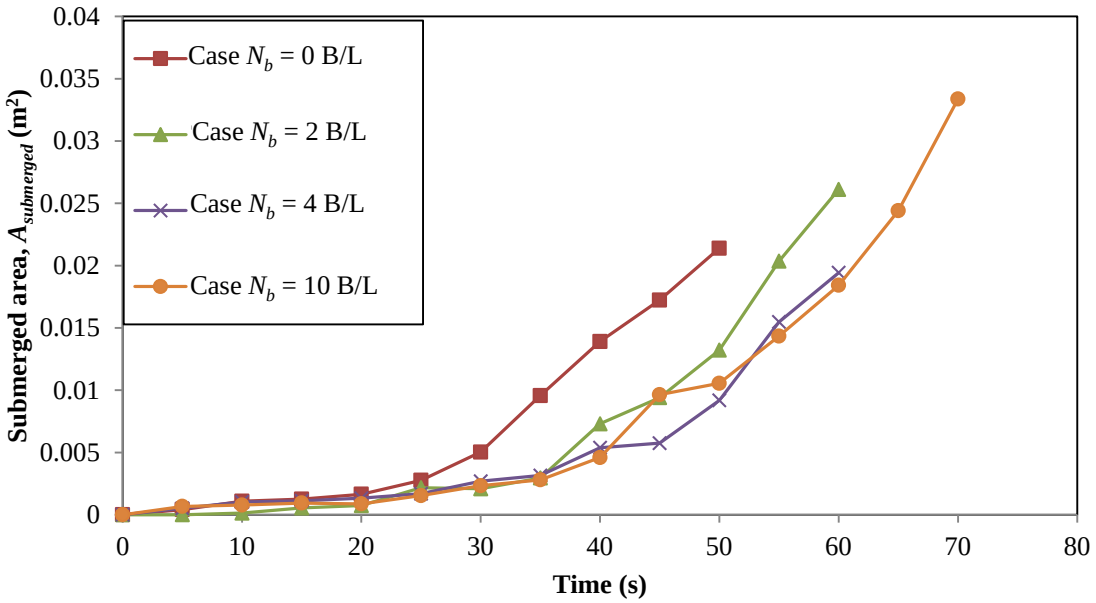

Figure 8.11 Time series of the submerged area along the centerline of the levee crest for four levels of compaction

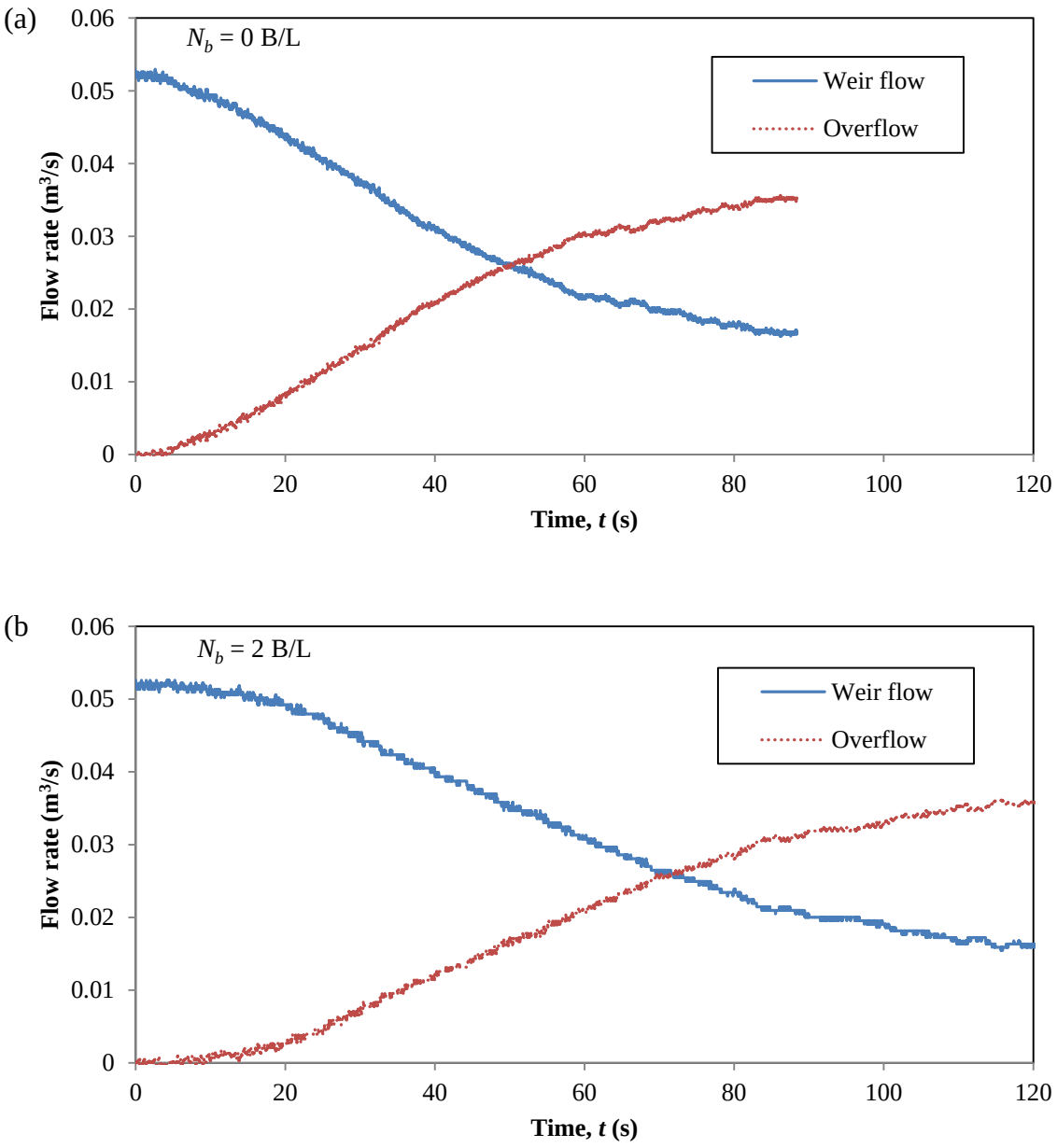

Figure 8.12 Weir flow and breach overflow for four levels of compaction: (a) N_b = 0; (b) N_b = 2; (c) N_b = 4; and (d) N_b = 10

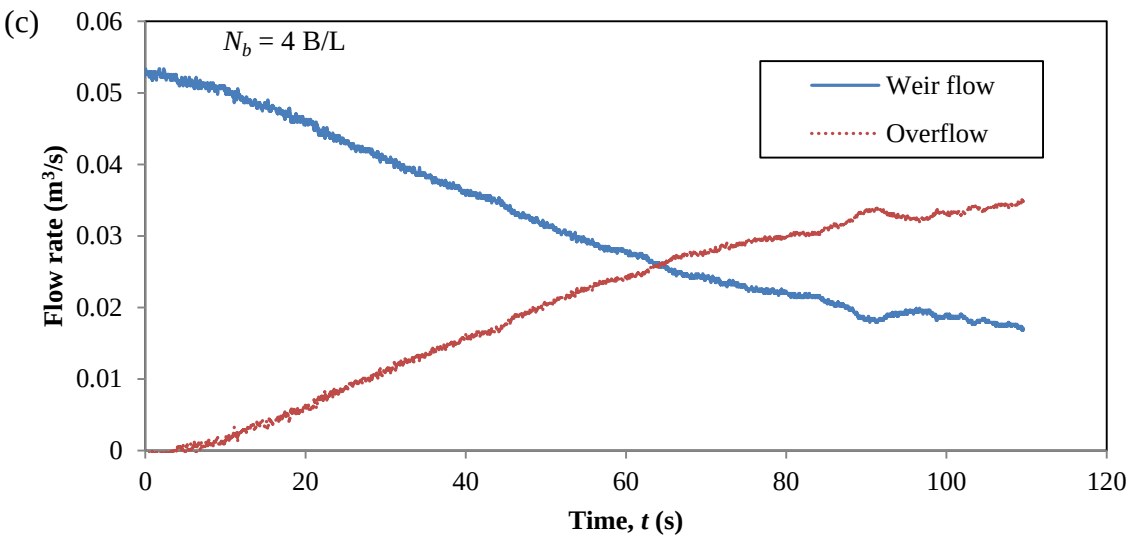

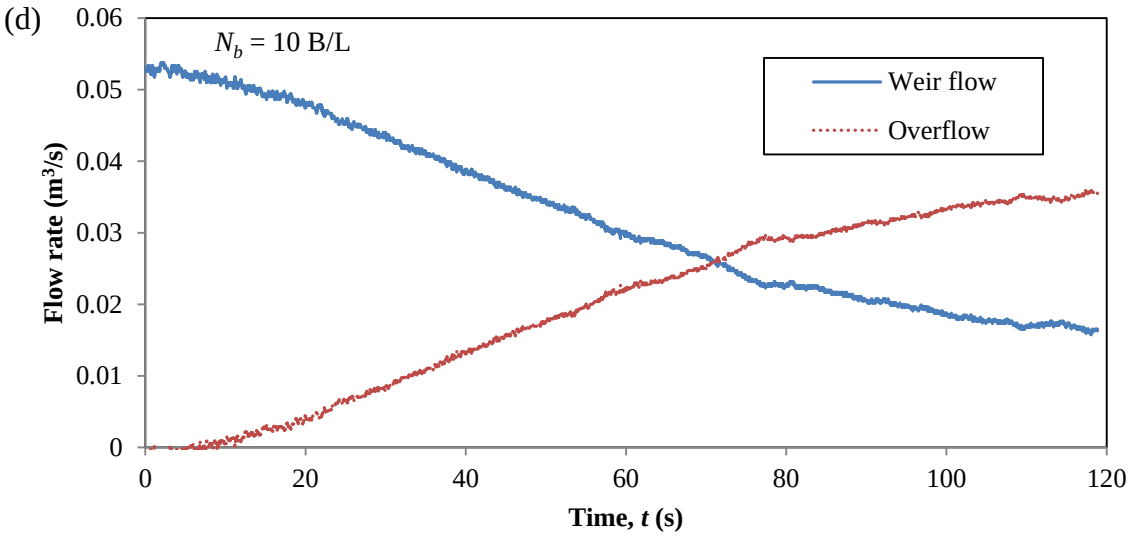

Figure 8.12 (Continued) Weir flow and breach overflow for four levels of compaction: (a) N_b = 0; (b) N_b = 2; (c) N_b = 4; and (d) N_b = 10

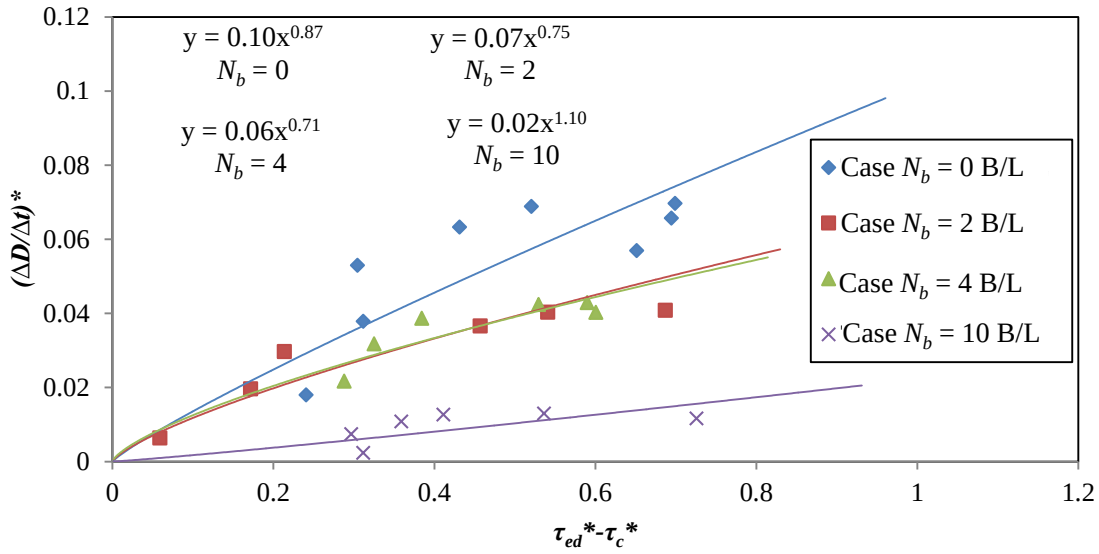

Figure 8.13 Correlation of the breach deepening rate along the crest centerline and the excess shear stress on the bed

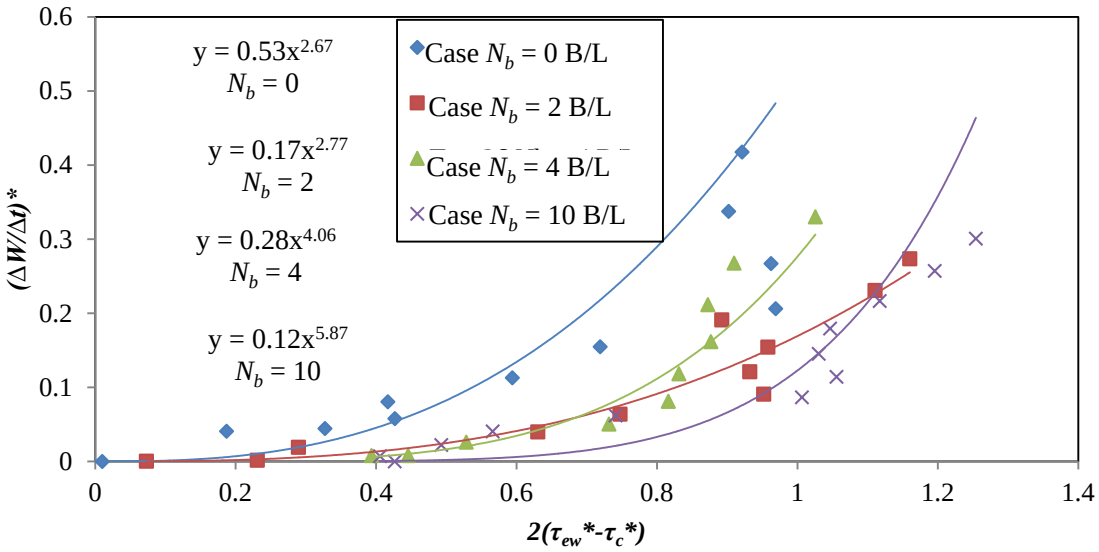

Figure 8.14 Correlation of the breach widening rate along the crest centerline and the excess shear stress on the sidewalls

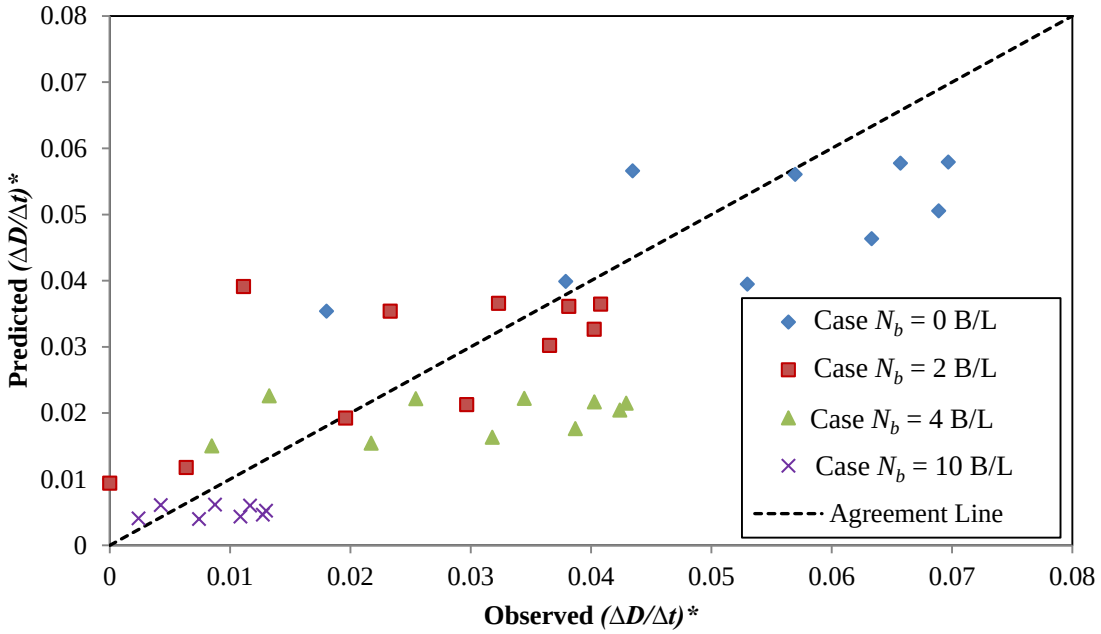

Figure 8.15 Comparisons of observed and predicted normalized deepening rate

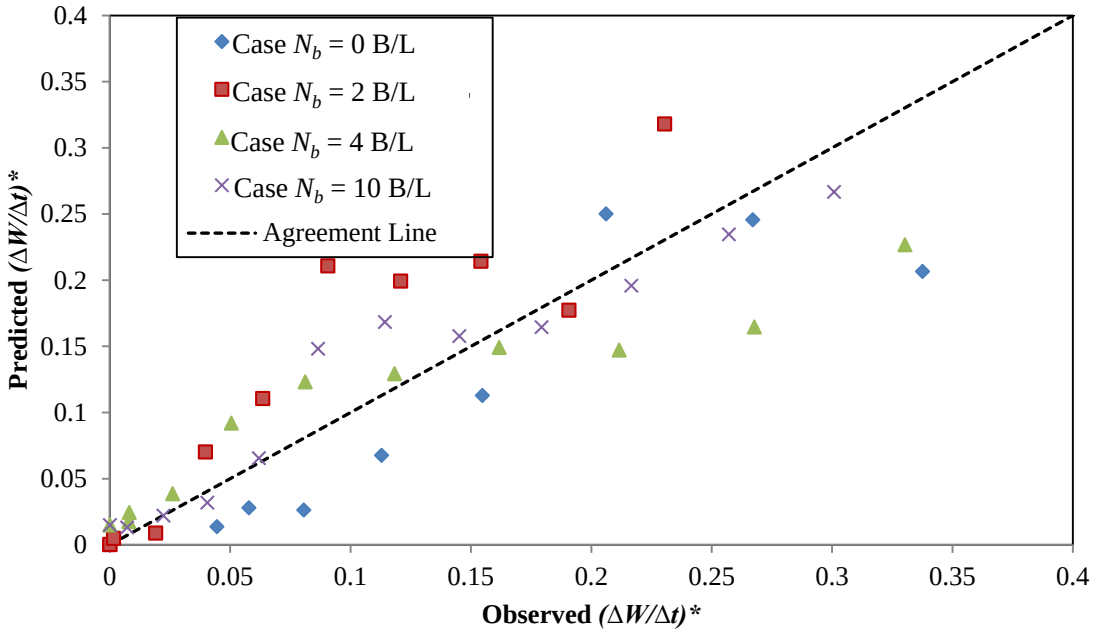

Figure 8.16 Comparisons of observed and predicted normalized widening rate

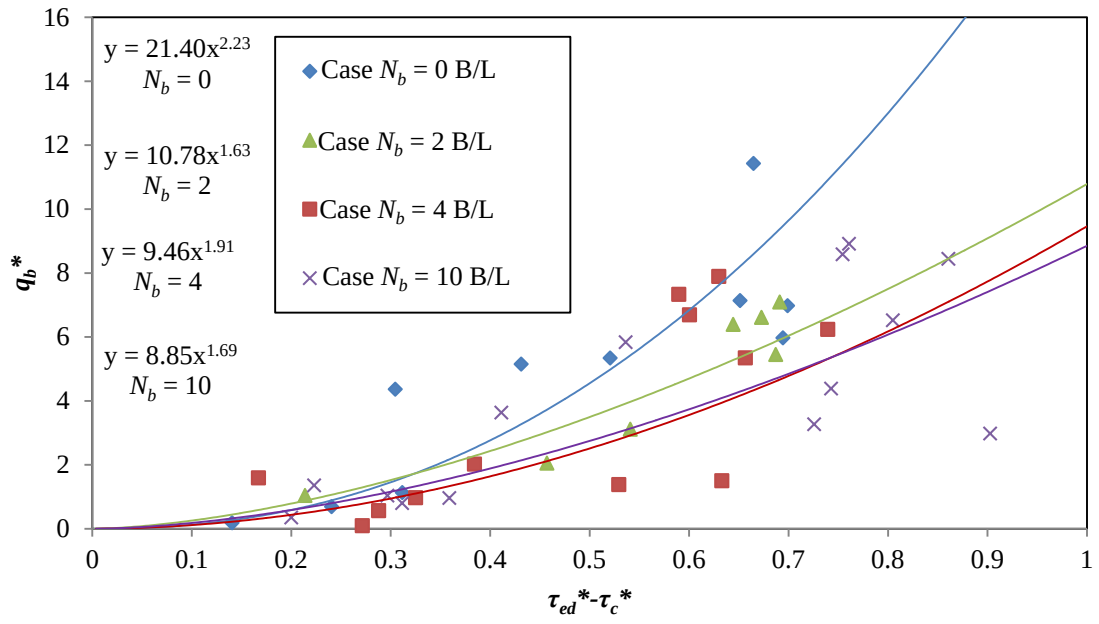

Figure 8.17 Normalized eroded load versus the excess Shields number for different tests

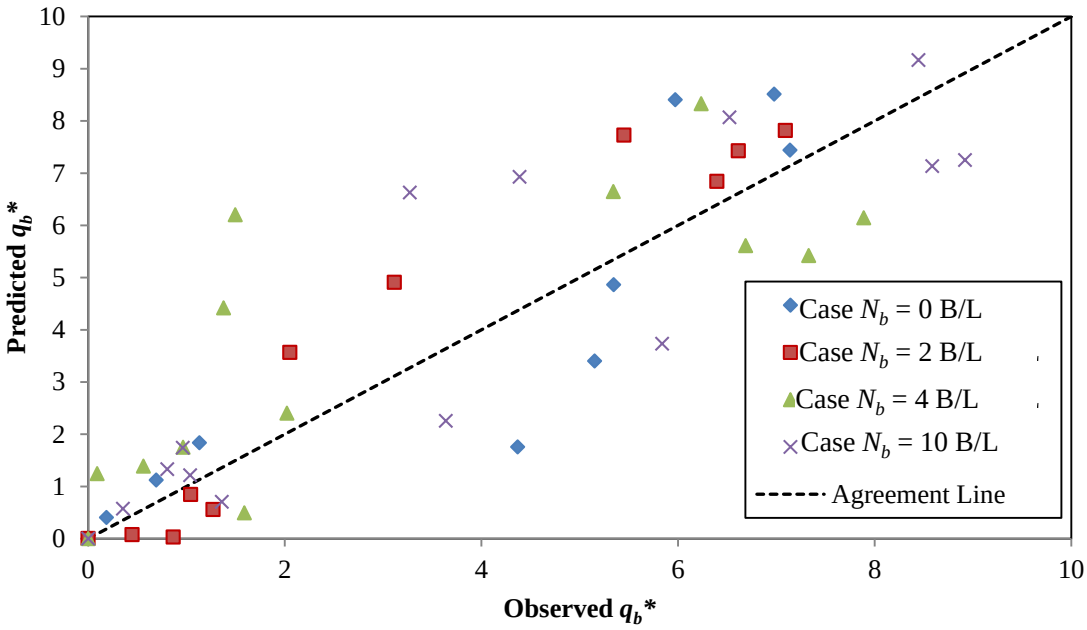

Figure 8.18 Comparisons of observed and predicted normalized eroded volume

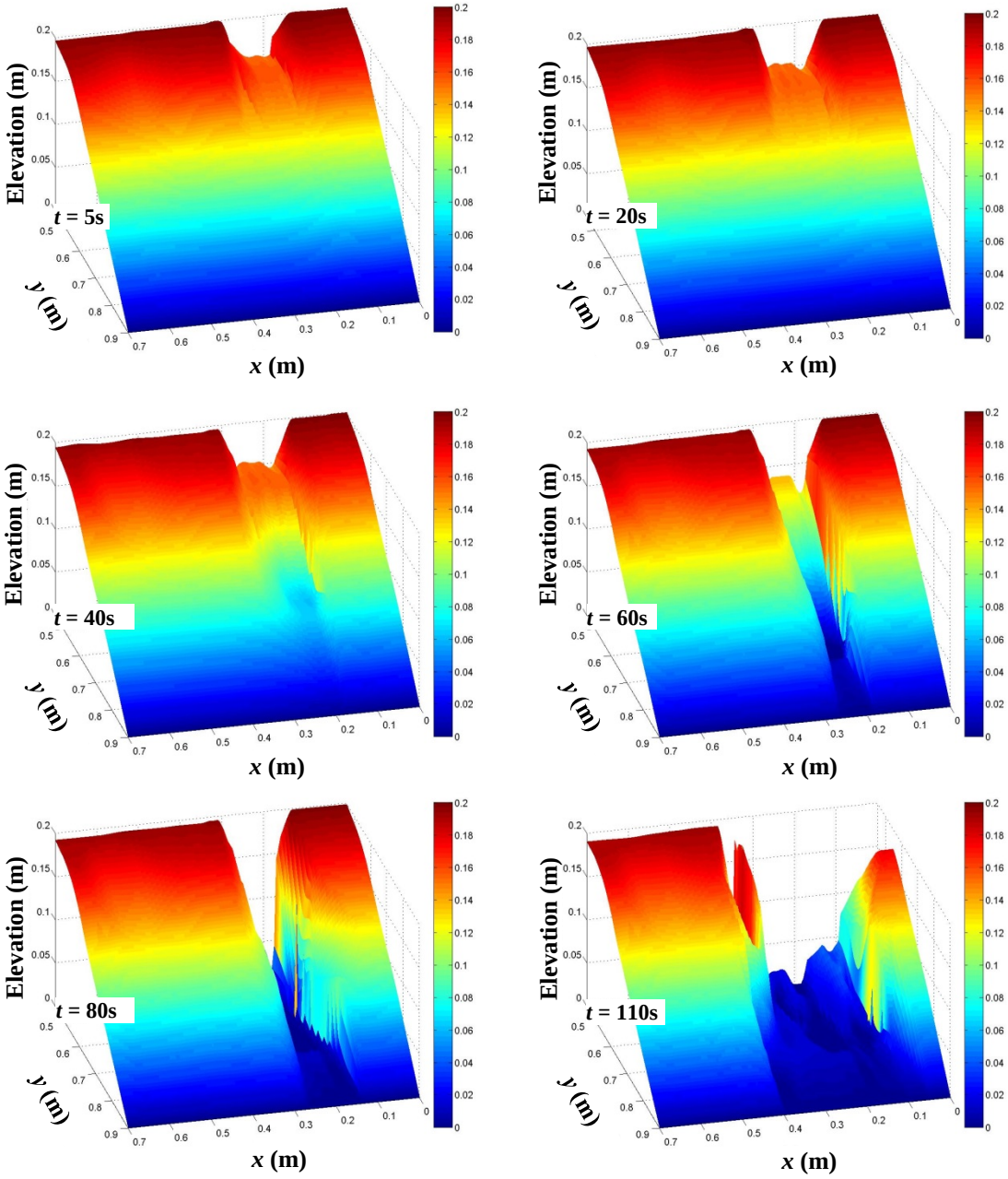

Figure 8.19 Breach evolution for Test 5 at t = 5, 20, 40, 60, 80, and 110 s

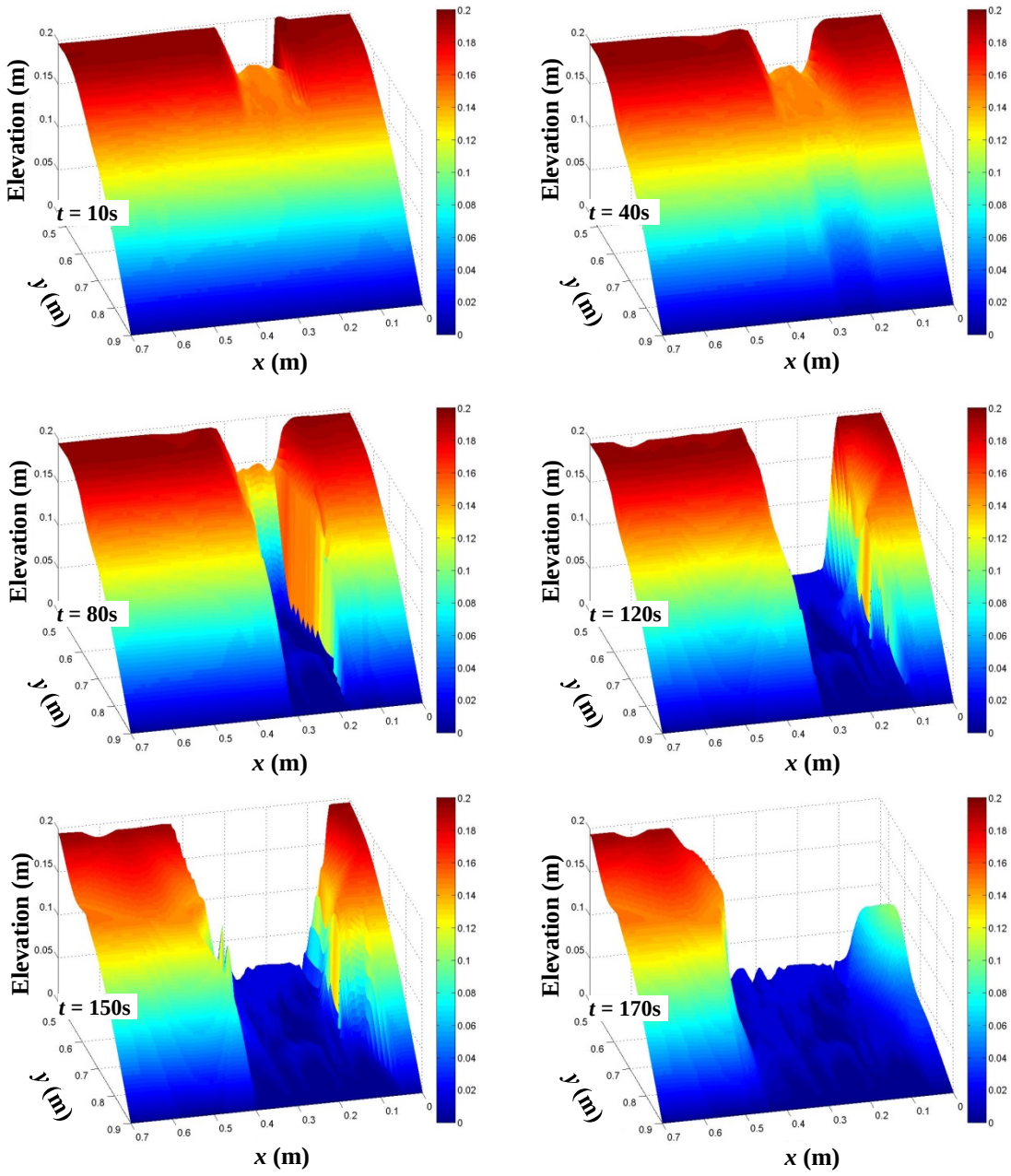

Figure 8.20 Breach evolution for Test 6 at t = 10, 40, 80, 120, 150, and 170 s

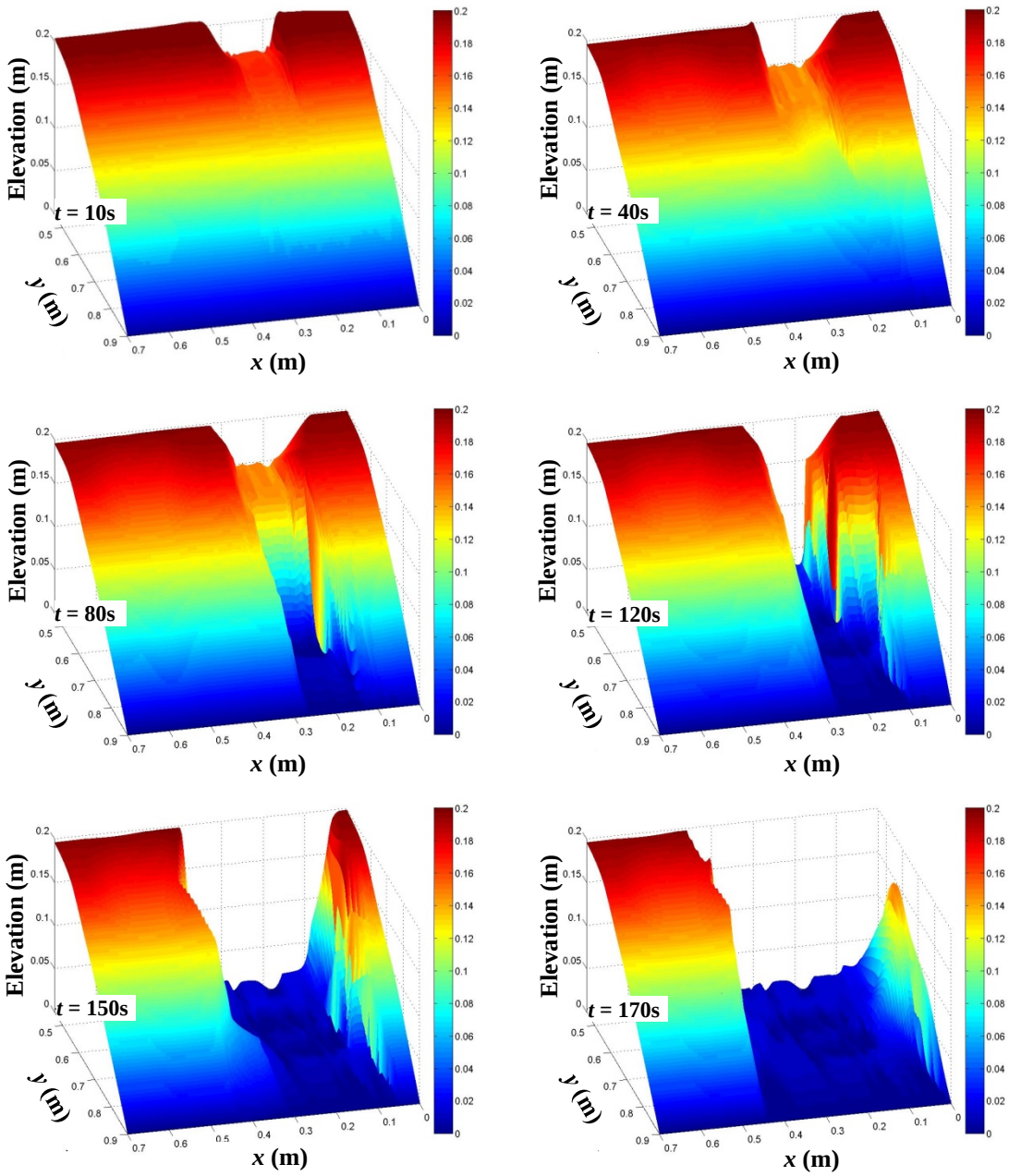

Figure 8.21 Breach evolution for Test 7 at t = 10, 40, 80, 120, 150, and 170 s

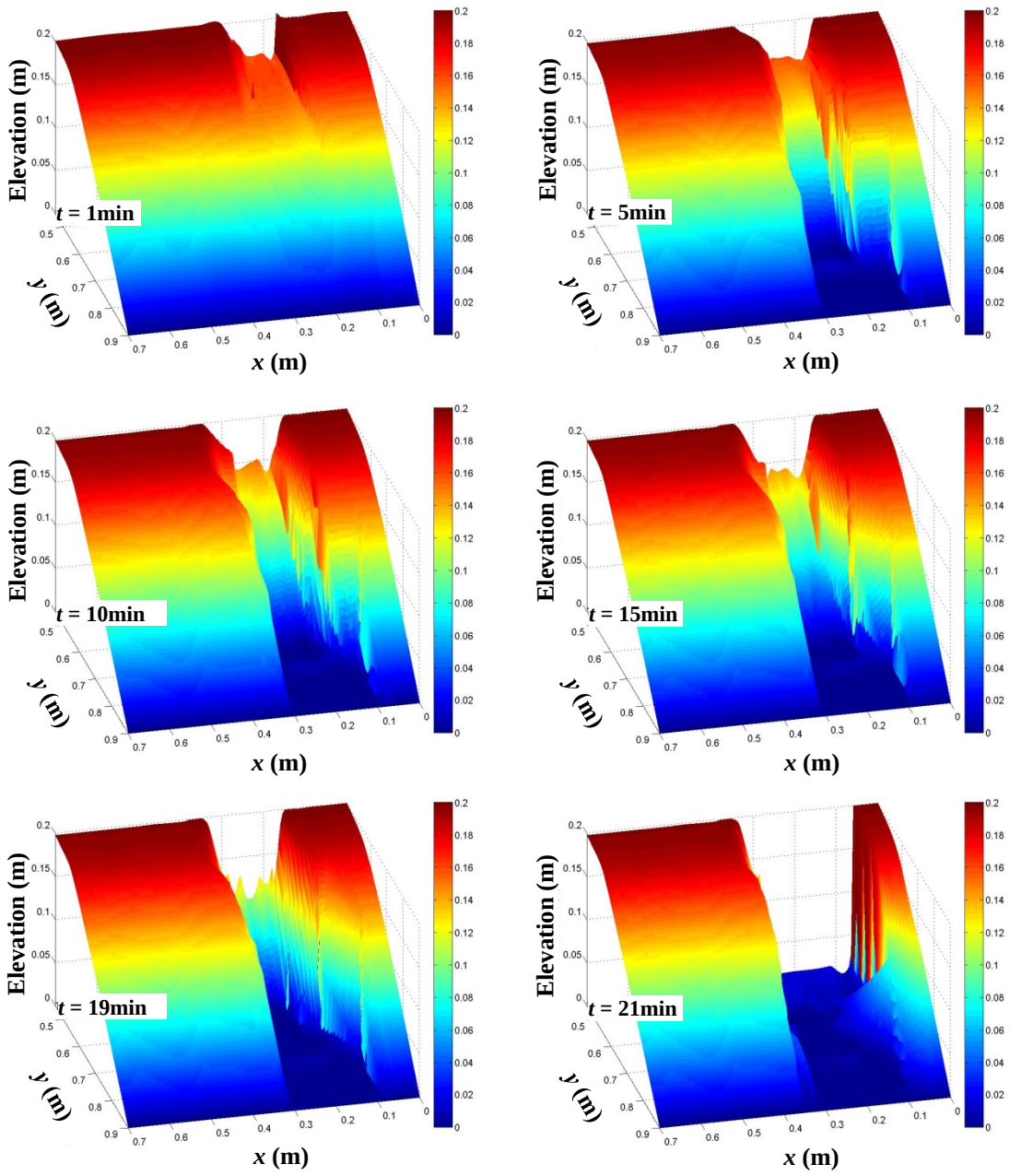

Figure 8.22 Breach evolution for Test 8 at t = 1, 5, 10, 15, 19, and 21 min

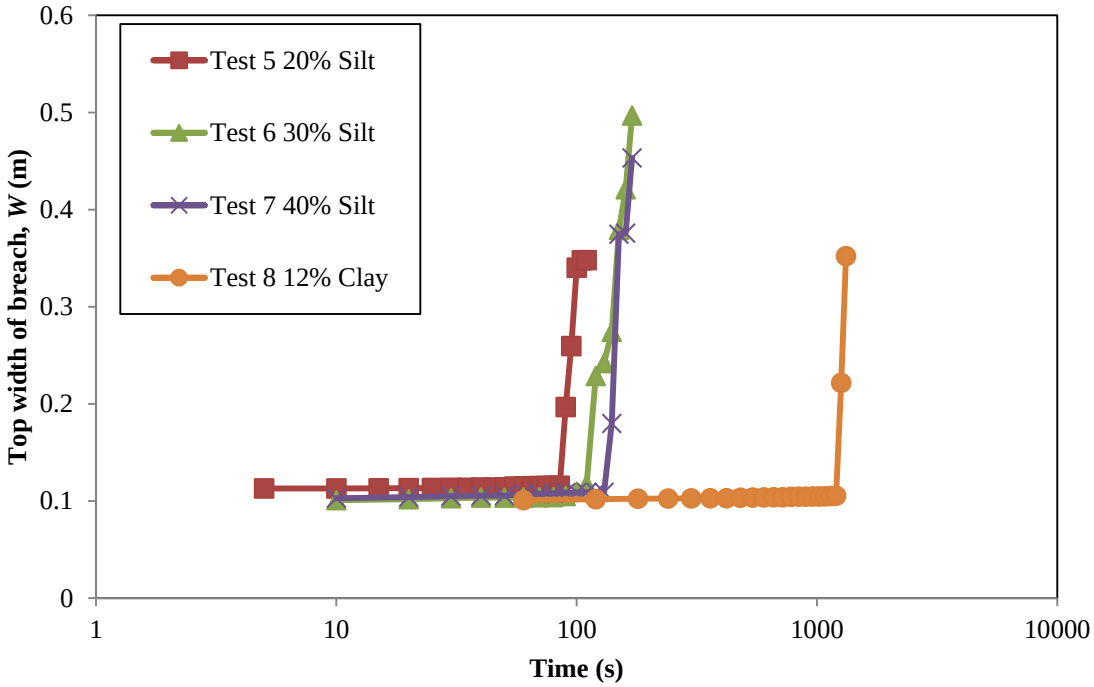

Figure 8.23 Time changes of breach top width for levees with different cohesion

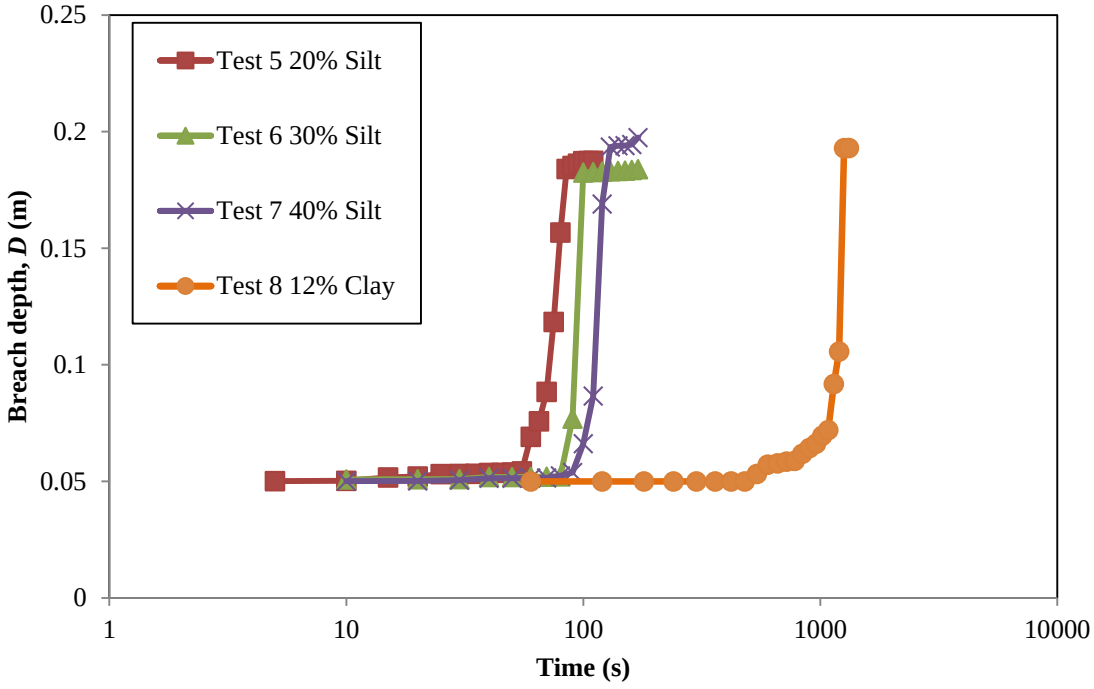

Figure 8.24 Time changes of breach depth for levees with different cohesion

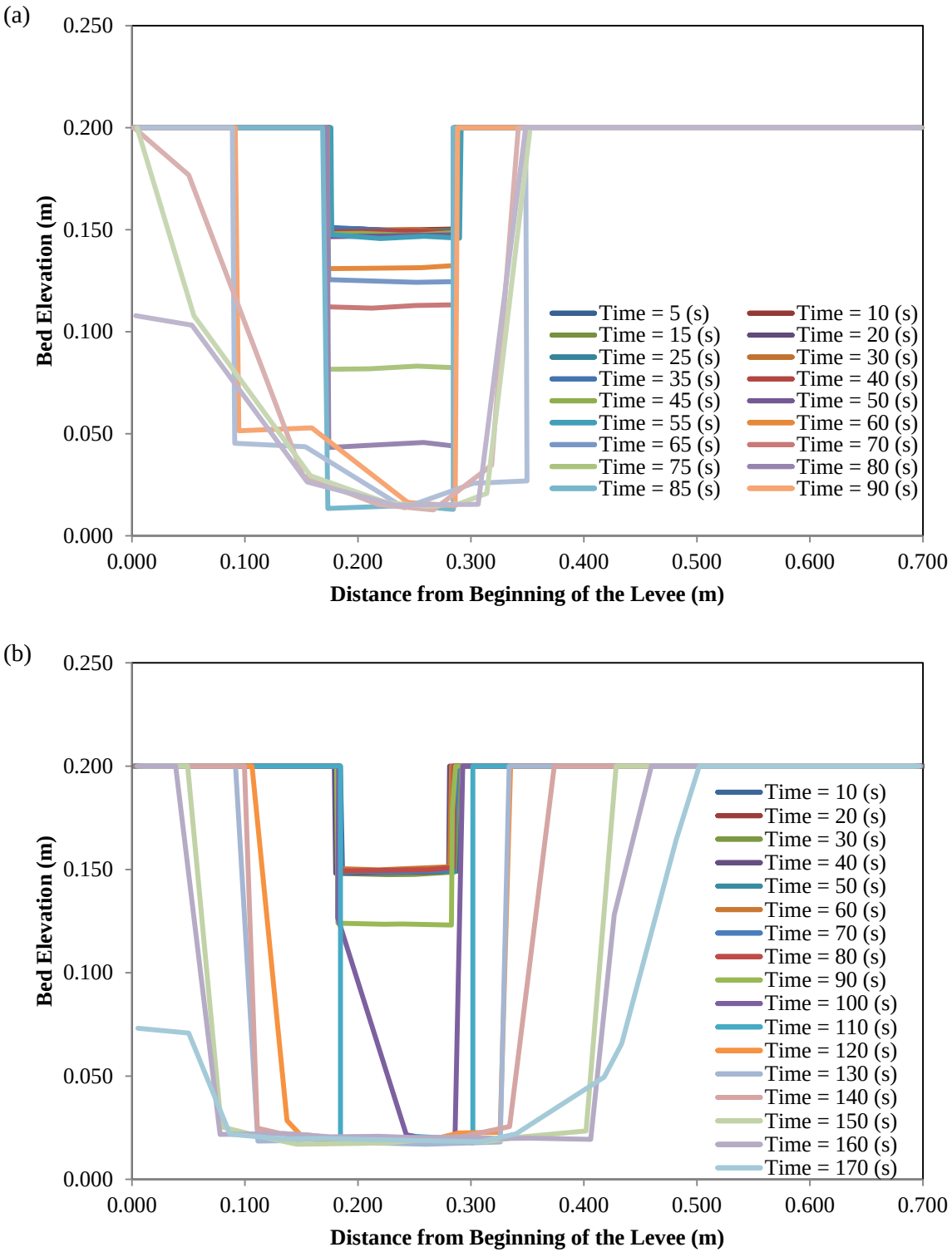

Figure 8.25 Breach profiles at different times for: (a) Test 5; (b) Test 6; (c) Test 7; and (d) Test 8

(c)

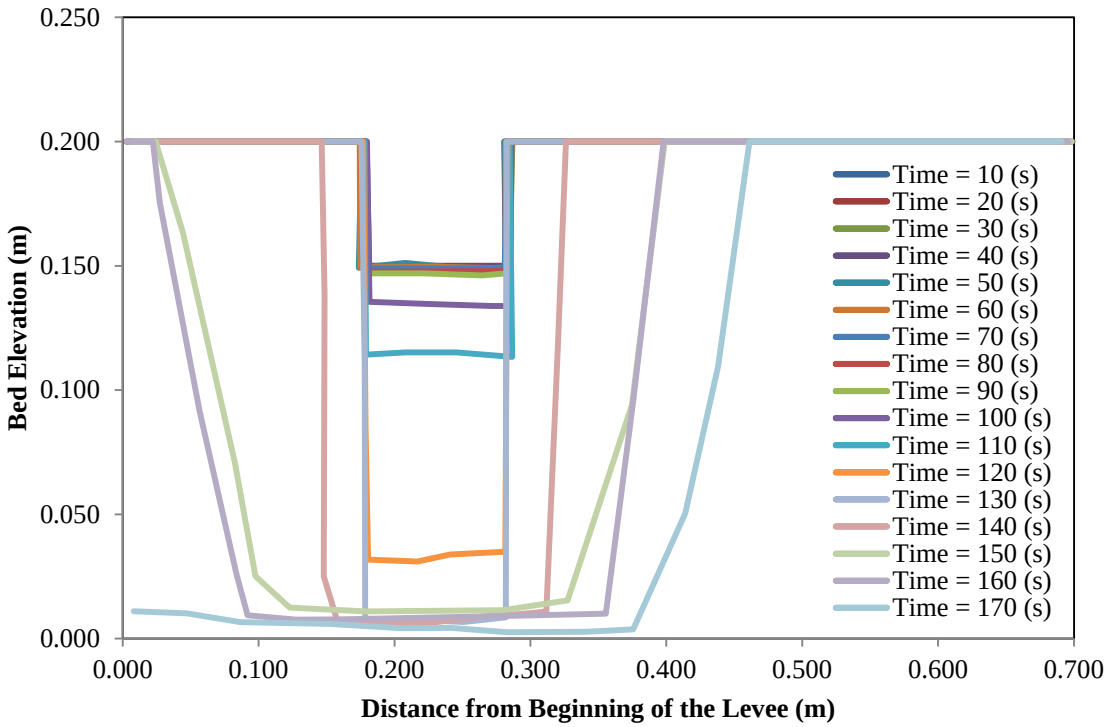

(d)

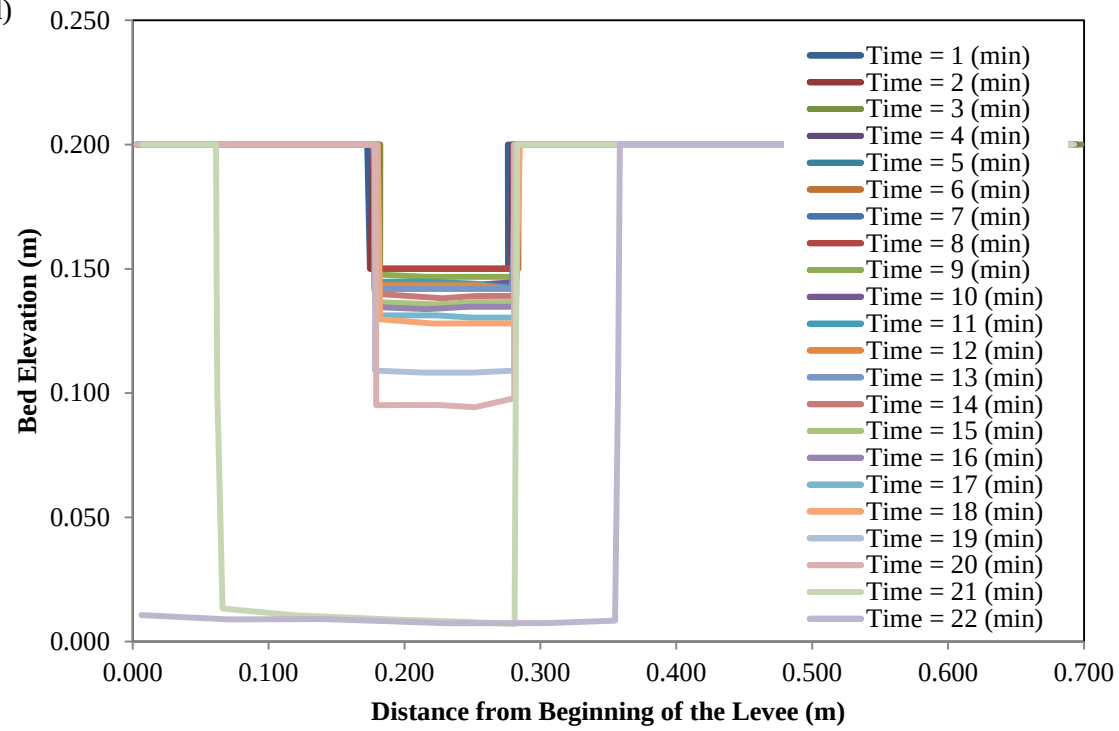

Figure 8.25 (continued) Breach profiles at different times for: (a) Test 5; (b) Test 6; (c) Test 7; and (d) Test 8

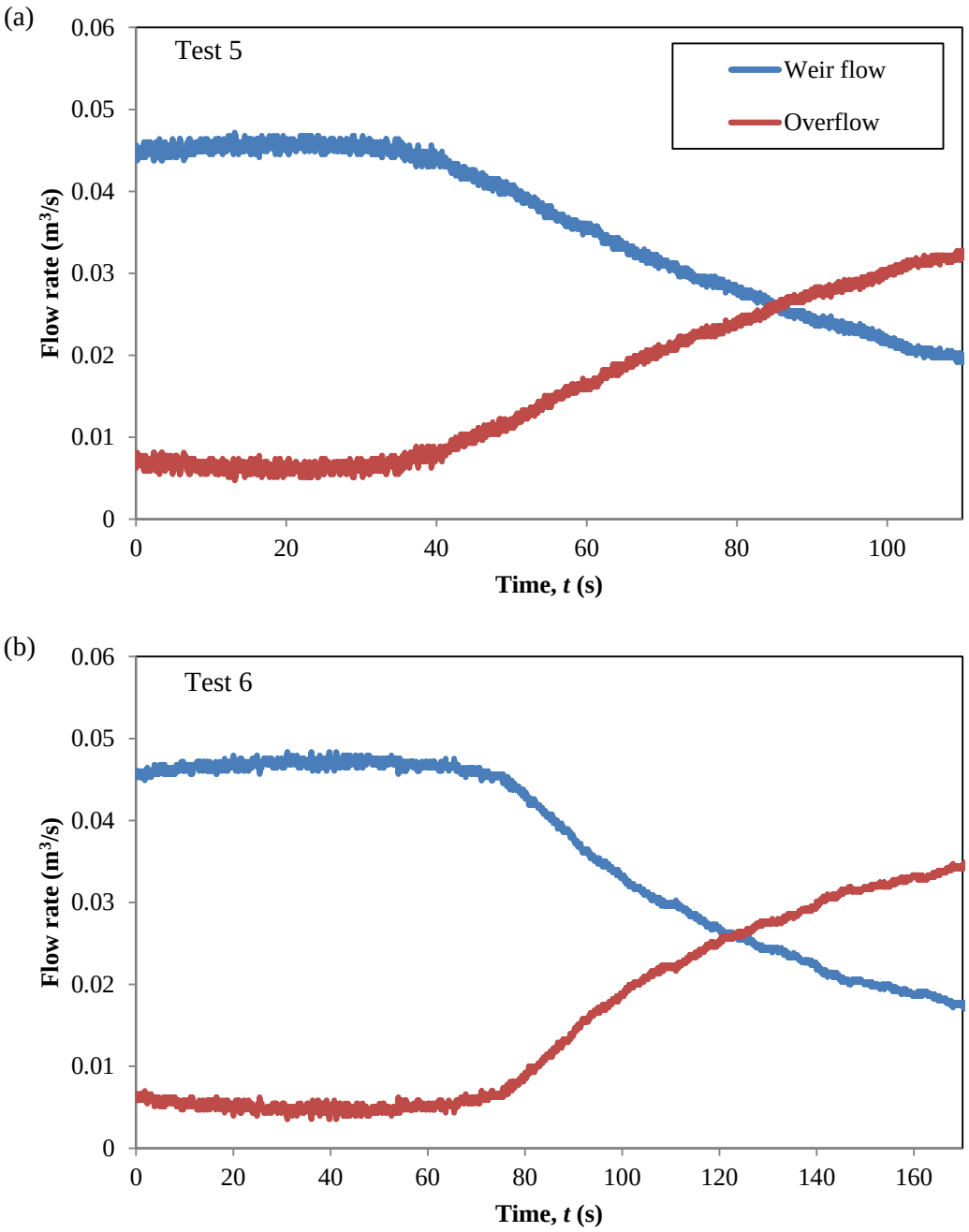

Figure 8.26 Weir flow and breach overflow for four levels of cohesion: (a) Test 5; (b) Test 6; (c) Test 7; and (d) Test 8

(c)

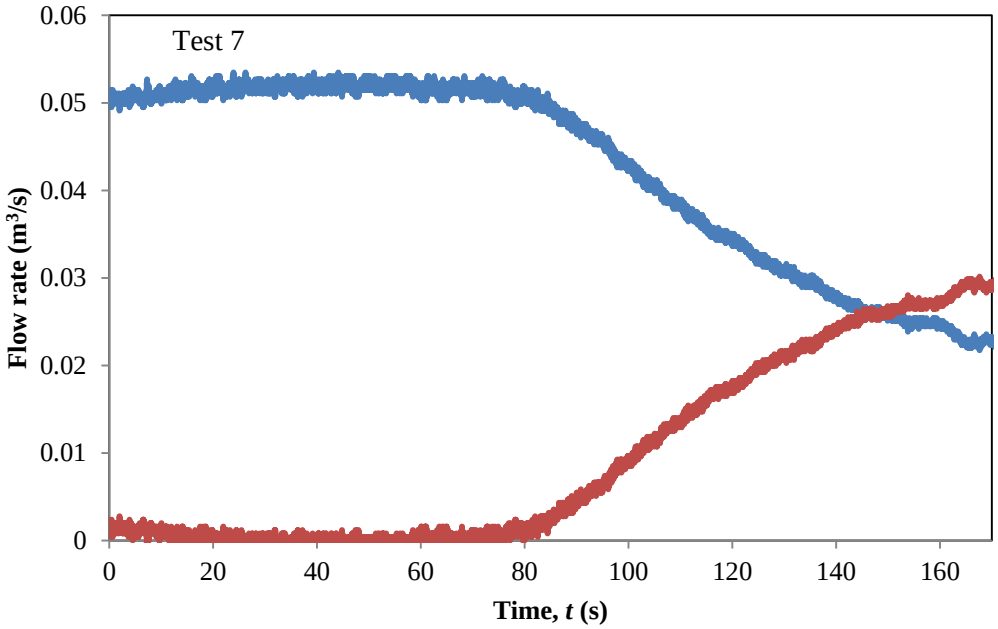

(d)

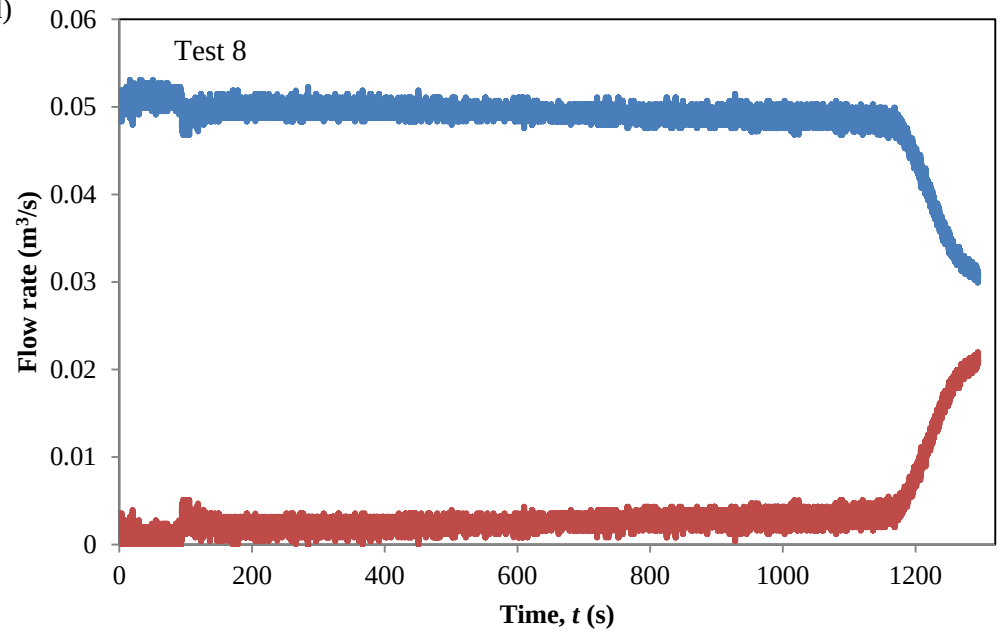

Figure 8.26 (continued) Weir flow and breach overflow for four levels of cohesion: (a) Test 5; (b) Test 6; (c) Test 7; and (d) Test 8

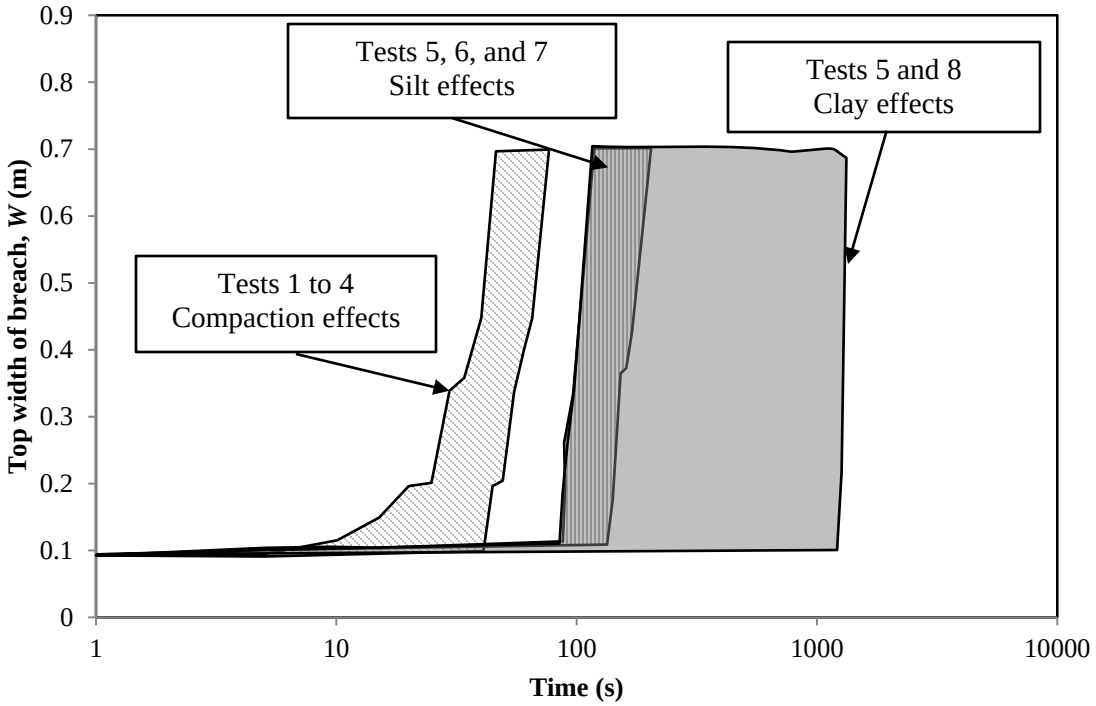

Figure 8.27 Envelope curves of breach top width for different levels of compaction and cohesion

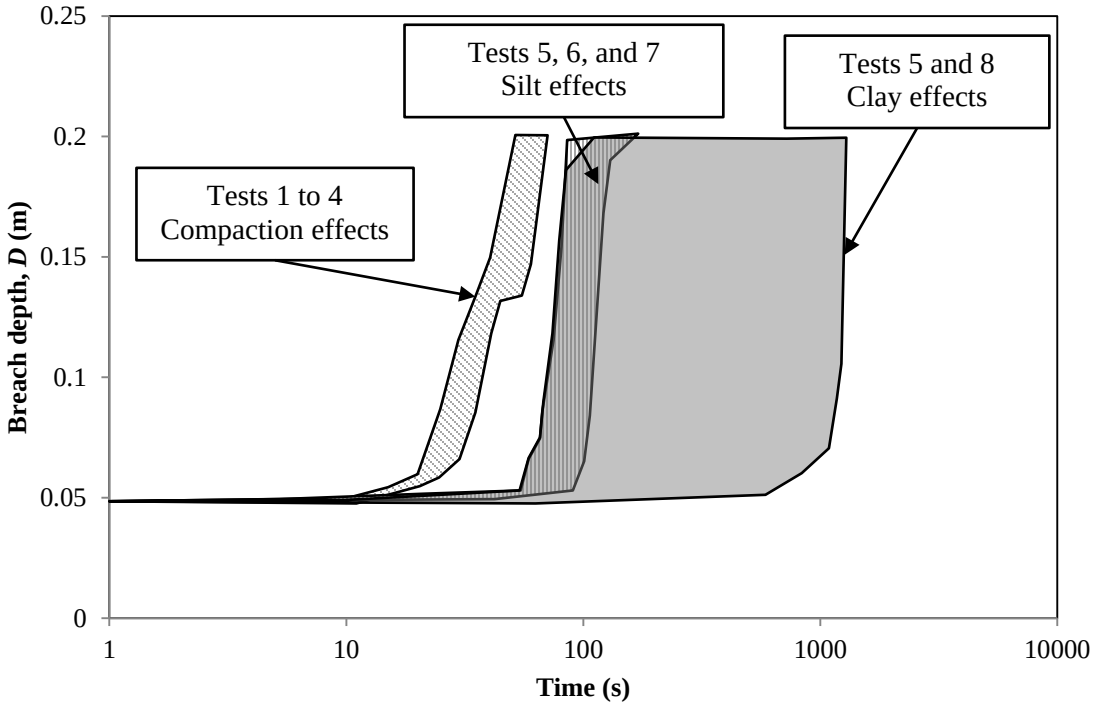

Figure 8.28 Envelope curves of breach depth for different levels of compaction and cohesion

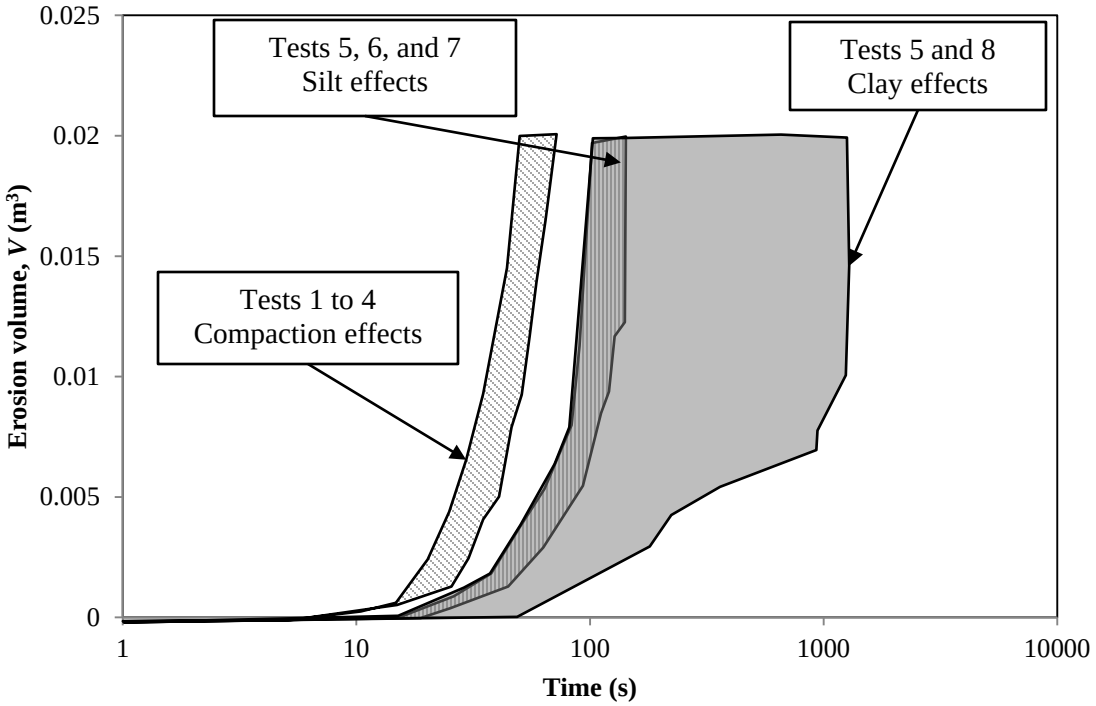

Figure 8.29 Envelope curves of breach eroded volume for different levels of compaction and cohesion

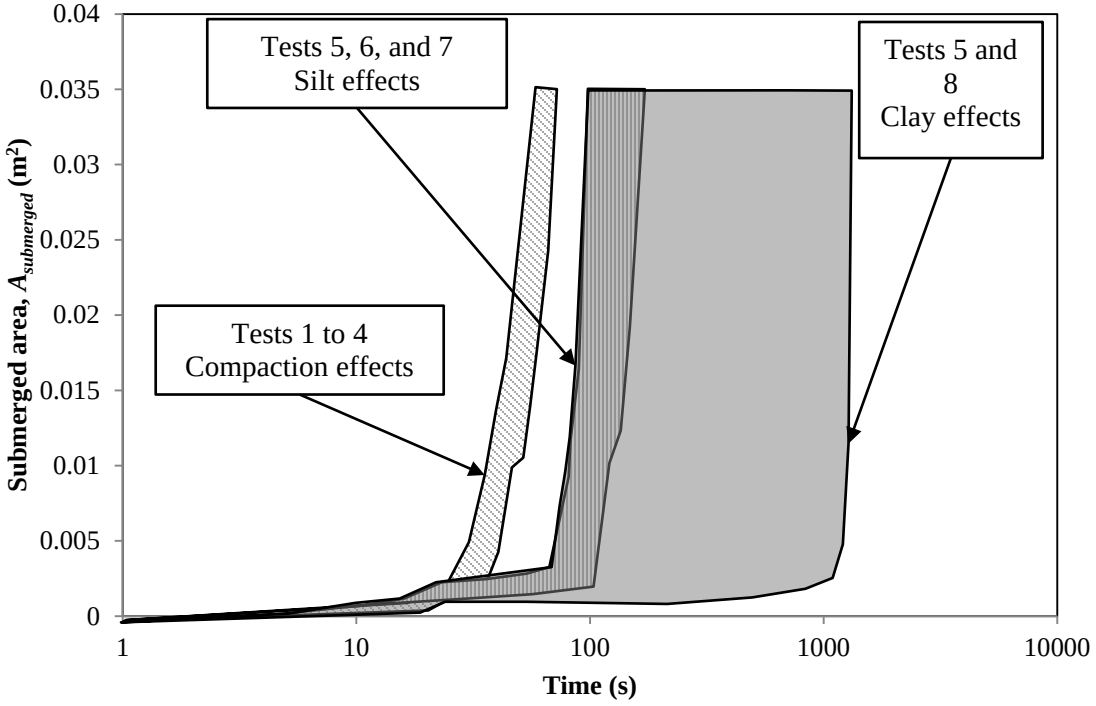

Figure 8.30 Envelope curves of breach submerged area for different levels of compaction and cohesion

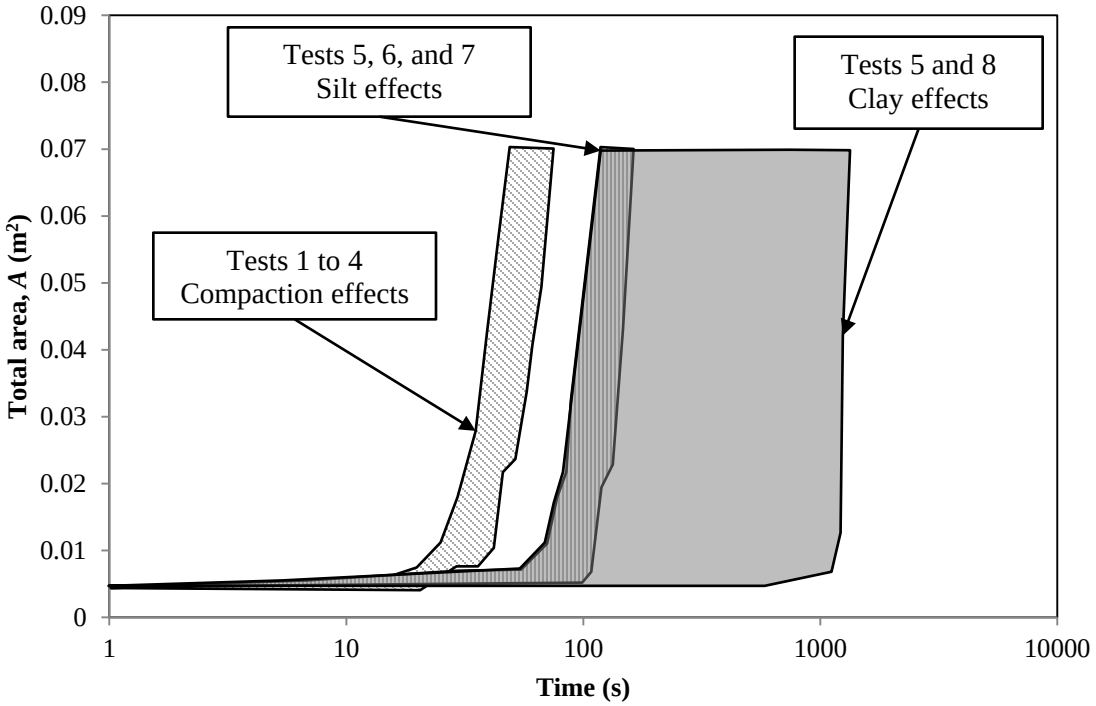

Figure 8.31 Envelope curves of breach total area for different levels of compaction and cohesion

CHAPTER 9

SUMMARY AND CONCLUSIONS

9.1 Experimental Study on Embankment Breach due to Overtopping: Effects of Compaction

A series of embankment overtopping tests were conducted to investigate the effect of compaction on the failure of a homogenous non-cohesive embankment. The temporal changes of the embankment surface profiles and the downstream hydrographs were measured for all cases. The soil used for building the embankment was sand, and four levels of compaction were applied. The repeatability of the tests was confirmed and different stages of failure are described in detail. Degradation rate of the embankment crest and the equilibrium crest height were compared for different compaction levels.

It has been found that the peak discharge decreased with the compaction level, while the time to peak increased. Non-dimensional relations are derived to describe the peak discharge and time to peak as functions of compaction effort. Two non-dimensional equations are proposed that express the rising and the falling limb of the breach outflow hydrograph for different levels of compaction. Furthermore, based on the measured data, two dimensionless 3rd order polynomial equations are developed to predict the crest height and embankment bottom length with time as a function of dry unit weight of the embankment. Finally, a simple triangular model is proposed to predict the development of the breach shape with time for different compaction levels of the embankment. Except for the very initial stage of the failure, the proposed model matches well with the

observed data. The applicability of the present study to predict the maximum crest height is confirmed against another laboratory study available in the literature with different embankment dimension, inflow discharge, and erosion process as well as three recent real cases of dam failures.

The developed equations and the simple triangular model presented in this study are based on non-dimensional parameters and therefore they can be applied as an approximation to predict the breach characteristics (i.e., crest height, bottom length, and breach outflow) at different scales. However, the present findings and the proposed models are limited to homogenous, non-cohesive, small embankments. More systematic experiments are required to develop a complete model which incorporates other key parameters affecting the failure process (e.g., soil mixture and cohesion, embankment geometry, and approach flow rate). Furthermore, large scale experiments are necessary to confirm the applicability of the proposed model in the field.

9.2 Numerical Modeling of Earthen Dam Breach due to overtopping: Influence of Different model Parameters

Two-dimensional numerical simulations by using the iRIC-Nays2D model as well as the experimental tests of homogenous non-cohesive embankment failure due to overtopping are conducted to assess the effect of various modeling parameters namely: (1) turbulence model; (2) finite-difference approximation of the advection term; (3) sediment transport type; and (4) bedload transport formula. The main affecting parameter was demonstrated to be the bedload transport formula. A comparison between the simulated and observed breach outflow hydrograph indicates that the simulations are in better agreement with the

M.P.M. formula. However, the A.M. formula gives a better prediction of bed and water surface profiles after the initial failure stage.

9.3 Investigating the Effect of Compaction Characteristics on the Erodibility of a Cohesive Soil Using the JET Method

The results from the series of laboratory JET tests on a Sandy Loam soil showed that: 1) a wide range of erodibility, from very erodible to very resistant, was produced by changes in the compaction characteristics; 2) for a given compaction energy, the erosion resistance based on the detachment rate coefficient k_d tends to become maximum near the optimum compaction water content. On the dry side of optimum compaction water content, k_d decreases with steep gradients by increasing the water content, while it increases with a flatter gradient on the wet side; 3) At a given water content, the soil erosion resistance increases with compaction efforts; 4) compaction water content influences soil erodibility more than compaction energy, especially on the dry side of the optimum compaction water content; and 5) for a given compaction effort, the critical shear stress increases with water content up to an optimum water content and then it decreases which is in consistent with the k_d trends.

9.4 Experimental Modeling of Levee Failure Process due to Overtopping

A series of tests are conducted to quantitatively determine the failure process of an overtopped homogenous, non-cohesive, and non-compacted levee. Water surface velocity distributions, breach evolution, breach outflow, and time series of the water surface elevations at breach location are measured using proper techniques. Erodibility coefficients in both vertical and horizontal directions are determined from the experimental results and the corresponding bed-load transport formulas are proposed.

The proposed models may be used as input for estimating the breach process of a non-cohesive non-compacted levee in numerical models. However, the importance of modeling the failure of compacted and cohesive levees is recognized as they represent the typical levees. This chapter only considers a simple case of a non-compacted sand only levee to remove the complex effects of the compaction and cohesion. In the next phases of the study the effects of compaction, water content, and cohesion are considered. Also to confirm the applicability of the proposed model in the field, large scale experiments will be necessary.

9.5 Experimental Modeling of Earthen Levee Failure by Overtopping: Effects of Hydraulic Loads

The failure process of a non-cohesive and non-compacted levee is investigated by conducting six experiments by varying the inflow discharge and the downstream water depth. The temporal changes of the breach shape and the breach overflow hydrographs are measured for all the tests using the sliding rods technique and an ultrasonic water level sensor, respectively. Surface velocity distribution is measured using particle image velocimetry. Furthermore, the time history of the breach top width and the breach depth along the centerline of the levee crest are compared along with the time variation of the eroded volume for different test cases. It has been observed that the different stages of the erosion process for a levee is similar to that of a dam except for the asymmetry of erosion occurring on the upstream and downstream sides. The erosion process of the upstream bank of the breach is mainly due to the surface erosion only while for the downstream bank is due to both surface erosion and slope instability. The downstream boundary condition in the main channel significantly affects the breach overflow. Based on the

measured data, three dimensionless equations are developed to predict the breach top width, breach depth, and eroded breach volume with time as a function of the inflow discharge and downstream water depth. Finally, based on the derived empirical equations for the top width and the depth of the breach, a trapezoidal model with a constant bottom width is proposed to predict the breach shape with time along the centerline of the crest.

Only few studies on levee breach are available in the literature. Therefore, the detailed observations of the levee breach process from this study may be used by other researchers to validate their numerical models. The proposed trapezoidal model is simple and satisfactorily predicts the breach profile and total area along the centerline of the crest which is important for flood mitigation plans. However, additional experiments with different soil mixture, scales, and compaction are necessary to corroborate the applicability of the developed empirical relations at the field scale.

9.6 Experimental Modeling of Earthen Levee Failure by Overtopping: Effects of Compaction and cohesion

The effects of compaction on the overtopping failure of a non-cohesive levee are investigated by conduction a series of laboratory tests with four different levels of compaction. Breach geometry (i.e., breach top width and breach depth along the crest centerline, three-dimensional breach shape, and longitudinal bed surface profiles along the centerline of the pilot channel), and water surface elevations in the channel are monitored with time for all the tests using the sliding rods technique and an ultrasonic water level sensor, respectively. Breach outflow is calculated for all the tests from the balance of the constant inflow into the channel and the weir flow at downstream end of the channel. Breach eroded volume and breach submerged area along the crest centerline

are also calculated from the observations of the breach evolution and water surface elevations above the pilot channel. The compaction energy of the embankment material is found to be a controlling factor in the failure process.

The observed first three levee failure stages in this study (i.e., levee breach initiation, onset of widening, and widening acceleration) are consistent with those observed in the large-scale levee breach experiments of Kakinuma and Shimizu (2014), except the last stage of widening deceleration which is not captured in the current study due to the limited length of the earthen section. Beside, a non-symmetric breach development is observed in all the experiments as the downstream bank of the breach is struck by higher shear stresses comparing to the upstream side which results in a faster erosion on the downstream side-wall of the breach.

To quantify the breach morphology, two non-dimensional equations are proposed which express the deepening and widening rates of a breach along the crest centerline as a function of the excess shear stress and compaction level of the embankment material. The proposed models are then compared against the measurements from the laboratory tests presented in the current study. Moreover, another non-dimensional relation is developed to predict the breached-load as a function of effective shear stress and compaction energy. The comparison between the experimental observations from this study and the predicted values from the model demonstrates that the proposed equation may be used satisfactorily to approximate the eroded volume of the levee material.

Moreover, the effects of cohesion on the failure of an overtopped levee are investigated by conducting four extra experiments with varying the silt and clay content of the embankment material. Increasing the clay content is significantly increasing the

levee erosion resistant, while changing the silt content is not as effective as the clay content. Envelope curves are developed to compare the effects of soil compaction with soil cohesion on the failure process. The cohesion and specifically the clay content is found to be the most dominant parameter controlling the breaching process.

9.7 Recommendations

Due to the complex nature of the earthen embankment and parameters and mechanisms affecting their failure, it is not possible to cover all these components in this study. Therefore, the following future research opportunities are suggested to further develop the knowledge of earthen embankment failures:

a) Conduct field-scale experiments: To remove the scale effects and to develop more reliable relations, it is necessary to conduct earthen embankment failure tests at large-scale. Series of tests can be done with systematically changing the compaction and cohesion, to investigate the effects of these components on the levee and dam failure.

b) Study the embankment shape effects: Several experimental tests with different shapes of the embankment (i.e., different downstream and upstream slopes, embankment height, and crest width) can be conducted to assess the shape effects on the failure process.

c) Study the piping failure of a levee: After overtopping, piping is considered to be the most common cause of the embankment failures. Therefore, it is beneficial to investigate this mechanism of failure, especially for the levee failures since there are not many studies on this topic in the literature.

d) Laboratory experiments under constant head: To better simulate a large storage behind the dams and levees, aforementioned tests in this study should be conducted with a constant head reservoir.

REFERENCES

Andrews, D. P. (1998). *Embankment failure due to overtopping flow*. ME thesis, Univ. of Auckland, Auckland, New Zealand.

ASCE/EWRI Task Committee on Dam/Levee Breaching (2011). "Earthen Embankment Breaching." *J. Hydraul. Eng.*, 10.1061/(ASCE)HY.1943-7900.0000498, 1549-1564.

Ashida, K., Michiue, M. (1972). Study on Hydraulic Resistance and Bedload Transport Rate in Alluvial Streams. *Proc. JSCE* 206, 59–69 (in Japanese).

Briaud, J. L., F. C. K. Ting, H. C. Chen, Y. Cao, S. W. Han, and K. W. Kwak. 2001. Erosion function apparatus for scour rate predictions. *J. of Geotechnical and Geoenvironmental Engineering,* ASCE 127(2): 105-113.

Cao, Z., Yue, Z., and Pender, G. (2011). "Landslide dam failure and flood hydraulics. Part I: Experimental investigation. Part II: Coupled mathematical modeling." *Natural Hazards*, 59(2), 1003–1045.

Chinnarasri, C., Jirakitlerd, S., & Wongwises, S. (2004). Embankment dam breach and its outflow characteristics. *Civil Eng. Envir. Systems, 21(4)*, 247–264.

Chinnarasri, C., Tingsanchali, T., Weesakul, S., & Wongwises, S. (2003). Flow patterns and damage of dike overtopping. *Intl. J.Sediment Res., 18(4)*, 301–309.

Chow, V. T. (1959). *Open-Channel Hydraulics*. New York, N.Y.: McGraw-Hill.

Clark, L.A., and T. M. Wynn. 2007. Methods for determining streambank critical shear stress and soil erodibility: implications for erosion rate predictions. Trans ASABE 50(1): 95–106.

Coleman, S. E., Andrews, D. P., & Webby, M. G. (2002). Overtopping breaching of noncohesive homogenous embankments. *J. Hydraulic Eng., 128(9)*, 829–838.

Coleman, S. E., Jack, R. C., & Melville, B. W. (1997). Overtopping breaching of noncohesive embankment dams. *Proc., 27th Congress of the Int. Association for Hydraulic Research, San Francisco*, D42– D47.

Dillaha, T. A., and D. B. Beasley. 1983. Distributed parameter modeling of sediment movement and particle size distribution. *Transactions of the ASAE* 26(6): 1716-1722.

Dupont, E., Dewals, B.J., Archambeau, P., Erpicum, S., & Pirotton, M. (2007). Experimental and numerical study of the breaching of embankment dam. *Proc. 32nd IAHR Congress Venice 1(178)*, 1–10.

Foster, G. R., L. D. Meyer, and C. A. Onstad. 1977. An erosion equation derived from basic erosion principles. *Transactions of the ASAE* 20(4): 678-682.

Franca, M. J., and Almeida, A. B. (2004). "A computational model of rockfill dam breaching caused by overtopping (RoDaB)." *J. Hydr. Res.*, 42(2), 197–206.

Fread, D. L. (1984). "DAMBRK: The NWS dam break flood forecasting model." National Oceanic and Atmospheric Administration, National Weather Service, Silver Spring, MD.

Fread, D. L. (1988). "BREACH: An erosion model for earthen dam failures (Model description and user manual)." National Oceanic and Atmospheric Administration, National Weather Service, Silver Spring, MD.

Froehlich, D. C. (1995). Embankment dam breach parameters revisited. *Proc., 1995 Conf. on Water Resources Engineering , ASCE, New York*, 887–891.

Gheibi, E. (2016). "Improved assessment of the magnitude and acceleration of prehistoric earthquakes in the South Carolina Coastal Plain" Ph.D. Dissertation Submitted to the University of South Carolina, Columbia. SC. DOI: 10.13140/RG.2.1.1484.2486

Hagen, V. K. (1982). "Re-evaluation of design floods and dam safety." *Proc., 14th Congress of Int. Comm. on Large Dams*, Int. Comm. On Large Dams, Paris.

Hager, W. (1987). "Lateral Outflow Over Side Weirs." *J. Hydraul. Eng.*, 10.1061/(ASCE)0733-9429(1987)113:4(491), 491-504.

Hanson, G. J. 1989. Channel erosion study of two compacted soils. *Transactions of the ASAE* 32(2): 485-490.

Hanson, G. J., and K. R. Cook. 2004. Apparatus, test procedures and analytical methods to measure soil erodibility in situ. *Applied Engineering in Agriculture* 20(4): 455-462.

Hanson, G. J., and S. L. Hunt. 2007. Lessons learned using laboratory JET method to measure soil erodibility of compacted soils. *Applied Eng. in Agric.* 23(3):305-312.

Hanson, G. J., Cook, K. R., Hahn, W., & Britton, S. L. (2003). Evaluating erosion widening and headcut migration rates for embankment overtopping tests. ASAE Paper No. 032067. St. Joseph, Mich.: ASAE.

Hunt, S. L., Hanson, G. J., Cook, K. R., and Kadavy, K. C. (2005). “Breach widening observations from earthen embankment tests.” *Trans. ASAE*, 48(3), 1115–1120.

Hutchinson, D. L. 1972. Physics of erosion of cohesive soils. Ph.D. thesis. New Zealand: University of Aukland.

Itakura, T., Kishi, T. (1980). Open channel flow with suspended sediments. *J. Hydraulics Division*. 106(8), 1325-1343.

Iwagaki, Y. (1956). Fundamental study on critical tractive force. *Trans JSCE.* 41, 1–21.

Jack, R. (1996). *The mechanics of embankment failure due to overtopping flow*. ME thesis, Univ. of Auckland, Auckland, New Zealand.

Jarrett, R. D., and Costa, J. E. (1986). “Hydrology, geomorphology, and dam-break modeling of the July 15, 1982 Lawn Lake Dam and Cascade Lake Dam failures, Larimer County, Colorado.” *U.S. Geological Survey Professional Paper 1369,* Denver Federal Center, CO.

Kakinuma, T. and Shimizu, Y. (2014). "Large-Scale Experiment and Numerical Modeling of a Riverine Levee Breach." *J. Hydraul. Eng.*, 10.1061/(ASCE)HY.1943-7900.0000902, 04014039.

Kamphius, W. J., and K. R. Hall. 1983. Cohesive material erosion by unidirectional current. *J. of Hydr. Eng.,* ASCE 109(1): 1076-1081.

Kirkpatrick, G. W. (1977). “Evaluation guidelines for spillway adequacy.” *The evaluation of dam safety: Engineering Foundation Conf. Proc.*, ASCE, New York, 395–414.

MacDonald, T.C., Langridge-Monopolis, J. (1984). Breaching characteristics of dam failures. *J. Hydraulic Engineering*. 110(5), 567-586.

Meyer-Peter, E., Mu¨ller, R. (1948). Formulas for bed-load transport. *2nd IAHR Congress,* Stockholm, 39– 64.

Mohamed, A. A. A., Samuels, P. G., Morris, M. W., and Ghataora, G. S. (2002). “Improving the accuracy of prediction of breach formation through embankment dams and flood embankments.” *Proc., Int. Conf. on Fluvial Hydraulics (River Flow 2002),* Louvain-la-Neuve, Belgium.

Morris, M.W., Kortenhaus, A., and Visser, P. J. (2009). “Modeling breach initiation and growth.” *FLOODsite Rep. T06-08-02*, FLOODsite Consortium, ⟨www.floodsite.net⟩.

Parker, G., Toro-Escobar, C. M., Ramey, M. and S. Beck, (2003). “The effect of floodwater extraction on the morphology of mountain streams.” *J. Hydraul. Eng.*, 129(11), 885-895.

Pierce, M. W., Thornton, C. I., and Abt, S. R. (2010). “Predicting peak outflow from breached embankment dams.” *J. Hydrol. Eng.*, 15(5), 338–349.

Ponce, V. M. (1982). “Documented cases of earth dam breaches.” Res. Rep. SDSU Civil Eng. Series, No. 82149, San Diego State Univ., CA, 43.

Pontillo, M., Schmocker, L., Greco, M., & Hager, W. H. (2010). 1D numerical evaluation of dike erosion due to overtopping. *J. Hydraulic Res. 48(5)*, 573-582.

Powledge, G. R., Ralston, D. C., Miller, P., Chen, Y. H., Cloppner, P. E., & Temple, D. M. (1989). Mechanics of overflow erosion on embankments II: Hydraulic and design considerations. *J. Hydraulic Eng., 115(8)*, 1056–1075.

Pugh, C. A. (1985). “Hydraulic model studies of fuse plug embankments.” REC-ERC-85-7. Denver, Colo.: U.S. Bureau of Reclamation.

Rubey, W.W. (1933). Equilibrium-conditions in debris-laden streams. *Trans. AGU*. 14(1), 497-505.

Schmocker, L. (2011). Hydraulics of dike breaching. *PhD Dissertation, VAW-Mitteilung* 218, R.M. Boes, ed. ETH Zurich, Zürich.

Schmocker, L., & Hager, W.H. (2009). Modelling dike breaching due to overtopping. *J. Hydraulic Res. 47(5)*, 585–597.

Schmocker, L., & Hager, W.H. (2012). Plane dike breaching due to overtopping: Effects of sediment, dike height and discharge. *J. Hydraulic Res. 50(6)*, 576–586.

Schmocker, L., Halldórsdóttir, B. R. and Hager, W. H. (2011). Effect of weir face angles on circular-crested weir flow. J. Hydraulic Eng., 137(6): 637–643.

Simmler, H., & Sametz, L. (1982). Dam failure from overtopping studied on a hydraulic model, ICOLD, Fourteenth Congress, Vol. I, Q.52, R.26, 427-445.

Singh, V.P., Scarlatos, P.D. (1988). Analysis of gradual earth-dam failure. *J. Hydraulic Engineering*. 114(1), 21-42.

Smerdon, E. T., and R. P. Beasley. 1959. The tractive force theory applied to stability of open channels in cohesive soil. Research Bull. 715. Univ. of Missouri. Ag. Exp. Station. Columbia, Mo.

Stein, O. R., and D. D. Nett. 1997. Impinging jet calibration of excess shear sediment detachment parameters. *Transactions of the ASAE* 40(6): 1573-1580.

Temple, D. M. 1985. Stability of grass-lined channels following mowing. *Transactions of the ASAE* 28(3): 750-754.

Temple, D.M., Hanson, G.J., Nielsen, M.L., and Cook, K., 2005. Simplified breach analysis model for homogeneous embankments: Part 1, Background and model components. USSD Technologies to Enhance Dam Safety and the Environment, 25th Annual USSD Conference, Salt Lake City, Utah.

Thielicke, W. (2014): The Flapping Flight of Birds - Analysis and Application. Phd thesis, Rijksuniversiteit Groningen.

Thielicke, W. and Stamhuis, E. J. (2014a): PIVlab - Time-Resolved Digital Particle Image Velocimetry Tool for MATLAB (version: 1.35).

Thielicke, W. and Stamhuis, E.J. (2014b): PIVlab – Towards User-friendly, Affordable and Accurate Digital Particle Image Velocimetry in MATLAB. Journal of Open Research Software 2(1):e30.

Tingsanchali, T., and Chinnarasri, C. (2001). “Numerical modeling of dam failure due to flow overtopping.” *Hydrol. Sci. J.*, 46(1), 113–130.

Tinney, R. E., and H. Y. Hsu. (1961). “Mechanics of washout of an erodible fuse plug.” *J. Hydraulics Division of ASCE*, 87(3): 1-30.

U.S. Bureau of Reclamation (USBR). (1988). Downstream hazard classification guidelines. ACER Tech. Memorandum No. 11 , U.S. Department of the Interior, Denver, 57.

Visser, P. J. (1998). Breach growth on sand-dikes. In Communications on Hydraulic and Geotechnical Engineering. Report No. 98.1. Delft, The Netherlands: Delft University of Technology.

Von Thun, J. L., and Gillette, D. R. (1990). “Guidance on breach parameters.” *Internal Memorandum*, Bureau of Reclamation, U.S. Dept. of the Interior, Denver, 17.

Wahl, T. L. (2007). Laboratory investigations of embankment dam erosion and breach processes. Rep. T032700-0207A, EA Technologies (CEATI), Montréal, Canada.

Wan, C. F., and R. Fell. 2004. Investigation of rate of erosion of soils in embankment dams. *J. of Geotechnical and Geoenvironmental Engineering,* ASCE 130(4): 373-380.

Wang, G. Q., Zhong, D. Y., Zhang, H.W., Sun, Q. C., and Hu, D. C. (2008). "Numerical modeling of breach process of Tangjiashan landslide dam generated by Wenchuan earthquake." *Sci. Commun.*, 53(24), 3127–3133 (in Chinese).

Wang, Z., and Bowles, D. S. (2006). "Three-dimensional non-cohesive earthen dam breach model. Part 1: Theory and methodology." *Adv. Water Resour*., 29(10), 1528–1545.

Xu, Y., and Zhang, L. M. (2009). "Breaching parameters for earth and rockfill dams." *J. Geotech. Geoenviron. Eng.*, 135(12), 1957–196

APPENDIX A

PERMISSION TO REPRINT

Gmail Ali Tabrizi <ali.a.tabrizi@gmail.com>

RE: TJHR 1238014 - author needs confirmation to reuse in dissertation
2 messages

Norris, Eilise <Eilise.Norris@tandf.co.uk> Thu, Nov 17, 2016 at 9:11 AM
To: "ali.a.tabrizi@gmail.com" <ali.a.tabrizi@gmail.com>
Cc: "Gough, Helen" <Helen.Gough@informa.com>

Dear Ali,

In answer to your query about obtaining permission to reprint your paper in your dissertation, I can confirm that you have the following:

The right to include the article in a thesis or dissertation that is not to be published commercially, provided that acknowledgement to prior publication in the Journal is given.

I hope this helps.

Best wishes,

Eilise

Eilise Norris – Editorial Assistant

Earth and Environmental Science Journals

Taylor & Francis Group.

4 Park Square, Milton Park, Abingdon, Oxon, OX14 4RN, UK.

Tel: 020 7551 9561

Web: www.tandfonline.com

e-mail: eilise.norris@tandf.co.uk